Experimental measurements of thermal barrier coating interfacial fracture toughness as a function of mode-mix

by

Simon Lockyer-Bratton

A thesis submitted to Johns Hopkins University in conformity with the requirements for the degree of Doctor of Philosophy

Baltimore, Maryland

July 2016

ABSTRACT

Mechanism-based lifetime assessment models of thermal barrier coating (TBC) systems for gas turbine engines rely on accurate knowledge of the experimentally measured interfacial fracture toughness over a range of mode mix and especially at mode-II. Previously no reliable test method had been employed to evaluate these properties under pure mode-II conditions, which are most representative of critical TBC spall delamination upon turbine engine cool down.

A newly developed compression edge-delamination (CED) test, based off of theoretical considerations by John Hutchinson, has been employed to measure the strain energy release rate (G_c) associated with delamination between the bond coat and top coat layers under a nearly pure mode-II loading condition. Utilizing modified 4-point bend experiments and the CED methodology, has allowed for direct measurement of coating interfacial toughness as a function of mode mix.

The material system examined was provided by collaborators at GE and consists of an Electron-Beam Physical Vapor Deposited (EBPVD) 7% Yttria-Stabilized Zirconia (YSZ) top coat, which is deposited on a Pt-modified diffusion aluminide β-(Ni,Pt)Al bond coat on a single crystal René N5 substrate. Using the CED test, a 50% reduction in mode-II interfacial toughness was associated with thermal cycling. Results for as-deposited samples tested using a modified 4-point bend technique matches previously reported data, and a mode-mix dependent toughness function for the as-deposited interfacial toughness has also been discovered using results from this study and from previously reported values.

Specimen design and preparation and the use of starter cracks to assure proper delamination are discussed. Crack face friction is shown to play a significant role in calculation of the interfacial toughness and details regarding the experimental characterization of the interfacial friction coefficient and implementation into the finite element model used to extract the interfacial toughness are examined. Details regarding the use of Digital Image Correlation (DIC) to calculate the critical stress for crack growth in the CED test are also be discussed. Results from the both the CED and the modified 4-point bend experiments are examined and analyzed along with microstructural and chemical observations of degradation of the coating interfaces as a result of thermal cycling.

Advisor: Professor Kevin J. Hemker

Readers: Professors Kevin J. Hemker and Jaafar El-Awady and Dr. Jeremiah MacSleyne of GE Aviation

ACKNOWLEDGEMENTS

After five years in the Hemker Group at Johns Hopkins University I owe the successful completion of this chapter of my life to many people. I would like to begin by thanking my Ph.D. advisor, Professor Kevin Hemker, for his inspiration and guidance over the course of my time in his research group. His continual encouragement and support helped me to grow as both a scientist and as a professional. His reassurance helped me to overcome the many challenges associated with experimental research and my success would not have been made possible without his supportive presence. I am very grateful for the time I have been able to spend under his guidance and will forever be indebted to him. I would also like to thank Dr. Jaafar El-Awady, Dr. Jeremiah MacSleyne and Dr. Doug Konitzer for their continual guidance throughout the course of my studies as well as their help in reading and editing my thesis.

I had the pleasure of working with many amazing people at Johns Hopkins and especially in the Hemker Group. The list of people I would like to thank includes, in no particular order; Binwei Zhang, Brady Butler, Glenn Balbus, Evan Langdale, Neha Dixit, Kelvin Xie, Zafir Alam, Yong Zhang, Stephen Ryan, Alex Caffee, Ahmed Hussein, Vignesh Kannan, Devin Burns, Gi-Dong Sim, Betsy Congdon, David Eastman, Barbara Murienne, Gianna Valentino, and Paul Rottmann. I apologize for anybody whose name I have forgotten to mention. I would like to especially thank Suman Dasgupta for his many years of friendship and support. Suman and I both started at the same time in the Hemker Group and we became lifelong friends immediately. I must particularly thank him for all the Chole and Parathas he prepared for Nadia and I when we invited ourselves over for dinner on numerous occasions.

I would like to give special thanks my wonderful mother, Kathleen Moorhead, whose love and caring nature has made me the person that I am today. I would also like to thank my extended family, Hassan Rezakhani and Amin Fotowat. Hassan has been a great brother in-law and a constant source of humor, legal advice and fanciful tales. I would like to especially thank Amin as he is the whole reason I was able to get to Johns Hopkins and for his constant kindness and his ability to comfort you no matter what the situation is.

I dedicate this thesis to my loving and beautiful wife Nadia Rezakhani. Without her encouragement and support I would not have been able to make it through my research and studies. She means everything to me and has provided me with the will to persevere through times that seemed insurmountable. I would also like to thank (and apologize) for her dealing with me when I became unbearable to be around during the times leading up to my qualifying exams. She also spent countless late-night hours in the lab with me when I was having difficulty with my research and was a great source of encouragement and advice that was invaluable. I cannot express how fortunate I am to have her in my life and will continue to love “my little bird” more and more every day that passes.

I would lastly like to thank all my wonderful pets, both past and present, for bringing so much joy into my life; Chloe, Sheba, Kimberley, Bert, Tinkerbell, Sophie, Casey, Calvin, Heidi, Jessie, Shirin and Niloo.

TABLE OF CONTENTS

LIST OF FIGURES

CHAPTER 1: INTRODUCTION AND BACKGROUND

The continued research and development of thermal barrier coating (TBC) systems over the past few decades has led to dramatic increases in the performance of modern gas turbine engines. This research has led to longer lasting coatings that can withstand higher operating temperatures for longer periods of time. This chapter will serve to provide the motivation behind previously conducted research and development activities and will introduce the issues present in the TBC system that have motivated this study. A brief background on interfacial fracture testing provides the groundwork necessary for the remainder of the chapter. A summary of the constituent layers and materials found in gas turbine engines are then presented. Details regarding damage mechanisms and life prediction methodologies will be discussed with additional emphasis on limitations present in current testing techniques. This chapter concludes with a brief overview of the remainder of the thesis.

1.1 Motivation and Focus of Research

The development of lighter and tougher materials coupled with innovations in engineering design has had a profound effect on contemporary life. Modern gas turbine engines are a testament to the change that can occur when novel material design and exemplary engineering come together. This feat of engineering design has allowed mankind to travel all over the world and helps to provide power to both homes and businesses. Unfortunately, the power source for these engines has historically been provided by the combustion of non-renewable fossil fuels, which include both oil and natural gas. Due to issues regarding depletion of natural resources, degradation of the environment during oil drilling and issues of dependence on oil from regions with political unrest has led to a key focus of scientific

research to find more efficient ways of using this energy source. One of the ways to achieve higher efficiency is to run turbine engines at higher operating temperatures, but with that comes many new problems, one of which is new failure mechanisms leading to delamination of the protective coatings in the engine. It is therefore of utmost importance to understand the failure mechanisms of these protective coatings so that they can be designed against failure to ensure a safe and long lasting coating.

1.2 Brief Background on Interfacial Fracture Testing

During a fracture event in a homogeneous material, decohesion between atoms and/or molecules happens as crack propagation occurs. The field of fracture mechanics has been developed to address the analysis of fracture events and design against fracture. The foundations of fracture mechanics were laid down by A.A. Griffith in 1921 in his seminal article *The Phenomena of Rupture and Flow in Solids* [1]. Important distinctions need to be recognized regarding the bonding of material: cohesion is the property of like atoms to bond together whereas adhesion relates to the bonding of two dissimilar materials. The core approach to characterize the energy release during crack propagation is essentially the same for cohesion and adhesion, but the experimental methodologies and analytic methods can be vastly different due to the inclusion of two different materials with different material properties present in the same test specimen. A number of different test methods exist for testing bi-material and multi-layered material systems [2-5].

Complications arise when studying a material system with a substrate and coating layer if the coating cannot be manipulated in the same manner as the substrate. This can occur when the coating layer is either very thin compared to the substrate or when the coating is much weaker than the substrate. One approach to investigate interlaminar fracture was first

published by Charalambides et al. in 1989, in which a four-point bend test specimen is implemented to measure the critical strain energy release rate during crack propagation [4]. In this test a constant moment is applied to the sample to ensure a constant strain energy release rate, G_c, that is independent of the crack length during delamination.

Recently a new test methodology was proposed by Hutchinson and Hutchinson [6], called the compression edge-delamination test, that has the potential to measure the interfacial toughness under pure mode II conditions ($\phi = -90°$), which is most representative of the loading experienced by the coating during delamination upon engine cool down. This methodology is developed beyond its theoretical framework in CHAPTER 3: COMPRESSION EDGE-DELAMINATION TEST and is the core focus of this study.

1.3 Gas Turbine Engines

The concept of utilizing hot gasses passing through nozzles to generate power has been around for many centuries, with the first patent for a gas turbine engine being issued in 1791 [7]. It took almost another 140 years for the first modern gas turbine engine to be constructed; in the 1930's Frank Whittle, from England, and Hans von Ohaim, from Germany, each independently created their own turbine engines over a several year period [8]. With the advent of World War II came the desire to achieve air warfare superiority and the drive to create turbine engines, whose power to weight ratios were far greater than internal combustion engine counterparts, was hastened. As time progressed five distinct types of gas turbine engines were created: turbojets, turboprops, turboshafts, low-bypass turbofans and the high-bypass turbofans.

Turbojets were the earliest developed and are the simplest of all the gas turbine engines. The engines operate through a high velocity gas that provides the sole source of thrust for the engine. A schematic of this engine type can be seen in Figure 1-1.

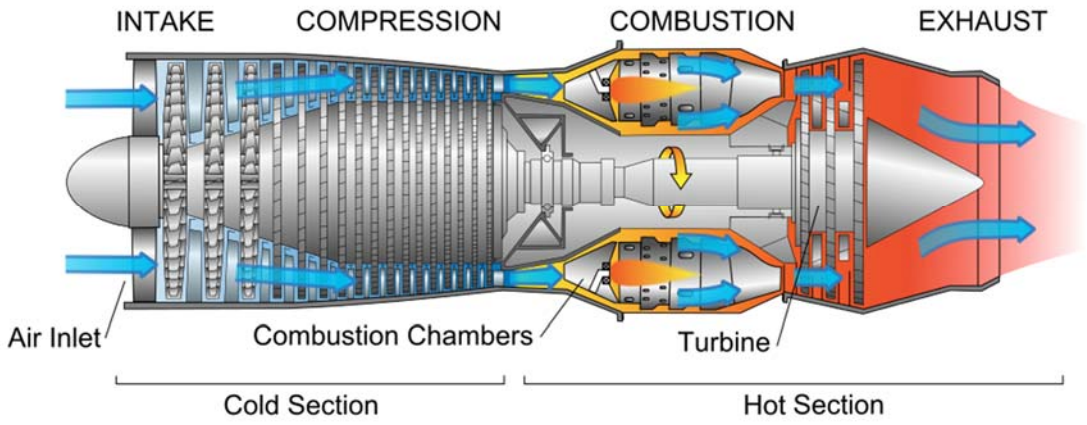

Figure 1-1: Schematic of turbojet engine (taken from [9])

Since all of the air that is drawn through the air inlet is compressed and used for combustion this engine typically exhibits high levels of both noise and fuel consumption. This design is now considered to be inefficient and the advent of turbofans has all but made turbojets obsolete, save for military applications where maximum thrust is more important than noise and fuel economy.

Turboprops are an extension of turbojets that incorporate a geared connection between the turbine shaft and a propeller that is used to provide the thrust for the engine. In this engine the turbine engine is used to provide power to a propeller, which rotates and acts on a large volume of air to provide thrust. A schematic of this engine type is shown in Figure 1-2.

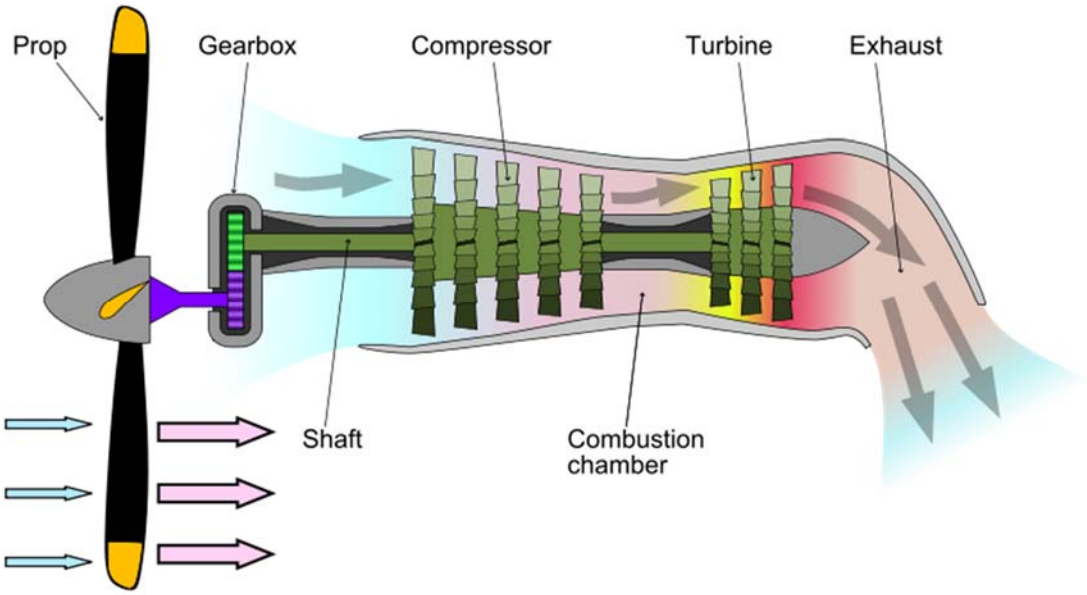

Figure 1-2: Schematic of turboprop turbine engine (taken from [10])

These types of engines are limited by the rotational speed of the propeller, as it can become unstable at higher speeds, and are typically used in low speed applications. Turboprops are typically used on smaller commercial aircraft as well on large cargo planes, where a high speed is not necessary.

Turboshaft engines are very similar to turbojets, but are optimized for power generation rather than thrust generation. The turboshaft generates its power by driving a rotating free turbine blade that is attached to a power shaft, which is in turn attached to an electrical generator through a gear box. A schematic of a turboshaft engine can be seen in Figure 1-3. These engines are used as large land-based turbines for power generation as well as being used to power helicopters, navy vessels and modern tanks such as the M1 Abrams. It should be noted that in land-based turbines the power to weight ratio is not of principal concern and can be quite large.

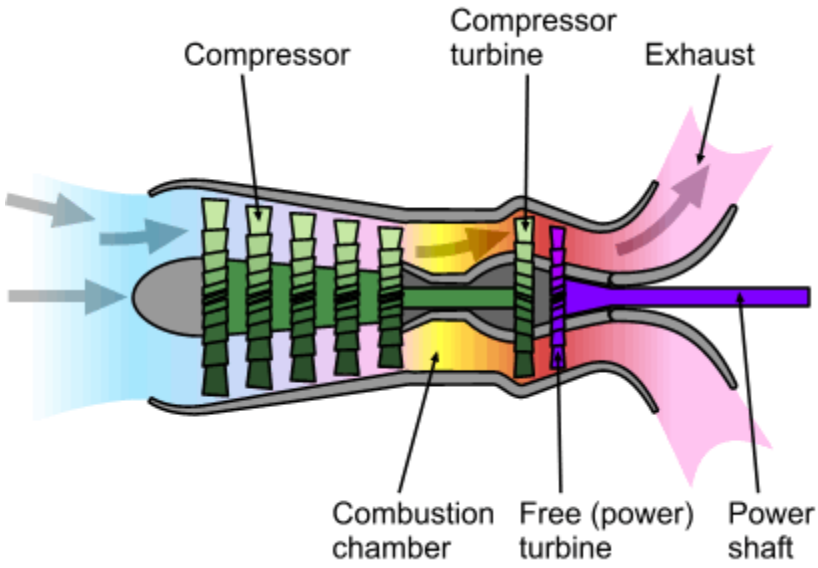

Figure 1-3: Schematic of turboshaft jet engine (taken from [11])

Both the low-bypass turbofan and the high-bypass turbofan are based off of the turbojet design, but make use of an air-bypass. This air-bypass allows some of the air that passes through the main fan to be used for thrust instead of passing through the jet engine. The implementation of the air bypass allows for a simultaneous reduction in the noise and fuel consumption of the engine. A low-bypass turbofan allows for some of the inlet air to be bypassed around the body of the turbine engine to provide thrust as opposed to the turbojet engine where all of the inlet air is compressed and combusted in the turbine engine. A schematic of this engine type can be seen in part (a) of Figure 1-4. Low-bypass engines typically operate more efficiently at higher speeds than at lower speeds and are capable of supersonic flight operation. These engines can also have an additional afterburner component that injects and burns fuel after the low-pressure turbine and before the nozzle, which serves to provide a significant increase in thrust at the expense of large amounts of consumed fuel.

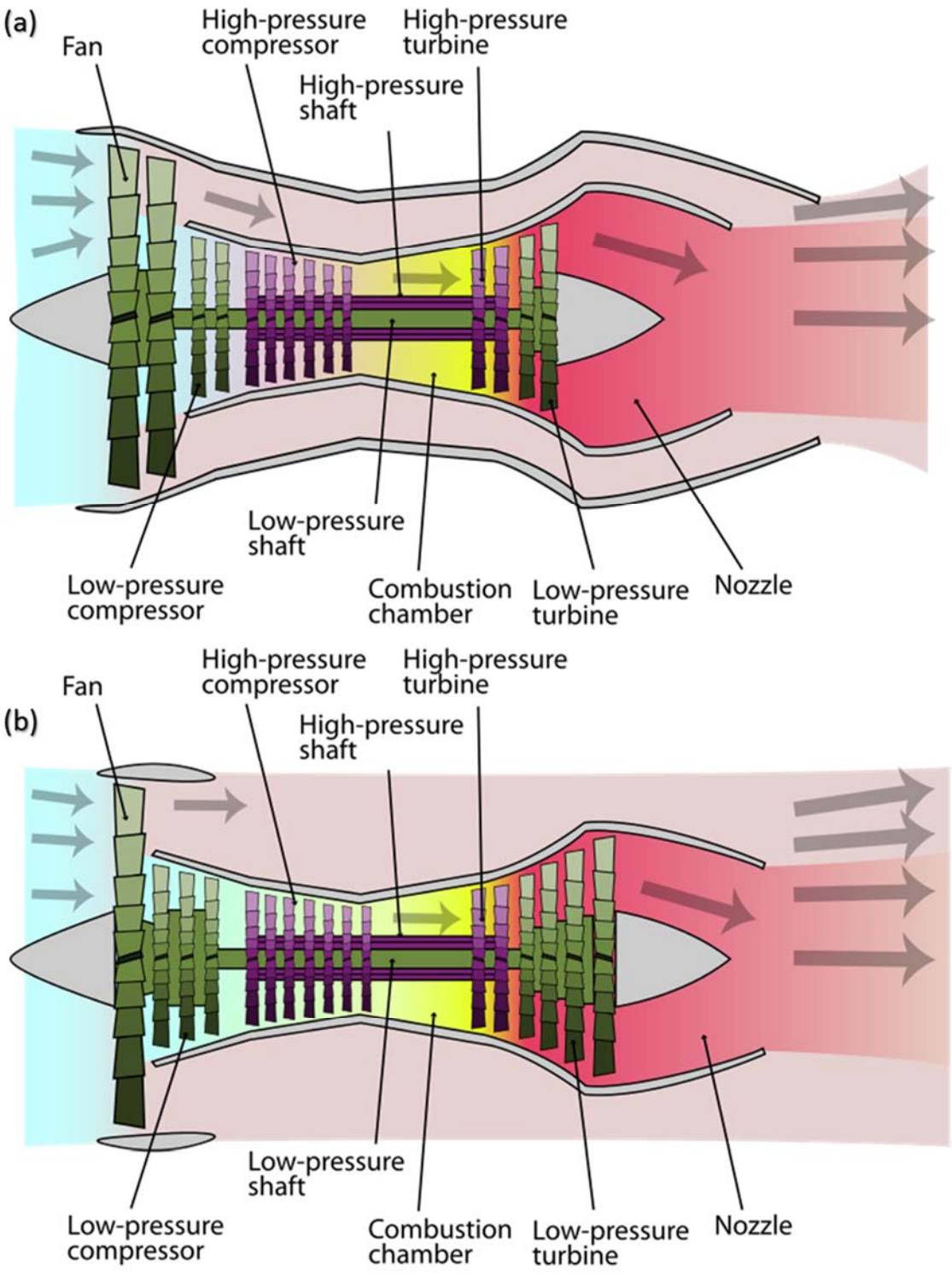

Figure 1-4: Schematic of a (a) low-bypass turbofan jet turbine engine and a (b) high-bypass turbofan jet turbine engine (taken from [12, 13])

The afterburner feature is typically reserved for take-off and for combat situations. These aspects typically reserve the low-bypass engine for use on military aircraft where higher performance is desired at the expense of fuel efficiency.

The high-bypass turbofan jet engine evolved from the low-bypass design and allows for a higher fuel economy at the expense of a lower specific thrust. This is accomplished by allowing more of the inlet air to be used to provide the thrust as opposed to the low-bypass turbofan design and especially the "zero-bypass" turbojet design. The high-bypass turbofan provides an engine whose maximum aircraft speed is higher than a turboprop but lower than a low-bypass turbofan.

The primary thermodynamic aspect of these engines that can be easily changed is the amount of fuel added to the combustion chamber. Adding more fuel to the combustion chamber will results in an increase in the combustion temperature. Open cycle gas turbine engines, such as in turbofans, operate on the Brayton cycle, which is shown schematically in Figure 1-5.

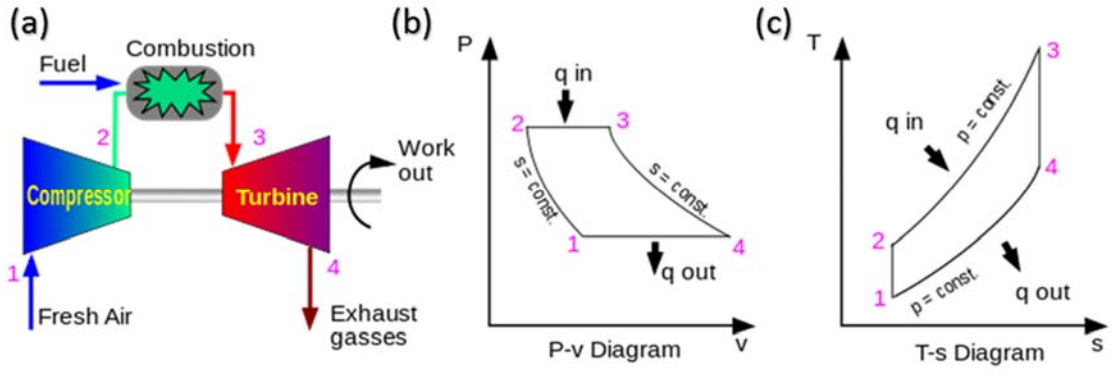

Figure 1-5: (a) schematic of Brayton cycle, (b) pressure vs. volume diagram for Brayton cycle and (c) temperature vs. entropy diagram for Brayton cycle (taken from [14])

This cycle is composed of four thermodynamic processes: a) $1 \rightarrow 2$: isentropic compression, b) $2 \rightarrow 3$: reversible isobaric heat addition, c) $3 \rightarrow 4$: isentropic expansion and d) $4 \rightarrow 1$: reversible isobaric heat rejection. This process is also commonly referred to as a) suck, b) squeeze, c) bang and d) blow, as described by Todd Wetzel, an aerospace engineer and thermal systems leader at GE Global Research Center [15]. The efficiency of the Brayton cycle can be defined in terms of both temperature and pressure:

Equation 1-1

$$\eta_{Brayton} = 1 - \frac{T_1}{T_2} = 1 - \left(\frac{P_1}{P_2}\right)^{\frac{(\gamma-1)}{\gamma}}$$

where T_i is temperature at step i, P_i is the pressure at stage i and γ is the heat capacity ratio. Typical thermal efficiencies for gas turbine engines range from 35 to 60%, which is far more efficient than the 25% efficiency attributed to internal combustion engines [16]. As the inlet temperature is governed by ambient conditions it is readily seen that in order to increase the efficiency of the Brayton cycle, one must increase the temperature at stage 2. Ultimately, the temperate increase that is possible is limited by the high temperature material properties present in the turbine engine that correspond to stage 3: in the high-pressure turbine (HPT) region. The increases made in efficiency over the years of development has been made possible by use of advanced Ni-based superalloys, cooling and thermal barrier coatings (TBC), which all allow for higher temperature in the HPT portion of the turbine. The primary focus of this dissertation work will be on the TBC's used in the HPT region of high-bypass turbojet engines.

1.3.1 Modern Components

Modern turbofan gas turbine engines consist of an inlet fan, low-pressure compressor, high-pressure compressor, combustion chamber, high-pressure turbine, lower-pressure turbine, various shafts and an outlet nozzle. These components were also previously shown in Figure 1-4. Materials development in the latter part of the 20th century has led to an extraordinary transformation of the gas turbine engine. The schematic shown in Figure 1-6 helps to emphasize this point by showing a color coded map of the materials used in different parts of a Rolls Royce Trent high-bypass turbofan jet turbine engine.

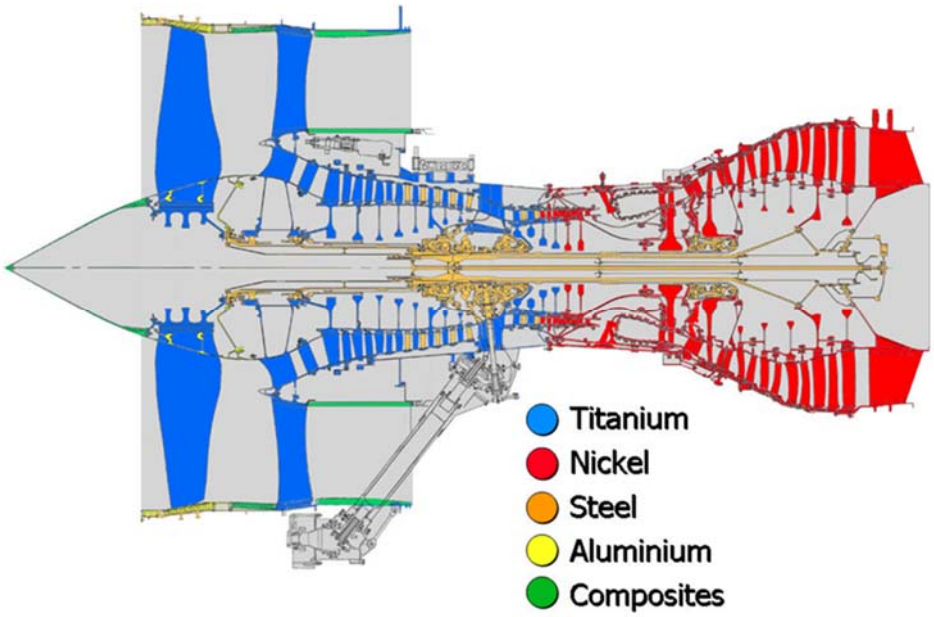

Figure 1-6: Schematic of Rolls Royce Trent high-bypass turbofan jet turbine engine color coded to show materials used in each section of the engine (taken from [17])

Early gas turbine engines relied heavily on stainless steel alloys, whereas Ni and Ti are now the primary materials for nearly all of the rotating components. The high specific strength of Ti at intermediate temperatures in the compressor portion of the engine make it ideal for fan and compressor blades while bringing the total weight of the engine down. The HPT portion of these engines is composed almost entirely of Ni-based superalloys,

which are chosen for their extraordinary high temperature strength and creep resistance. This has led to roughly 40% to 50% of the total weight of the engine due to Ni and Ni-based superalloys [18]. As previously mentioned, the drive for higher efficiency is achieved by running the engine at higher operating temperatures. The combustion gasses in a jet turbine engine could reach as high as $2000\ °C$, whereas the Ni-based superalloys present in the combustor can only withstand maximum service temperatures of $1300\ °C$ [19]. This is accomplished through the use of innovative cooling methods and, more importantly, thermal barrier coatings that have allowed the combustion gasses to operate at temperatures higher than the underlying metallic materials would be able to withstand. Cooling of the blades requires air to be bled off from the compressor. TBC's with higher temperature capabilities can reduce the needed cooling or result in longer TBC life under the same conditions.

1.3.2 Thermal Barrier Coatings

There are four primary layers present in a TBC system used in jet turbine engines: a) a superalloy substrate, b) an aluminum-rich bond coat deposited on the surface of the substrate, c) a thermally grown oxide (TGO) that grows on top of the bond coat and d) a ceramic top coat layer. A cutaway of an Engine Alliance GP7200 high-bypass turbofan engine showing the high-pressure and temperature blade and SEM micrograph of thermal barrier coating system can be seen in Figure 1-7. In the HPT of region of the engine, the turbine blades are composed of a single-crystal Ni-based superalloy. The core of the turbine blade is designed with internal cooling channels to help keep the blade within operating temperatures. Deposited on top of the substrate is a roughly $100\ \mu m$ thick Al-rich bond

coat, which is typically either a NiCoCrAlY low pressure plasma sprayed (LPPS) or a β-(Pt,Al) platinum modified diffusion aluminide bond coat.

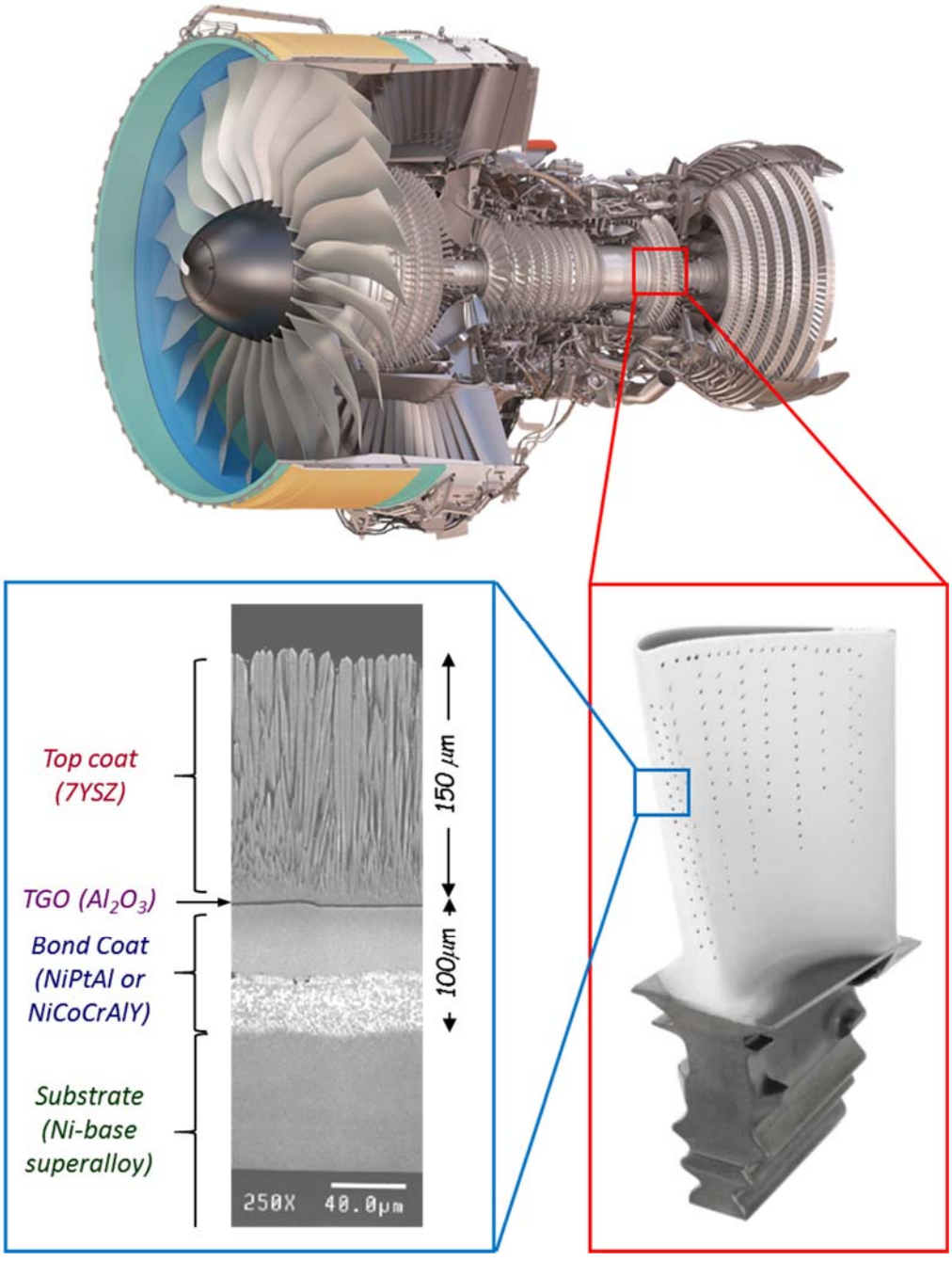

Figure 1-7: Cutaway of Engine Alliance GP7200 high-bypass turbofan engine (taken from [20]) showing high-pressure and temperature blade (taken from [21]) and SEM micrograph of thermal barrier coating system

In either case the bond coat layer contains excess aluminum that allows for the growth of the thermally grown oxide (TGO) layer. This layer, which is composed primarily of α-Al_2O_3, provides the oxidation resistance to the coating and protects the underlying substrate and bond coat from the hot oxidizing combustion gasses. The final layer is an approximately $150\ \mu m$ thick 7% Yttria-Stabilized Zirconia (YSZ) layer, which provides the thermal protection for the system. The top coat is deposited using electron-beam physical vapor deposition (EBPVD) and exhibits a columnar microstructure with each column being composed of a single crystal of 7% YSZ. YSZ is highly permeable to oxygen, and growth of the TGO through interaction of the hot oxidizing gasses with the excess Al in the bond coat provides protection against oxidation.

One of the most important aspects of the columnar microstructure is that it allows for a high in-plane compliance of the coating. This is especially important because when the turbine blades heat up and cool down large thermal stresses develop due to differences in the thermal expansion coefficients. If the top coat was composed of a dense YSZ then it would develop larger internal stresses than a low density coating and would fail prematurely. By allowing the coating to accommodate in-plane strain it can still provide thermal protection and increase coating durability. As the top coat plays such an important role in protecting the underlying material layers, large scale spallation of the top coat can lead to premature failure and degradation of the turbine blade. By gaining an understanding of the failure mechanisms and the overall coating lifetime, not only can designers develop inspection methods for assessing in-service blade health, but more importantly they can help to design against failure to create longer lasting blades. This insight can also guide development of new coating systems.

1.3.3 Empirical vs. Mechanistic Life Prediction Methodology

There are two general life prediction methodologies that can be used to assess hardware. The first and most straightforward method is an empirical life prediction methodology where accelerated life testing is conducted to determine the failure statistics of the coating. The lifetime of the coating can then be determined as being below some accumulative probability where failure can be expected to occur. The furnace cycle test is a common empirical life prediction method used to assess the durability of TBC systems. Samples for this test usually consist of a 1-inch diameter, superalloy button that is coated with a bond coat and top coat. The sample is placed in a furnace and heated up to a maximum hot temperature, held at this maximum temperature, T_H, for a certain period of time and is then removed from the furnace and is typically air cooled for a period of time until it reaches a prescribed cold temperature, T_C. An example of the heating and cooling profile for a typical 1-hour furnace cycle test is shown in Figure 1-8.

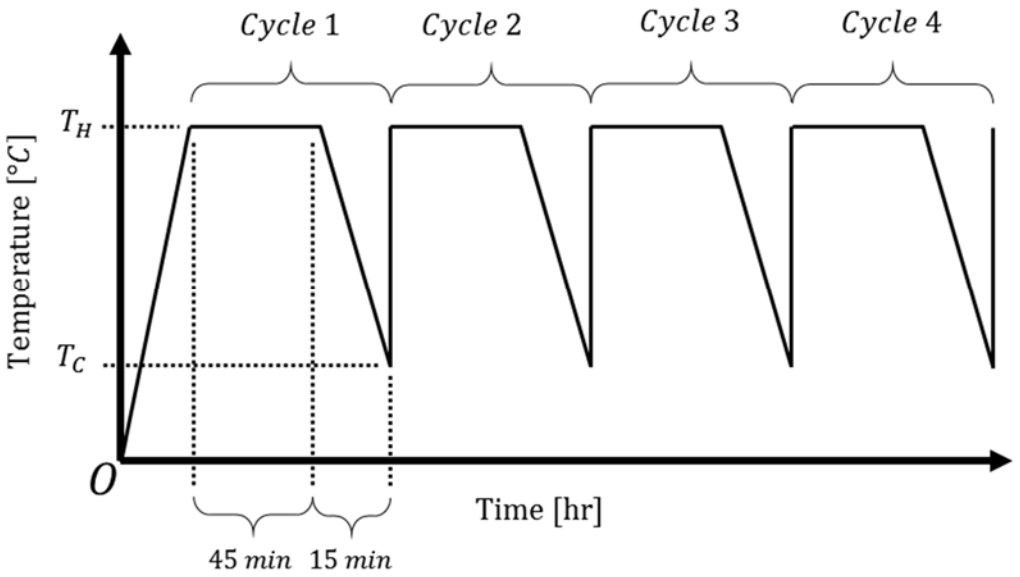

Figure 1-8: Example of furnace cycle test temperature profile with a 10-minute heat-up, 45-minute hold at 1150°C and 10-minute cool-down.

For this study the cycle consists of holding the sample at a hot temperature, $T_H = 1150\ °C$ for 45 minutes and then allowing the sample to air cool for 15 minutes. This cycle is then repeated until the coating visibly spalls from the sample.

Another method of conducting a similar 1-hour cycling procedure involves the use of TBC coated cylindrical or vane-shaped superalloy rod or the TBC coated superalloy button that is placed in the path of hot oxidizing flame for a period of time. The sample is then removed from the flame and allowed to cool in air before being inserted into the flame again. It should be noted that even though care is taken to have these accelerated tests closely mimic in-service conditions, there are too many variables to draw direct one-to-one conclusions of the performance of in-service hardware. Instead the empirical test is best suited to test a variety of coatings under development to compare their relative performance.

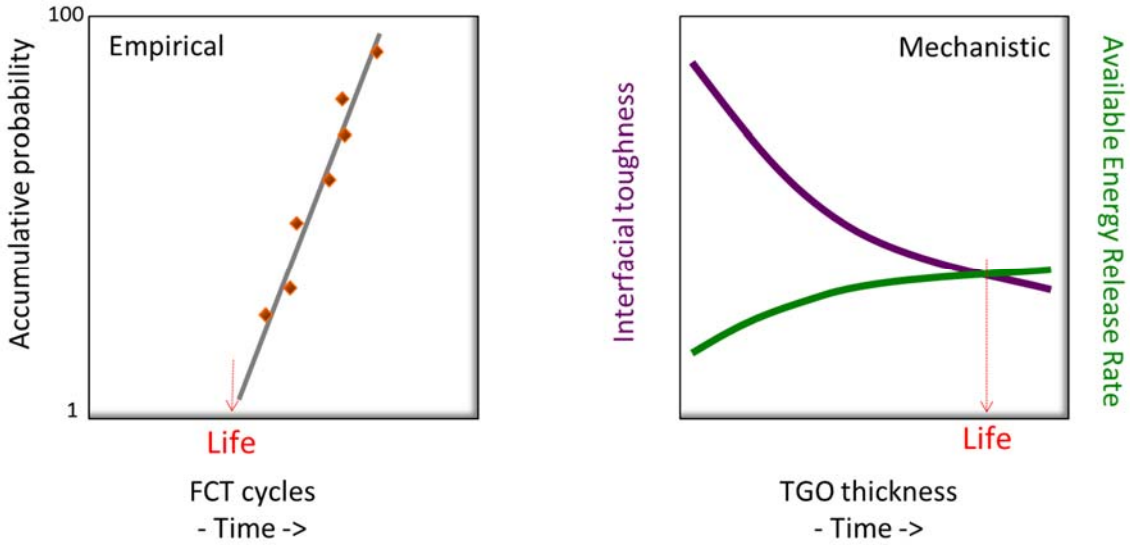

Figure 1-9: Examples of lifetime evolution for both empirical and mechanistic life prediction methodologies

Empirical lifetime assessment has been widely used by engine hardware manufacturers, but it suffers from one primary short coming; it does not explain the underlying

mechanisms that lead to spallation. A mechanistic lifetime approach seeks to alleviate this issue through direct understanding of morphological and chemical changes and the evolution of stress and adhesive properties in the system. This approach involves the balance between the stored strain energy in the system and the interfacial toughness. As the lifetime of a coating progresses, TGO growth is accommodated by flow of oxygen through the top coat and reaction with the Al in the bond coat. As the TGO grows a significant amount of elastic strain energy is developed in the dense α-Al_2O_3 TGO. At the same time high temperature sintering of the top coat can lead to large tensile stresses developing. These lead to a net parabolic increase of total available strain energy that is available for release during coating delamination as time progresses. At the same time as strain energy is developing in the TGO, various damage mechanisms occur that lead to a decrease in the interfacial toughness of the coating. This behavior is shown schematically in Figure 1-9. When the total amount of available energy per unit interface area is equal to the interfacial toughness, delamination of the coating will occur since the driving force for crack growth is equal to the crack resistance of the interface. Detailed modelling of the total available strain energy evolution in the coating can be accomplished though microstructural observations, stress evolution measurements and detailed finite element (FE) modelling. Direct measurement of the interfacial toughness is the last necessary component to develop a mechanistic life prediction methodology. This is an important aspect to consider when developing coatings and was very well summarized by John Hutchinson:

In the absence of mechanism-based predictive models, direct measurement of coating adherence as a function of thermal exposure must be a component of any practical approach toward lifetime assessment. [6]

It is therefore necessary to not only characterize the interfacial toughness evolution as a function of thermal history, but also at various levels of mode-mix to fully understand the degradation behavior.

1.3.4 TBC Damage Initiation Mechanism

There are many different ways that a TBC can spall from the underlying metallic layers. These failure mechanisms can be categorized into two different broad categories, based off of where the damage originates, as either intrinsic or extrinsic damage. A schematic of various intrinsic and extrinsic failure mechanisms is shown in Figure 1-10.

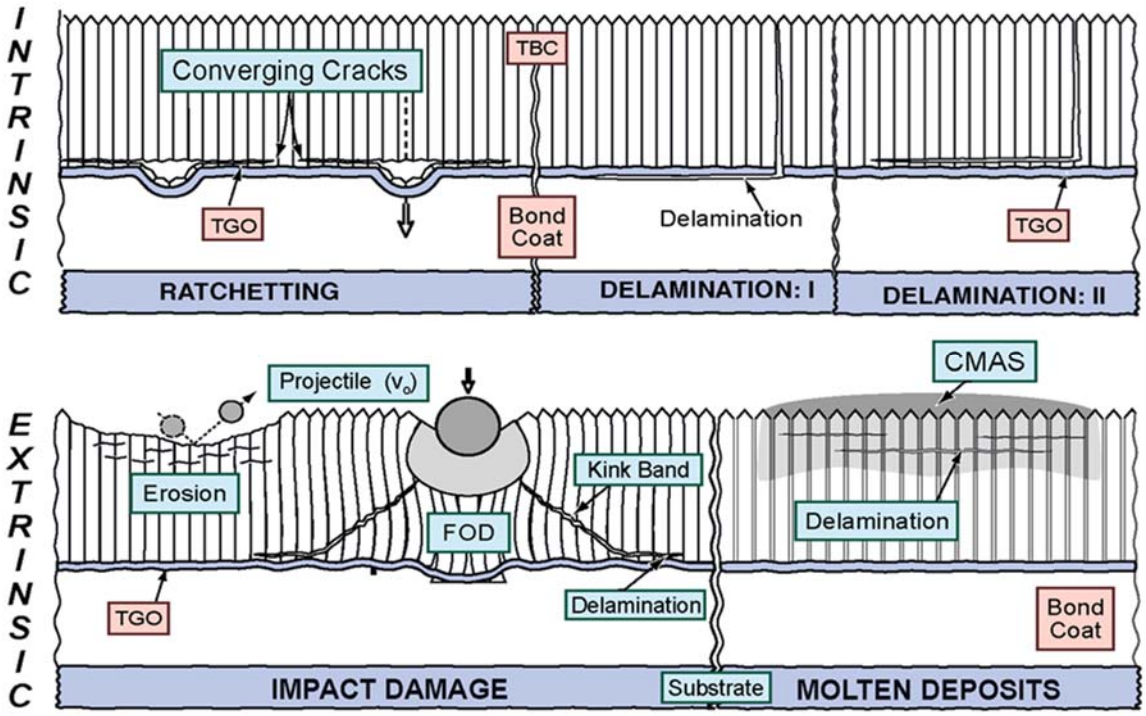

Figure 1-10: Schematic of intrinsic and extrinsic TBC damage mechanisms (taken from [19])

Intrinsic damage originates from chemical and morphological changes in the system that drive imperfections to form that lead to spallation. Spallation can occur from sources such as i) ratcheting of the TGO that leads to interfacial voids and from delamination of the TGO due to vertical cracks originating in the top coat created by sintering. This damage causes delamination either i) below or ii) above the TGO. Extrinsic damage is caused by external factors that initiate direct damage to the TBC system. Some example of this include, i) erosion of the top coat due to small particles ($\sim 10\mu m$), ii) foreign object damage (FOD) caused by large particle impact ($\sim 100\mu m$) and iii) calcium-magnesium-alumino-silicate (CMAS) deposition, melting and wicking into the top coat that leads to spallation.

For the purpose of this study the intrinsic damage mechanism involving delamination of the top coat either directly above or below the TGO will be examined. This failure mechanism originates from sintering of the top coat columns to each other that causes a tensile stress to develop in the top coat. A schematic of this mechanism is shown in Figure 1-11. This tensile stress leads to the formation of vertical cracks between columns that propagate to the top coat/bond coat interface and begin to run along the interface. At the high temperatures experienced in the HPT region of the turbine engine, (>1000°C), it is generally believed that stresses in the TBC layers are relaxed due to creep [19]. When the turbine begins to cool down, which could be due to either a plane landing or shutdown of a power generation turbine, the large CTE mismatch between the underlying metallic layers (substrate and bond coat) and the ceramic upper layers (TGO and top coat) leads to tensile stresses developing in the metallic layers and compressive stresses in the ceramic layers, with stresses in the TGO on the order of GPa's. The tensile and compressive stresses either

side of the interface lead to large shear stresses that develop between the top coat and bond coat. These large shear stresses (Mode II loading) act on the crack tip of the initial delamination between the top coat and bond coat (either side of the TGO) and act as a driving force for delamination. At the same time the free surface created by the vertical crack in the top coat allows for the contraction of the TGO and top coat to occur, thus allowing the necessary delamination displacement for spallation to occur.

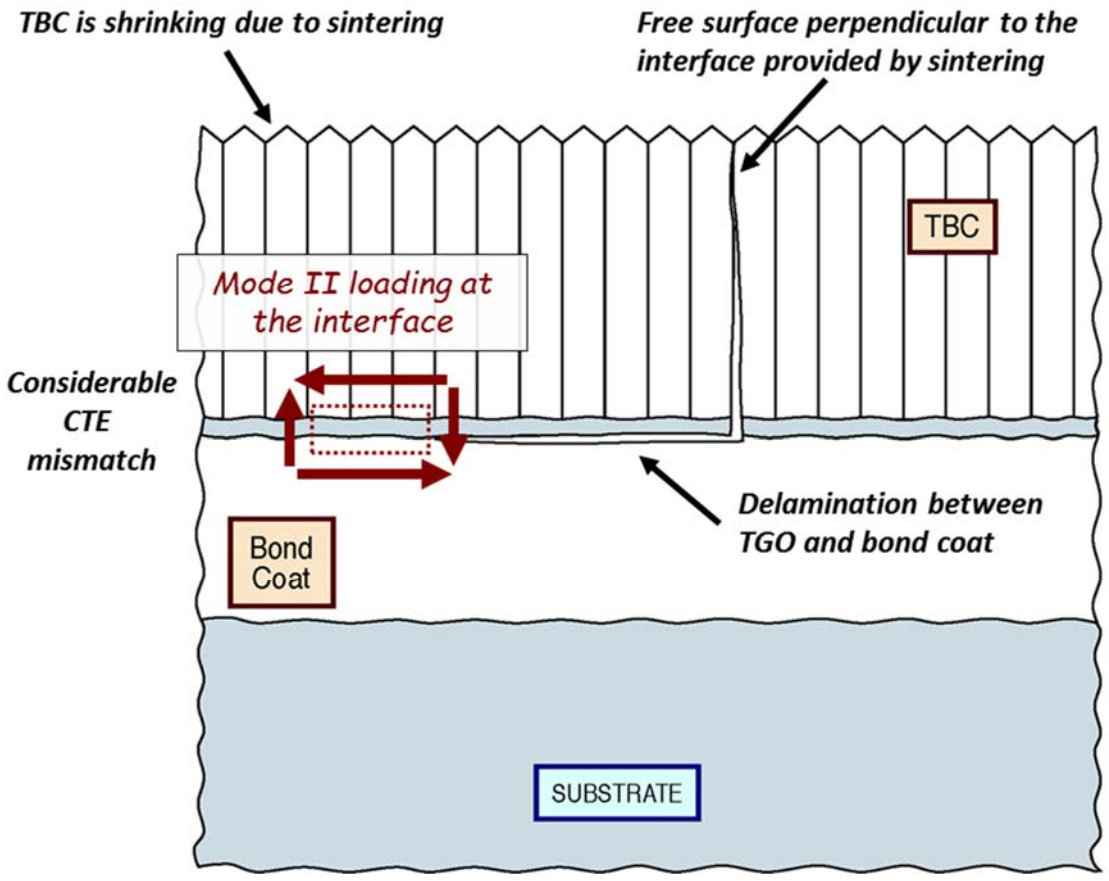

Figure 1-11: Schematic of damage mechanism most representative of TBC spallation during engine cool down (taken from [19])

It is important to note that spallation occurs due to shear stresses at the interface and not due to normal stresses. It is also important to note that due to the CTE mismatch and the stress relaxation at high temperature, the largest driving force for delamination will occur

at ambient conditions. It is for this reason that room temperature interfacial toughness values are of the highest importance. The motivation for conducting the work in this dissertation arose because, no test method had previously been able to successfully experimentally measure the pure mode II interfacial fracture toughness between the top coat and bond coat. Understanding how this property evolves as a function of thermal exposure to the TBC system will allow material and hardware designers to create more durable coatings that will be able to withstand the higher temperatures demanded by the quest for ever better efficiency.

1.4 Dissertation Overview

This chapter introduces the reader to the relevant background, concepts and motivations for the research presented in this dissertation. The key focus of this study is to successfully characterize the pure Mode II interfacial fracture toughness for the TBC systems using the CED test method and to understand how the toughness degrades with thermal exposure.

Chapter 2 presents a general overview of fracture mechanics principles and definitions used in this thesis. Importance is placed on the use of the J-integral to calculate interfacial toughness both analytically and in FE implementation. The important concepts behind interfacial fracture mechanics are then presented with special interest focused on the relevant criteria used to characterize the interfaces experimentally. Finally, a number of well-established test methods are presented as potential candidates for characterizing the interfacial toughness.

Chapter 3 covers in detail the underlying mechanics of the CED test method used to characterize the pure Mode II interfacial toughness as well as the procedure by which the

sample geometry was chosen. The sample preparation procedure is then discussed and the chapter ends with an overview of the DIC to calculate the critical stress at which cracking occurs.

Chapter 4 outlines the underlying mechanics of the modified 4-point bend test used to characterize the interfacial toughness under mixed-mode conditions. Details of the sample preparation procedure are discussed and the conditions under which the testing procedure is conducted is detailed.

Chapter 5 details the FE models created for analysis of the CED and modified 4-point bend tests. The effect of interfacial friction on the steady-state interfacial toughness for the CED sample is presented. In addition, the method by which the CED model accounts for changes in the TGO thickness due to thermal cycling is detailed. This dependence of the interfacial toughness on the TGO thickness and interfacial friction coefficient for the CED sample is combined into an analysis framework that is used to calculate toughness values from the experimental results. The investigation of interfacial toughness for the modified 4-point bend specimens is accomplished by way of an inverse FE method utilizing the virtual crack closure technique (VCCT).

Chapter 6 presents the experimental results for both CED tests and modified 4-point bend tests. Details regarding the determination of the TGO thickness as a function of lifetime and characterization of the interfacial friction coefficient are discussed. These values are used to calculate the interfacial toughness as a function of lifetime for the CED test specimens. Interfacial toughness results from the modified 4-point bend tests are presented and an asymmetric toughness function is derived using this data, the CED data and data

from previous studies. Details regarding the fractographic and microstructural observations are discussed in terms of how the can help to explain the decrease in toughness observed during thermal cycling.

Concluding remarks, a summary of the research presented in this thesis and recommendation for future research directions are presented in Chapter 7.

1.5 References for Chapter 1

1. Griffith, A.A., *The Penomena of Rupture and Flow in Solids.* Philosophical Trans. Royal Society, 1921. **A221**: p. 163-198.
2. Cao, H.C.E., A.G., *An experimental study of the fracture resistance of bimaterial interfaces.* Mechanics of Materials, 1988. **7**(4): p. 295-304.
3. Evans, A.G.R., M.; Dalgleish, B.J.; Charalambides, P.G., *The fracture energy of bimaterial interfaces.* Materials Science and Engineering, 1989. **126**.
4. Charalambides, P.G., et al., *A Test Specimen for Determining the Fracture Resistance of Bimaterial Interfaces.* Journal of Applied Mechanics, 1989. **56**(1): p. 77-82.
5. Klingbeil, N.W. and J.L. Beuth, *Interfacial fracture testing of deposited metal layers under four-point bending.* Engineering Fracture Mechanics, 1997. **56**(1): p. 113-126.
6. Hutchinson, R.G. and J.W. Hutchinson, *Lifetime Assessment for Thermal Barrier Coatings: Tests for Measuring Mixed Mode Delamination Toughness.* Journal of the American Ceramic Society, 2011. **94**: p. s85-s95.
7. Barber, J., *UK Patent No. 1833*. 1791: United Kingdom.
8. Schafrik, R.S., R., *The saga of gas turbine materials.* Advanced Materials and Processes, 2004. **162**: p. 33-36.
9. Dahl, J., *Turbojet engine schematic*, J. Engine.svg, Editor. 2007, Wikipedia Commons: Wikipedia.
10. M0tty, *Turboprop engine schematic*, T. operation-en.svg, Editor. 2009, Wikipedia Commons: Wikipedia.
11. Emoscopes, *Turboshaft engine schematic*, T. operation.png, Editor. 2005, Wikipedia Commons: Wikipedia.
12. Aainsqatsi, K., *Low-Bypass Turbofan engine schematic*, T.o. lbp.svg, Editor. 2008, Wikipedia Commons: Wikipedia.
13. Aainsqatsi, K., *High-Bypass Turbofan Engine Schematic*, T. operation.svg, Editor. 2008, Wikipedia Common: Wikipedia.
14. Dil, *Brayton Cycle Overview*, B. cycle.svg, Editor. 2006, Wikipedia Commons: Wikipedia.
15. Thurston, B., *GE Masterclass with Baratunde Thurston - How Does a Jet Engine Work?*, G. Electric, Editor. 2014, YouTube. p. 2:11.
16. Radovic, L.R., *Energy and Fuels in Society: Analysis of Bills and Media Reports*. 1997: McGraw-Hill Custom Publishing.
17. Cervenka, M., *The Rolls Royce Trent Engine*, T.R.R.T.E.-O.p.g.a.U.o. Cambridge, Editor. 2000.

18. Pollock, T.T., S., *Nickel-based superalloys for advanced turbine engines: chemsitry, microstructure and properties.* Journal of Propulsion and Power, 2006. **22**(2): p. 361-374.

19. Evans, A.G., et al., *Mechanisms controlling the durability of thermal barrier coatings.* Progress in Materials Science, 2001. **46**(5): p. 505-553.

20. Alliance, E., *Engine Alliance GP7200 Front to Back Cutaway*, GP7200-front-to-back-lores-1.png, Editor. 2015.

21. Aviation, G. *Repair Brocure*. 2014.

CHAPTER 2: FRACTURE MECHANICS OVERVIEW

As was briefly mentioned in the introduction, in order to characterize the interfacial strength between the TBC top coat and bond coat layers, a fracture mechanics based experimental methodology must be employed. Readers familiar with fracture mechanics may choose skip this chapter if desired. This chapter will first cover the theory and development of the mathematical framework behind the fracture mechanics method for both homogeneous materials and for bimaterial cracks (cracks between two dissimilar materials). A succinct background on fracture mechanics is provided to acquaint the reader with the necessary theory and terminology used in this thesis. For a more detailed introduction to fracture mechanics the books *Principles of Fracture Mechanics* by R.J. Sanford [1], *Elementary Engineering Fracture Mechanics* by David Broek [2] and *Engineering Mechanics of Composite Materials* by Daniel and Ishai [3] are recommended. The mechanics of a crack between two dissimilar materials is more complicated than in homogenous materials and the concept of interfacial fracture between dissimilar materials will be developed with special interest focused on the relevant criteria used to characterize the interfaces experimentally [1, 4]. Finally, a number of established test methods that have been developed for studying the strength of adhesives, composite laminates and film coatings will be reviewed as potential tests for studying the thermal barrier coating material system.

2.1 The Fracture Energy Criterion

There are two general deformation mechanisms that can happen if a material is stressed past its elastic limit. For ductile materials, plasticity will occur due to dislocation movement

within the material. For brittle materials very little or no plastic deformation occurs and failure happens either though cleavage, for crystalline materials, or through conchoidal fracture, for amorphous or fine grained materials. A combination of brittle and ductile failure mechanisms can also occur for many metals and alloys. For composite and layered material structures additional failure mechanisms can exist, such as void growth, composite matrix cracking, fiber pull-out or interfacial delamination. Interfacial delamination, between either two homogeneous or dissimilar material layers, is a special type of fracture where a crack propagates along the interface between the layers and is of special interest in this thesis.

There are a number of important energetic terms to consider when analyzing crack propagation. The first term to consider is the energy required to grow the crack, labeled F. For purely ductile materials this is the required energy to propagate the plastic zone ahead of an advancing crack tip and for purely brittle materials this term is the required energy to form two new surfaces during fracture. As previously mentioned, this term can also contain a combination of the two mechanisms. The energy required to grow a crack comes from three different sources. The first is from the total external work done on the system, labeled V. The second source comes from the elastic energy stored in the system, labeled U. The last term is a kinetic energy term that exists when dynamic crack growth is occurring and the crack is travelling close to the speed of sound in the material, labeled E_k. The relationship between these terms and the energy required for crack growth is:

Equation 2-1

$$F = V - U - E_k$$

Only under rapid crack growth conditions must E_k be accounted for, but under steady-state conditions where quasi-static crack growth occurs $E_k \approx 0$.

Following work done by Irwin [5], a quantity called the strain energy release rate, G, is defined under as the spatial rate of change of the total stored strain energy in the system with a crack area A.

Equation 2-2

$$G = \frac{dF}{dA} = \frac{d(V - U)}{dA}$$

It is important to note that the strain energy rate is an area rate of change, not a time rate of change, and typically has units of J/m^2. Crack growth will occur when the amount of energy available to be released, G, is greater than the critical strain energy release rate, G_c. In order to analyze Equation 2-2 it is necessary to define the incremental work expended during crack growth, $dV = Pd\delta$, and the strain energy released during fracture, $U = \frac{1}{2}P\delta$. For a sample with unit thickness $dA = 2da$, where $2a$ is the crack length:

Equation 2-3

$$G = \frac{1}{2}\left(P\frac{d\delta}{da} - \delta\frac{dP}{da}\right)$$

It is important to distinguish between the critical strain energy release rate, G_c and the strain energy release rate G. The critical strain energy release rate, G_c, is a material property that is not dependent on sample geometry or crack length. It is defined as the area rate change of energy that must be released for a crack to grow and is a constant for a particular material

and loading conditions. The strain energy release rate, G, will increase proportionally as the sample is loaded. When the value of G reaches G_c, the crack will begin to grow. The crack will continue to grow until complete failure occurs or until the value of G decreases below G_c due to a change in the loading.

2.1.1 Effect of Test Configuration

From inspection of Equation 2-3 it is clear that there is a work component and elastic component that can contribute to crack growth. Through control of the testing conditions, the analysis can be simplified through reduction of terms. The most common way to achieve this goal is by changing the testing conditions between displacement control ("system-isolated" condition) and load control ("dead load" condition). For displacement control conditions the deformation of the sample is accomplished through controlled and incremental displacement applied to the sample. When a fracture event occurs under displacement control, there is a sudden vertical drop in the load deflection curve with no change in displacement. For load control conditions the deformation of the sample is accomplished through controlled and incremental loading of the sample. When a fracture event occurs under load control, there is a sudden horizontal increase in the displacement with no change in the load. These concepts can be seen visually in Figure 2-1.

It is apparent that under displacement control conditions there is no change in the displacement during crack growth and the strain energy release rate becomes:

Equation 2-4

$$G|_{\delta} = \frac{1}{2}\left(P\frac{d\delta}{da} - \delta\frac{dP}{da}\right)_{\delta} = -\frac{\delta}{2}\frac{dP}{da}$$

By incorporating the relationship between displacement and load, $\delta = CP$, where C is the compliance of the sample, a new relation can be derived.

Equation 2-5

$$G|_{\delta} = -\frac{\delta}{2}\frac{d}{da}\left(\frac{\delta}{C}\right) = -\frac{\delta^2}{2}\frac{d}{da}\left(\frac{1}{C}\right) = \frac{\delta^2}{2C^2}\frac{dC}{da} = \frac{P^2}{2}\frac{dC}{da}$$

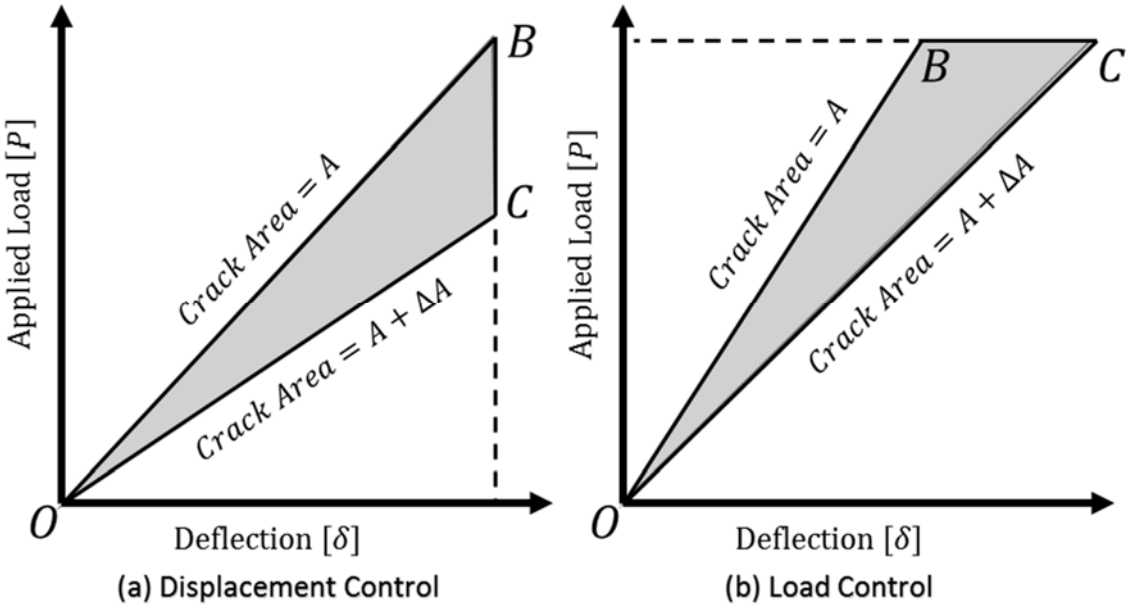

Figure 2-1: Schematic representation of load/displacement curves for (a) displacement control and (b) load control during linear-elastic loading with crack extension event (point B to C) where the shaded area corresponds to the elastic energy U

Under load control conditions there is no change in the load during crack growth and the strain energy release rate becomes:

Equation 2-6

$$G|_{P} = \frac{1}{2}\left(P\frac{d\delta}{da} - \delta\frac{dP}{da}\right)_{P} = -\frac{P}{2}\frac{d\delta}{da}$$

Again, incorporation the relationship for the compliance of the sample:

Equation 2-7

$$G|_P = -\frac{P}{2}\frac{d}{da}(CP) = -\frac{P^2}{2}\frac{d}{da}(C) = \frac{P^2}{2}\frac{dC}{da}$$

Thus both Equation 2-5 and Equation 2-7 show that the definition of the strain energy release rate, defined in terms of the compliance of the system, is the same whether assuming displacement or load control conditions. Using the relation for the compliance, $C = \delta/P$, and the strain energy, $U = \frac{1}{2}P\delta$, a relationship between the strain energy release rate and the strain energy can be calculated.

Equation 2-8

$$G|_\delta = \frac{P^2}{2}\frac{dC}{da} = \frac{P^2}{2}\frac{d}{da}\left(\frac{\delta}{P}\right) = \frac{\delta P^2}{2}\frac{d}{da}\left(\frac{1}{P}\right) = -\frac{\delta}{2}\frac{dP}{da} = -\frac{dU}{da}$$

Equation 2-9

$$G|_P = \frac{P^2}{2}\frac{dC}{da} = \frac{P^2}{2}\frac{d}{da}\left(\frac{\delta}{P}\right) = \frac{P}{2}\frac{d}{da}(\delta) = \frac{P}{2}\frac{d}{da}\left(\frac{2U}{P}\right) = \frac{dU}{da}$$

The most profound results of this derivation is that the strain energy release rate can simply be defined in terms of the elastic strain energy U, making sure to use the correct sign depending on the testing conditions.

Equation 2-10

$$G = \left(-\frac{dU}{da}\right)_\delta = \left(\frac{dU}{da}\right)_P$$

The reason for the difference in sign between the two testing conditions comes from the source of energy provided during crack growth. In the case of displacement control, crack growth does not accompany any change in displacement. Since no displacement occurs, no work is done and so all the energy must come from the stored elastic strain energy of the

system and $\frac{dU}{da}$ is negative. The energy lost during crack propagation can be seen by the triangle created by points OBC on the plot (a) in Figure 2-1.

When a crack grows under load control conditions all of the energy provided for crack propagation comes from the work done on the sample through the applied load and subsequent displacement of the loading boundary. As a result, the elastic energy in the sample increases due to the increase in the compliance not associated with a decrease in the load. By observing plot (b) in Figure 2-1, it is apparent that the area under line OC is greater than the area under line OB. The consequence of this is that there is a larger amount of energy in the system after crack propagation occurs. As previously mentioned, the reason for this is that work is done during crack propagation, shown by the area under line BC, after which the elastic energy increases in the system making $\frac{dU}{da}$ positive.

The displacement and load control conditions are unique, in that, either all of the elastic strain energy or work done, provides the energy for crack propagation. In the more general case of a real cracking body, the energy consumed or expended during crack growth comes from multiple sources. This behavior can be seen in the load/deflection curve in Figure 2-2.

As the crack grows by an amount ΔA, the displacement boundary moves by an amount $\Delta\delta$ with a corresponding change in compliance. Unlike the displacement control or load control conditions, not all of the shaded area OBC is due solely to pure changes in elastic strain energy or in work done, but is instead a combination of the two.

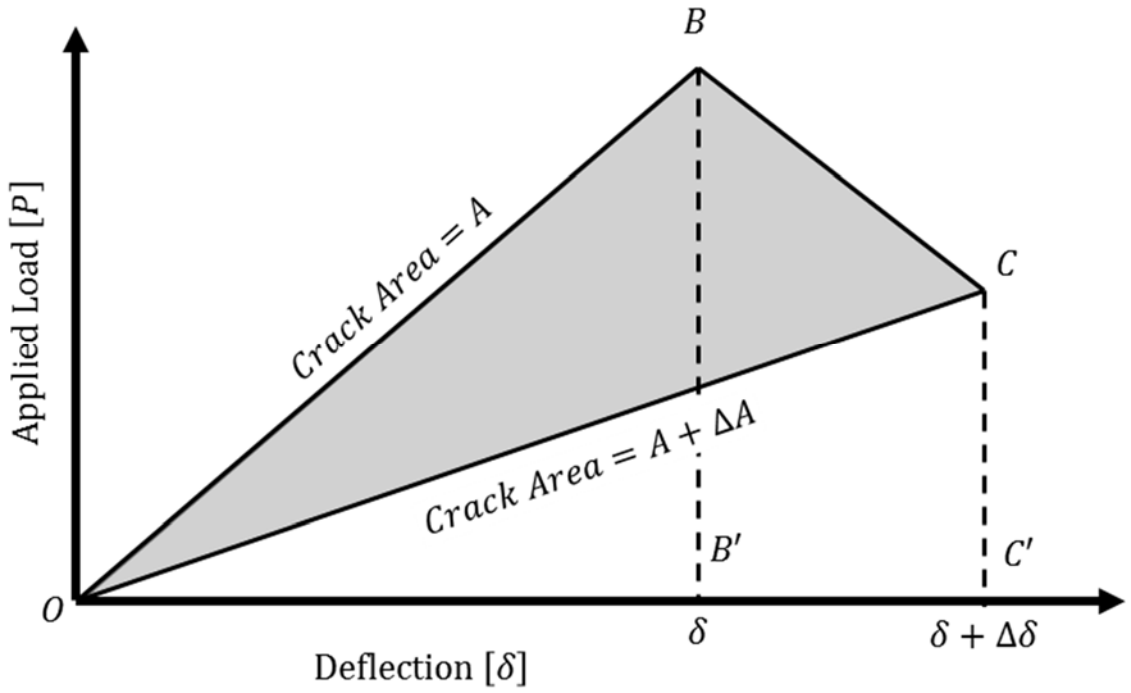

Figure 2-2: Schematic representation of load/displacement curve for generalized case of a fracture event

The area OBC can be decomposed into different components for an easier analysis as shown in Equation 2-11.

Equation 2-11

$$OBC = OBB' + B'BCC' - OCC'$$

In a first order approximation, the area $B'BCC'$ can be approximated by $Pd\delta$, which corresponds to the external work done during crack extension. Since $OCC' - OBB'$ is the total change in elastic strain energy, dU, the energy for crack extension is given by:

Equation 2-12

$$OBC = GdA = Pd\delta - dU$$

Rearranging of the equation yields:

Equation 2-13

$$G = P\frac{d\delta}{dA} - \frac{dU}{dA}$$

By incorporating the relation for a sample of unit thickness and crack length of $2a$:

Equation 2-14

$$G = \frac{1}{2}\left(P\frac{d\delta}{da} - \frac{dU}{dA}\right)$$

Using this graphical method, the original relation from Equation 2-3 can be recovered if the behavior is assumed to be linear $\left(U = \frac{1}{2}P\delta\right)$. If the behavior cannot be assumed to be linear, then Equation 2-14 can be used to calculate the strain energy release rate.

2.1.2 The Griffith Criterion

In papers published in 1921 and 1925, Griffith conducted tests on thin glass threads and subsequently formulated a theory of brittle fracture based on a number of essential elements [6, 7]. The brief summary of these conditions are:

1. All materials contain an initial population of fine cracks. This conditions helps to explain why materials tend to fail at much lower strengths than their theoretical strengths.
2. Some cracks are oriented in the most favorable direction relative to the loading direction as to promote the maximum stress concentration factor at the crack tips. This argument allowed Griffith to ignore the difficult analysis of arbitrarily oriented crack with some angle relative to the loading direction.
3. At one of the cracks present, the theoretical material strength is reached at the crack tip, which leads to subsequent crack growth. This condition allowed Griffith to treat the analysis as an extreme-value problem and not a statistical one.

4. The strain energy released as the crack extends is the sole source of energy for crack extension. Griffith assumed displacement control conditions and was able to show that the change in strain energy as crack extension occurs is finite.
5. An increase in surface energy is the result of crack growth. As previously mentioned, Griffith assumed displacement control conditions and needed to account for the loss of strain energy as the crack grows. He postulated that, as new surfaces were being created during crack extension, the associated surface of the newly created crack surfaces was the probable source. It was also advantageous that the surface energy was a well-defined property of the materials he tested and experimentally measured values were accessible.
6. Crack growth will continue provided the rate of released strain energy exceeded the energy required to form new surfaces. This final condition was used to determine the critical criterion for crack growth for brittle solids.

With these conditions, Griffith was able to construct a mathematical formulation for the critical stress required to cause failure that was cast in terms of experimentally measureable quantities. At the time the only complete solution for a crack-like defect was the solution of the stress around an elliptical hole derived by Inglis [8]. By comparing the strain energy in an infinite plate of unit thickness with a similar plate but containing a crack of length $2a$, Griffith was able to determine the decrease in strain energy for the plane stress condition to be:

Equation 2-15

$$U = -\frac{\pi^2 a^2 \sigma^2}{E}$$

where σ is the applied stress and E is the elastic modulus of the material. There are two surfaces associated with the crack, above and below the crack path, that contains a certain amount energy. The surface energy, E_s, necessary to form a crack of length $2a$ in a body of unit thickness is:

Equation 2-16

$$E_s \equiv (Surface\ Energy)(Crack\ Length)(Thickness)$$

With the surface energy per unit area of the bulk material, γ_s:

Equation 2-17

$$E_s = (2\gamma_s)(2a)(1) = 4a\gamma_s$$

With the change in energy given by $\Delta U = U + E_s$, Griffith was able to define his criterion for sustained crack growth:

Equation 2-18

$$\frac{d(\Delta U)}{da} \geq 0$$

Since this condition specifies the overall condition for sustained crack growth, Griffith observed that at the onset of fracture the critical stress, σ_C, is given by the lower bound of Equation 2-18. This condition requires that the area rate of supplied strain energy is equal to the rate of energy required to form two new surfaces.

Equation 2-19

$$\frac{d}{da}\left(4a\gamma_s - \frac{\pi a^2 \sigma^2}{E}\right) = 0$$

The solution of this relation and rearrangement yields the criterion for the critical stress for crack growth under plane stress conditions:

Equation 2-20

$$\sigma_c = \sqrt{\frac{2E\gamma_s}{\pi a}}$$

The same relation but under plane strain conditions is:

Equation 2-21

$$\sigma_c = \sqrt{\frac{2E\gamma_s}{\pi a(1-\nu^2)}}$$

It should be noted that for other geometrical and loading considerations, pre-factors can be included to account for the difference between the assumptions made in this derivation. In addition, as Griffith made the assumption of purely brittle fracture, this analysis may not provide accurate results if a certain amount of ductile fracture also occurs. This detail was demonstrated by Orowan when he demonstrated that even for very brittle fracture in low-carbon steels, a significant amount of plastic deformation occurs along the fracture surface and Griffith's equations provide spurious results. [9]. Orowan recognized that the amount of plastic work during fracture was many orders of magnitude higher than the surface energy and this needed to be accounted for in the Griffith equation. He contended that if the plastic deformation during crack growth was contained within a thin layer right at the fracture surface, then the amount of plastic work would be related to the cracked area and could be described by the surface plastic work. γ_s. Orowan noted that a modification could

be made to the Griffith equation by replacing the surface energy term, γ_s, with a summation of the surface energy and surface plastic work $(\gamma_s + \gamma_p)$, which for plane stress conditions yields:

Equation 2-22

$$\sigma_c = \sqrt{\frac{2E(\gamma_s + \gamma_p)}{\pi a}}$$

And for plane strain conditions yields:

Equation 2-23

$$\sigma_c = \sqrt{\frac{2E(\gamma_s + \gamma_p)}{\pi a(1 - \nu^2)}}$$

In 1957 Irwin collected all of the terms for resistance to crack grown into a single term called the critical strain energy release rate, G_c. As with the strain energy release rate, G_c is an area rate and not a time rate value. Irwins modification to Griffiths equation yields, for plane stress:

Equation 2-24

$$\sigma_c = \sqrt{\frac{2EG_c}{\pi a}}$$

And for plane strain conditions yields:

Equation 2-25

$$\sigma_c = \sqrt{\frac{2EG_c}{\pi a(1 - \nu^2)}}$$

The summation of all of the terms for crack growth resistance into the critical strain energy release rate is an important finding because, for cases where there are a number of factors

that can affect the resistance to crack growth, G_c provides one terms that can be determined experimentally that describes the critical condition for crack growth without the need to determine and solve for the other contributing terms.

2.1.3 Modes of Cracking (or Loading)

The deformation fields that are produced by both symmetric (tensile/compressive) and asymmetric (shear) stress fields result in distinctly different motions of the crack faces. The case of uniaxial stress applied normal to the crack face results in an opening displacement of the crack faces which is known as Mode I fracture, or opening mode fracture. When a shear stress is applied tangent to the crack front and tangent to the crack plane normal, a shear displacement is applied to the crack faces and is known as Mode II fracture, or in-plane shear fracture. Similarly, when a shear stress is applied normal to the crack front and tangent to the crack plane normal, a shear displacement is applied to the crack faces and is known as Mode III fracture, or anti-plane shear fracture. A schematic of the three fracture modes can be seen in Figure 2-3.

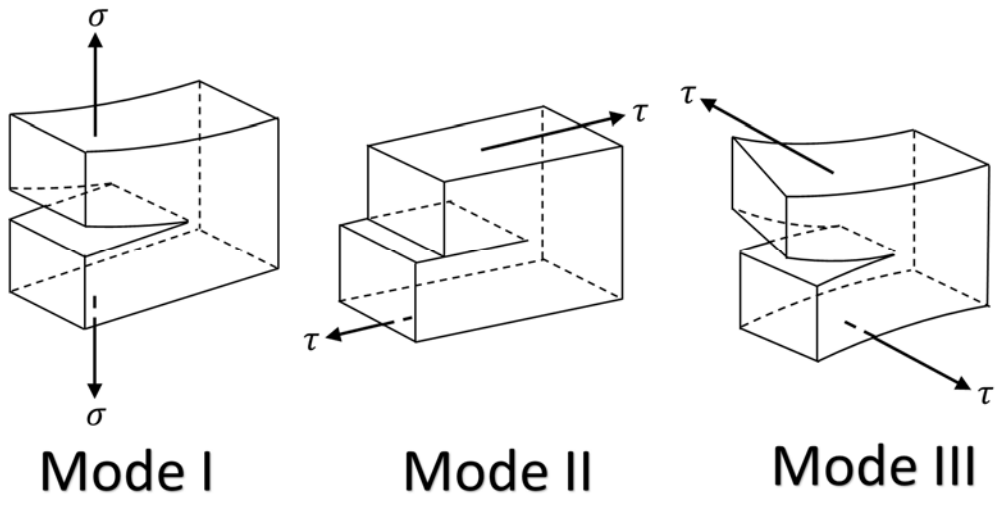

Figure 2-3: Schematic representation of the three modes of fracture

The opening mode of fracture is by far the important mechanism the controls the failure of homogenous, isotropic materials. It is widely known that, unless constrained, a crack growing in a homogenous, isotropic material will align itself so that it minimizes or completely eliminates any in-plane shear at the crack tip [1]. Mode II fracture is of special importance to interfaces composed of different materials (bimaterial interfaces) and will be discussed in detail throughout this thesis. Mode III fracture is of notable importance as it, along with the opening mode, are responsible for the formation of river lines on crystallographic cleavage facets which are widely used in fractography failure analysis to determine crack initiation locations. Cracks do not have to follow one single fracture mode and can be a combination of all three modes. In this generalized case of fracture it has been shown that any fracture event can be described by a superposition of the stress fields associated with all three modes [1]. This also means that the strain energy release rate during crack growth is also a superposition of the strain energy release rates associated with each mode of fracture ($G = G_I + G_{II} + G_{III}$). In the scope of this thesis, only mode I and mode II fracture will be considered. The fracture tests used will be a combination of mode I and mode II, with their relative components described by the phase angle of loading which will be further discussed in Section 2.2.1.2.

2.1.4 J-Integral Method

The subject of Linear Elastic Fracture Mechanics (LEFM) is essentially an applied elasticity study concerning bodies containing cracks [1]. Limited amounts of plasticity can be accounted for at the crack tip by incorporating the principles of small scale yielding in the fracture process zone [1]. The argument is made that the region of plasticity is small enough that it can be accounted for and the subsequent analysis can be made assuming the rest of the behavior is purely elastic. The LEFM approach works well many for many cases such as fatigue where the peak stresses are less than 30% of the yield strength and in materials that are purely brittle: glass, ceramics and high strength metals with limited ductility prior to fracture. Linear Elastic Fracture Mechanics does not apply when the loading and geometry of the sample yields a plastic zone that is not confined to a small area around the crack tip. Such a condition can occur in a ductile plate containing a central crack, where the plastic zone will radiate from the crack tip at approximately 45° from the crack plane and will extend to the free boundaries. The LEFM approach will also not apply when there is significant plastic deformation prior to failure. When the net section stress is close to the yield strength of the material, traditional plastic flow rules can be applied.

One way to aid in the characterization of nonlinear elastic bodies is to expand on the concepts of the energy of fracture previously developed in section 2.1.1. Figure 2-4 shows the load-deflection curve for a general nonlinear elastic material.

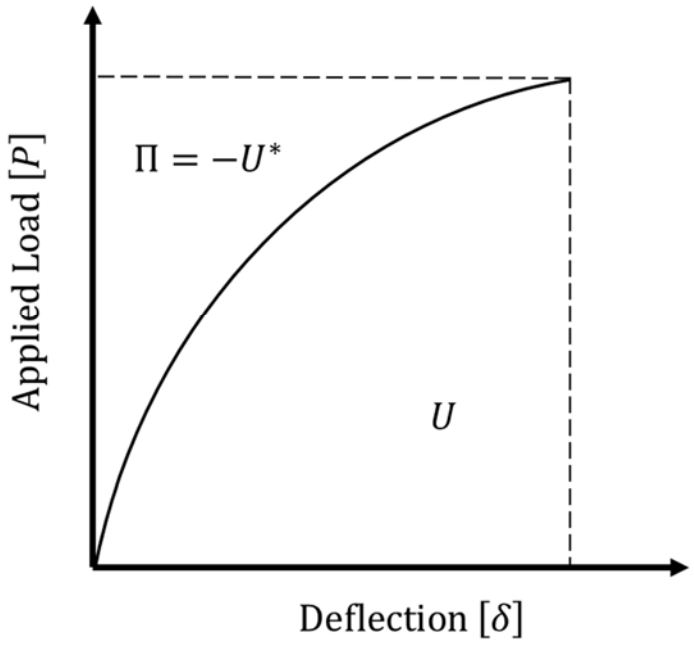

Figure 2-4: Load-deflection diagram for a general nonlinear elastic material with components of energy shown on plot

The strain energy, U, is shown as the area under the load-deflection curve. A complementary strain energy, U^*, can be defined as shown in the figure and can be related to the potential energy of the system, Π, by the following relation:

Equation 2-26

$$U^* = P\delta - U = -\Pi$$

If a two-dimensional body is considered, with cross-sectional area A, surface tractions T_i that act over a boundary Γ, the potential energy Π is given by:

Equation 2-27

$$\Pi = \int_{\Gamma} W dA - \int_{\Gamma} T_i u_i ds$$

In this equation W is the strain energy density defined as:

Equation 2-28

$$W = \int \sigma_{ij} d\epsilon_{ij}$$

An energy release rate for nonlinear elastic bodies, J, with a crack area A, can be defined as follows:

Equation 2-29

$$J = \frac{\partial \Pi}{\partial A}$$

By incorporating Equation 2-27 into Equation 2-29 and assuming unit thickness, a formal definition of J can be determined:

Equation 2-30

$$J = \frac{d\Pi}{dA} = \int_A \frac{dW}{da} dA - \int_\Gamma T_i \frac{du_i}{da} ds$$

Through some manipulation Equation 2-30 can be written in the following form:

Equation 2-31

$$J = \int_\Gamma \left(W dy - T_i \frac{du_i}{dx} ds \right)$$

Equation 2-31 is commonly known as the J-integral [1]. It is a contour path integral that is used to calculate the strain energy release rate, or work per unit fracture surface area, in a material. The method was developed independently by both Cherepanov [5] in 1967 and by Jim Rice [10] in 1968. One of the true benefits of the analysis lies in that the calculation is independent of the path taken around the crack and the path can be chosen to simplify the analysis. One of the consequences of the J-integral is that it satisfies the principle of conservation of energy momentum for a body containing a singularity with $J = 0$ around

any closed path not encircling the singularity. This can be easily seen by observing Figure 2-5.

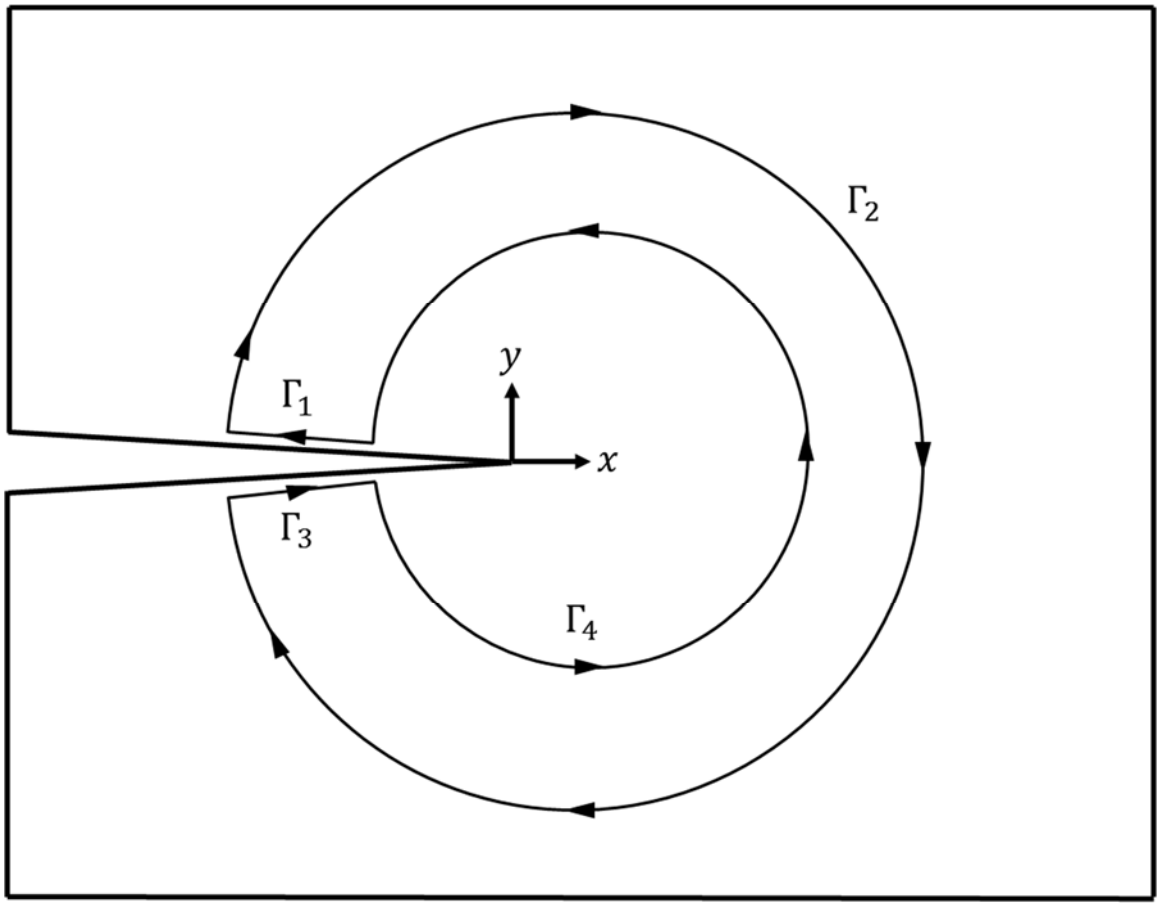

Figure 2-5: Schematic of a closed J-integral path that does not encircle the singularity of the crack tip

The path of the J-integral can be broken up into the independent paths and superimposed to calculate the entire path integral value. For this example, the path is defined as:

$$J_\Gamma = J_{\Gamma_1} + J_{\Gamma_2} + J_{\Gamma_3} + J_{\Gamma_4}$$

Since traction free crack faces are assumed, $T_i = 0$ on paths Γ_1 and Γ_3. In addition, on those segments $dy = 0$ and therefore $J_{\Gamma_1} = J_{\Gamma_3} = 0$. Since paths Γ_2 and Γ_4 can be taken infinitesimally close to one another and since their directions are opposite in sign it is easily

observed that $J_{\Gamma_2} = -J_{\Gamma_4}$. This consequence results in $J_{\Gamma} = 0$ and conservation of energy momentum is satisfied.

While the J-integral method has particular interest in elastoplastic fracture mechanics, it is also invaluable in derivation of the strain energy release rate for sample geometries and loading conditions where analytical solutions would not be possible. This aspect of the J-integral will be used to determine the value of the strain energy release rate for the Compression Edge-Delamination specimen presented in section 3.1.2.

2.2 Interfacial Fracture Mechanics of Bilayers

Many different kinds of interfaces exist in solid materials, such as phase boundaries, fiber/matrix boundaries in polymer reinforced composites and metal/ceramic interfaces found in the thermal barrier coating systems that are the topic of this thesis. Significant work has been done to understand the physics and properties of interfaces and the importance of their understanding is exemplified by an exert from a manuscript by John Arnold Oliver of the University of Sheffield from 1894:

> "…many cases occurring in metallurgy in which the study of molecules alone is of secondary importance when compared with the investigation of the junction lines of collective masses containing innumerable molecules and grouped into crystals." [11]

It is of importance to note that the mechanics of cracks between two dissimilar materials is quite different from that of cracks in homogeneous materials. A number of different methods have been established for the testing of bi-material interfaces; they have been used to investigate the toughness of composite laminates, adhesives and film coatings. Many of

the developed tests have been applied to thermal barrier coating systems, but for this study only the compression edge-delamination test theorized by John Hutchinson [12], presented in section 3.1, and the modified 4-point bend test originally proposed by Charalambides [13], presented in section 4.1, were ultimately selected.

2.2.1 Basic Principles of Linear Elastic Interfacial Fracture Mechanics

The analysis of cracks between a bimaterial interface, also known as interfacial fracture, is noticeably more complex than facture occurring in homogenous linear elastic materials. This is due to the fact that the stresses and energetic terms come from two distinct materials and also needs to account for the transfer of these stresses and energies across the boundary. There are a number of journal articles that offer an in-depth summary of the topic [13-21]. The best of these articles is "Elastic fracture mechanics concepts for interfacial cracks" by J.R. Rice [17] and provides an in-depth overview of the subject. This section will include a collection of the necessary elements from these articles required to analyze the experimental results presented later. Additional background on interfacial fracture will also be presented in the interest of completeness.

2.2.1.1 Definitions of Bimaterial Interfacial Fracture Mechanics

For the remainder of this section, plane strain stress fields, and subsequently plane strain crack solutions will be considered only. The first definitions discussed are the Dunders elastic mismatch parameters [16]:

Equation 2-32

$$\alpha = \frac{\bar{E}_1 - \bar{E}_2}{\bar{E}_1 + \bar{E}_2}$$

and

Equation 2-33

$$\beta = \frac{1}{2}\frac{\mu_1(1-2\nu_2)-\mu_2(1-2\nu_1)}{\mu_1(1-\nu_2)+\mu_2(1-\nu_1)}$$

where ν_i is Poisson ratio of material i, $\bar{E}_i$ is the plane strain modulus of material i defined as $\bar{E}_i = E_i/(1-\nu_i^2)$ and μ_i is the shear modulus of material i defined as $\mu_i = E_i/2(1+\nu_i)$. In these equations material 1 is considered the substrate layer and material 2 is considered the coating layer. An additional mismatch parameter related to β is defined as:

Equation 2-34

$$\varepsilon = \frac{1}{2\pi} ln\left(\frac{1-\beta}{1+\beta}\right)$$

With these definitions made, the stresses acting on an interface within the singularity dominated zone and at a distance r ahead of the crack tip is defined as:

Equation 2-35

$$\sigma_{yy} + i\sigma_{xy} = \frac{(K_I + iK_{II})}{\sqrt{2\pi r}} r^{i\varepsilon}$$

In Equation 2-35, $i = \sqrt{-1}$, σ_{yy} is the mode I tensile opening stress, σ_{xy} is the mode II shear stress, K_I is the mode I stress intensity factor and K_{II} is the mode II stress intensity factor. For homogeneous material systems the mode I and mode II stress intensity factor are decoupled, but during the complex variable stress analysis method, the $r^{i\epsilon}$ terms couples them together.

There are a number of important aspects to note about Equation 2-35. The first is in regard to the inverse square root singularity $\left(1/\sqrt{r}\right)$ in the equation that is also present in the homogenous material solution. This indicates that the stress field will increase as the

distance, r, approaches the crack tip, with the stresses tending towards infinity very close to the crack tip. The second aspect is in regard the imaginary value present in the numerator $\left(r^{i\varepsilon}\right)$ that predicts an oscillatory nature to the stress field, where the frequency of the oscillations increases as r approaches the crack tip. The crack tip displacement can be defined by the following relation:

Equation 2-36

$$\delta_x + i\delta_y = 2\sqrt{\frac{r}{\pi\varepsilon}}\frac{\left[\frac{(1-v_!)}{\mu_1}+\frac{(1-v_2)}{\mu_2}\right]}{(1+2i\varepsilon)\,cosh(\pi\varepsilon)}Kr^{i\varepsilon}$$

Just as in Equation 2-35, from inspection of Equation 2-36 it is apparent that an oscillatory displacement field is predicted near the crack tip, with the oscillations becoming greater in frequency as the distance to the crack tip decreases. A problem arises due to the fact that the crack tip displacements cannot interpenetrate one another in the real material system. The analytical solutions for the stress and displacement fields can be used to analyze bimaterial fracture problems, but care must be taken to disregard the solution very close to the crack tip where the oscillations become large and penetration of the displacement fields is possible. It should also be noted that when the Dunders parameters are taken to be zero, $\alpha = 0$ and $\beta = 0$, the equations for homogeneous materials are recovered.

2.2.1.2 The Phase Angle of Loading

For homogeneous materials the phase angle of loading, can be described simply in terms of either the opening and shear stresses or in terms of the mode I and mode II stress intensity factors:

Equation 2-37

$$\psi = tan^{-1}\left(\frac{\sigma_{xy}}{\sigma_{yy}}\right) = tan^{-1}\left(\frac{K_{II}}{K_I}\right)$$

When bimaterial interfaces are concerned, and $\alpha \neq 0$ and $\beta \neq 0$, the definition becomes more complicated. From the previous section it is apparent that the ratio of the stresses is not independent of the distance from the crack tip, for which a specific location must be determined to evaluate the mode mix. Instead of the stresses being observed right at the crack tip, the stresses must be observed at a point $r = l$ away from the crack tip. The equation for the phase angle them becomes:

Equation 2-38

$$\phi = tan^{-1}\left(\frac{\sigma_{12}}{\sigma_{22}}\right)_{r=l} = tan^{-1}\left(\frac{Im\left((K_I + iK_{II})l^{i\varepsilon}\right)}{Re\left((K_I + iK_{II})l^{i\varepsilon}\right)}\right)$$

For both the homogeneous and bimaterial cases, a phase angle of $\psi = 0°$ corresponds to mode I conditions and a phase angle of $\psi = \pm 90°$ corresponds to mode II loading. The reason for the $\pm$ in the phase angle for the mode II case has to do with the relative signs of the stresses. The phase angle will be negative if one of the stresses is negative while the other is positive.

Dimensional analysis of Equation 2-38 yields:

Equation 2-39

$$(K_I + iK_{II}) = (Stress)(F)\left(L^{\frac{1}{2}-i\varepsilon}\right)$$

In Equation 2-39, L is characteristic material length, F is a complex function whose inputs are the dimensionless parameters α, β and ε. With this, Equation 2-38 can be altered to:

Equation 2-40

$$\phi = tan^{-1}\left(\frac{\sigma_{12}}{\sigma_{22}}\right)_{r=l} = \psi + \varepsilon\, ln\left(\frac{l}{L}\right)$$

The latter term in Equation 2-40 signifies that there is an intrinsic rotation of the phase angle in a bimaterial system due to the difference in material mechanical properties [12]. It is the effect of the change in the symmetry of the stress distribution either side of the crack plane that leads to a change in phase angle. This aspect of bimaterial fracture is such that even for a purely applied tensile stress, the phase angle does not necessarily correspond to pure mode I (0°) [12]. It is also apparent that for the case of a homogeneous, linear elastic material where the Dunders parameters are zero, the equation for the phase angle does not include an intrinsic rotation.

2.2.1.3 Relating the Phase Angle to Measureable Quantities

As mentioned in the previous section, it is essential to take account for the phase angle rotation (mode-mix change) due to bimaterial fracture. If one observes the far-field stresses and displacements, experimentally measurable quantities can be used to calculate bimaterial quantities as long as certain modifications are made to the equations. The stress field far from the crack tip and along the crack line at a distance r is given by:

$$\sigma_{yy} + i\sigma_{xy} = \frac{K^{\infty}}{\sqrt{2\pi r}}$$

In this equation K^{∞} is the complex stress intensity factor taken at far-field, whose magnitude is $|K^{\infty}| = \sqrt{K_I^2 + K_{II}^2}$.

The phase angle at far field is given by:

Equation 2-41

$$\phi^{\infty} = tan^{-1}\left(\frac{K_{II}}{K_I}\right)$$

This far-field effect also affects the crack surface displacements:

Equation 2-42

$$\delta_y + i\delta_x = \sqrt{\delta_x^2 + \delta_y^2}e^{i\phi^{\infty}}$$

The strain energy release rate at the crack tip due to the far-field components is:

Equation 2-43

$$G = \frac{1 - v_1^2}{E_1}|K^{\infty}|^2$$

It is important to note that in Equation 2-43 only the mechanical properties of material 1 (the substrate material) are considered. It should also be apparent that these equations also apply to homogeneous materials because of the way they have been cast in terms of the far-field parameters.

2.3 Descriptions of Potential, Established Test Methods

There have been numerous test methods developed for the purpose of analyzing interfacial fracture in bimaterial systems. Each of the test methods has unique aspects that equates to a different phase angle, ϕ, and strain energy release rate, G, associated with each test. For the purposes of this study the compression edge-delamination test, presented in section 3.1, and the modified 4-point bend test, presented in section 4.1, were chosen to assess the critical strain energy release rate during delamination at different phase angles of fracture.

2.3.1 Indentation

This test uses a conical brale indenter to indent the surface of a $100\ \mu m$ thick top coat and initiate a circular delamination from between the bond coat and top coat [22]. This can be seen schematically in Figure 2-6.

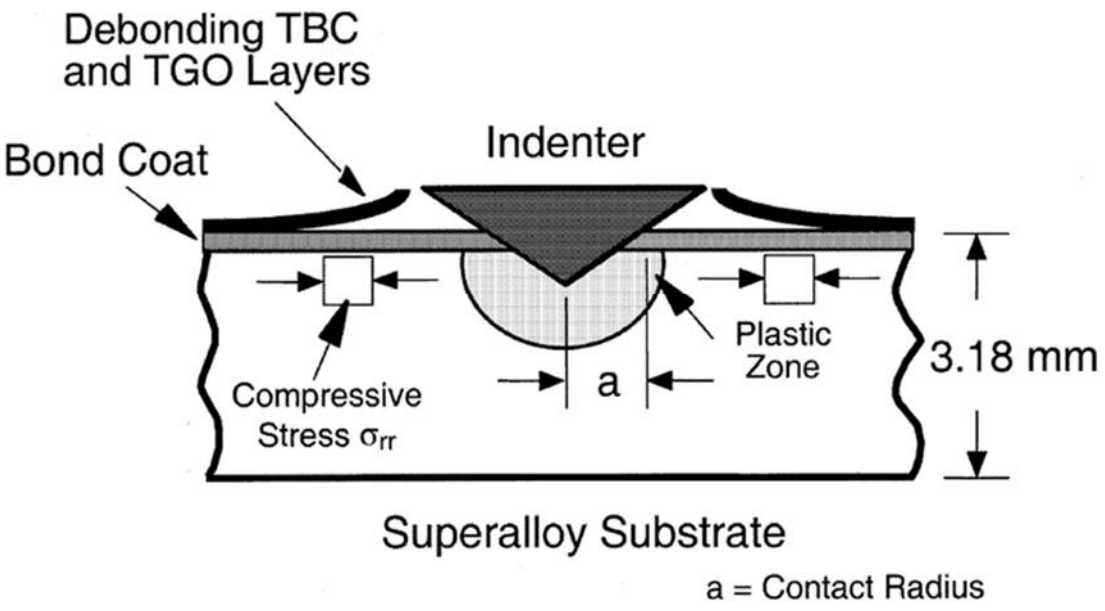

Figure 2-6: Diagram of indentation used to induce delamination of the top coat in a TBC system (courtesy of Vasinota and Beuth) [22]

The indenter is pushed, from the top coat side, through the top coat and oxide layer (TGO) and induces a plastic compressive stress in the substrate. The indentation prompts a plastic flow that radiates outwards from the point of indentation that decays as the distance increases. The compression in the substrate leads to a compressive stress developing in the top coat layers, which in turn increases the amount of elastic strain energy in the top coat. Where the indenter penetrates the top coat layer, an initial delamination front is formed and the stored elastic strain energy in the top coat and TGO cause the delamination to grow. When the strain energy release rate, G, falls below the critical strain energy release rate, G_c, the delamination front will cease to grow. The advantage of this test method over other

methods is that it can be conducted on samples with minimal sample preparation: only surface contaminants need to be removed from the top coat. The primary disadvantage of this test is that it is that finding a solution for G and ϕ requires the use of a detailed elasto-plastic finite element model and the assumptions made in this analysis can have a profound effect on the resultant values. Another issue is that if the compressive stress in the top coat is high enough, buckling may occur before stable delamination can occur, which further aids to increase the finite elements models complexity.

2.3.2 Barb and Pushout Tests

Two different, but similar tests, created by Kagawa et al. [23, 24], aim to apply a delamination displacement directly to the top coat layer and subsequently calculate the delamination toughness of the bond coat/top coat interface. In each of the tests, a load is applied to the substrate material and the displacement applied to the top coat compresses the coating until $G > G_c$ and the coating delaminates. The force at which delamination occurs is then used to calculate the interfacial toughness. A schematic of these two test methods can be seen in Figure 2-7. The schematic on the left (a) shows the barb test, where the substrate material is pulled relative to a fixture with support blocks that apply the resultant load P to the coating layers. The schematic on the right (b) shows the pushout test, where the substrate has a load applied to a punch that is just slightly smaller than the size of the substrate and bond coat layers. The support blocks are held stationary and the load is again applied directly to the top coat. Both the barb test and pushout test share the similarity is that the delamination displacement is applied directly to the top coat and a resultant shear stress is imposed on the interface, but the difference between the tests is that in the barb test the substrate is has a tensile stress applied and a compressive stress develops

in the top coat, whereas in the pushout test the substrate and top coat are both placed in compression.

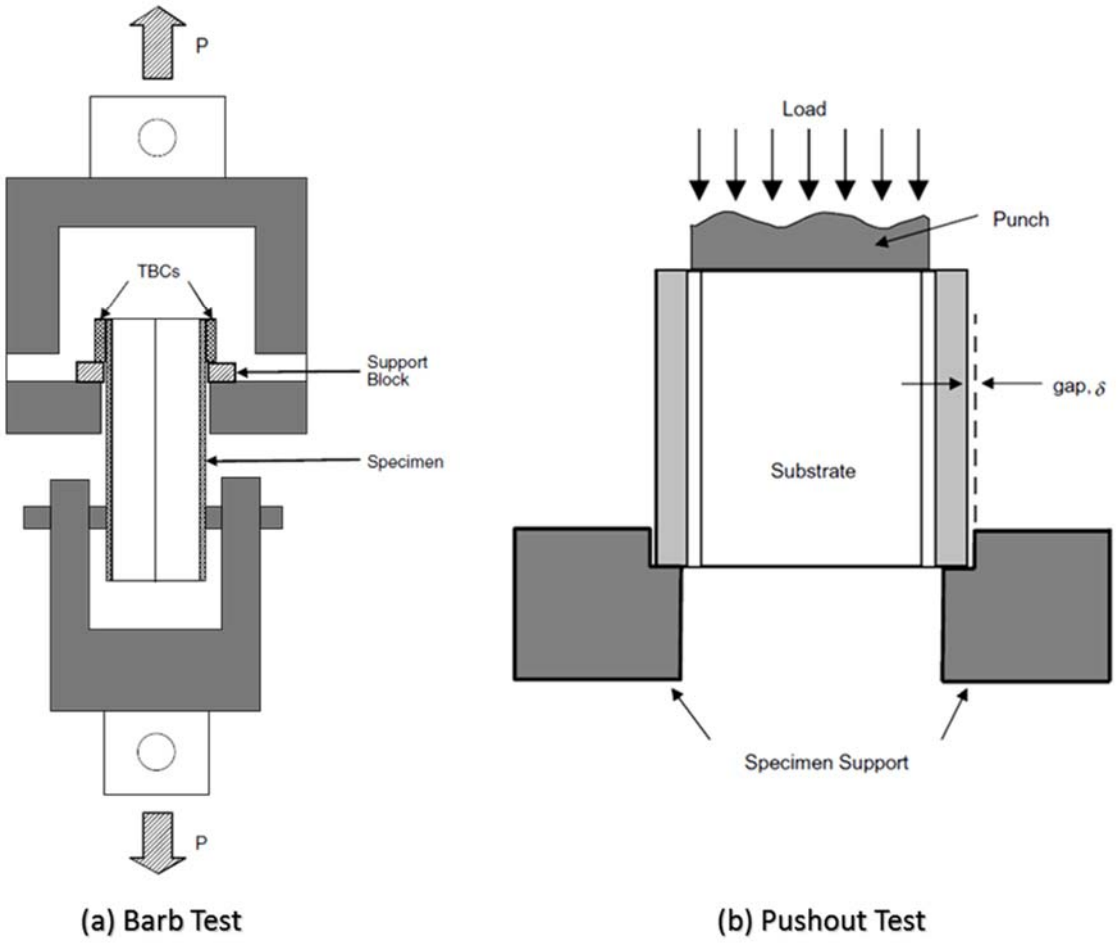

Figure 2-7: Schematics of the (a) Barb test [25] and (b) Pushout test [23] developed by Kagawa et al.

One of the negative aspects of this test is that the delamination displacement is in the opposite direction of what would be seen during top coat spallation in service; i.e. the TBC is being compressed. This finding results in a positive phase angle ($\phi > 0$) instead of the negative phase angle ($\phi < 0$) observed during real-world failure. A potential caveat with the test arises due to the fact that a detailed finite element model must be used to analyze the experimental results. From the FEM results, it is shown that the phase angle of fracture

is $\phi \cong 60°$, but can vary from this value if the sample geometry or loading conditions change. The very sophisticated specimen preparation and need to analyze the test results with numerical methods limits the use of the tests from routine fracture testing.

2.3.3 Micro-Bending

A test developed by Eberl et al. from Johns Hopkins University involved slicing a thin planar section of a TBC coated "burner-rig" bar. The bars were composed of cylindrical superalloy substrate with bond coat and top coat applied around the radial dimension. The thin slices were then prepared using micro-EDM to cut a window under the top coat layer, creating a bridge beam as shown in Figure 2-8.

After the window is cut out, the sample is fixed to the testing fixture through the hole in the lower part of the sample seen in panel (a). A point load is then applied to the center of the beam, as seen in panel (b), which initiates a central crack in the top coat layer that continues to grow until it intersects the top coat/bond coat interface and ceases to grow further. The load is then moved to slightly to one side of the initiation point, as seen in panel (c) and loaded until the crack grows and subsequently is arrested when the crack tip is vertically placed over the load application point. From here on the load application point is sequentially moved further away from the crack initiation point, shown in panel (d), and the crack is grown further. The load applied causes a distributed moment in the bridge that develops strain energy in the top coat layer, which provides the necessary energy for crack growth.

The merit of the test lies in that engine hardware can be directly tested at various points along the profile of a turbine blade. The three largest issues with this technique, however, lie in the sample preparation, experimental analysis and loading at the crack tip. The slicing

of the cross-section, polishing and subsequent micro-EDM of the sample are both time intensive and expensive.

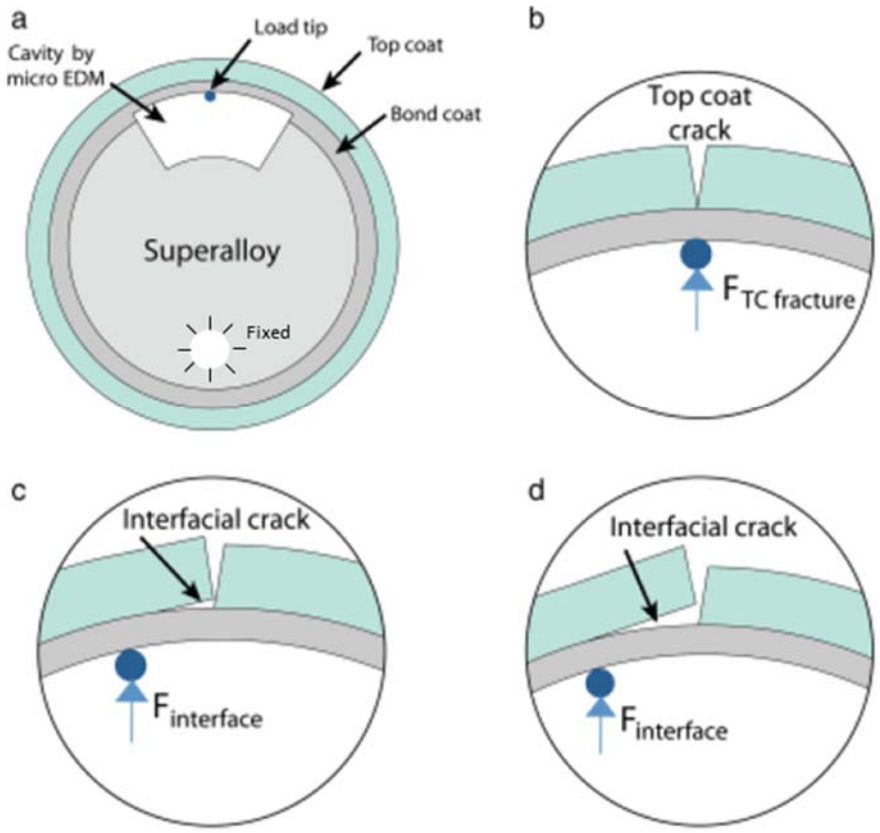

Figure 2-8: Schematic of the micro-bending tests for (a) window cut out using micro-EDM on sample, (b) vertical crack initiation, (c) initial crack growth and (d) subsequent further crack growth [26]

For the experimental analysis, the crack needs to be monitored and its length explicitly calculated during the multiple tests and then those results need to be inputted into a detailed finite element model to extract the material parameters. This can also be an extremely time intensive procedure. Results of the finite element modelling show that the phase angle of fracture increases as the crack length grows, with the average phase angle around $\phi = 19°$. This corresponds to a mode-mixity closer to pure mode I conditions, which is not

representative of TBC spallation behavior. Additional difficulties arise in that plasticity of the metallic substrate and bond coat layer can occur which further complicates the analysis. The issues present with this test preclude it from being a regular fixture in TBC property measurement programs.

2.3.4 The 4-Point Bend Test

Advancements were made by Charalambides et al. [13] in 1989 on a way to use the traditional 4-point bend test configuration to characterize the mixed-mode delamination toughness of bimaterial interfaces. The geometry and loading for this test can be seen in Figure 2-9.

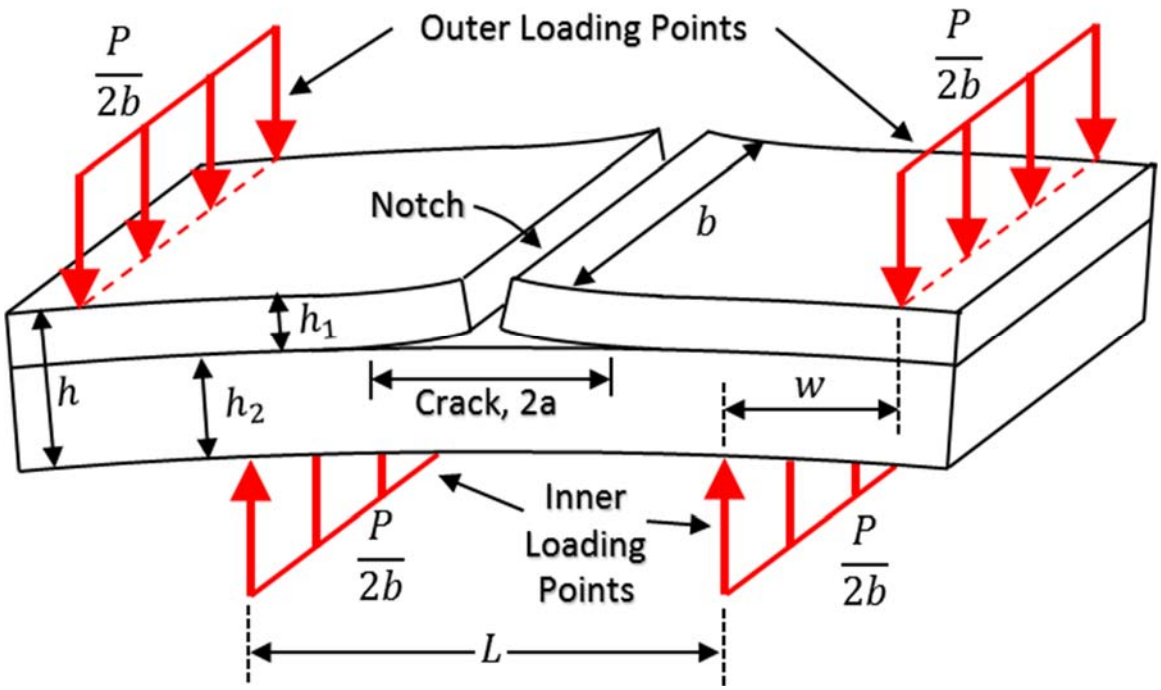

Figure 2-9: Schematic representation of the 4-point bend test for bimaterial systems

A vertical crack is initiated in a specimen coating layer, either through direct cutting or though stress application through 3-point bending that causes a vertical crack to initiate at the center of the coating layer (similar to the method for crack initiation for the micro-

bending test). The sample is then loaded in 4-point bending and with the coating layer in tension the vertical crack propagates to and then runs along the interface. The uniqueness of the 4-point bend methodology is that a constant bending moment is applied between the inner loading pins, which leads to a constant strain energy release rate during delamination. The related consequence of this is that the crack grows between the inner loading pins under a constant cracking load that can be used to calculate the interfacial toughness. It is important to note that the applied load is distributed to both of the loading pins on either side of the sample and is normalized by the width of the sample, b. The phase angle of fracture for this specimen is $\phi = 40.9°$ and the strain energy release rate is given by the following analytical relation:

Equation 2-44

$$G = \frac{21}{4}\frac{M^2}{\bar{E}h^3}$$

In Equation 2-44 $\bar{E}$ is either the plane strain modulus [$\bar{E} = E(1-v)/(1+v)(1-2v)$] or the plane stress modulus [$\bar{E} = E/(1-v^2)$] and the applied moment $M = Pw/2b$. One of the key benefits of the 4-point bend test is that material systems with multiple layers can be easily analyzed though the simple derivation of analytical equations that account for those layers, which will be presented further in section 4.1. One of the drawbacks of this test method is that if not enough strain energy can be developed in the coating to drive delamination then plastic deformation of the underlying metallic layers can occur. This, however, can be alleviated through the use of a stiffener layer adhered to the coating which aid to develop strain energy for delamination.

2.4 References for Chapter 2

1. Sanford, R.J., *Principles of Fracture Mechanics*. 2003: Prentice Hall.
2. Broek, D., *Elementary Engineering Fracture Mechanics*. 1978: Sÿthoff and Noordhoff.
3. Daniel, I.M. and O. Ishai, *Engineering Mechanics of Composite Materials*. 2006: Oxford University Press.
4. Evans, A.G.R., M.; Dalgleish, B.J.; Charalambides, P.G., *The fracture energy of bimaterial interfaces.* Materials Science and Engineering, 1989. **126**.
5. Cherepanov, G.P., *Crack propagation in continuous media.* PMM, 1967. **31**(3): p. 476-488.
6. Griffith, A.A., *The Penomena of Rupture and Flow in Solids.* Philosophical Trans. Royal Society, 1921. **A221**: p. 163-198.
7. Griffith, A.A.B., C.B.; Burgers, J.M., *The Theory of Rupture.* First International Congress for Applied Mechanics, 1925: p. 55-63.
8. Inglis, C.E., *Stresses in a Plate Due to the Presence of Cracks and Sharp Corners.* Trans. Inst. Naval Architects, 1913. **55**: p. 219-230.
9. Orowan, E., *Energy of Fracture.* Welding Journal, Research Supplement, 1955. **34**(3): p. 157-160.
10. Rice, J.R., *A Path Independent Integral and the Approximate Analysis of Strain Concentration by Notches and Cracks.* Journal of Applied Mechanics, 1968. **35**(2): p. 379-386.
11. Arnold, J.O., The Journal of the Iron and Steel Institute, 1894.
12. Hutchinson, R.G. and J.W. Hutchinson, *Lifetime Assessment for Thermal Barrier Coatings: Tests for Measuring Mixed Mode Delamination Toughness.* Journal of the American Ceramic Society, 2011. **94**: p. s85-s95.
13. Charalambides, P.G., et al., *A Test Specimen for Determining the Fracture Resistance of Bimaterial Interfaces.* Journal of Applied Mechanics, 1989. **56**(1): p. 77-82.
14. Williams, J.G., *On the calculation of energy release rates for cracked laminates.* International Journal of Fracture, 1988. **36**(2): p. 101-119.
15. Cao, H.C.E., A.G., *An experimental study of the fracture resistance of bimaterial interfaces.* Mechanics of Materials, 1988. **7**(4): p. 295-304.
16. Evans, A.G., et al., *Structural Materials: Properties, Microstructure and Processing The fracture energy of bimaterial interfaces.* Materials Science and Engineering: A, 1990. **126**(1): p. 53-64.
17. Rice, J., *Elastic fracture mechanics concepts for interfacial cracks.* Journal of applied mechanics, 1988. **55**(1): p. 98-103.

18. Suo, Z. and J.W. Hutchinson, *Sandwich test specimens for measuring interface crack toughness.* Materials Science and Engineering: A, 1989. **107**: p. 135-143.

19. Klingbeil, N.W. and J.L. Beuth, *Interfacial fracture testing of deposited metal layers under four-point bending.* Engineering Fracture Mechanics, 1997. **56**(1): p. 113-126.

20. Balint, D.S. and J.W. Hutchinson, *Mode II Edge Delamination of Compressed Thin Films.* Journal of Applied Mechanics, 2001. **68**(5): p. 725-730.

21. Hutchinson, J.W. and Z. Suo, *Mixed Mode Cracking in Layered Materials*, in *Advances in Applied Mechanics*, W.H. John and Y.W. Theodore, Editors. 1991, Elsevier. p. 63-191.

22. Vasinonta, A. and J.L. Beuth, *Measurement of interfacial toughness in thermal barrier coating systems by indentation.* Engineering Fracture Mechanics, 2001. **68**(7): p. 843-860.

23. Liu, Y.-F., Y. Kagawa, and A.G. Evans, *Analysis of a "barb test" for measuring the mixed-mode delamination toughness of coatings.* Acta Materialia, 2008. **56**(1): p. 43-49.

24. Tanaka, M., et al., *Delamination toughness of electron beam physical vapor deposition (EB-PVD) Y2O3–ZrO2 thermal barrier coatings by the pushout method: Effect of thermal cycling temperature.* Journal of Materials Research, 2008. **23**(09): p. 2382-2392.

25. Guo, S.Q., et al., *Measurement of interfacial shear mechanical properties in thermal barrier coating systems by a barb pullout method.* Scripta Materialia, 2005. **53**(9): p. 1043-1048.

26. Eberl, C., et al., *In Situ Measurement of the Toughness of the Interface Between a Thermal Barrier Coating and a Ni Alloy.* Journal of the American Ceramic Society, 2011. **94**: p. s120-s127.

CHAPTER 3: COMPRESSION EDGE-DELAMINATION TEST

A considerable portion of this thesis work was spent on developing, producing and testing Compression Edge-Delamination (CED) samples. This chapter introduces the underlying mechanics of the test method including the calculated phase angle of fracture and strain energy release rate associate with fracture. Considerations taken during the design and optimization of the geometry of the sample are presented as well as the final sample geometry that was chosen and used throughout the rest of this work. The sample preparation procedure is presented, which extends from orientation of the as-received single crystal superalloy to pre-crack initiation in the prepared samples right before testing. The chapter concludes with the description of the test analysis procedure that uses the Digital Image Correlation (DIC) technique to calculate the critical crack imitation stress from captured images.

3.1 Mechanics of Test Method

The CED test was originally proposed by Hutchinson and Hutchinson [1] as a theoretical framework for measuring coating interfacial toughness. The benefit of this test method is that it provides a relatively straightforward way to directly measure the mode II interfacial toughness of the interface, which most closely represents the conditions present during top coat spallation. In order to ensure that proper loading conditions are present during the test, a derivation of the phase angle (mode-mix) of fracture was conducted. Also, to understand the influence of the applied load and sample geometry on the strain energy release rate during delamination, it was derived using the J-integral analysis technique proposed by Rice [2].

3.1.1 Phase Angle of Fracture

Typically, analytical calculation of the phase angle of fracture requires knowledge of the analytical stress intensity factors (K_I and K_{II}). For the case of the CED sample, the phase angle of fracture can be easily determined simply by observing the crack face displacements. Figure 3-1 shows a schematic of the CED sample loaded with a compressive stress, σ, and with a crack present. In the upper right of the figure both the area above the interface (in the stiffener) and below the interface will both be under compression. In the upper left of the figure an area where the crack has advanced and delaminated a part of the interface is shown. The area below the crack is still under compression, while the stiffener has relieved its stress, which is accompanied by a relaxation of the upper crack face with a displacement in the negative *x*-direction. It should be noted that the vertical separation in the crack faces is shown purely for illustrative purpose and in actuality there is no relative vertical displacement of the crack faces. The phase angle of fracture can be calculated using the following relationship:

Equation 3-1

$$\emptyset = \tan^{-1}\left(\frac{\delta_x}{\delta_y}\right)$$

The vertical displacement is zero, $\delta_y = 0$, and the relative horizontal displacement is negative, $\delta_x < 0$. Plugging these values into Equation 3-1 yields:

Equation 3-2

$$\emptyset = tan^{-1}\left(\frac{< 0}{0}\right) = tan^{-1}(-\infty) = -90°$$

It should be noted that this determination of the phase angle assumes a homogeneous sample with no coating layer: inclusion of further layers leads to a decrease of the phase

angle. Further calculation of the phase angle using Finite Element Methods and assuming all material layers present will be discussed in Section 5.1.

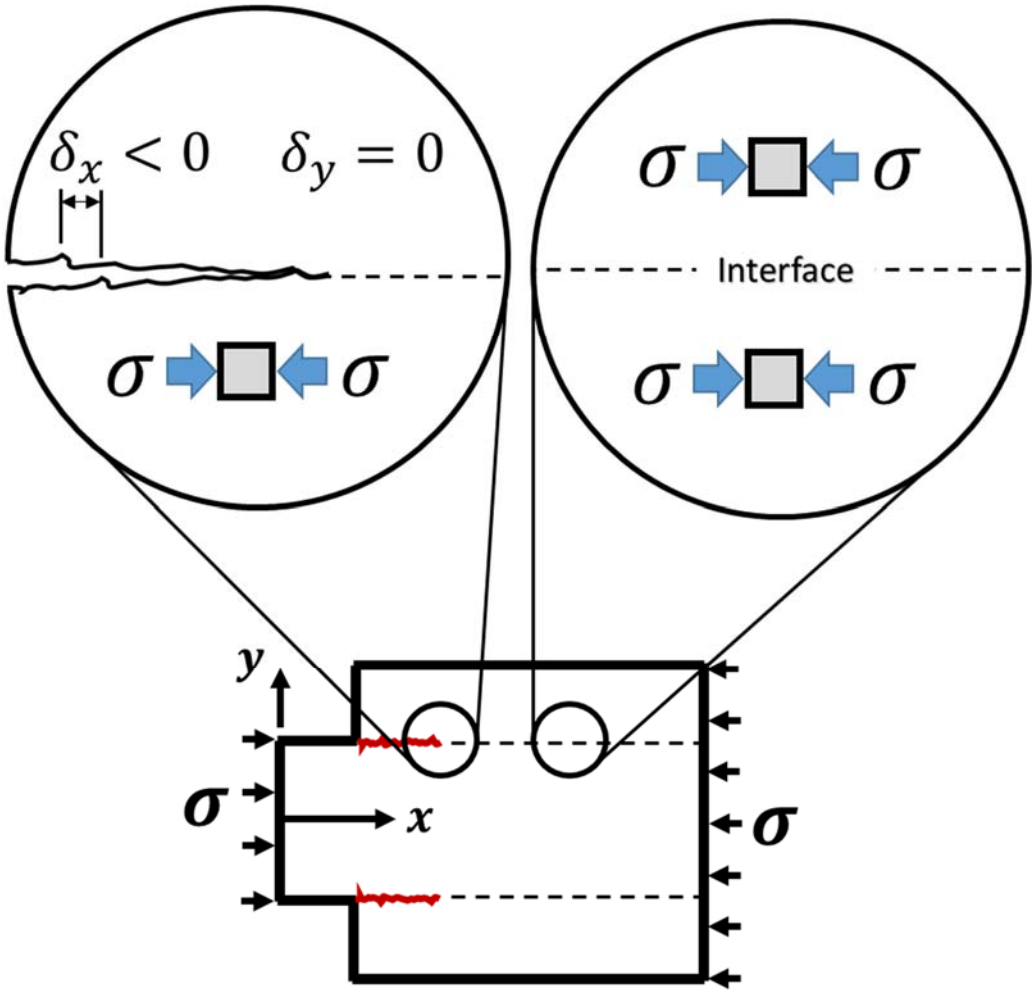

Figure 3-1: Schematic of Compression Edge-Delamination Sample crack face displacement used to calculate phase angle of fracture

3.1.2 J-Integral Derivation

The calculation of the J-integral can be broken down into n different path lengths and superimposed to calculate the whole path integral as defined as:

Equation 3-3

$$J_\Gamma = J_{\Gamma,1} + J_{\Gamma,2} + \cdots + J_{\Gamma,n}$$

where

Equation 3-4

$$J_\Gamma = \int_\Gamma \left(W dy - \frac{\partial u}{\partial x} ds \right)$$

The schematic geometry for the compression edge-delamination sample showing the path taken during the J-integral analysis is shown in Figure 3-2.

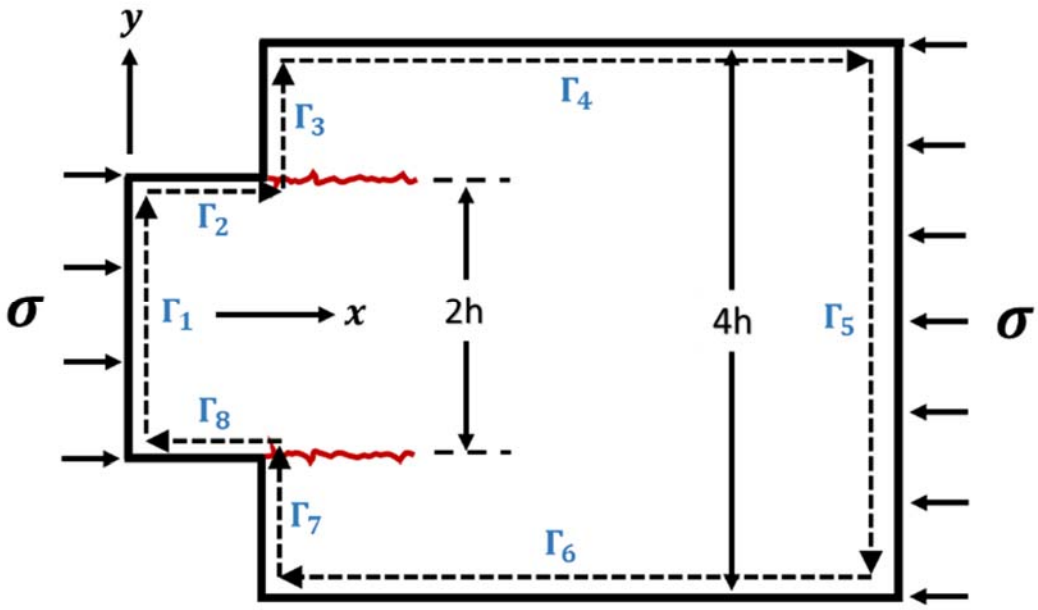

Figure 3-2: Schematic representation of Compression Edge-Delamination geometry and path segments taken during J-integral analysis

For the path selection defined, the contour is defined as $\Gamma = \sum_{i=1}^{8} \Gamma_i$. By making certain assumptions regarding the boundary conditions, the contribution of J vanishes along certain paths. It is readily shown that $J_2 = J_4 = J_6 = J_8 = 0$ since $dy = 0$ and $t = 0$ and $J_3 = J_7 = 0$ since $W = 0$, and $t = 0$.

On the loading surface Γ_1, the following conditions are present:

$$W = \frac{1}{2}\sigma\varepsilon \quad dy = ds$$
$$t = -\sigma \quad \frac{\partial u}{\partial x} = \varepsilon$$

On the loading surface Γ_9, the following conditions are present:

$$W = \frac{1}{2}(-\sigma)\varepsilon \quad dy = -ds$$
$$t = -\sigma \qquad \frac{\partial u}{\partial x} = -\varepsilon$$

With these terms defined the J-integral is defined as:

Equation 3-5

$$J_\Gamma = \int_{-h}^{h}\left(\frac{1}{2}\sigma\varepsilon - (-\sigma)\varepsilon\right)ds + \int_{-2h}^{2h}\left(-\frac{1}{2}(-\sigma)\varepsilon - (-\sigma)(-\varepsilon)\right)ds$$

Equation 3-6

$$J_\Gamma = \int_{-h}^{h}\left(\frac{3}{2}\sigma\varepsilon\right)ds + \int_{-2h}^{2h}\left(-\frac{1}{2}\sigma\varepsilon\right)ds$$

Equation 3-7

$$J_\Gamma = \int_{-h}^{h}(\sigma\varepsilon)ds$$

Equation 3-8

$$J_\Gamma = \sigma\varepsilon h$$

Since the value of the J-integral around the sample is equal to the strain energy release rate present during delamination and with the Hooke's Law for a linear elastic and isotropic material, the interface toughness is defined as:

Equation 3-9

$$G = \frac{\sigma^2 h}{E}$$

3.2 Sample Design Considerations

Design of the Compression Edge-Delamination sample was influenced by a number of important factors. First, a modification of the proposed Hutchinson model to address

potential challenges with the experimental testing of samples is proposed. The design process consisted of an initial set of optimization conditions that were used to generate a landscape of possible configurations. Different geometries were considered and compared to a set of conditions used to validate the sample geometries. Subsequent to this procedure a final choice of geometry was made and further verified using the verification conditions presented. With the final sample geometry defined, production schematics were generated using Solidworks 2013 and appropriate geometric tolerance were applied to ensure proper testing of samples.

Initial design considerations were given by Hutchinson et al. [1] and were used as the basis of the design analysis. These considerations were to make sure that 1) elastic buckling of the sample does not occur and 2) that plastic deformation in the substrate and bond coat layers are precluded. An additional constraint was added to ensure that crack propagation would be possible under the limits of the test machine capabilities for an assumed critical strain energy release rate. The purpose of this condition was to make sure that a high enough stress could be applied to the sample for delamination to occur. In the case of the MTS compression machine used, an applied load for delamination would need to be less that the 100 kN limit of the machines load cell.

3.2.1 Modification to Compression Edge-Delamination Geometry

Before the design process of defining the actual geometry of the test specimen, certain logistical considerations were taken into account regarding the sample configuration. When looking at how the sample geometry proposed by Hutchinson would be loaded an issue arose where, if the two loading surfaces are not perfectly parallel, premature failure could occur through asymmetric loading of the sample. This asymmetric loading applies a

greater displacement to one stiffener than to the other, which could lead to premature delamination. In addition, since one of the loading surfaces contains all the material layers (stiffener-epoxy-top coat-bond coat-substrate-bond coat-top coat-epoxy-stiffener) any foreign material on the loading platen could lead to a stress concentration at the interface, which could cause premature delamination. In order to remedy this potential problem, a modification to the Hutchison model is made to move the stiffener plates from the bottom of the sample towards the middle of the sample. This model, the Modified-Hutchinson model, is shown schematically in Figure 3-3.

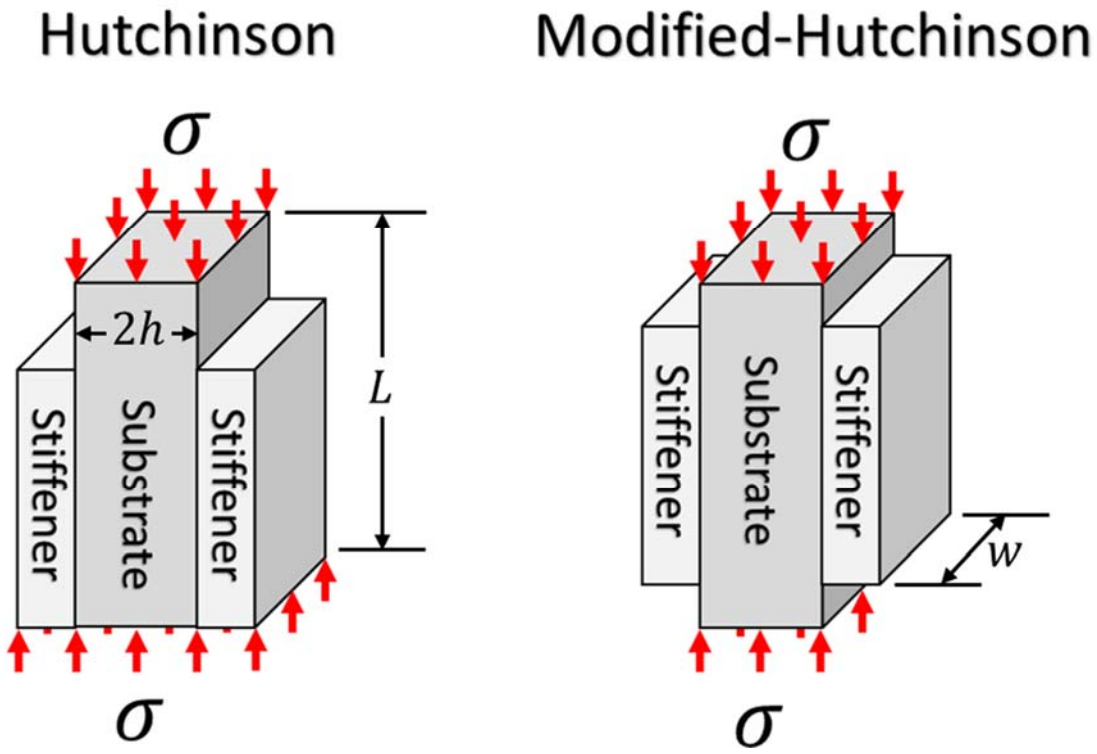

Figure 3-3: Schematic representations of the (left) original Hutchinson model and (right) Modified-Hutchinson model

By moving the stiffener plates towards the center of the sample, the problem of asymmetric loading and foreign object premature delamination is mitigated. FE calculations conducted

in Section 5.3 show that the analysis for both models is the same and that both model geometries can, and are, used interchangeably throughout the work presented in this thesis.

3.2.2 Buckling Design Consideration

The first constraint to preclude buckling can be derived from the Euler-Beam buckling equation given below:

Equation 3-10

$$P_{buckle} = \frac{\pi^2 EI}{L_{eff}^2}$$

In this equation P_{buckle} is the load at which buckling will occur, E is the elastic modulus of the material, I is the polar moment of inertia of the beam with respect to the axis of buckling deformation and L_{eff} is the effective length of the beam. For the loading conditions applied during the test it is assumed that both ends can be modelled as being fixed and an L_{eff} value of $L/2$ is used. In order to preclude buckling the following conditions must be met:

Equation 3-11

$$P_{max,buckling} \leq \frac{\pi^2 EI}{L_{eff}^2}$$

This will ensure that the maximum load applied during testing will not cause the sample to buckle. With the polar moment of inertia of the column being $I = wh^3/12$ and the effective length of $L/2$, where w is the width of the sample and h is the thickness, the equation for the maximum load to preclude buckling becomes:

Equation 3-12

$$P_{max,buckling} \leq \frac{\pi^2 E w h^3}{3L^2}$$

In order to define the equation for buckling in terms of the geometric factors, the maximum load before buckling occurs needs to be related to the applied load, or stress, needed for delamination. With the strain energy release rated defined as $G = \sigma^2 h/E$, and the applied stress $\sigma = P/2wh$ the following condition for the minimum value of h to preclude buckling is:

Equation 3-13

$$h_{min,buckle} = \left(\frac{36L^4 G}{\pi^4 E(1+\nu)}\right)^{\frac{1}{5}}$$

It is important to note that this equation is based off of an assumed strain energy release rate. To understand the variably of the calculated geometry parameter it will be necessary to vary *G* within reasonable limits.

3.2.3 Substrate Yielding Consideration

In order to ensure that the substrate does not yield before delamination occurs, it is necessary to relate the thickness parameter *h* to the critical yielding stress. The importance of this parameter is two-fold. The first is that if plastic deformation occurs in the substrate, slip bands can form that will apply non-shear delamination displacements to the coating interface. This undermines the importance of the mode II loading present during the CED test. The second reason for precluding yielding prior to delamination is that the analysis used to extract the strain energy release rate would become much more complicated. A detailed Finite Element model would need to be constructed that takes into account the plastic flow of both the substrate and the bond coat layers. While possible, this would

increase the error in calculation of the interface toughness and avoiding yielding significantly simplifies the analysis. With the previously defined strain energy release rate and rearranging to isolate the height parameter, the minimum value of h to ensure that yielding does not occur before delamination is:

Equation 3-14

$$h_{min,yield} = \frac{GE}{\sigma_{yield}^2(1+\nu)}$$

3.2.4 Testing Machine Maximum Load Consideration

The last factor to be taken into account is whether or not the testing machine will be able to provide the necessary critical stress to ensure delamination before the load limit of the machine is reached. The maximum stress that can be applied to the sample before the machine reaches its upper load limit is defined as:

Equation 3-15

$$\sigma_{max} = \frac{P_{max,machine}}{2wh}$$

By incorporate this into the relation for the critical strain energy release rate from Equation 3-9 an expression for the maximum value of h to drive delamination below the load limit of the compression machine is:

Equation 3-16

$$h_{max,machine} = \frac{P_{max,machine}^2(1+\nu)}{4E}$$

It should be noted that a factor of safety should be included in the maximum load so that permanent damage to the loading frame or load cell does not occur during testing.

3.2.5 Combined Geometry Optimization

With the design equations defined they can now be combined to determine the design space for sample geometries. For these equations the substrate material is René N5, for which the following properties are taken to be: $E_{[100]} = 128\ GPa$, $\nu = 0.28$, $\sigma_{yield} = 855\ MPa$ [3]. Looking at values reported previously in literature [4-9], a lower estimate for the critical strain energy release rate can be taken at G_c = 50 J/m^2. The remaining unknowns in the design equations are the length, L, and the width, w. By making an assumption that the width will be ½ of the total length of the sample the remaining independent variable, the length, can be varied to calculate the height parameter h. The design curve for the case of G_c = 50 J/m^2 is shown in part (a) of Figure 3-4. In order to interpret the figure, it is important to remember that in order to satisfy the conditions present the chosen height parameter h must be above the minimum value for yielding, above the minimum value for buckling and below the maximum value for the machine limit. The valid design sample is indicated on the figure and indicates the area where a combination of the height parameter, h, and a sample length, L, will satisfy the design equations and results in successful delamination of the interface. It is important to provide a factor of safety in the design for the case where the actual interfacial toughness is much higher than previously reported values. An upper value of G_c = 500 J/m^2 was chosen to represent this case and the design curve for this conditions is shown in part (b) of Figure 3-4. Based off of the amount of substrate material available, an initial choice for the sample geometry was made to be: L = 20 mm, w = 10 mm, h = 3 mm such that a sufficient number of samples could be produced from the René N5 single crystal provided by GE. In order to verify this chosen geometry, the load required to satisfy the sample design conditions as well as the minimum load required for delamination to occur was plotted against the interfacial toughness of the sample, which

can be seen in Figure 3-5. The maximum load for buckling is not shown as it is much higher (≈28,000 kN) than the values shown on the figure. It is readily seen that the required load in order to drive delamination is significantly lower than any of the limiting loads (yielding, buckling and machine capability). This sample geometry was chosen to be the geometry used to machine the CED samples from the cast single crystal René N5 and is shown in Figure 3-6.

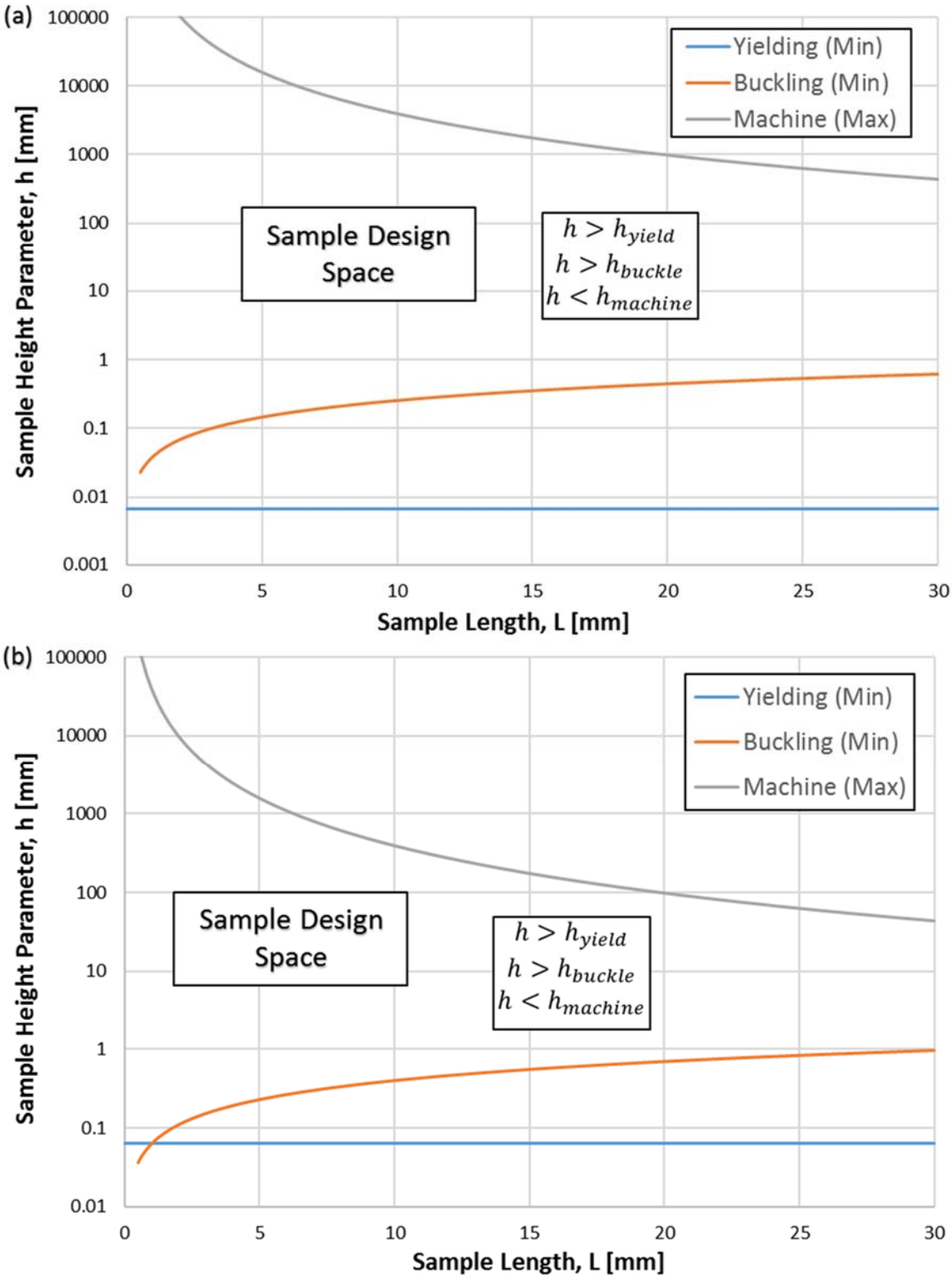

Figure 3-4: Sample height parameter vs. sample length for cases of (a) $G_c = 50$ J/m² and (b) $G_c = 500$ J/m²

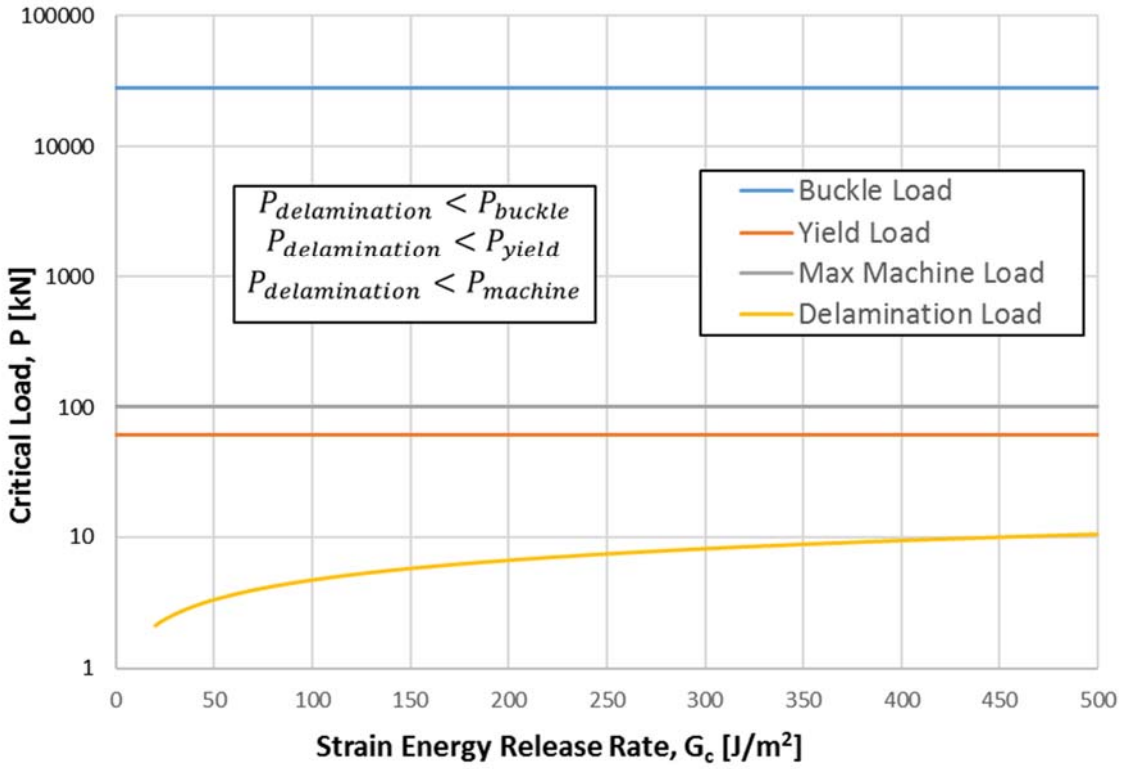

Figure 3-5: Critical load vs. strain energy release rate for chosen sample geometry (L = 20 mm, w = 10 mm, h = 3 mm)

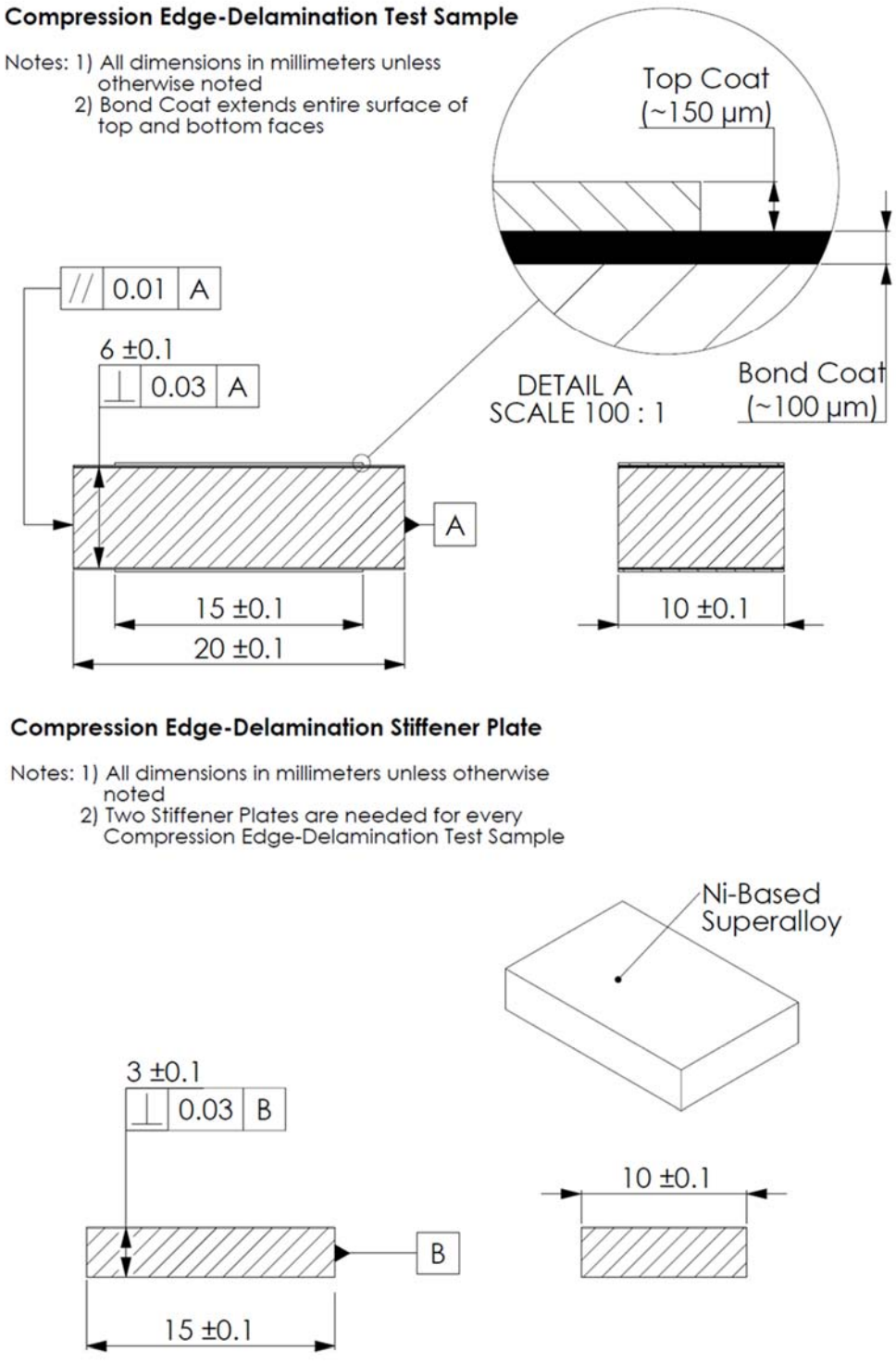

Figure 3-6: Production schematics with finalized geometry for Compression Edge-Delamination Specimen (top) and stiffener plate (bottom)

3.3 Sample Preparation

The René N5 crystal was oriented along a <001> crystal direction using Laue x-ray diffraction and samples were cut using Electric Discharge Machining (EDM). Samples were then polished with SiC polishing paper down to 1200 (P-4000) grit before being sent back to industrial partners for bond coat and top coat application. A custom designed top coat application fixture was designed in-house to allow samples to be coated on both sides of the sample at the same time in the same industrial EBPVD chambers used to coat in-service turbine blades.

3.3.1 Single Crystal Orientation (Laue X-Ray Diffraction)

A rectangular crystal of René N5 was cast by GE using directional solidification from a seed crystal oriented in the <001> crystallographic orientation. The dimensions of the crystal were 6 inches by 2 inches by 0.5 inches thick. The surface normal vectors of the single crystal were all nominally oriented in the [001] direction. To ensure precise orientation of the samples cut, the actual crystal orientation was measured with Laue x-ray diffraction. The method of using back-reflection Laue x-ray diffraction is described by Kikuchi [10] who outlines the procedure by which single crystals can be oriented to align with any crystallographic plane. In the back-reflection technique, a continuous spectrum of x-rays is collimated and directed through a hole in the x-ray detector and towards the single crystal sample, which is shown schematically in Figure 3-7.

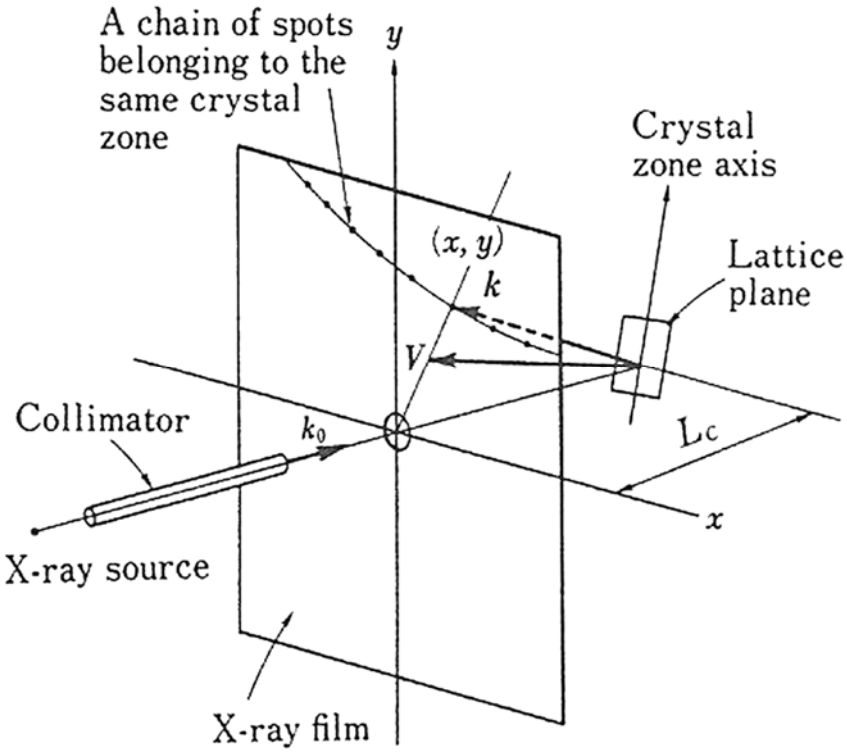

Figure 3-7: Schematic of the back-reflection Laue x-ray diffraction method for orientation of single crystals (taken from [10])

The range of wavelengths in the x-ray beam are sufficient to satisfy Bragg's law, $n\lambda = 2d\sin(\theta)$: where n is a positive integer, λ is the wavelength of the incident beam, d is the atomic lattice plane spacing and θ is the incident angle of the electron beam with respect to the atomic plane tangent. This relationship is shown schematically in Figure 3-8. When the diffraction condition satisfies Bragg's Law, diffraction spots are projected onto the x-ray film (or solid-state detector) and can be used, with knowledge of the material lattice parameters, to calculate the current orientation of the crystal.

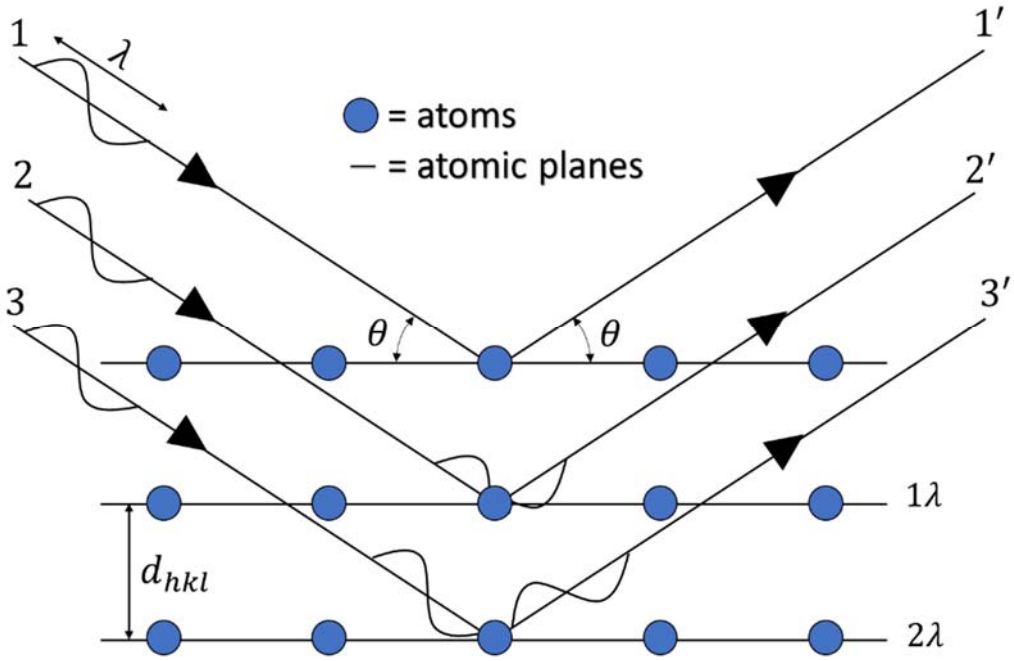

Figure 3-8: Schematic of Parallel Crystallographic Planes and Satisfaction of Bragg's Law Conditions

The machine used to orient the crystals is a Multi-Ware Laboratories 120 Real-Time-Laue-Backscattering-Camera system that uses the North Star v7.0 software package to analyze the recorded diffraction spots for crystallographic orientation determination. A picture of the setup and representative picture of the diffraction spot output can be seen in Figure 3-9. A South Bay Model 260 3-Axis goniometer that could be mounted in both the x-ray chamber and in the electric discharge machining (EDM) setup, was used to hold the René N5 crystal. A diffraction pattern was then capture and crystallographic orientation was determined. Subsequent angle adjustments on the goniometer were determined in order to have the crystal [001] plane lie directly parallel to the base of the goniometer. Another x-ray scan was conducted to ensure that proper alignment was achieved and locks were tightened to fix the goniometer angular positions. Once proper orientation of the crystal was obtained, the goniometer/René N5 assembly was then ready to be moved to the cutting setup for machining of the substrate samples.

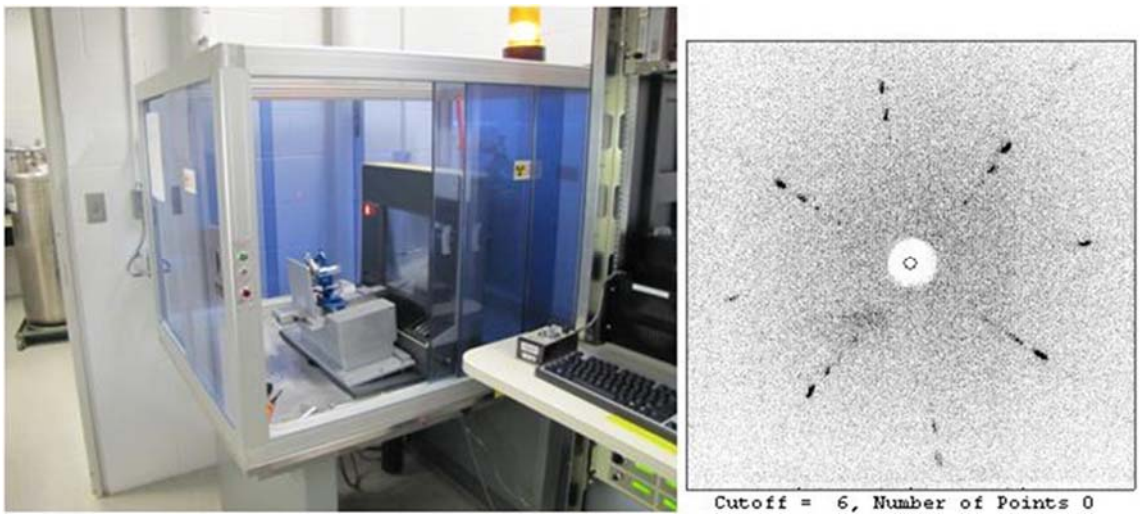

Figure 3-9: (left) Multi-Ware laboratories 120 Real-Time-Backscattering-Camera system x-ray Laue diffraction machine and (right) example of North Star v7.0 software output of measured diffraction spots (right)

3.3.2 Electric Discharge Machining (EDM) of Substrate

In order to ensure proper loading of the Compression Edge-Delamination specimen, appropriate geometric tolerances are necessary on the loading faces of the sample. A tight tolerance on the parallelism between the loading surfaces as well as the perpendicularity of the loading surfaces with respect to the direction of loading is crucial for successful testing. Metals commonly used in production of parts for industries that require highly tolerance parts typically use high-precision lathes and mills under strict temperature controlled conditions to ensure that produced parts can maintain their specified tolerances. For the case of materials that work harden readily during machining, such as in Ni-based superalloys, special procedures need to be employed to ensure proper tolerances are held. Work hardening occurs when the metal ahead of the cutting tool is plastically deformed and subsequently hardens due to dislocation entanglement. The hardened layer of material become very difficult to penetrate by the cutting tool and can lead to premature wearing and/or breaking of the tool bit and makes the work hardened layer significantly more

difficult to machine. There are a number of ways to avoid work hardening in nickel-based superalloys, such as the use of hardened carbide tools and careful selection of tool bit rotation and feed rate. The use of EDM on nickel-based superalloys provides an attractive alternative to traditional machining techniques while still being able to maintain proper tolerances and is widely used in the aerospace industry for this reason. The EDM process operates by rapid discharge of current between two electrodes separated by a dielectric liquid under the application of an electric potential voltage. For the wire-EDM process used to cut these samples, one of the electrodes is the wire and the other electrode is the work piece. By optimizing the machine parameters very thin recast layers, typically less than 40 μm, are present. A summary of the parameters used to produce the CED coupons can be seen in Figure 3-10. The settings were based of a pre-existing setting used for cutting of D2/A2 tool steel, with the wire feed rate (WF) decreased from setting 15 to 10, the water flow (FR) increased from 10 to 15 and the cutting speed (SPD) decreased from 0.385 to 0.267. The modification of these settings results in a more consistent surface finish, less chance of the feed wire breaking and a minimization of the damage layer.

The damage (or recast) layer present after EDM cutting of the samples consist of redeposited material both from the cutting process and potential contaminants in the dielectric liquid. After the cutting of samples using EDM, metallographic polishing with SiC polishing paper down to 1200 (P-4000) grit is used to remove the recast layer to ensure no impurities exist prior to subsequent bond coat and top coat application.

Setting #	Fanuc EDM Code	G-Code	Value
1	Cutting No.	NUM	1
2	Cutting mode	PM	21
3	No load v.	VS	3
4	Current cnt	CC	12
5	Cutting v.	VM	31
6	On time	ON	6
7	Off time	OFF	15.4
8	AC/DC	AC	1
9	Servo Mode	SVM	N/A
10	Servo v.	SVM	22
11	Servo gain	SVG	319
12	Power cnt-A	WP1A	15

Setting #	Fanuc EDM Code	G-Code	Value
13	Power cnt-B	WP1B	5
14	Off. cnt-A	WP2A	2
15	Off. cnt-B	WP2B	12
16	Tension	T	1300
17	Wire feed	WF	10
18	Water flow	FR	15
19	Water cnt.	FC	0
20	Cutting spd.	SPD	0.267
21	Skim pulst cnt.	SPC	N/A
22	Corner cnt.	AIC	30003
23	Straight. adj.	STOFST	0.00035
24	Offset	OFST	0.00673

Figure 3-10: Fanuc Alpha 0iE EDM settings for use when cutting Ni-based single crystal superalloys

3.3.3 Bond Coat and Top Coat Application

The machined and polished René N5 samples were sent to GE for both bond coat and top coat application. The bond coating process consists of electroplating of a thin layer of platinum on the substrate with a subsequent aluminization process to deposit aluminum on the surface. A subsequent heat treatment process homogenizes the bond coat to a uniform upper composition with an inter-diffusion zone between the bond coat and substrate. The bond coating process mirrored the same conditions present during bond coat application of commercial GE turbine blades.

A typical EBPVD coating system is shown in Figure 3-11. A loading chamber is used to place the samples in their holding fixtures for coating. During coating the blades are rotated about their central axis and about the holding fixture axis as shown in Figure 3-12. After the samples are placed in the loading chamber a vacuum is drawn and the sample are placed into a preheating chamber, which brings the sample up to the coating temperature (around 1000°C). Once the samples are up to temperature they are moved into the coating chamber

for deposition of the top coat. A schematic of the coating chamber is shown in Figure 3-13. Electron beam guns in the chamber heat up crucibles with the 7% YSZ ingots as well as impinging on the blades to keep them at an appropriate coating temperature. A vapor cloud forms as the YSZ evaporates and the blades rotate around the axes shown in Figure 3-12 top ensure an even thickness and microstructure.

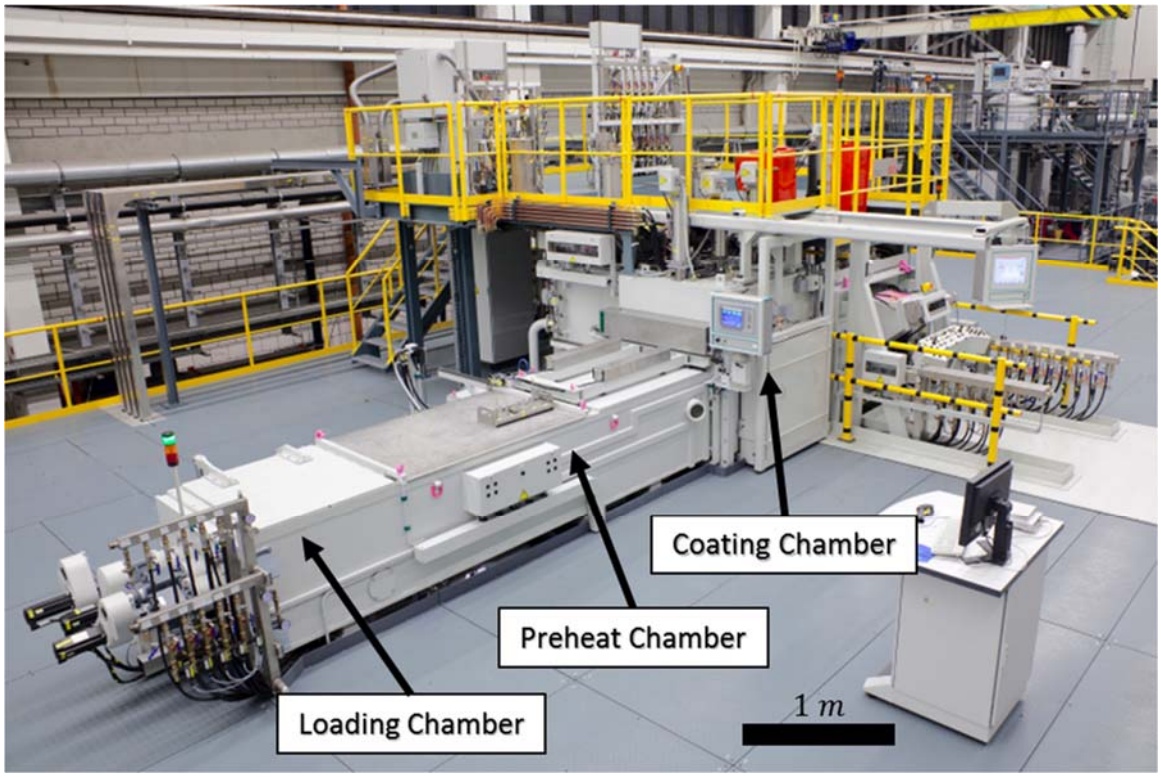

Figure 3-11: Overview of Electron Beam Physical Vapor Deposition (EBPVD) chamber for coating turbine blades (taken from [11])

Initial problems arose when the bond-coated specimens needed to have the top coat layer applied to them. As previously mentioned when the turbine blades have the EBPVD top coat applied they are held in the coating chamber by the base of the turbine blade. In order to have the samples coated they need to be contained within a fixture where the total size of the fixture could not exceed the size of a turbine blade and the fixture needed to be of similar shape and be able to be mounted in the loading frame.

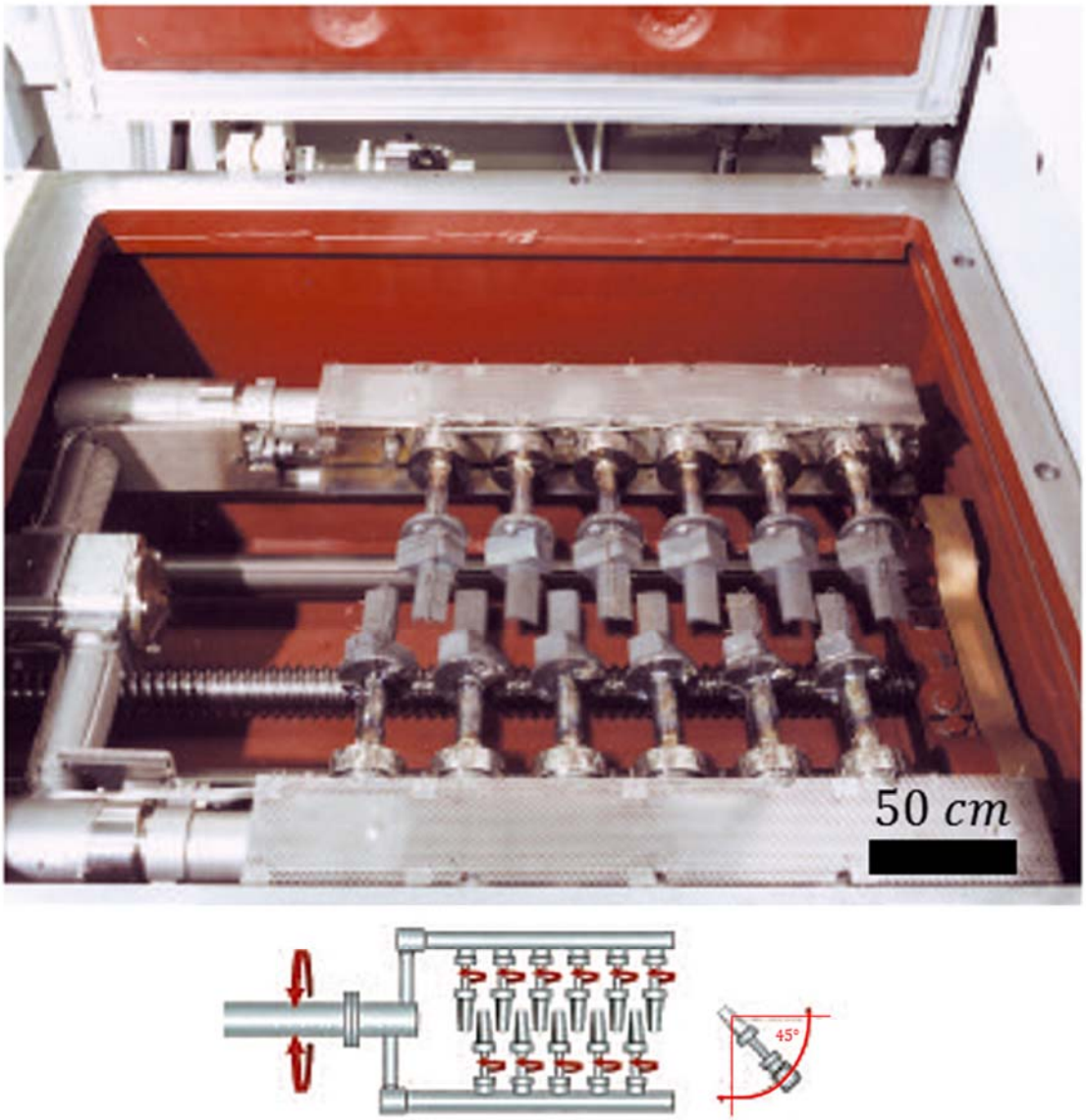

Figure 3-12: Overview of loading chamber of EBPVD coating setup (arrows indicate motion of travel of components during coating (taken from [12])

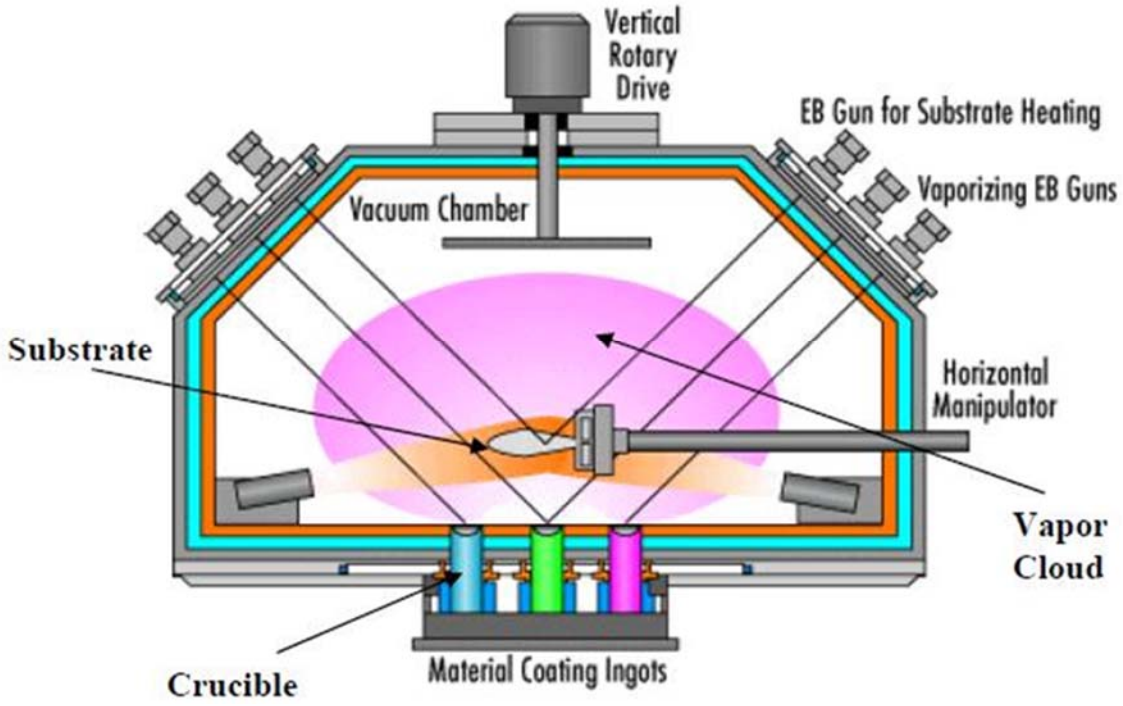

Figure 3-13: Schematic overview of Electron Beam Physical Vapor Deposition (EBPVD) process for coating turbine blades (substrate) (taken from [13])

3.3.3.1 Design of Coating Fixture

The top coat deposition process is desired to be conducted as closely to the same conditions as in-service engine hardware. This ensures that the chemical and morphological behavior of the CED samples will be identical to that of in-service hardware. In order to achieve a representative microstructure, it was determined that the best way to achieve this level of similarity would be to have the samples coated in a commercial coating chamber. This includes ensuring that the samples have as much angular exposure to the vapor cloud as possible to ensure the same top coat columnar geometry as in-service hardware has. One design constraint was that in order to accommodate coating of the samples, they would need to be contained in one of the slots usually reserved for a turbine blade. Design constraints for the fixture were imposed so that the fixture would not exceed the total allowable size for the turbine blades being coated in the coating chamber. The fixture also

needed to be composed of a temperature-stable Ni-based superalloy, so as to maintain structural stability at high temperature, approximately 1000°C, and also not contaminate the coating chamber with foreign elements. Hastelloy X was ultimately chosen to construct the coating fixture as it met the aforementioned requirements. The coating fixture also needed to have the flexibility to be fixed together either with Ni-based superalloy bolts and nuts or with Nickel wire ties, depending on which method the coating vendor had available. The final consideration was to ensure that that excess shadowing of the samples would not occur due to the geometry of the fixture. If the field of view of the sample surface was too small, changes in the top coat layer thickness and top coat morphology could occur that would not be representative of in-service hardware. A schematic of the coating fixture designed can be seen in Figure 3-14. In order to attach the coating fixture to the coating chamber holder, the base of the fixture needed to have the same geometry as that of a turbine blade. In order to accomplish this task, the base of a turbine blade was cut off using EDM and was then tack-welded to a post that screws to the base of the coating fixture. This process can be seen in Figure 3-15. After the samples were coated with the top coat, the fixture was sent back to JHU for unloading of the samples and for removal of the 7% YSZ from the coating fixture before being sent back to GE for coating of the next round of samples.

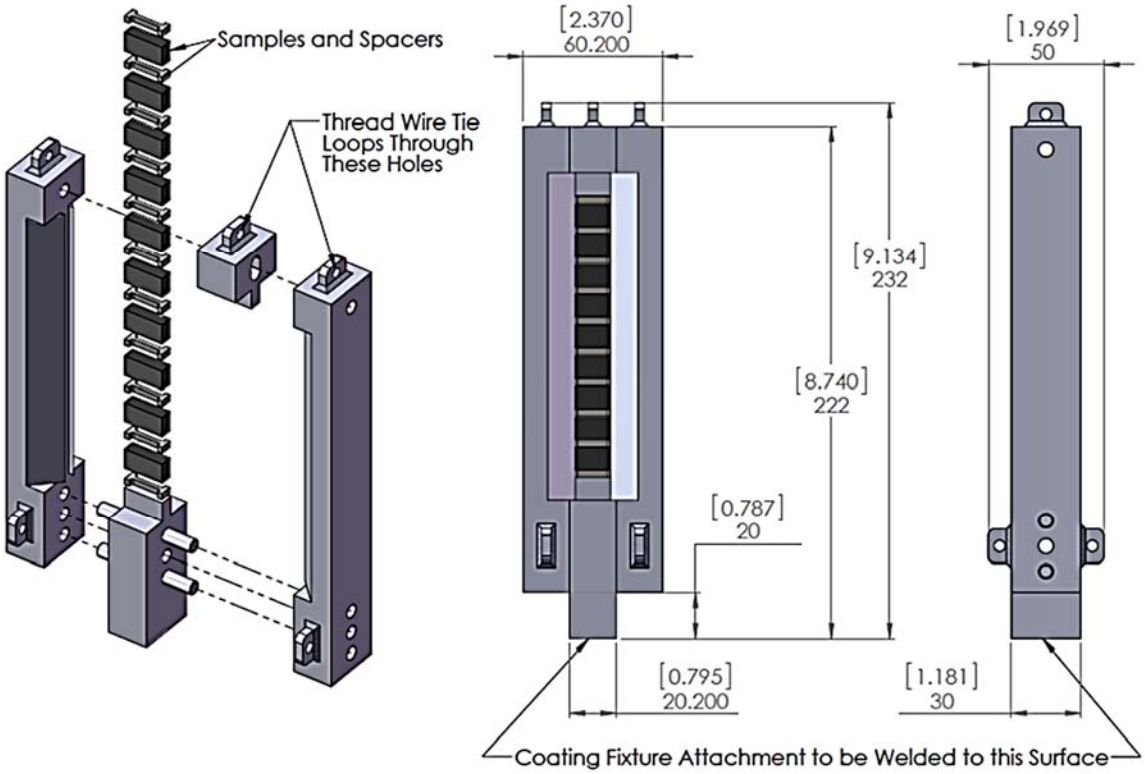

Figure 3-14: 3D Model of the top coat fixture used during application of the EBPVD 7% YSZ top coat

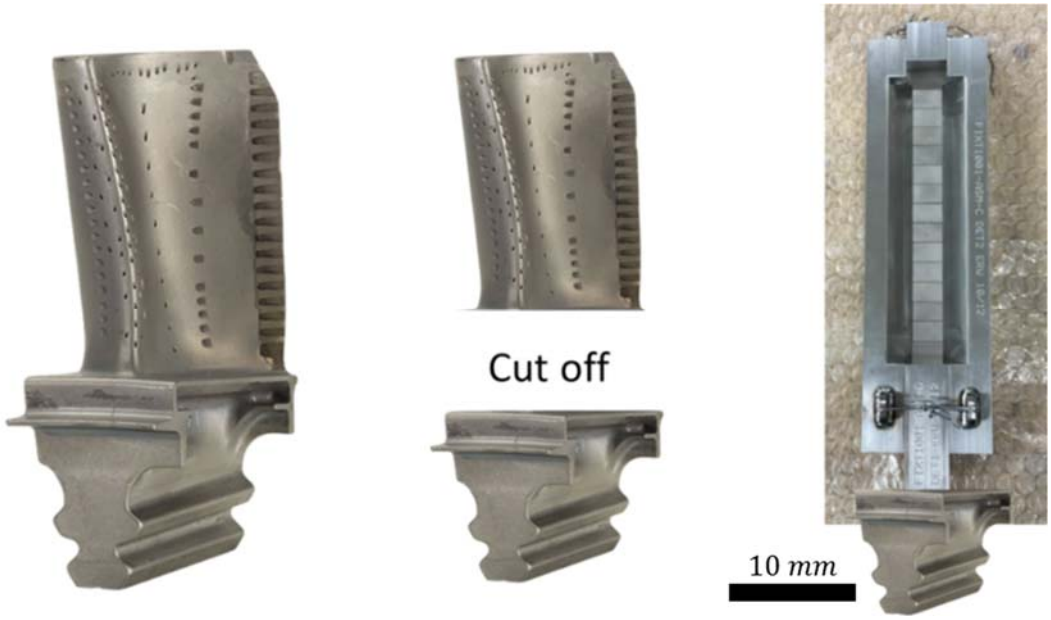

Figure 3-15: Schematic showing the procedure by which the coating fixture is adapted to fit in the coating chamber

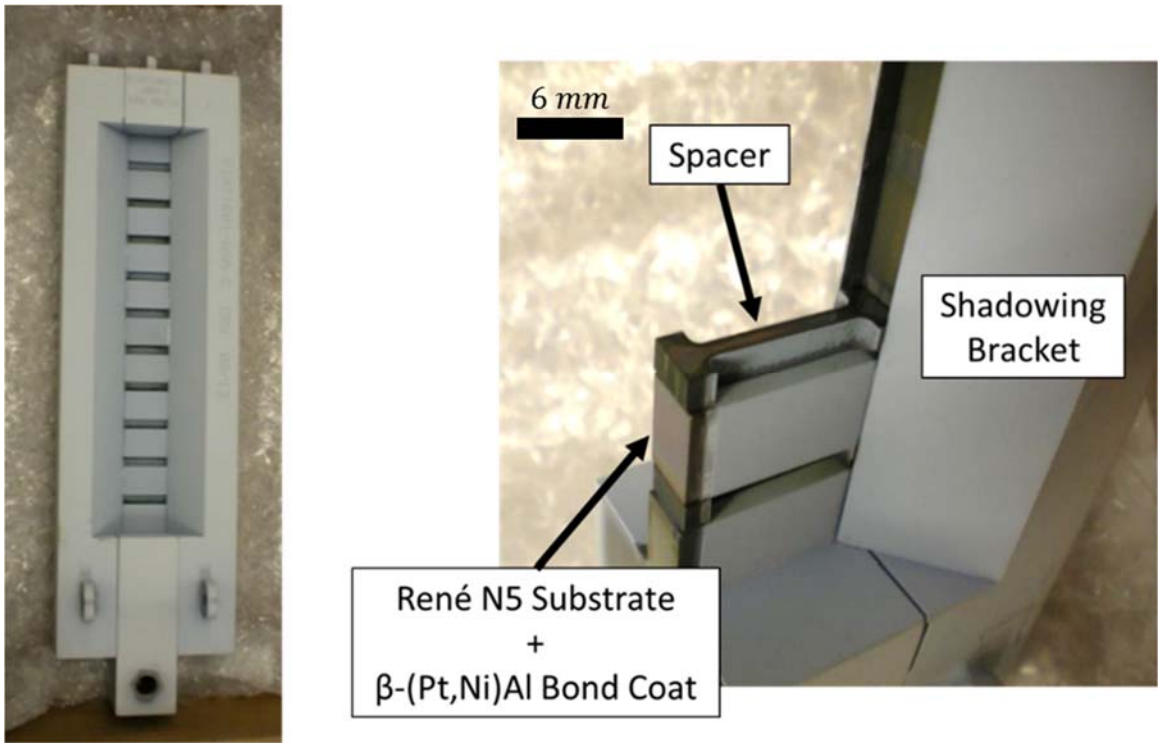

Figure 3-16: Top coating fixture after receiving it back from GE after TBC top coat application

3.3.4 Metallographic Polishing

After samples were received back from top coat application by GE, polishing of the non-top coated surfaces needed to be conducted to remove oxide formation that occurred during the deposition process. An Allied Technology Tech-Prep 8 automatic polished was used to polish the surfaces, which is shown in Figure 3-17. The unit contains a positioning head assembly that allows for rotation of the sample about the axis normal to the polished surface as well rotation that draws an arc over the polishing paper. This movement ensures that the polished surfaces are as flat as possible and free of contaminants. The assembly also contains a micrometer that allows for monitoring of the amount of material removed to ensure even removal over each sample.

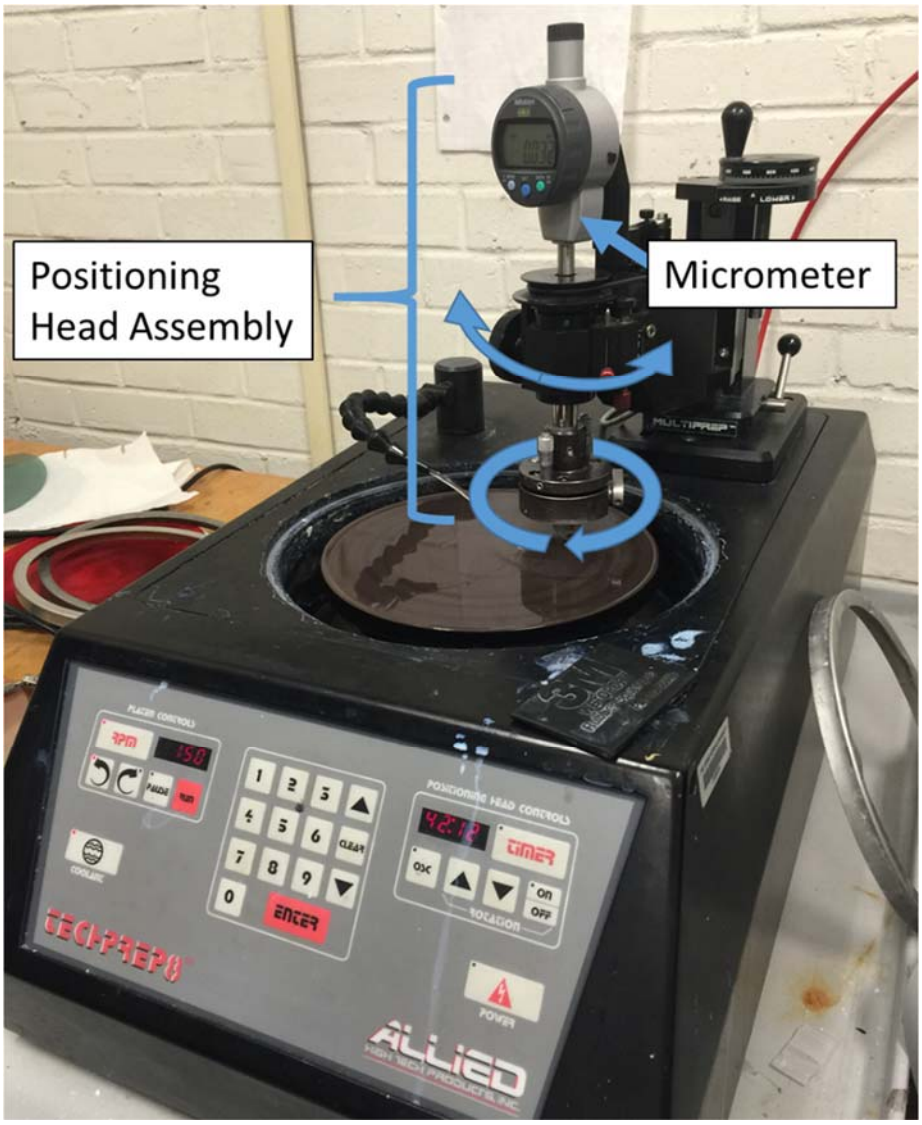

Figure 3-17: Allied Technologies Tech-Prep 8 automatic polished used to polish surfaces of sample to ensure parallelism and perpendicularity constraints are maintained during metallographic polishing

3.3.5 Stiffener Application with Epoxy

Stiffener plates were used in order to build up adequate strain energy to drive delamination without yielding of the underlying metallic layer. Stiffener plates composed of René N5 were cut using EDM to the dimensions specified in Figure 3-6. The epoxy chosen to attach the stiffeners to the top coat layer was Araldite 2011, due to its high viscosity, high shear strength and its previous success in other studies [8, 14]. An epoxy with a high viscosity is

desirable because a low viscosity epoxy will tend to wick down into the gaps between the top coat columns. When the low viscosity epoxy hardened it created a region, where the epoxy has wicked, that acts as a composite structure that is stiffer than the top coat layer. In order to preserve the mechanical response of the top coat a high viscosity epoxy that only bonded to the surface of the top coat and did not wick into the columnar gaps was used. A high shear strength epoxy is also necessary as the top coat/epoxy and epoxy/stiffener interfaces will be loaded in pure shear and if either of these interfacial strengths is less than the bond coat/top coat interfacial strength, premature failure of the epoxy bonding will occur before TBC delamination occurs. To apply the epoxy a thin layer is first applied to the stiffener. A large glass slide is then put in contact with the epoxy and the slide is pulled perpendicular to the normal of the stiffener. This smearing process produces a thin and even epoxy layer on the stiffener. The stiffener with epoxy is then placed on the top coat and a 1 lb weight is placed on top of the stiffener to provide an even weight distribution that further promotes an even epoxy thickness. Care was taken to ensure the epoxy layer was around $100\ \mu m$ this as the manufactures' specifications indicate this provide the strongest shear strength for the bond [15]. After the stiffener plates are applied the samples were cured for 24 hours at room temperature in a pressure chamber at 60 psi.

3.3.6 Initial Problems with As-Deposited Samples

There were a number of problems that initially arose during the testing process. Samples that were received in their as-deposited state were loaded as shown in Figure 3-18. For the case of the GE prepared material system, the first sample was loaded up to the point of substrate yielding at which point a shear band formed in the substrate and intersected with the top coat layer causing spallation of the left interface. In a parallel study of the Pratt &

Whitney material system, the sample was loaded below its substrate yield strength with no delamination occuring. For both material systems, delamination did not occur past the highest load for the expected failure region (corresponding to G_c = 500 J/m^2).

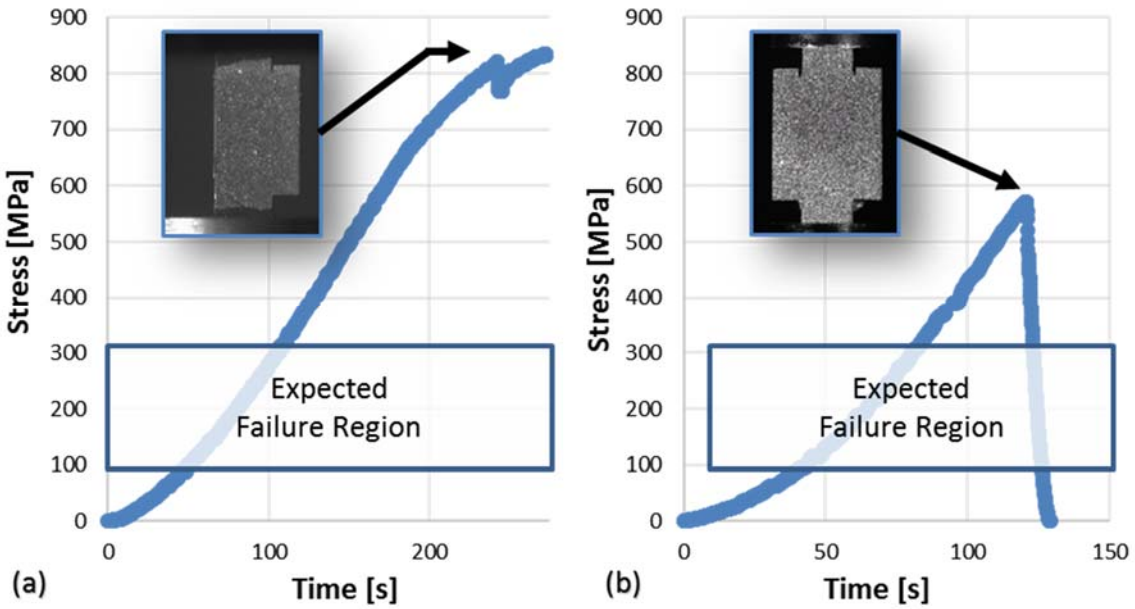

Figure 3-18: Representative stress vs. time plots for as-deposited compression edge sample composed of (a) Rene N5 substrate, β-Pt(Ni,Al) bond coat, EBPVD 7%YSZ top coat and (b) PWA 1484 substrate, LPPS NiCoCrAlY bond coat, EBPVD 7%YSZ top coat

3.3.6.1 Micro-indentation of Interface

In order to assess the reason why delamination did not occur in the expected load region, micro-indentation was conducted on the bond coat/top coat interface. The instrument used was a Leico M400 Microhardness tester with a diamond Vickers micro-indentation tip. An as-deposited sample, with surfaces polished with 2400 grit SiC polishing paper, was oriented so that indentations could be made directly at the bond coat/top coat interface. A total of 20 indentations were made along the interface, with a typical indentation shown in Figure 3-19. All of the indentations cracked both the bond coat and top coat layers, but did not delaminate the interface. This behavior led to the conclusion that the as-deposited

interface was too strong to effectively nucleate and grow a crack in the single-crystal substrate yielded. It was therefore deemed necessary to introduce a pre-crack in order to promote delamination.

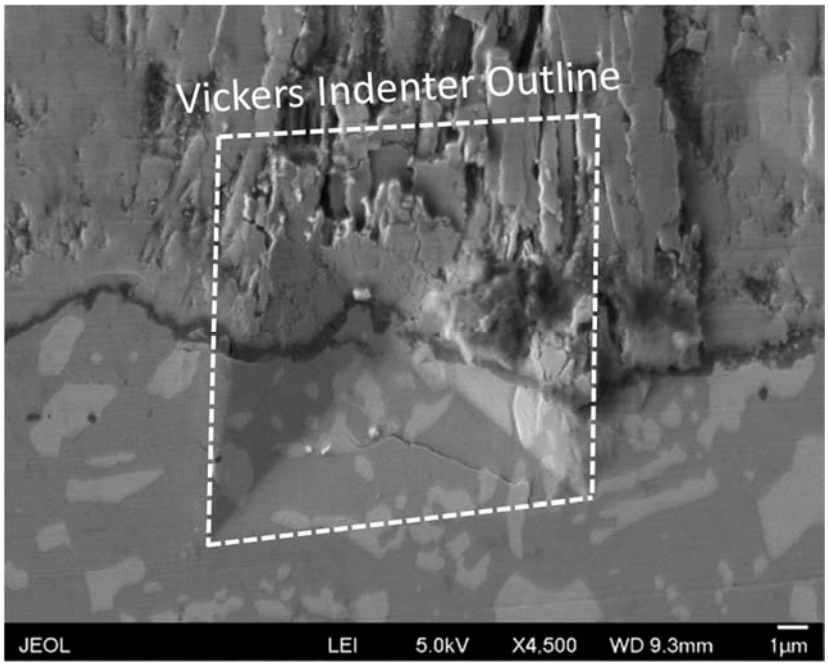

Figure 3-19: Typical indentation surface made as bond coat/top coat interface in as-deposited TBC system with René N5 Substrate, β-Pt(Ni,Al) Bond Coat and 7% YSZ Top Coat and sub-micron TGO

3.3.6.2 Pre-Crack Creation through Acid Etching

A number of methods were initially considered in order to create a starter crack in the samples. The first involved deposition of a thin layer of sacrificial material to act as a starter crack. The sacrificial layer could be deposited through either sputtering or vapor deposition, but this method was determined to not be possible as industrial partners, GE and Pratt & Whitney, would not allow for any foreign material present in the industrial coating chambers. The reason for this was to not contaminate the commercial turbine blades being coated. Another method utilizing femto-second laser machining being developed at Johns Hopkins was considered, but ultimately the system was not ready in

time for this study. The method ultimately settled upon was based off existing technologies utilized by coating companies to remove damaged bond coats and top coats from turbine blades. A solution of 35% H_2PO_4, 30% HCl and 35% H_2O is commonly used for selective removal of bond coats. This technique was adapted to selectively etch the bond coat layer in the CED sample so as to create a stress concentration. The CED samples were inverted in a roughly 5 mm deep acid bath as shown in Figure 3-20.

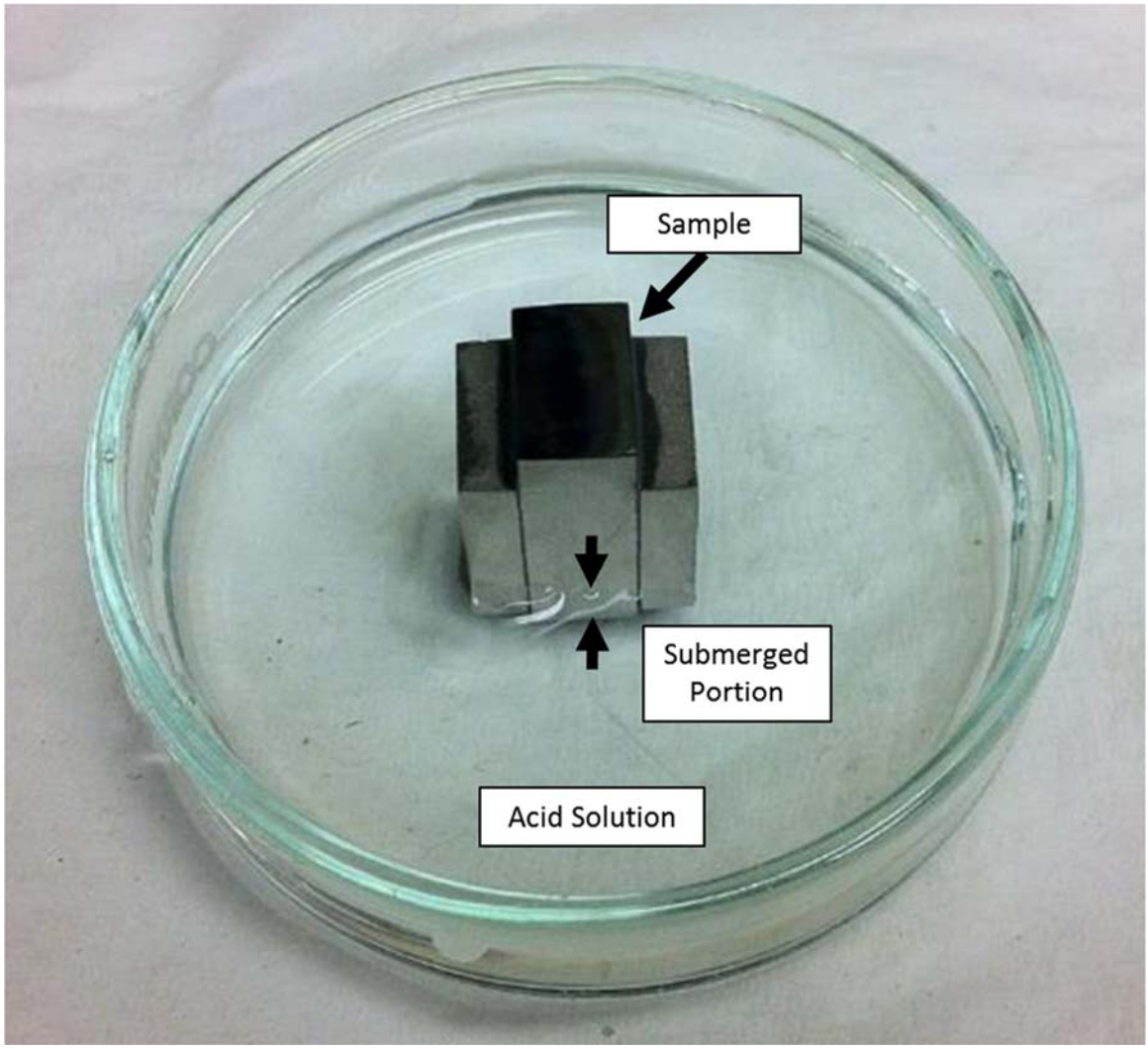

Figure 3-20: Sample with stiffener plates attached and epoxy cured that is partially submerged in $35H_2PO_4$-30HCl-$35H_2O$ acid bath for bond coat etching

The sample was left to etch in the room temperature acid bath for 1 hour and then removed, the acid was neutralized in a baking soda and water solution, and the sample put in an isopropyl alcohol bath in a sonic bath for 10 minutes to remove waste material. This process was repeated 3 more times or until a significant amount of the bond coat was removed. Figure 3-21 shows a series of stitched together SEM images of the sample after bond coat etching. The etching procedure removes a small “lip” of bond coat material from the front, left and back sides (not shown) of the sample. It also etched the material faster towards the top coat interface than at the substrate interface and therefore creates a layer of bond coat material that forms an acute angle to the top coat interface, which in turn acts as a further stress-concentration during testing of the sample.

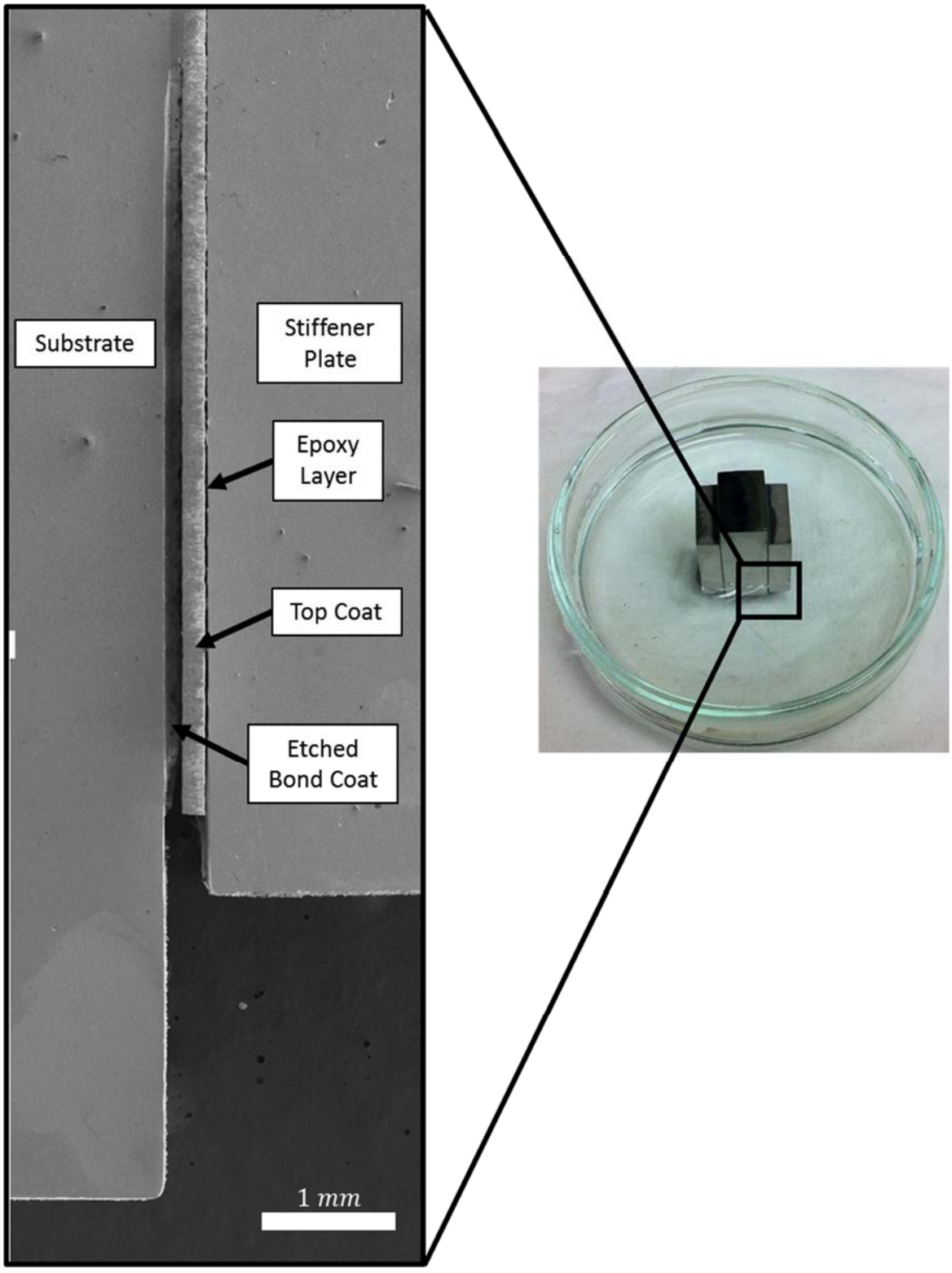

Figure 3-21: Series of SEM Images stitched together to show effect of bond coat etching on the bond coat layer in the Compression Edge-Delamination Sample

3.4 Test Analysis Procedure

Analysis of the CED sample requires the ability to calculate in-plane shear maps from the surface of the sample. An introduction to various non-contact strain measurement techniques will be introduced in this section. A more detailed description of the DIC technique is presented with corollaries drawn between the theoretical framework and practical application of the technique. Details of the speckle pattern applied to the sample surface for displacement and strain calculation using DIC are presented. The details of the uniaxial compression of the samples and details regarding loading and image capture rates as well as the necessity for the use of the DIC technique are discussed. Finally, the procedure by which DIC is used to calculate the critical cracking load during the test is presented.

3.4.1 Non-Contact Strain Measurement Techniques

Non-contact strain measurement techniques have been widely used for aiding with the problem of measuring in-situ deformation of a material or structure where typical strain measurements techniques, such as strain gauges and linear variable differential transformers, cannot be used due to geometrical or other constraints. A number of different techniques have been utilized, such as Moire patterns [16], diffraction gratings [17], Fraunhofer diffraction [18], interferometric strain displacement gages [19], and digital image correlation [20-23]. A detailed overview of these different analytical techniques has been given by Dally [24] and Hild [25]. For this study DIC was chosen to measure both the uniaxial stress-strain response during the compression-delamination test as well as to generate in-plane strain maps to aid in the analysis method used for calculating the critical cracking load. The DIC technique is an appropriate choice for strain measurement due to

the following features it exhibits: (i) high spatial resolution capable of resolving local variations in strain across the sample surface, (ii) full-field displacement/strain measurement capabilities with the appropriate choices of imaging lens system and (iii) length-scale independence where relative pixel displacements are used to calculate strain.

3.4.1.1 Introduction to DIC Method

The DIC technique was first implemented at the University of South Carolina by Sutton [26, 27]. Advancements have been made in patterning procedures by Daly and colleagues that allows for extension of the DIC method to in-situ tests conducted in an SEM, which has allowed for displacement resolutions as low as 4 nm/pixel. [28]. Displacements are ultimately calculated through an affine transformation that compares relative pixel intensities from an image to an un-deformed reference image, typically taken at time $t = 0$. In the reference image a region of interest (ROI) is defined that specifies areas over which displacement calculations will be made. Each image captured during a test is then divided into a series of sub-images, over the ROI, that are of a predefined size and shape. The size of these sub-images remains the same throughout all of the images analyzed and the shape is typically taken as a square with *n* pixels on each edge. The distribution of the pixel intensities in each of the sub-images of the deformed images are matched to the un-deformed image in order to calculate pixel displacements for the sub-image. The result of this comparison is the mapping function χ, that maps pixel points from the reference image to the current image, which is shown schematically in Figure 3-22. The pixel coordinates used to construct the deformation mapping function are calculated from 2D cross correlation between the un-deformed and deformed sub-images. The 2D cross correlation procedure utilizes maximization of the 2D cross correlation coefficient, C_{ij}, through non-

linear optimization techniques, that calculates the relative goodness of fit of the matching of the sub-images. The correlation coefficient, defined in Equation 3-17,depends on both pixel displacements (u, v) and the pixel displacements gradients $\left(\frac{\partial u}{\partial x}, \frac{\partial u}{\partial y}, \frac{\partial v}{\partial x}, \frac{\partial v}{\partial y}\right)$.

Equation 3-17

$$C_{ij} = \frac{\sum_i \sum_j [\{F(x_i, y_i) - \bar{F}\} \times \{G(x_i^*, y_i^*) - \bar{G}\}]}{\sqrt{\left[\sum_i \sum_j \{F(x_i, y_i) - \bar{F}\}^2\right] \times \left[\sum_i \sum_j \{G(x_i^*, y_i^*) - \bar{G}\}^2\right]}}$$

In Equation 3-17, the pixel gray scale values for the un-deformed image, which can vary from either 0 to 1 or from 0 to 255 for 8-bit images, is represented in $F(x_i, y_i)$, where x_i and y_i are the pixel locations in the un-deformed image. Similarly, the portion $G(x_i^*, y_i^*)$ represents the gray scale values for the deformed image at pixel coordinates x_i^* and y_i^*. The values $\bar{F}$ and $\bar{G}$ are the mean values of the gray scale intensities of the matrices F and G. Through cross correlation between the sub-images in the un-deformed and deformed configurations using Equation 3-17, the deformation function χ relates the coordinates (x_i, y_i) and (x_i^*, y_i^*). For in-plane displacements only, Equation 3-17 can be approximated by a 2D affine transformation. An affine transformation is a transformation between affine spaces, which are essentially Euclidean spaces independent of a fixed coordinate system, that preserve points, straight lines and planes. What this means is that distances are measured relative to one another and not to a fixed origin and that only certain types of deformation can be allowed. Some examples of affine transformation are shown in Figure 3-23 and include translation, dilation, shear and rotation. All of these transformations satisfy the condition that parallel trace lines on each area will remain parallel to each other after transformation. Also shown in Figure 3-23 is an example of a transformation that is

not an affine transformation: a projection that does not preserve parallel lines. This condition would arise if the sample was rotated or sheared out of the imaging plane and would not provide accurate results through DIC. When the material deformation can be represented by pure in-plane affine transformations, the in-plane displacements can be approximated by the following 2D affine transformation:

Equation 3-18

$$x^* = (x + u\,) + \left(\frac{\partial u}{\partial x}\Delta x + \frac{\partial u}{\partial y}\Delta y\right)$$
$$y^* = (y + v\,) + \left(\frac{\partial v}{\partial x}\Delta x + \frac{\partial v}{\partial y}\Delta y\right)$$

For these relations, u and v represent rigid-body $x - y$ translations between the center of the sub-images and Δx and Δy are the distances to the center of the sub-image at any point (x, y) in the sub-image. When the correlation coefficient is maximized, as close to 1, a successfully match has been found that maps the deformation. This can be seen schematically in Figure 3-24, where the left reference image and the upper right deformed image represent a match in deformation mapping and the lower right deformed image represents a false match. By rastering over a search region, a map of the correlation coefficient can be produced as seen in Figure 3-25, which shows the variation of the 2D cross correlation coefficient over a 5 by 5 pixel search region. The point at which the correlation coefficient is maximal corresponds to the point at which perfectly maps the deformation between the un-deformed and deformed images. It is readily seen that not only from Figure 3-24, but from the underlying mathematical foundations of the Digital Image Correlation technique that adequate contrast across the image is required in order to effectively map displacements. Image contrast that corresponds to a random gray scale

intensity distribution in the different sub-images helps to increase the chance that a successful match can be made. It is therefore necessary to create a random speckle-pattern on the imaging surface of the sample in order to track in-plane displacements and ultimately calculate in-plane strains. The software packages used to calculate uniaxial strain in the substrate a custom in-house MATLAB code written by previous members of the Hemker group [29] and to calculate the in-plane shear maps a MATLAB code developed at Georgia Tech called Ncorr was used [30].

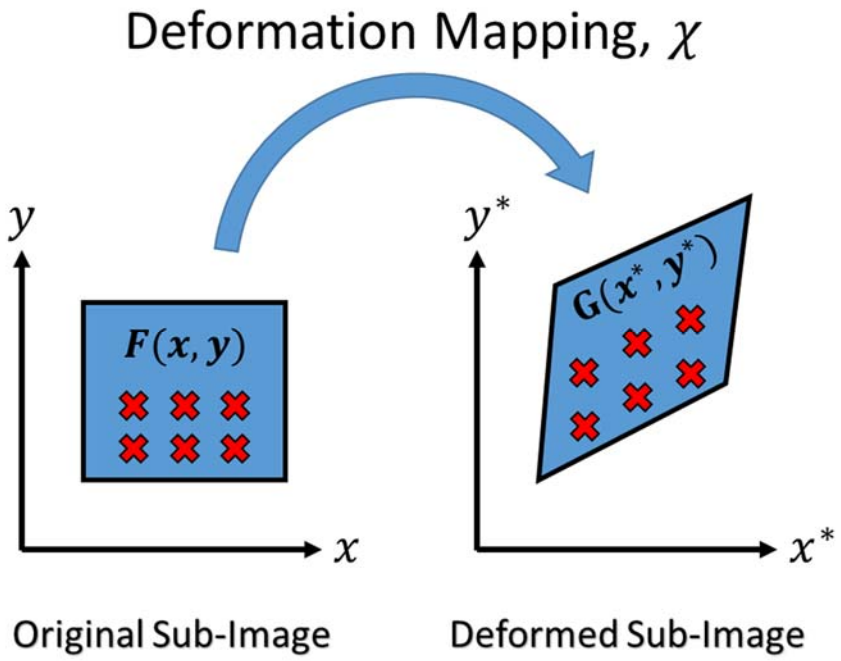

Figure 3-22: Schematic of deformation mapping calculated by digital image correlation.

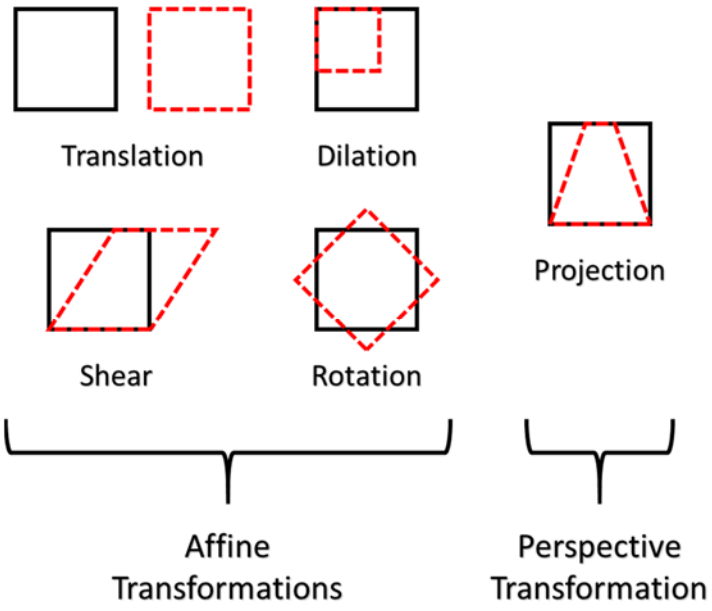

Figure 3-23: Examples of possible affine transformations and a perspective transformation.

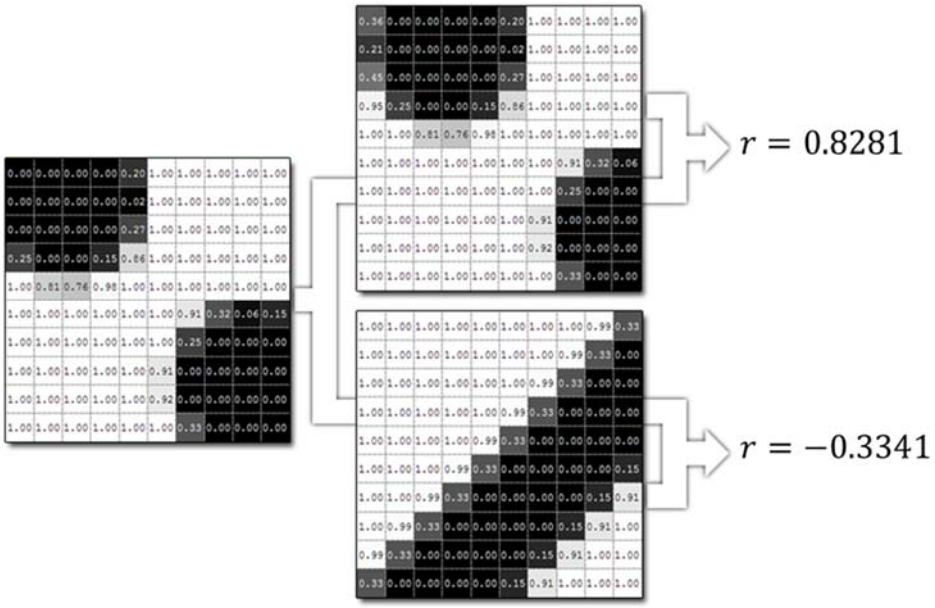

Figure 3-24: Example of 2D cross correlation coefficient for actual and false sub-image matching (taken from [30]).

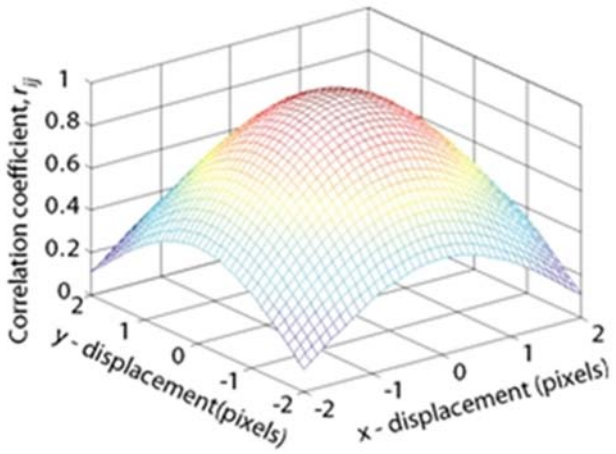

Figure 3-25: Example output of 2D cross correlation coefficient over a 5 by 5 pixel search region (taken from [30])

3.4.2 Speckle Pattern Application for DIC Tracking

In order to calculate in-plane displacement and strain, a randomly applied speckle pattern needs to be applied to the surface of the sample. Prior to testing, the sample surface was cleaned using isopropyl alcohol and a thin and even layer of matte black spray paint was applied directly to the face of the sample as shown in part (a) of Figure 3-26. Once the surface had completely dried, matte white spray paint was applied in 4-6 bursts that last between ½ to 1 second. The nozzle of the spray paint is directed roughly 30° upwards from the surface of the sample as shown in part (b) of Figure 3-26. By pointing the direction of flow above the sample the perfectly atomized spray will be directed over and away from the sample, that would otherwise coat the surface pure white, and the larger particle trajectories will intersect with the sample surface. A sample that has had a random speckle pattern applied in this manner can be seen in part (c) of Figure 3-26.

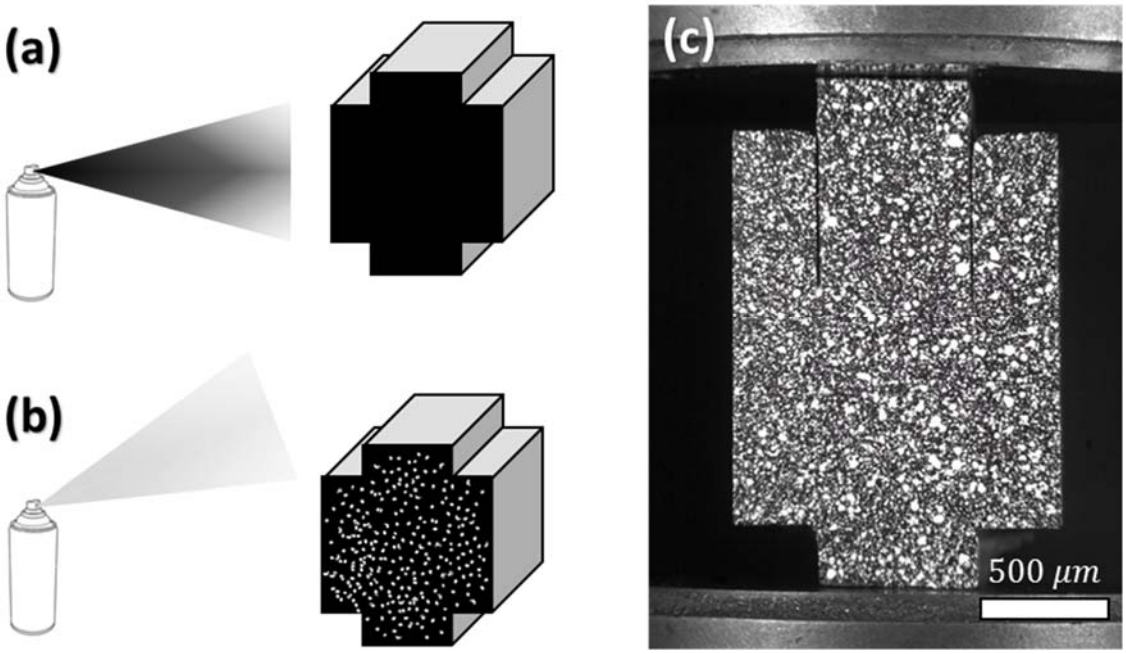

Figure 3-26: (a) Schematic of Compression Edge-Delamination Sample during black spray paint application, (b) during white speckle application and (c) speckle patterned sample in compression setup during testing

3.4.2.1 Uniaxial compression of CED Samples

Once prepared samples had the speckle pattern applied and had ample time for the paint to dry, around 1 day, they were loaded into a MTS servo-hydraulic machine. Additional information regarding the MTS machine setup, control software and machine calibration can be viewed in APPENDIX A: MTS Servo-Hydraulic System Overview. Samples were compressed under displacement control with an applied displacement rate of $\dot{\delta} = 0.006\ mm/s$ which corresponds to a macroscopically applied quasi-static strain rate of $\dot{\varepsilon} = 3 \times 10^{-5}\ \frac{1}{s}$. The sampling rate for both the 100 kN load cell and the Linear Variable Displacement Transducer (LVDT) on the machine is 1kHz, which means every load value is recorded corresponding to an incremental macroscopically applied strain of $0.03\ \mu$-strain. The results of a representative CED test are shown in Figure 3-27. The images shown in the figure represent (a) the beginning of the test, (b) the point at which the first

visual signs of cracking occur and (c) the end of the test where both of the interfaces have fully delaminated. The point at which visual cracking occured corresponded to a stress value of 508 MPa and occurred before the substrate deformed plastically and is contained within the linear portion of the stress-strain curve. The significance of this is that it means that a critical cracking stress cannot be determined by observing the behavior of the stress-strain curve as is done in the 4-Point Bend test. The reason that there is no observed change in the loading curve upon delamination is best described by calculating the equivalent stiffness of the sample as the crack propagates through the sample, which is shown in Figure 3-28. It is readily apparent that even for sudden and complete delamination, the total change in stiffness will be at most a change of 35%. For incremental crack growth, which is desired, the change in compliance of the sample will be difficult to detect simply though analysis of the stress-strain curve. It is therefore necessary to use another method to calculate the critical crack initiation and propagation stress. To accomplish this task, DIC was used to observe crack initiation and propagation with in-plane shear maps.

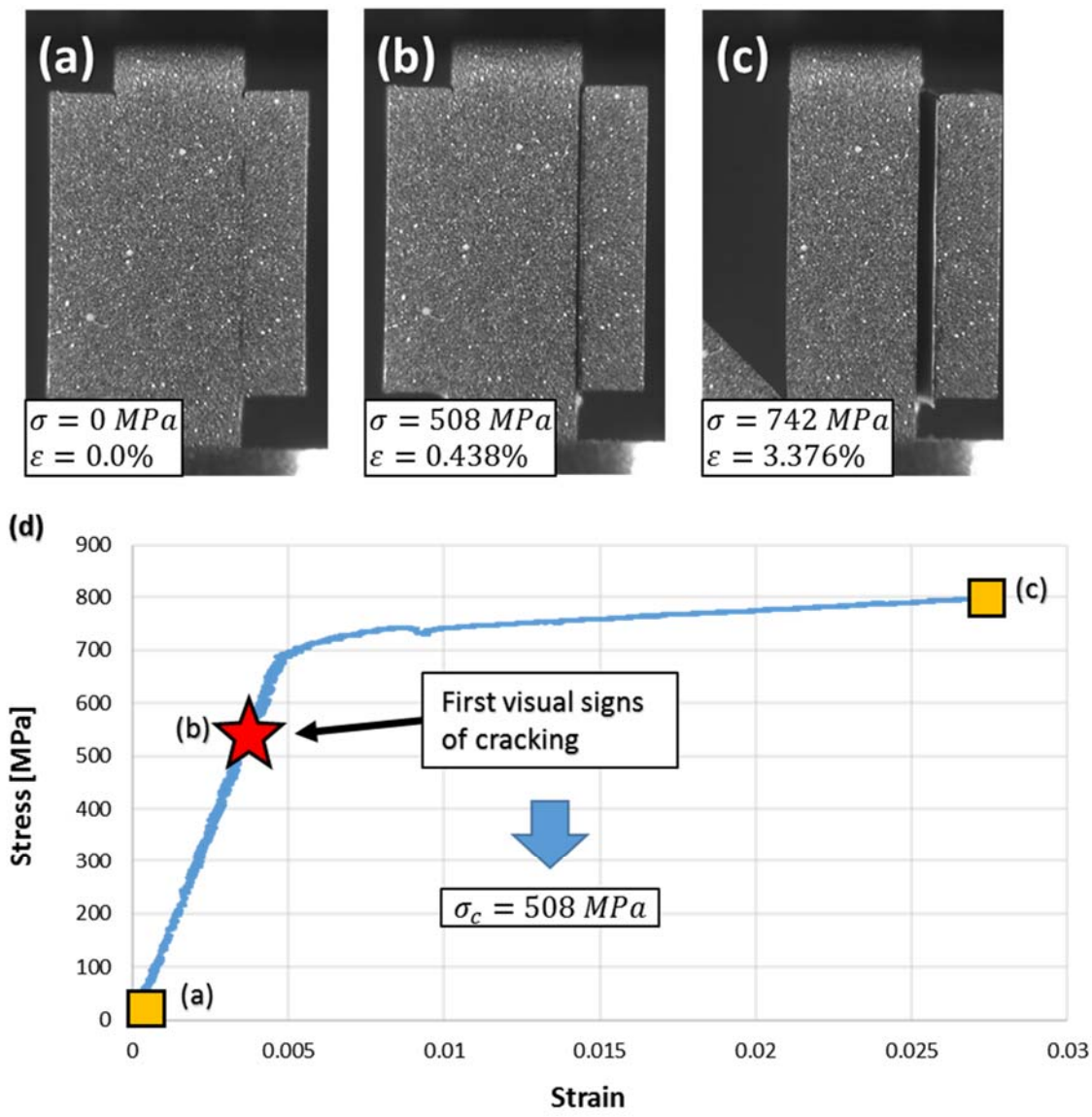

Figure 3-27: Representative stress/strain curve for CED test (d) with images at (a) beginning of test, (b) point at which visual signs of cracking occurs and (c) end of test where both interfaces have fully delaminated

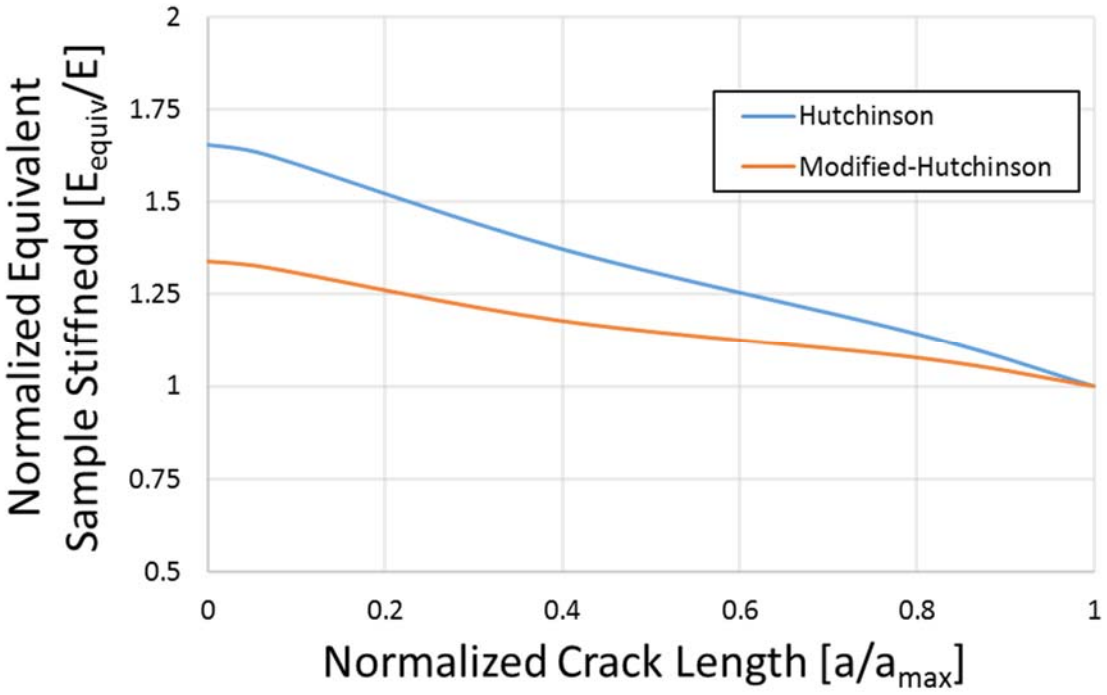

Figure 3-28: Plot of normalized equivalent sample stiffness vs. normalized crack length for both the Hutchinson and Modified-Hutchinson Compression Edge-Delamination samples

3.4.2.2 Method for Calculating Critical Cracking Load

As the image capture rate corresponds to 1 image captured every second, the maximum amount of strain variation from image-to-image is $\varepsilon = 3 \times 10^{-5}$. After the test was conducted, the images were processed though the in-house MATLAB code [29] to calculate the uniaxial stress-strain curve shown in the lower portion of Figure 3-29. The MATLAB program Ncorr [30] was then used to generate in-plane shear maps for the ≈500-2,000 images captured during the test. The generated in-plane shear maps were analyzed visually to see where and when strain localization occurred. Selected in-plane shear maps can be seen in the upper portion of Figure 3-29. Image (a) is the point right before crack initiation, image (b) is the critical stress at which crack propagation begins and image (c) is the point right after crack propagation begins. Using this method of observing changes

in strain localization, the critical applied stress for crack initiation can be used to calculate the interfacial toughness using the FE model that will be outlined in Section 5.3.

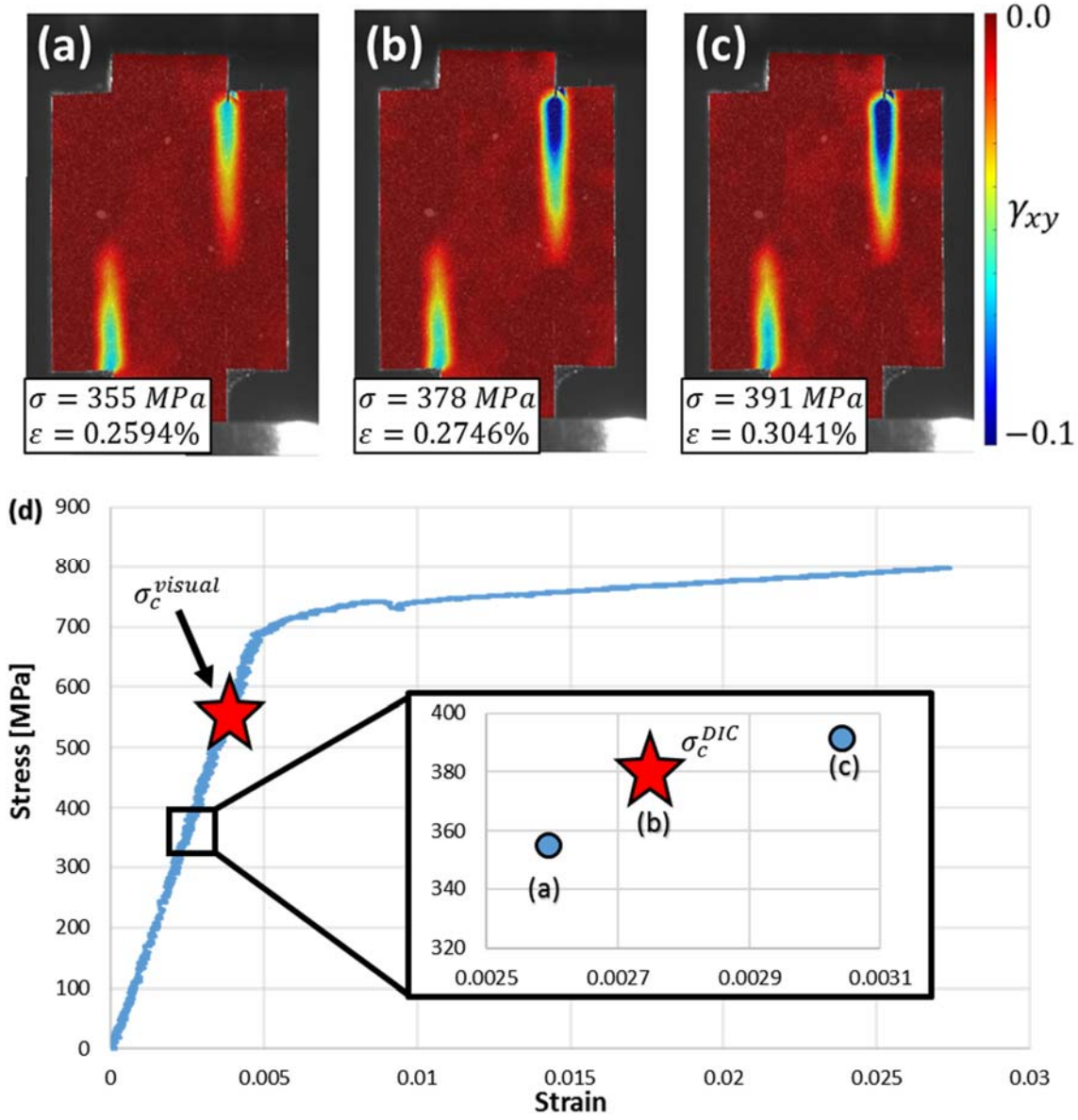

Figure 3-29: Uniaxial applied stress vs. strain curve (d) with accompanying in-plane shear maps for (a) right before crack initiation, (b) critical load point right as crack propagation begins and (c) point right after crack propagation occurs. Also shown is the stress at which visual cracking was observed and is approximately 125 MPa higher than calculated through DIC analysis.

3.5 References for Chapter 3

1. Hutchinson, R.G. and J.W. Hutchinson, *Lifetime Assessment for Thermal Barrier Coatings: Tests for Measuring Mixed Mode Delamination Toughness.* Journal of the American Ceramic Society, 2011. **94**: p. s85-s95.
2. Rice, J.R., *A Path Independent Integral and the Approximate Analysis of Strain Concentration by Notches and Cracks.* Journal of Applied Mechanics, 1968. **35**(2): p. 379-386.
3. Institute, N.D., *High-temperature high-strength nickel base alloys*. 1995.
4. Vasinonta, A. and J.L. Beuth, *Measurement of interfacial toughness in thermal barrier coating systems by indentation.* Engineering Fracture Mechanics, 2001. **68**(7): p. 843-860.
5. Guo, S.Q., et al., *Measurement of interfacial shear mechanical properties in thermal barrier coating systems by a barb pullout method.* Scripta Materialia, 2005. **53**(9): p. 1043-1048.
6. Tanaka, M., et al., *Delamination toughness of electron beam physical vapor deposition (EB-PVD) Y2O3–ZrO2 thermal barrier coatings by the pushout method: Effect of thermal cycling temperature.* Journal of Materials Research, 2008. **23**(09): p. 2382-2392.
7. Eberl, C., et al., *In Situ Measurement of the Toughness of the Interface Between a Thermal Barrier Coating and a Ni Alloy.* Journal of the American Ceramic Society, 2011. **94**: p. s120-s127.
8. Théry, P.-Y., et al., *Spallation of two thermal barrier coating systems: experimental study of adhesion and energetic approach to lifetime during cyclic oxidation.* Journal of Materials Science, 2008. **44**(7): p. 1726-1733.
9. Hutchinson, J.W., M.Y. He, and A.G. Evans, *The influence of imperfections on the nucleation and propagation of buckling driven delaminations.* Journal of the Mechanics and Physics of Solids, 2000. **48**(4): p. 709-734.
10. Kikuchi, T., *Single crystal orientation measurement by x-ray methods.* The Rigaku Journal, 1990. **7**(1): p. 27-35.
11. Technologies, A.V., *EB-PVD Coating Machine*, Bild_EBPVD.jpg, Editor. 2010.
12. Technologies, A.V., *EB-PVD Chamber*, chamber_ebpvd.jpg, Editor. 2010.
13. Arun Prabu, M.B.R., S.; Kuppuraj, M.; Mahendran, S.; , *EB-PVD Coating Chamber Schematic*, 4.jpg, Editor. 2011.
14. Thery, P.Y.P., M.; Dupeux, M.; Braccini, M., *Adhesion energy of a YPSZ EB-PVD layer in two thermal barrier coating systems.* Surface & Coating Technology, 2007. **202**: p. 648-652.
15. Materials, H.A. *Araldite 2011 Technical Data Sheet*. 2007.
16. Post, D., *Moiré interferometry with white light.* Applied Optics, 1979. **18**(24): p. 4163-4167.

17. Ruud, J.A., et al., *A new method for tensile testing of thin films.* Journal of Materials Research, 1993. **8**(01): p. 112-117.

18. Baily, E.D. and P. York, *An apparatus for the study of strain recovery in compacts.* Journal of Materials Science. **11**(8): p. 1470-1474.

19. Sharpe Jr., W.N., *An interferometric strain-displacement measurement system*. 1989, NASA Langley Research Center: Hampton, VA. p. 67.

20. Helm, J.D., S.R. McNeill, and M.A. Sutton, *Improved three-dimensional image correlation for surface displacement measurement.* Optical Engineering, 1996. **35**(7): p. 1911-1920.

21. Scrivens, W.A., et al., *Development of Patterns for Digital Image Correlation Measurements at Reduced Length Scales.* Experimental Mechanics, 2006. **47**(1): p. 63-77.

22. Tao, G. and Z. Xia, *A non-contact real-time strain measurement and control system for multiaxial cyclic/fatigue tests of polymer materials by digital image correlation method.* Polymer Testing, 2005. **24**(7): p. 844-855.

23. Sharpe, W.N., et al., *Strain Measurements of Silicon Dioxide Microspecimens by Digital Imaging Processing.* Experimental Mechanics, 2007. **47**(5): p. 649-658.

24. Dally, J.W.R., W.F., *Experimental Stress Analysis*. 4th Edition ed. 2005: College House Enterprises.

25. Hild, F. and S. Roux, *Digital Image Correlation: from Displacement Measurement to Identification of Elastic Properties – a Review.* Strain, 2006. **42**(2): p. 69-80.

26. Chu, T.C., W.F. Ranson, and M.A. Sutton, *Applications of digital-image-correlation techniques to experimental mechanics.* Experimental Mechanics. **25**(3): p. 232-244.

27. Bruck, H.A., et al., *Digital image correlation using Newton-Raphson method of partial differential correction.* Experimental Mechanics. **29**(3): p. 261-267.

28. Kammers, A.D. and S. Daly, *Self-Assembled Nanoparticle Surface Patterning for Improved Digital Image Correlation in a Scanning Electron Microscope.* Experimental Mechanics, 2013. **53**(8): p. 1333-1341.

29. Eberl, C.T., R.; Gionalo, D.S.; Sharpe Jr.; W.N.; Hemker, K.J. 2010 [cited 2016; Available from: http://www.mathworks.com/matlabcentral/fileexchange/12413-digital-image-correlation-and-tracking.

30. Blaber, J.A., Antonia. *Ncorr v1.2*. 2016 [cited 2016; Available from: http://www.ncorr.com/.

CHAPTER 4: THE MODIFIED 4-POINT BEND TEST

This chapter introduces the underlying mechanics of the test method including two different analytical methods for calculating the strain energy release rate associated with fracture; a simplified model assuming an isotropic material system and a more detailed model that explicitly accounts for each material layer. Considerations taken during the design and optimization of the geometry of the sample are explained as well as the final sample geometry that was chosen is used throughout the rest of this work. The sample preparation procedure is presented, which extends from orientation of the as-received single crystal superalloy to pre-crack initiation in the prepared samples right before testing. The chapter concludes with the description of the test analysis procedure and subsequent calculation of the critical plateau cracking loads.

4.1 Mechanics of the Modified 4-Point Bend Test Method

The 4-point bend method has been used in many studies to assess the strength of materials, for flexural bending, and to measure the adhesion of coatings on substrates [1-6]. Well-defined solutions for both the phase angle of fracture and the strain energy release rate for interfacial delamination have been derived by Hutchinson and Suo [7]. A modification was made to the traditional 4-point bend test by Charalambides et al. where a stiffener is attached to the coating to increase the strain energy used to drive delamination cracks [8]. A schematic of both the (a) 4-point bend and (b) modified 4-point bend test sample geometries is shown in Figure 4-1. The modified geometry allows for substantially more strain energy and is especially important when the coating is very thin or compliant.

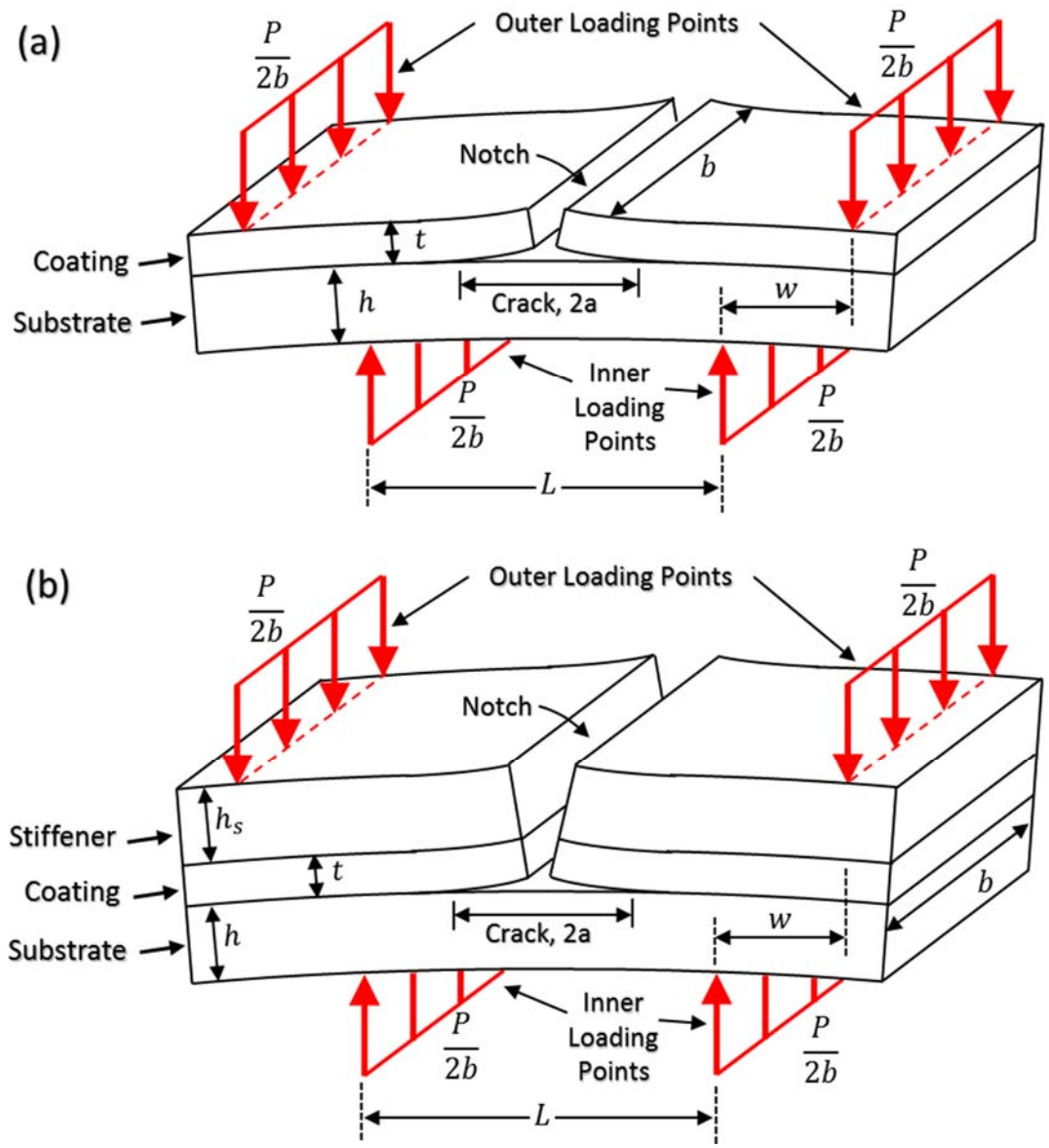

Figure 4-1: Schematic representations of both the (a) 4-point bend specimen with substrate and coating layers and (b) modified 4-point bend specimen with substrate, coating and stiffener layers

By increasing the amount of strain energy, the sample can be subjected to a smaller load to cause delamination and yielding in the underlying metallic layers can be avoided, which greatly simplifies the experimental analysis. For this test the phase angle was determined to be $\phi = 40.9°$ [8] and the critical strain energy release rate associated with delamination is:

Equation 4-1

$$G_c = \frac{7}{16}\frac{M^2}{B_{simplified}}$$

In Equation 4-1 M is the applied moment to the beam and $B_{simplified}$ is a simplified representation of the bending modulus of the beam that assumed the beam is composed of the substrate material. The applied moment is further expressed as:

Equation 4-2

$$M = P_c w$$

where P_c is the critical plateau cracking load and w is the distance between the inner and outer loading pins. The bending modulus can also be further expressed as:

Equation 4-3

$$B_{simplified} = \frac{1}{12}\bar{E}_{Sub} b h_{avg}^3$$

where $\bar{E}_{sub}$ is the plane strain or plane stress modulus, b is the width of the beam and h_{avg} is defined as $h_{avg} = \frac{1}{2}(h + t + h_s)$, where h, t and h_s are the heights of the substrate, coating and stiffener respectively. This definition provides the most accurate results when $h_s = h$ and $t \ll h$. By combining Equation 4-2 and Equation 4-3 into Equation 4-1 the following relation is obtained:

Equation 4-4:

$$G_{c,simplified} = \frac{21}{4}\frac{P_c^2}{\bar{E}_{Sub} b h_{avg}^3}$$

A more detailed analytical solution can also be derived by using Euler-Bernoulli beam theory to find the difference in the total elastic strain energy before and after incremental crack growth [8]. So far the stiffener has been considered to be perfectly bonded to the

substrate, but it is really bonded to the coating using a thin layer of epoxy. For the definitions of terms presented in this study, the strain energy release rate during delamination is:

Equation 4-5

$$G_{C,full} = \frac{8\bar{E}_{sub}b^2}{w^2}\left(\frac{1}{I_{Sub+BC+TGO}} - \frac{1}{I_{comp}}\right)P_C^2$$

In Equation 4-5 $I_{Sub+BC+TGO}$ is the composite bending moment of inertia of the substrate, bond coat and TGO ($I_{Sub+BC+TGO} = I_{Sub} + I_{BC} + I_{TGO}$) and I_{comp} is the composite bending modulus of all the layers $\left(I_{comp} = I_{Sub} + I_{BC} + I_{TGO} + I_{TC} + I_{Epoxy} + I_{Stiff}\right)$. The bending moduli of each layer is calculated using the parallel axis theorem and using the transformed area method, which results in:

Equation 4-6

$$I_{Sub} = \frac{1}{12}h_{sub}^3 + h_{sub}\left(\bar{y} - \frac{h_{Sub}}{2}\right)^2$$

Equation 4-7

$$I_{BC} = \frac{1}{12}\eta_{BC}h_{BC}^3 + \eta_2 h_{BC}\left(\bar{y} - h_{Sub} - \frac{h_{BC}}{2}\right)^2$$

Equation 4-8

$$I_{TC} = \frac{1}{12}\eta_{TC}h_{TC}^3 + \eta_3 h_{TC}\left(\bar{y} - h_{Sub} - h_{BC} - \frac{h_{TC}}{2}\right)^2$$

Equation 4-9

$$I_{Epoxy} = \frac{1}{12}\eta_{Epoxy}h_{Epoxy}^3 + \eta_4 h_{Epoxy}\left(\bar{y} - h_{Sub} - h_{BC} - h_{TC} - \frac{h_{Epoxy}}{2}\right)^2$$

Equation 4-10

$$I_{Stiff} = \frac{1}{12} h_{Stiff}^3 + h_{Stiff} \left(\bar{y} - h_{Sub} - h_{BC} - h_{TC} - h_{Epoxy} - \frac{h_{Stiff}}{2} \right)^2$$

In Equation 4-6 through Equation 4-10, h_{sub}, h_{BC}, h_{TGO}, h_{TC}, h_{Epoxy} and h_{Stiff} are the thicknesses of the substrate, bond coat, TGO, top coat, epoxy and stiffener layers respectively. In addition, $\bar{y}$ is the neutral axis position and the transformed area ratios η_i are defined as:

Equation 4-11

$$\bar{y} = \frac{\sum \eta_i h_i y_i}{\sum \eta_i h_i}$$

Equation 4-12

$$\bar{y} = \frac{h_{Sub}\bar{y}_{Sub} + \eta_{BC} h_{BC}\bar{y}_{BC} + \eta_{TGO} h_{TGO}\bar{y}_{TGO} + \eta_{TC} h_{TC}\bar{y}_{TC} + \eta_{Epoxy} h_{Epoxy}\bar{y}_{Epoxy} + h_{Stiff}\bar{y}_{Stiff}}{h_{Sub} + \eta_{BC} h_{BC} + \eta_{TGO} h_{TGO} + \eta_{TC} h_{TC} + \eta_{Epoxy} h_{Epoxy} + h_{Stiff}}$$

Equation 4-13

$$\eta_{BC} = \frac{E_{BC}}{E_{Sub}}$$

Equation 4-14

$$\eta_{TGO} = \frac{E_{TGO}}{E_{Sub}}$$

Equation 4-15

$$\eta_{TC} = \frac{E_{TC}}{E_{Sub}}$$

Equation 4-16

$$\eta_{Epoxy} = \frac{E_{Epoxy}}{E_{Sub}}$$

In Equation 4-12 the neutral axis positions for each layer are defined as:

Equation 4-17

$$\bar{y}_{Sub} = \frac{h_{Sub}}{2}$$

Equation 4-18

$$\bar{y}_{BC} = h_{Sub} + \frac{h_{BC}}{2}$$

Equation 4-19

$$\bar{y}_{TGO} = h_{Sub} + h_{BC} + \frac{h_{TGO}}{2}$$

Equation 4-20

$$\bar{y}_{TC} = h_{Sub} + h_{BC} + h_{TGO} + \frac{h_{TC}}{2}$$

Equation 4-21

$$\bar{y}_{Epoxy} = h_{Sub} + h_{BC} + h_{TGO} + h_{TC} + \frac{h_{Epoxy}}{2}$$

Equation 4-22

$$\bar{y}_{Stiff} = h_{Sub} + h_{BC} + h_{TGO} + h_{TC} + h_{Epoxy} + \frac{h_{Stiff}}{2}$$

By combining Equation 4-17 though Equation 4-22 into Equation 4-12 an explicit equation for the position of the neutral axis can be determined:

Equation 4-23

$$\bar{y} = \frac{\left\{\begin{array}{c} h_{Sub}^2 + 2\eta_{BC}h_{BC}h_{Sub} + \eta_{BC}h_{BC}^2 + 2\eta_{TGO}h_{TGO}h_{Sub} + 2\eta_{TGO}h_{TGO}h_{BC} + \\ \eta_{TGO}h_{TGO}^2 + 2\eta_{TC}h_{TC}h_{Sub} + 2\eta_{TC}h_{TC}h_{BC} + 2\eta_{TC}h_{TC}h_{TGO} + \eta_{TC}h_{TC}^2 + \\ \eta_{Epoxy}h_{Epoxy}h_{Sub} + 2\eta_{Epoxy}h_{Epoxy}h_{BC} + 2\eta_{Epoxy}h_{Epoxy}h_{TGO} + \\ 2\eta_{Epoxy}h_{Epoxy}h_{TC} + \eta_{Epoxy}h_{Epoxy}^2 + 2h_{Stiff}h_{Sub} + 2h_{Stiff}h_{BC} + \\ 2h_{Stiff}h_{TGO} + 2h_{Stiff}h_{TC} + 2h_{Stiff}h_{Epoxy} + h_{Stiff}^2 \end{array}\right\}}{2\left(h_{Sub} + \eta_{BC}h_{BC} + \eta_{TGO}h_{TGO} + \eta_{TC}h_{TC} + \eta_{Epoxy}h_{Epoxy} + h_{Stiff}\right)}$$

This formalization of the strain energy release rate can be used to calculate the substrate and stiffener thicknesses such that the neutral axis will lie as close to the TGO/top coat

interface as possible. As the level of tensile and compressive stress will increase linearly as the position moves away from the interface, to ensure that the top coat is under least amount of tensile stress the neutral axis must be designed to lie as close to the bond coat/TGO/top coat interfaces as possible. If the neutral axis lies within the TGO, it will ensure that the top coat, epoxy and stiffener will be in tension and substrate and bond coat will be in compression. This is an important design factor of the bending specimen because excessive tension in the top coat layer can lead to inter-columnar cracking of the top coat which would decrease the total amount of strain energy. This energy lost due to cracking of the top coat would be extremely difficult to quantify in-situ and would need to be quantified to get an accurate measure of the interfacial toughness. It is also important to limit the amount of tensile loading that occurs at the delamination interface as that could lead to a change in the mode-mix and in the delamination behavior.

4.2 Sample Design Considerations

In order to ensure that the neutral axis lies on the TGO/top coat interface, the equations defined in the previous section were discretized into a MATLAB script. In addition, it was important for the majority of the strain energy release during delamination to come directly from the stiffener as it would ensure a more accurate calculation of the strain energy release rate from the analytical equations. For the TBC material system large residual stresses can develop in the TGO and top coat and are difficult to measure. It has been shown that only a small fraction of the total residual stress in a coating is used to drive crack propagation if the coating is very thin and/or compliant as compared to the stiffener [9]. In order for the effect of residual stress in a coating on the interfacial toughness to be minimized, it is therefore desirable to make the stiffener of sufficient thickness as to mitigate the effects. It

is also important to minimize the effect of residual stress as the measurement of this property is not trivial and is well beyond the scope of this study. Figure 4-2 shows a plot from Hutchinson [9] that shows how the fraction of top coat strain energy (from residual stress) that is released during delamination as a function of the stiffener to coating thickness $(h_s + t)/t$. This figure follows the geometry shown in Figure 4-1 (b).

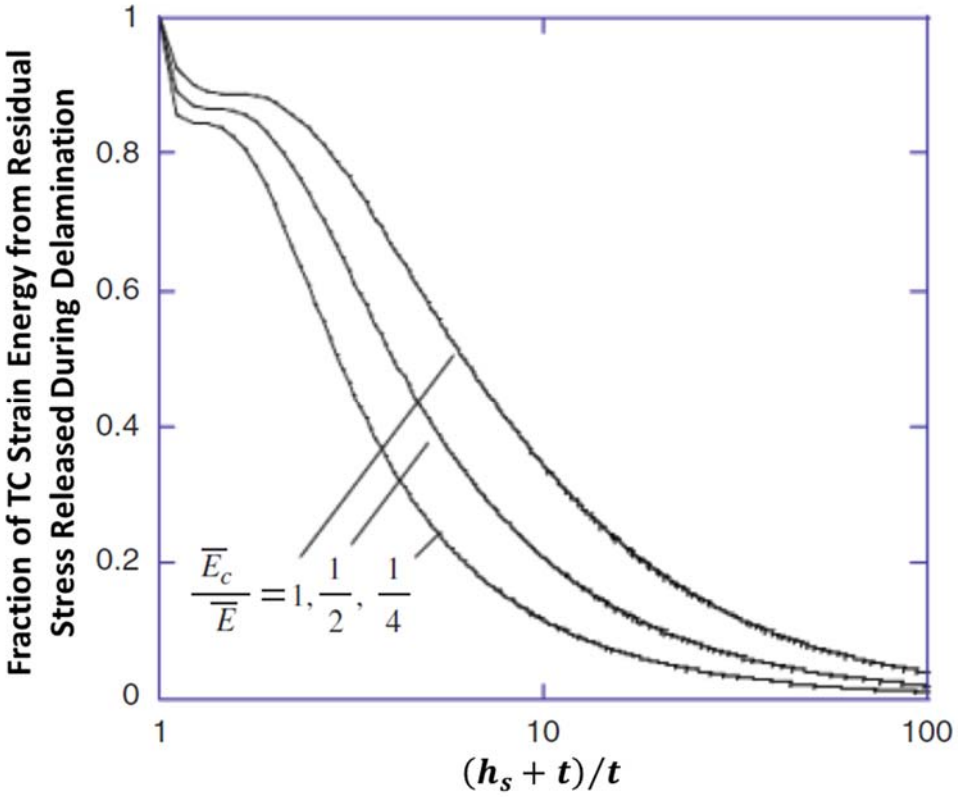

Figure 4-2: "The fraction of elastic energy stored in the top coat that is released to delaminate a coating+stiffener bilayer from the substrate. The stress in the coating before delamination is assumed to be uniform." (Taken from Hutchison [9])

In this plot $\bar{E}_c$ is the top coat modulus, $\bar{E}$ is the substrate/stiffener modulus, h_s is the stiffener thickness and t is the top coat thickness. In the limit of the top coat being much thicker than the stiffener all of the energy from residual stress in the coating is released during crack growth as the stiffener cannot constrain the top coats movement. As the top coat become thinner relative to the stiffener, the amount of residual stress released during

crack growth diminishes because the stiffener constrains the delaminated top coat. To interpret this figure the ratio of the coating modulus to the substrate and stiffener modulus is necessary. The substrate/stiffener in this study were both René N5 with elastic modulus $\bar{E} = 128\ GPa$ [10] and the coating is EB-PVD 7%YSZ with elastic modulus $\bar{E}_c = 50\ GPa$ [11]. This figure was digitized in MATLAB and then a curve corresponding to $\bar{E}_c/\bar{E} = 50\ GPa/128\ GPa = 0.39$ was interpolated from the digitized curves. A curve fit was then conducted to implement the curve into the calculation function using the MATLAB *cftool* functions. The resulting curve fit is:

Equation 4-24

$$\%\ SE_{released} = 1.586\left(\frac{h_s + t}{t}\right)^{-1.116}$$

This equation and the equation for the neutral axis were implemented into a MATLAB script called *Geometry_Calculation.m* which is attached in APPENDIX C: 4-Point Bend Neutral Axis MATLAB File. The program flow first starts with a specification for the desired percentage of the total energy release that comes from the top coat. This is then used to calculate the stiffener thickness. Since bond coat, TGO, top coat and epoxy properties and thicknesses are known, the substrate thickness is then calculated using the derived neutral axis equation.

To calculate a first estimate for the stiffener dimensions an initial value of 10% energy release from the coating is prescribed. The thickness of the top coat was measured using an optical microscope to be $t = 150\ \mu m$. This results in a substrate thickness of $h_{Sub} = 2.73\ mm$ and a stiffener thickness of $h_{Stiff} = 2.59\ mm$. Due to materials available with

industrial partners the available substrate thickness was ultimately limited to a maximum thickness of $h_{sub,max} = 1.5\,mm$ and 1-inch and 4-inch width and length values respectively. Subsequent polishing on the non-coated side was conducted to using SiC polishing paper down to 1200 (P-4000) grit with subsequent polishing with a colloidal alumina suspension with $0.05\,\mu m$ diameter particles. The substrate thickness of each sample was measured using an optical microscope with the average being $h_{Sub} = 1.397\,mm$. To keep the neutral axis as close to the interface, the substrate thickness results in a desired stiffener thickness of $h_{Stiff} = 1.267\,mm$. This value of the stiffener thickness results in 19% of the residual stress (and subsequent strain energy) in the top coat being released from the coating during delamination. This increased amount of energy due to residual stress released from the coating during delamination will have some effect on the interfacial toughness calculated using the analytical equations, but cannot be quantified unless the magnitude of the residual stress in the top coat is known.

The final geometric parameter to be determined is the sample was width, which is limited by the load capacity of the testing system. A plot of the strain energy release rate versus the width *b* was calculated using the full analytical equation (Equation 4-5) and is shown in Figure 4-3. It should be noted that this figure calculates the dependence of the strain energy release rate versus the width parameter *b* at a fixed load of 500 lb, the maximum load the load cell can sustain. The reason the strain energy release rate decreases as the sample thickness increases is because a wider sample will require more force to drive delamination. With a limit placed on the load, the strain energy release rate shown is the maximum possible strain energy release rate that can be obtained for the sample geometry under the 500lb maximum load constraint. Typically, a wider sample is desired as it is

easier to handle when the width is larger than the total thickness. To accomplish this would result in a small ($> 100\ J/m^2$) available strain energy release rate. By comparison, a 1 mm width would result in a maximum possible strain energy release rate of $325\ J/m^2$. To achieve a balance between a large strain energy release rate and as wide a sample as possible, the width was chosen to be 1 mm. The resultant sample geometry is shown in Figure 4-4.

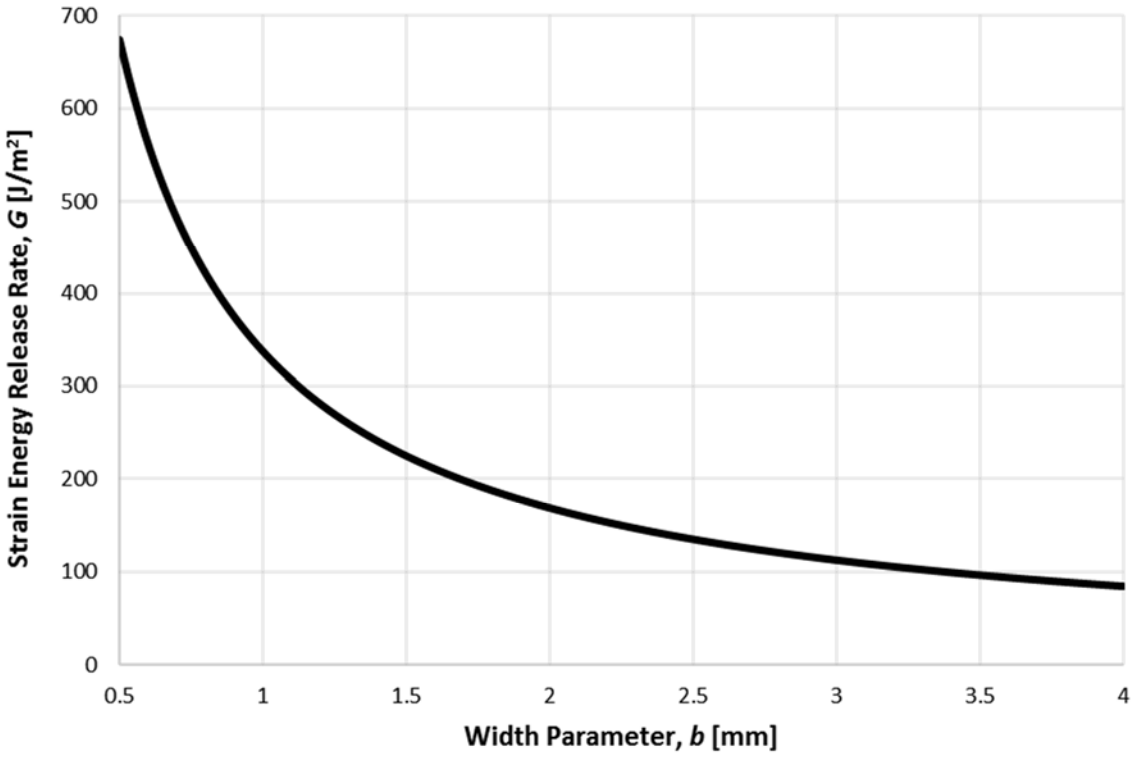

Figure 4-3: Variation of strain energy release rate with width parameter for chosen substrate and stiffener thicknesses at a fixed applied load of 500 lb

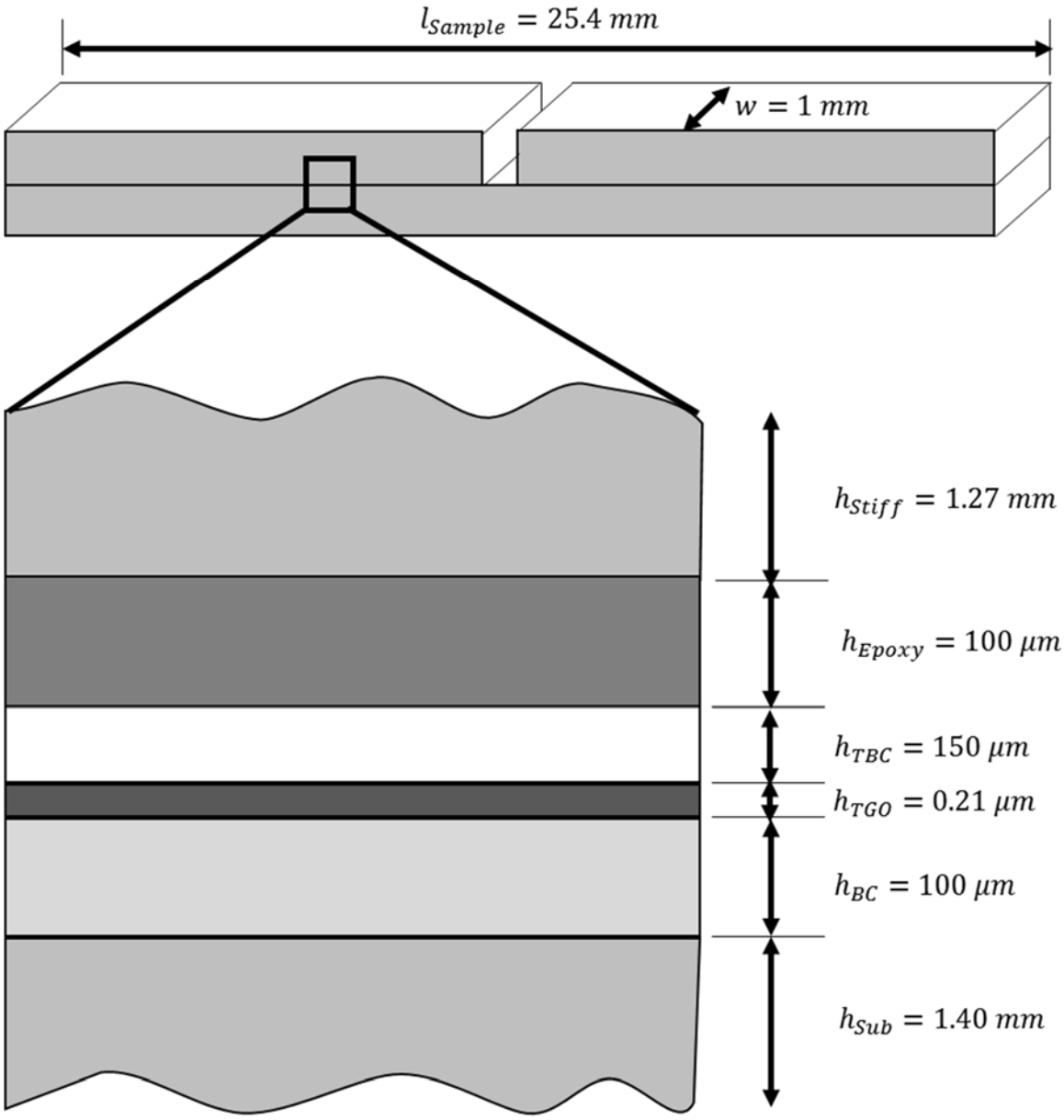

Figure 4-4: Sample geometry for 4-Point Bend specimen

4.3 Sample Production

A total of eight sheets of René N5 (4 inches by 1 inch by 1.5 mm thick) were cut by GE from a [100] oriented crystal using wire EDM. Four of these sheets were then bond coated and had the same 7% YSZ top coat layer applied as the CED samples using the same

EBPVD production procedure as in-service engine hardware undergoes. The other four sheets were used as stiffener plates.

4.3.1 Stiffener Application

The sheets were cleaned by immersion in an ultrasonic isopropyl alcohol twice and a subsequent ultrasonic bath in deionized pure water. The samples were then allowed to dry for 48 hours in a desiccating vacuum chamber. Following this period, the stiffener plates were applied to the top coat surface using the same Araldite 2011 epoxy that was used for the CED samples. To apply the epoxy a thin layer is first applied to the stiffener. A large glass slide is then put in contact with the epoxy and the slide is pulled perpendicular to the normal of the stiffener. This smearing process produces a thin and even epoxy layer on the stiffener. The stiffener with epoxy is then placed on the top coat and a 1 lb weight is placed on top of the stiffener to provide an even weight distribution that further promotes an even epoxy thickness. Care was taken to ensure the epoxy layer was around $100\ \mu m$ this as the manufactures' specifications indicate this provide the strongest shear strength for the bond [12]. It should be noted that this same epoxy has been used in previous studies on TBC delamination toughness under 4-point bend conditions [13, 14]. After the stiffener plates are applied the samples were cured for 24 hours at room temperature in a pressure chamber at 60 psi.

4.3.2 Sectioning of the Beams

The finished sheets were secured in an Allied High Tech Products Inc. TechCut 5 high speed saw and a 5-inch diameter rubber bonded SiC cutoff wheel was used to cut 1.1 mm wide beams. These beams were then polished with SiC polishing paper down to 1200 (P-4000) grit with subsequent polishing with a colloidal alumina suspension with $0.05\ \mu m$

diameter particles. This polishing reduced surface roughness and reduced the width of the beams to their prescribed 1 mm width.

4.3.3 Cutting Vertical Starter Notches

After the samples were sectioned and polished to their proper widths a vertical notch was then cut into each sample. The vertical notch was cut through the stiffener, the epoxy and down into the top coat layer using a Well Precision diamond wire saw. The notch allows for symmetrical interface cracks to form, which is a necessity of the 4-point bend test.

4.3.4 Pre-crack Creation Through Acid Etching

The initiation of a pre-crack with acid etching was conducted in a similar manner to that used for the CED samples. A difficulty arose in that the CED samples could have one end completely submerged in the acid solution during etching. With the 4-Point bend specimen it is necessary to have only the center of the sample (the area right around the central notch) to be etched by acid. In order to accomplish this a novel method for applying the acid etch solution was devised. The sample is suspended over an acid resistant plastic sheet and small drops of acid are applied using a dropper to the notch cut out using the diamond saw. This technique can be seen schematically in Figure 4-5. When the acid droplets come into contact with it, capillary forces draw the acid mixture into the notch. Once the notch is full of acid additional droplets begin to coat the outer surface of the sample in the area right around the notch due to surface tension. Careful application of the acid mixture ensures that a small, less than 1 mm long crack relative to the sample length, can be achieved. As the acid mixture will evaporate off the surface of the sample it necessitates the reapplication of the mixture every 15 to 30 minutes. After the sample has etched for a total of 1 hour it is then removed and the acid is neutralized in a baking soda and water solution. The sample

is then put in an isopropyl alcohol bath in a sonicating bath for 10 minutes to remove waste material. This process is then repeated 3 more times or until the bond coat layer has a significant amount of bond coat removed.

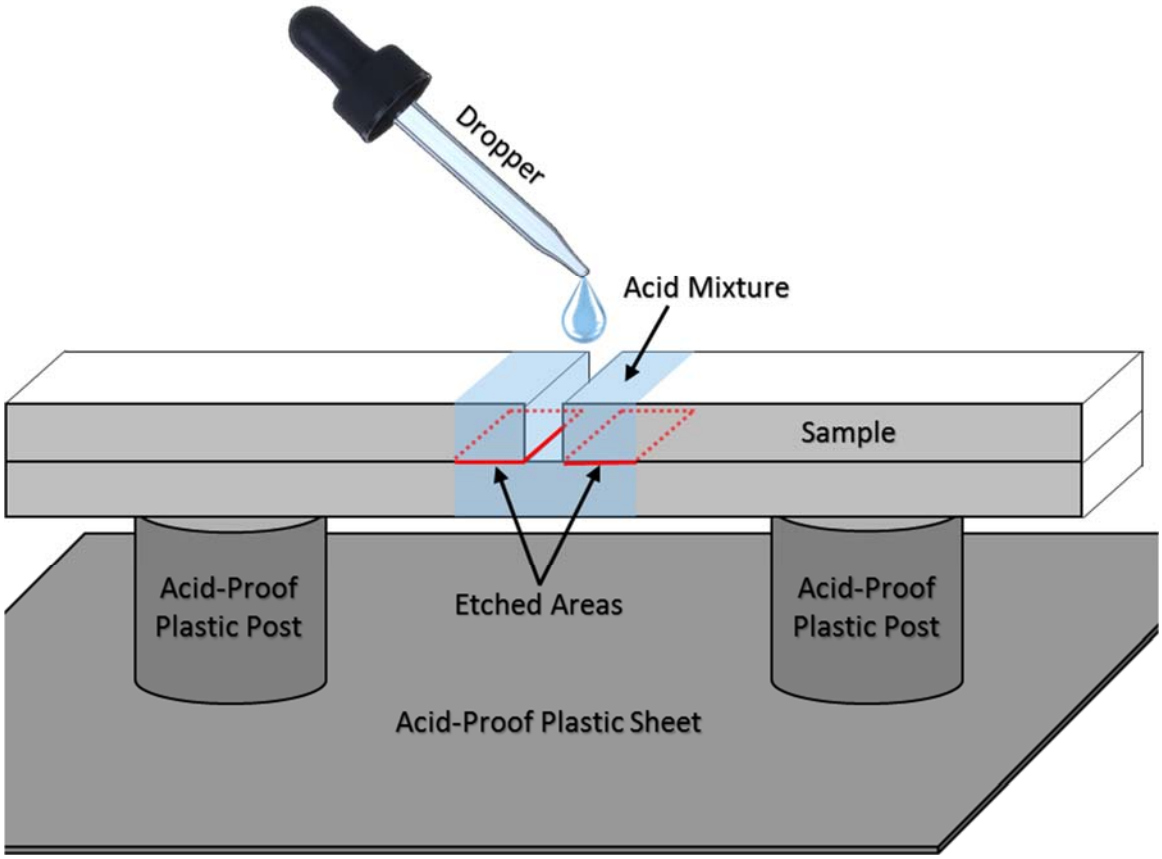

Figure 4-5: Schematic of 4-Point Bend sample acid etching to initiate pre-cracks

4.4 Test Procedure

Samples were loaded under displacement control conditions with an applied displacement rate of $\dot{\delta} = 1\ \mu m/s$. Due to compliance of the loading frame a constant outer surface strain rate is not achieved upon initial sample loading but instead varies from $\dot{\varepsilon} = 2 \times 10^{-6}\ \frac{1}{s}$ initially to $\dot{\varepsilon} = 1 \times 10^{-4}\ \frac{1}{s}$, after roughly 10 μm of displacement. The displacement rate applied ensures that quasi-static conditions exist during crack propagation so that dynamic

effects do not need to be accounted for. It should also be noted that the strain rate specified as the maximum strain rate that would be experienced on the outer surface. The sampling rate for the Futek 500 lb load cell is 4.8kHz and images are captured at a rate of 4Hz. This image capture rate corresponds to maximum incremental strain of $1.2\ \mu$-strain in between each image.

4.5 References for Chapter 4

1. Zhao, P.F., et al., *Fracture toughness measurements of plasma-sprayed thermal barrier coatings using a modified four-point bending method.* Surface and Coatings Technology, 2010. **204**(24): p. 4066-4074.
2. Lin, Z.X., et al., *In situ observation of fracture behavior of canine cortical bone under bending.* Materials Science and Engineering: C, 2016. **62**: p. 361-367.
3. Abdelhadi, O.M., L. Ladani, and J. Razmi, *Fracture toughness of bonds using interfacial stresses in four-point bending test.* Mechanics of Materials, 2011. **43**(12): p. 885-900.
4. Ključar, L., et al., *Effect of 4-point bending test procedure on crack propagation in thin film stacks.* Microelectronic Engineering, 2015. **137**: p. 59-63.
5. Fu, H., et al., *Plastic deformation behavior and bonding strength of an EBW joint between 9Cr-ODS and JLF-1 estimated by symmetric four-point bend tests combined with FEM analysis.* Fusion Engineering and Design, 2016. **102**: p. 88-93.
6. Kikuchi, S., et al., *Characterization of the hydroxyapatite layer formed by fine hydroxyapatite particle peening and its effect on the fatigue properties of commercially pure titanium under four-point bending.* Surface and Coatings Technology, 2016. **288**: p. 196-202.
7. Hutchinson, J.W. and Z. Suo, *Mixed Mode Cracking in Layered Materials*, in *Advances in Applied Mechanics*, W.H. John and Y.W. Theodore, Editors. 1991, Elsevier. p. 63-191.
8. Charalambides, P.G., et al., *A Test Specimen for Determining the Fracture Resistance of Bimaterial Interfaces.* Journal of Applied Mechanics, 1989. **56**(1): p. 77-82.
9. Hutchinson, R.G. and J.W. Hutchinson, *Lifetime Assessment for Thermal Barrier Coatings: Tests for Measuring Mixed Mode Delamination Toughness.* Journal of the American Ceramic Society, 2011. **94**: p. s85-s95.
10. Institute, N.D., *High-temperature high-strength nickel base alloys*. 1995.
11. Zhang, B., *Experimental characterization of thermal barrier coatings using micro-scale bending techniques*, in *Department of Mechanical Engineering*. 2015, Johns Hopkins University: Baltimore, MD.
12. Materials, H.A. *Araldite 2011 Technical Data Sheet*. 2007.
13. Thery, P.Y.P., M.; Dupeux, M.; Braccini, M., *Adhesion energy of a YPSZ EB-PVD layer in two thermal barrier coating systems.* Surface & Coating Technology, 2007. **202**: p. 648-652.
14. Théry, P.-Y., et al., *Spallation of two thermal barrier coating systems: experimental study of adhesion and energetic approach to lifetime during cyclic oxidation.* Journal of Materials Science, 2008. **44**(7): p. 1726-1733.

CHAPTER 5: FINITE ELEMENT MODELLING RESULTS

FE modelling, using ABAQUS 6.13-3 CAE was used to created detailed models representative of both the CED and modified 4-point bend test geometries. Expanding on previous numerical studies conducted on TBC systems [1], the models developed in this study were utilized to calculate the phase angle of fracture and the critical strain energy release rate during fracture. The models were constructed by explicitly accounting for all of the material layers as well as their thicknesses and elastic properties so as to most closely mimic the behavior of the experimental results. Work was also done to understand the effects of interfacial crack face friction and oxide (TGO) thickness on the calculated strain energy release rate for the compression edge-delamination test. The information from this analysis was then used to create a unified analysis method for processing experimental results at various levels of thermal cycling life (i.e. different TGO thicknesses) and for any arbitrary interfacial friction coefficient. Finally, an energetic based approach, the Virtual Crack Closure Technique (VCCT), is used to create an analysis procedure for the 4-point bend test.

5.1 Overview of Sample Finite Element Models

FE models were created that would closely mimic the geometry of the samples prepared and used in this study. The models were made to explicitly account for the following material layers; substrate, bond coat $(100\ \mu m\ thick)$, thermally grown oxide layers $(0-4\ \mu m\ thick)$, top coat $(150\ \mu m\ thick)$, epoxy bond line $(100\ \mu m\ thick)$ and stiffener. For the models, 2D isotropic, linear elastic, plane strain elements were used. The assumption of isotropic material properties is made for the purpose of simplicity, but a

more detailed model accounting for the tension/compression asymmetry present in the top coat layer would be more representative of the material and best suited for future studies. The material properties used in all of the finite element models presented can be seen in Table 5-1.

Table 5-1: Material properties used in FE models and analytical equations

Material	Layer	Elastic Modulus [GPa]	Poisson Ratio	Thickness (CED) [4-point]	Reference
René N5	Substrate/Stiffener	128*	0.38	(6/3) mm [1.4/1.27] mm	*[2]*
β-(Pt-Al)	Bond Coat	156	0.28	100 µm	*[3]*
α-Al2O3	Thermally Grown Oxide	300	0.1	0-4 µm	*[4]*
7% Yttria Stabilized Zirconia	Top Coat	50	0.1	150 µm	*[5]*
Araldie 2011	Epoxy	1.9	0.12	100 µm	*[6]*

** Along <100> direction*

All of the interfaces, both bonded and crack faces, were assumed to be perfectly flat for all the models. This assumption is valid when observing the sample macroscopically because the interface roughness is on the order of $10\,\mu m$ and the substrate thickness is $6\,mm$. Statistically modelling the interface roughness and tortuosity would be more accurate, but would also have been computationally intensive and outside the scope of this study. It is also crucial to use the correct material properties in the FE model as they can have a profound effect on the measured interfacial toughness. A preliminary sensitivity study was conducted to understand the effect of the top coat elastic modulus on the calculated interfacial toughness. Both the CED and modified 4-point bend models discussed in the next sections were used to conduct the sensitivity analysis. Halving of the top coat elastic

modulus resulted in a 14.6% reduction in the interfacial toughness and doubling of the top coat elastic modulus resulted in a 16.5% increase in the interfacial toughness.

5.1.1 Compression Edge-Delamination Specimen

The geometry and loading conditions of the compression edge-delamination sample are given in Figure 5-1. The model consists of 247,872 CPS4R (4-node bilinear plane stress quadrilateral element with reduced integration and hourglass control) and 4,238 CPS3 (3-node linear plane stress triangle) elements and the loading platens are composed of 4228 R2D2 (2-node 2-D linear rigid link) element each.

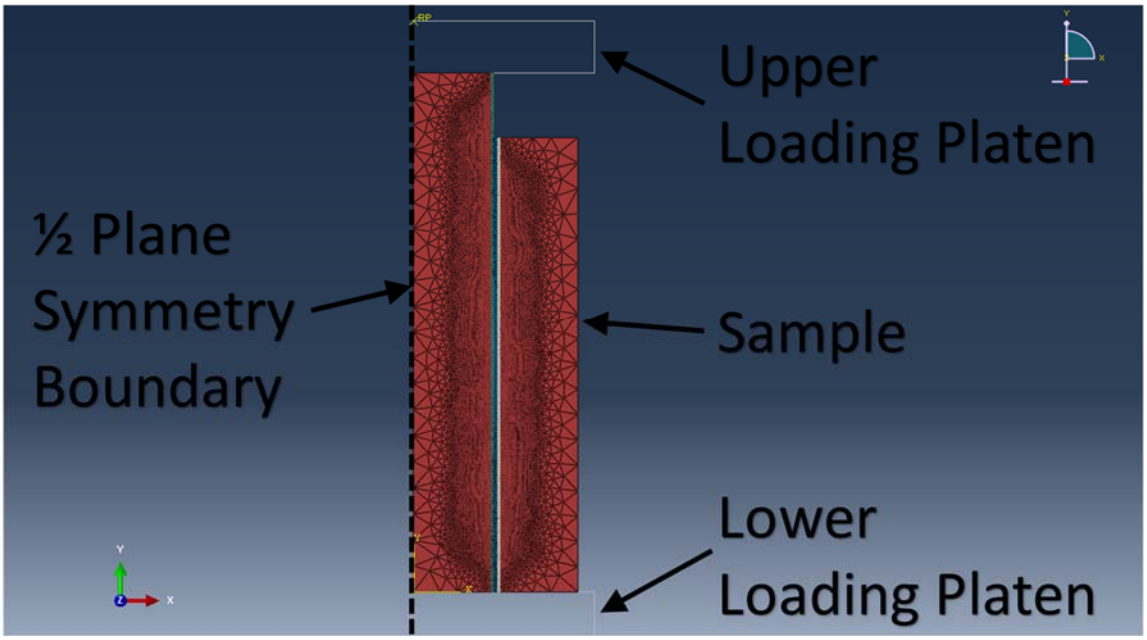

Figure 5-1: FE model of CED specimen showing sample, loading platens, mesh and 1/2 plane symmetry boundary condition

A compressive displacement is applied through the upper and lower loading platens, which are composed of rigid wire elements. The upper loading platen is constrained so that it cannot rotate or displace in any direction. The lower platen is constrained so that it cannot rotate in any direction and cannot move in the x-direction, but is free to move in the y-direction. Frictionless contact between the loading platens and sample is assumed. The

geometry of the model is the same as the schematics shown in Figure 3-6. For the calculation of the phase angle and the initial work on the steady-state strain energy release rate, the TGO is not explicitly considered, but work is done later in section 5.3.1.2 to modify the calculated steady-state strain energy release rate to account for the change in the TGO thickness during thermal cycling. It should also be noted that only the right ½ of the sample is modelled as there was a half-symmetry plane boundary condition placed on the right vertical boundary shown in Figure 5-1.

5.1.2 4-Point Bend Specimen

The geometry and loading conditions of the 4-point bend specimen are shown in Figure 5-2. The model consists of 35,650 CPS4R (4-node bilinear plane stress quadrilateral element with reduced integration and hourglass control) and 281,050 CPS3 (3-node linear plane stress triangle) elements and the loading pins are composed of 785 R2D2 (2-node 2-D linear rigid link) elements each.

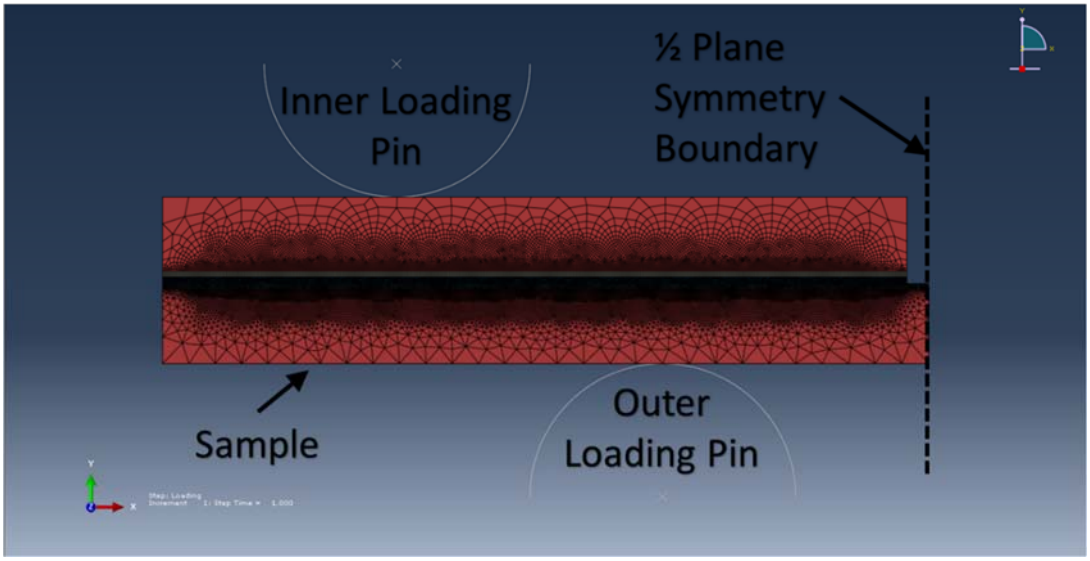

Figure 5-2: FE model of 4-point bend specimen showing sample, loading pins, mesh and 1/2 plane symmetry boundary condition

Bending forces are applied through the inner and outer loading pins, which are composed of rigid wire elements. The outer loading pin is constrained so that it cannot rotate in any direction and cannot displace in any direction. The inner loading pin is constrained so that it cannot rotate in any direction and cannot move in the x-direction, but is free to move in the y-direction. The bending forces are accommodated though a vertical displacement applied to the inner loading pin. Frictionless contact is assumed between the loading pins and the sample. This combination of frictionless contact and rigid pin geometry mimics the rotating bearings used to load the sample. It should also be noted that only the left ½ of the sample is modelled as there is a half-symmetry plane boundary condition placed on the sample as shown in Figure 5-2.

5.2 Phase Angle of Fracture

As described in section 2.2.1.2, the relative displacements of the crack faces can be used to calculate the phase angle of loading according to the following equation [7]:

Equation 5-1

$$\phi = tan^{-1}\left(\frac{\delta_{shear}}{\delta_{opening}}\right)_{r=l}$$

For a crack oriented with the crack plane parallel to the x-direction, the shear direction is the x-axis and the opening direction is the y-axis. Work conducted by Charalambides et al. [8], recommends that the value of l that the phase angle should be evaluated at be approximately $1/100$ to $1/1000$ of the coating thickness away from the crack tip. It is also noted that care should be taken to avoid the first few finite elements near the crack tip as spurious results can occur. As this material system has numerous layers, the phase angle

was calculated at a number of points away from the crack tip, until convergence of the phase angle occurred.

5.2.1 Compression Edge-Delamination Specimen

Previous work has been conducted by Hutchinson et al. [1] to calculate the phase angle of fracture for the compression edge-delamination specimen. This work reported that for a sample composed only of the substrate material, a phase angle of $\phi = -90°$ could be expected (or pure mode II fracture). It is noted in their work that a shift in the phase angle will occur due to the inclusion of a bimaterial interface, with values tabulated vs. the effect of the material properties either side of the interface as well as with geometric parameters. Work was done in the sample geometry design phase, presented in section 4.2, to ensure that the phase angle is as close to pure mode II conditions as possible. An interfacial seam crack was introduced between the bond coat and top coat layers as shown in Figure 5-3, which also shows the individual material layers and layer thicknesses used in the FE model.

The crack was modelled to have grown to a length where steady-state conditions would exist ($a > 2h$). For the geometry chosen the value of h is 3 mm and a steady-state crack length of $a = 8\ mm$ was chosen to ensure steady-state conditions exist. To understand if interfacial friction affects the phase angle, the friction was varied between the frictionless case and a friction coefficient of $\mu_f = 0.5$ in increments of 0.1. The frictional contact was accounted for through the penalty method of contact friction. An arbitrary displacement was applied to the sample in the finite element model to simulate loading. For the frictionless case, the average ratio of the shear to opening displacement was found to be $\frac{\delta_{shear}}{\delta_{opening}} = 170.83$, which corresponds to a phase angle of $\phi = -89.66°$. It was found that

the effect of friction played a negligible role on the phase angle ($< 0.1\%$) and was therefore taken to be $\phi = -89.66°$. The value of the phase angle helps to exemplify the importance of the sample design phase as Hutchinson predicted that deviations of the phase angle of up to 12° could occur under non-ideal conditions.

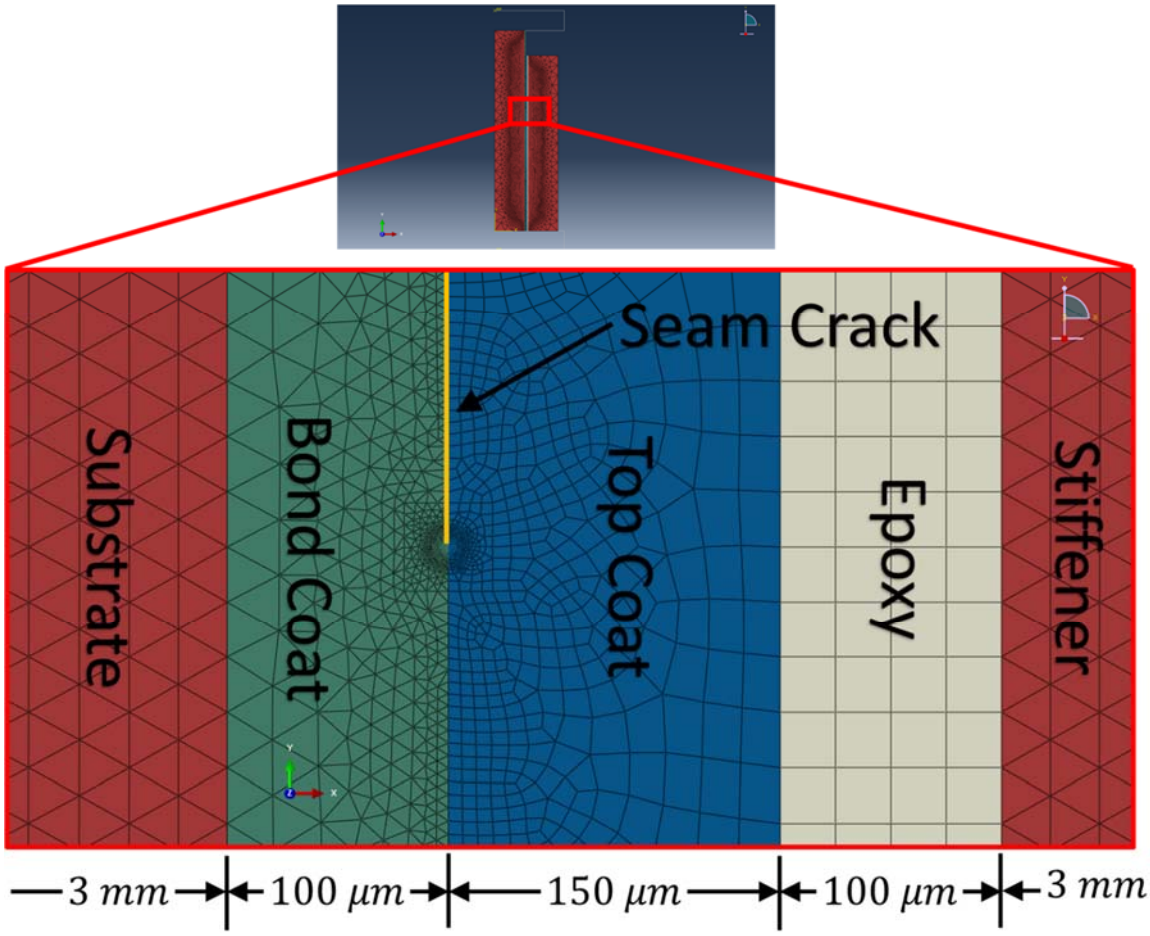

Figure 5-3: Close-up view of Finite Element model of Compression Edge-Delamination Specimen showing location of seam crack, material layers modelled and thicknesses of layers used

5.2.2 4-Point Bend Specimen

Numerous elastic and numerical studies have been conducted on the phase angle of the 4-point bend specimen and have all reported phase angles of $\phi = 40.9°$ [1, 9-11]. In order to ensure that the model used in this study was obtaining accurate results and to account for

the effect of the material layers on the phase angle a similar analysis was done for the 4-point bend specimen. A 3 mm long seam crack was introduced into the sample with friction accounted for in the same way as with the CED sample. A seam crack was introduced between the bond coat and top coat layers as shown in Figure 5-4, which also shows the individual material layers and layer thicknesses used in the Finite Element model.

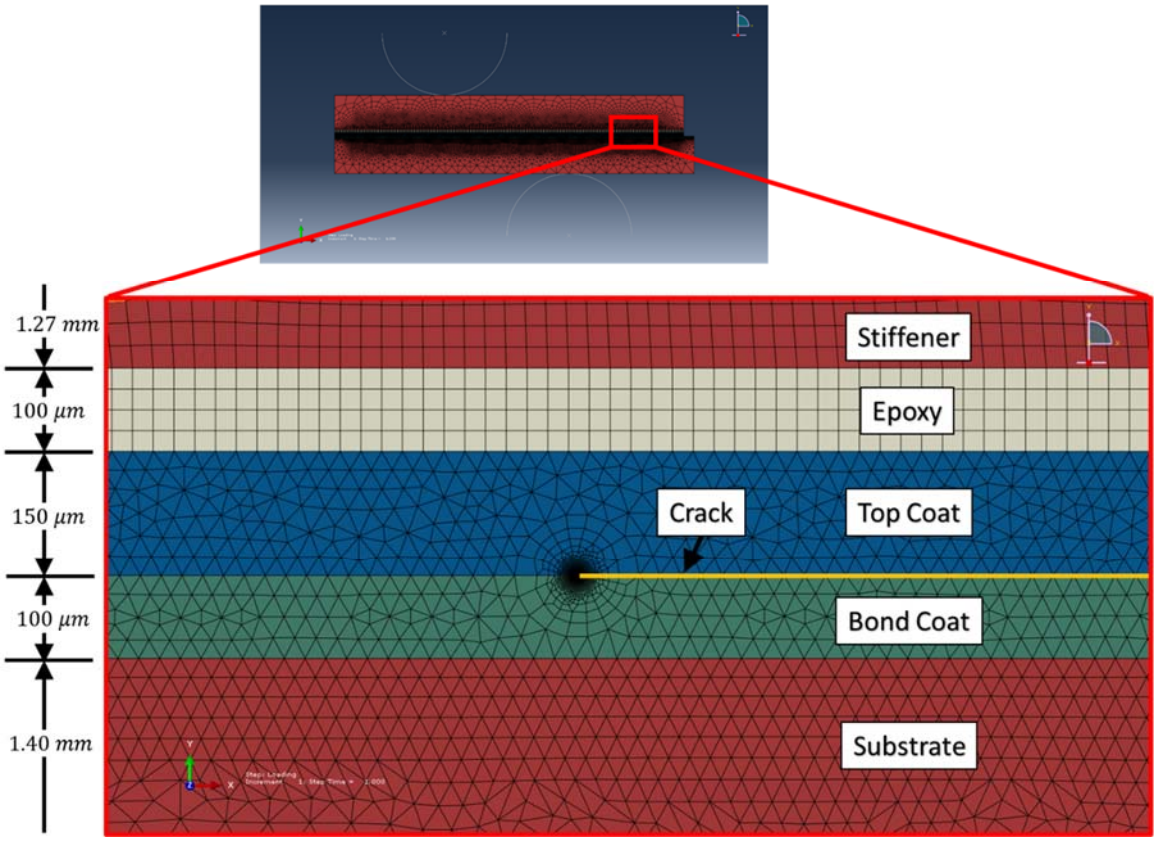

Figure 5-4: Close-up view of Finite Element model of 4-Point Bend Specimen showing location of seam crack, material layers modelled and thicknesses of layers used

It was found that friction played no role on the phase angle with $\frac{\delta_{shear}}{\delta_{opening}} = 0.913$, which corresponds to a phase angle of $\phi = 42.41°$. The slight deviation of the phase angle from the previously published values is due to the explicit inclusion of all the material layers and layer thicknesses in the finite element model, which previous studies did not account for.

5.3 Steady State Strain Energy Release Rate

The critical strain energy release rate can be calculated by taking experimental results for the critical cracking load and use that as an input into the finite element model for that applicable test and geometry. The way the energy release rate is calculated is through a discretized contour integral around the crack tip. This method calculates the value of the J-integral, discussed in section 2.1.4, over paths around the crack tip. This method of integrating the J-integral method into finite element procedures was based off of the virtual crack extension and domain integral methods developed by Parks in 1977 [12] and Shih et al. in 1986 [13]. The equation that is discretized around the crack tip is shown as:

Equation 5-2

$$J = -\int_{\Gamma}\left[\boldsymbol{H}:\frac{\partial \bar{q}}{\partial x}+\left(\boldsymbol{f}\cdot\frac{\partial u}{\partial x}-\boldsymbol{\sigma}:\frac{\partial \boldsymbol{\varepsilon^{th}}}{\partial x}\right)\cdot\bar{q}\right]d\Gamma-\int_{\Gamma_{Crack\ Face}} t\cdot\frac{\partial u}{\partial x}\cdot\overline{\boldsymbol{q}}\,d\Gamma$$

In Equation 5-2, $\boldsymbol{H}=W\boldsymbol{I}-\boldsymbol{\sigma}\cdot\frac{\partial \boldsymbol{u}}{\partial \boldsymbol{x}}$, W is the elastic strain energy, $\boldsymbol{f}$ is the body force per unit volume, $\boldsymbol{\varepsilon^{th}}$ is the thermal strain and $\overline{\boldsymbol{q}}$ is the crack propagation direction. It should also be noted that the integral on the left side is the whole contour integral around the crack tip and the right side of the equation is only taken on the crack face surfaces. This equation is discretized and evaluated around numerous concentric paths around the crack tip. Typically, as the controls move away from the crack tip, the value of the J-integral will converge to a steady-state value. An example of these contours around a crack tip can be seen in Figure 5-5. It should be noted that contours in only one of two directions is shown. There are a few important things to note about the geometry of the finite elements that border the crack tip. All of finite elements are 4-noded quadrilateral elements with 4 integration points (analysis points) in each element. The elements whose points directly

touch the crack tip appear to be triangular elements, but are in fact collapsed 4-noded quadrilateral elements. The procedure by which these elements were collapsed can be seen visually in Figure 5-6. The elements start out as fully quadrilateral finite element with 4 integration points. Two adjacent nodes of the element are then collapsed (merged) together to form a 3-noded element with 4 integration points as shown. When implemented around a crack tip the crack tip contains many 3-noded collapsed elements, such that many more integration points are at the crack tip than there would have been if it was simple composed of all quadrilateral elements. This can be seen visually in Figure 5-7. At the crack tip there is a high concentration of integration points that can accurately capture the singular nature of the stress field close to the crack tip.

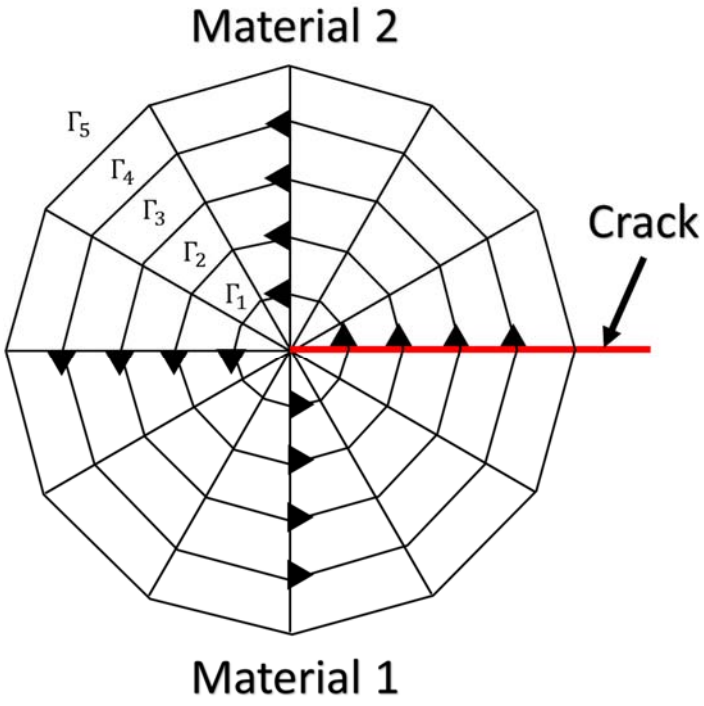

Figure 5-5: Schematic of FE mesh around a crack tip and example J-integral contour paths. (Note direction of J-integral path can be either clockwise or counter-clockwise)

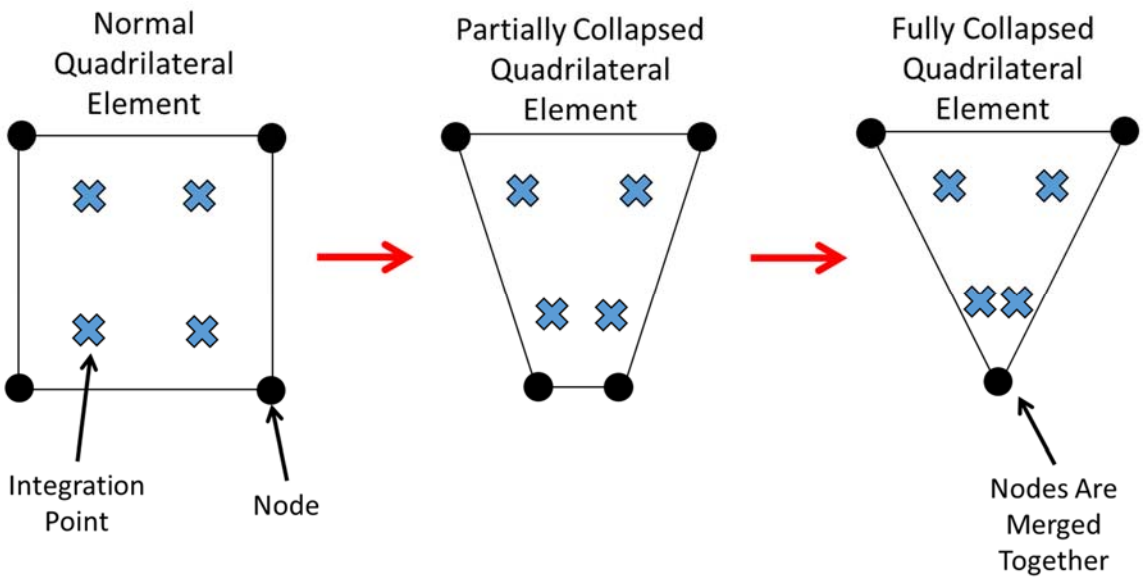

Figure 5-6: Schematic representation of normal quadrilateral finite element, a parially collapsed quadrilateral finite element and a fully collapsed quadrilateral finite element with merged nodes

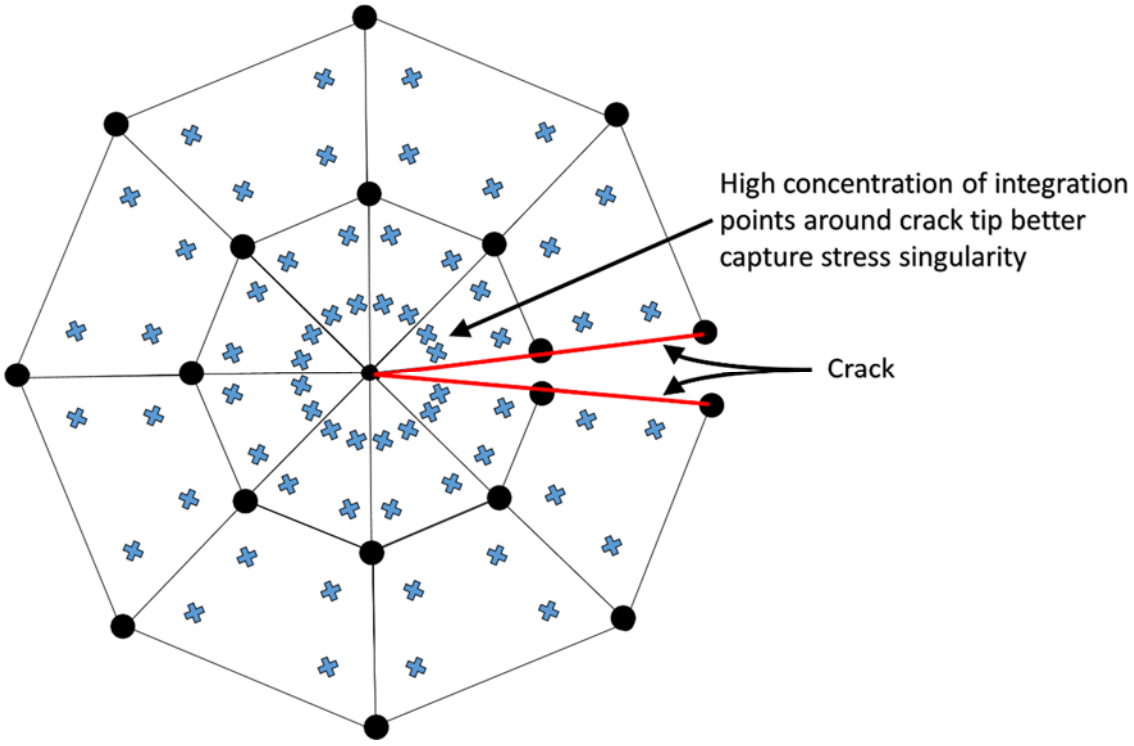

Figure 5-7: Schematic representation of finite element mesh around a crack with collapsed quadrilateral finite elements at the crack tip

5.3.1 Compression Edge-Delamination Specimen

To understand the effect of the strain energy release rate as the crack grows the FE model discussed in the previous sub-section was used. Cracks of different lengths were implemented as seam cracks in the FE model and the discretized J-integral contour method was used to calculate the energy release rate for a given load and crack length. For this model 20 successive contour integrals were taken around the crack tip that radiate away from the crack tip location. The same compressive displacement of $100\ \mu m$ was applied to the models with different crack lengths and the resultant load and converged J-integral values were recorded. An example of this convergence is shown in Figure 5-8.

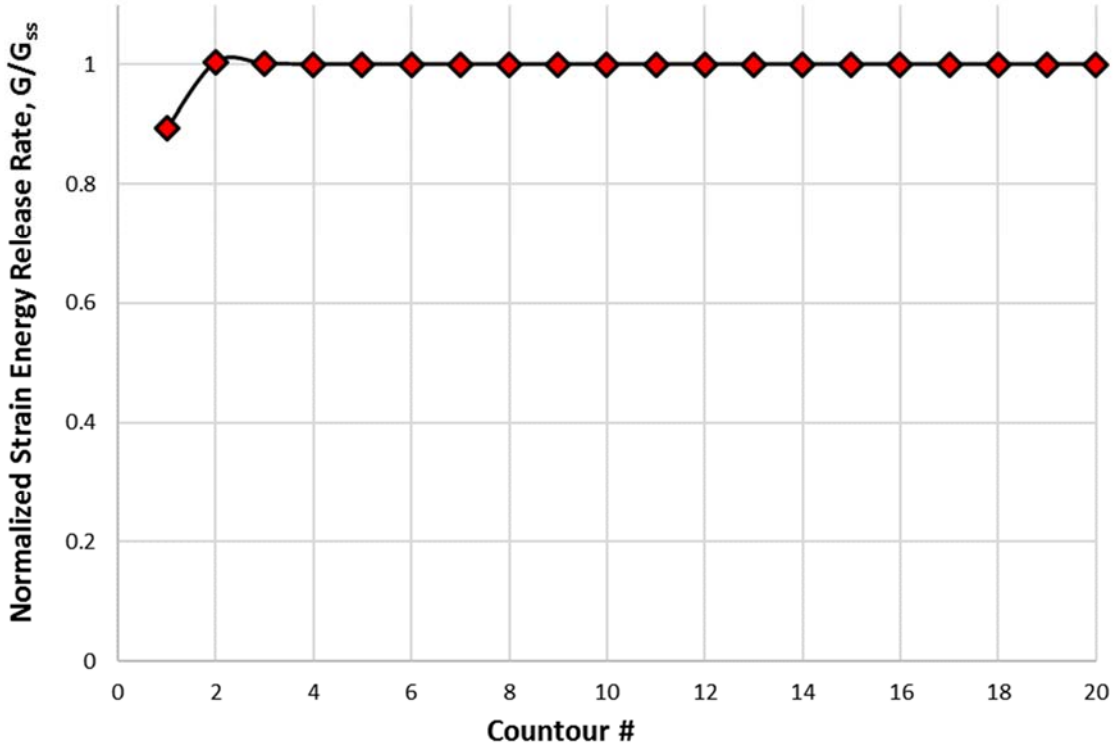

Figure 5-8: Representative plot of convergence of the strain energy release rate versus the countour #. (Note: contour # increases as contour moves away from the crack tip)

The raw values of the finite element J-integral were then normalized by the value of the J-integral predicted by the analytical equation for the total applied stress to the loading interface by the following relation:

Equation 5-3

$$\frac{G}{G_{ss}} = \frac{G_{FEM}}{G_{Analytical}} = \frac{G_{FEM}}{\frac{\sigma^2 h}{E}}$$

In this equation the applied stress, σ, is defined by:

Equation 5-4

$$\sigma = \frac{P_{resulant}}{2hw}$$

where $P_{resultant}$ is the resultant load from the finite element simulation, h is the thickness parameter and w is the width of the sample.

Equation 5-5

$$\frac{G}{G_{ss}} = \frac{4G_{FEM}Ehw^2}{P_{resultant}^2}$$

The result of this analysis for a FE model composed of only the substrate material with cracks between the substrate and stiffener can be seen in Figure 5-9. The most important aspect of this analysis is that the strain energy release rate does not reach a steady-state value until the crack length is approximately twice the height parameter ($a \approx 2h$). The reason that the energy release rate does not exhibit steady-state behavior after initial crack growth is due a region of interfacial pressure behind the advancing crack tip [1].

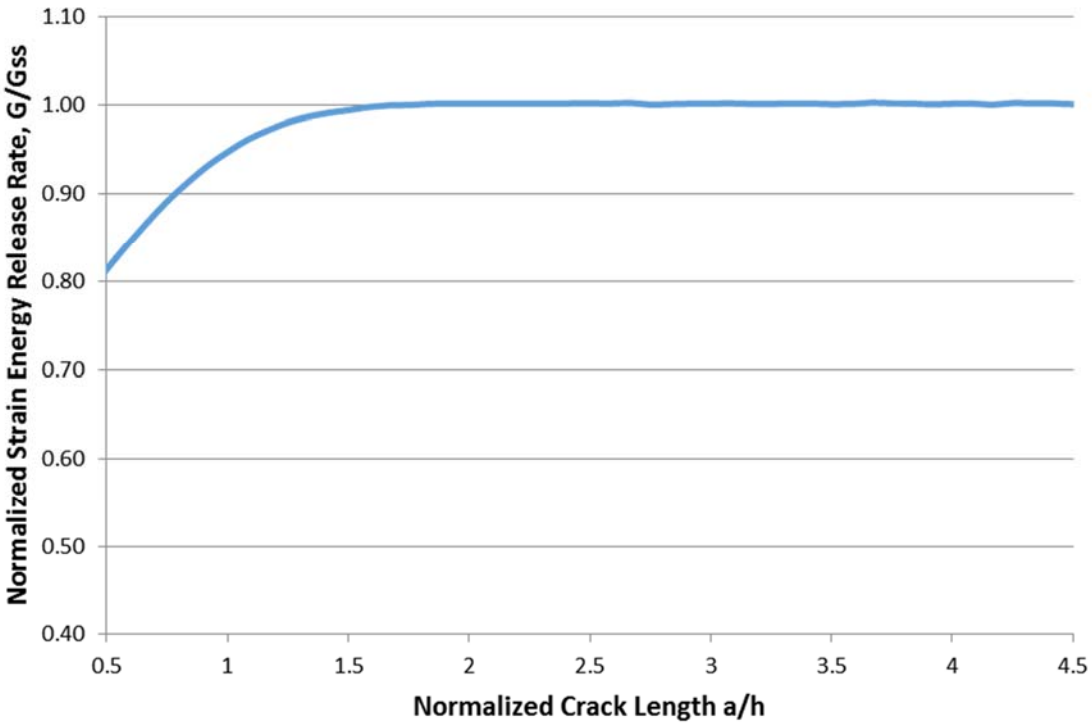

Figure 5-9: Normalized strain energy release rate vs. normalized crack length for FE model composed of only substrate material and no interfacial friction

Although the loading at the crack tip is $-90.0°$, there is a certain amount of pressure present on the cracked faces. This region of interfacial pressure does not reach its full profile until the crack is approximately twice the height parameter. After the crack grows beyond this length, the profile of the pressure region stays the same, but follows behind the advancing crack front. As the pressure region is still developing before the crack length is equal to $2h$ the strain energy release rate does not reach its steady-state value. This behavior can be seen in the plots in Figure 5-10. The plots show the normalized pressure along the interface for cracks of (a) length 3h and of (b) length 4h. It is readily observed that the pressure region follows the same magnitude and profile behind the advancing crack front. It is also apparent that the region of interfacial pressure is approximately 2h. These results are directly in line with initial observations made by Hutchinson et al. [1].

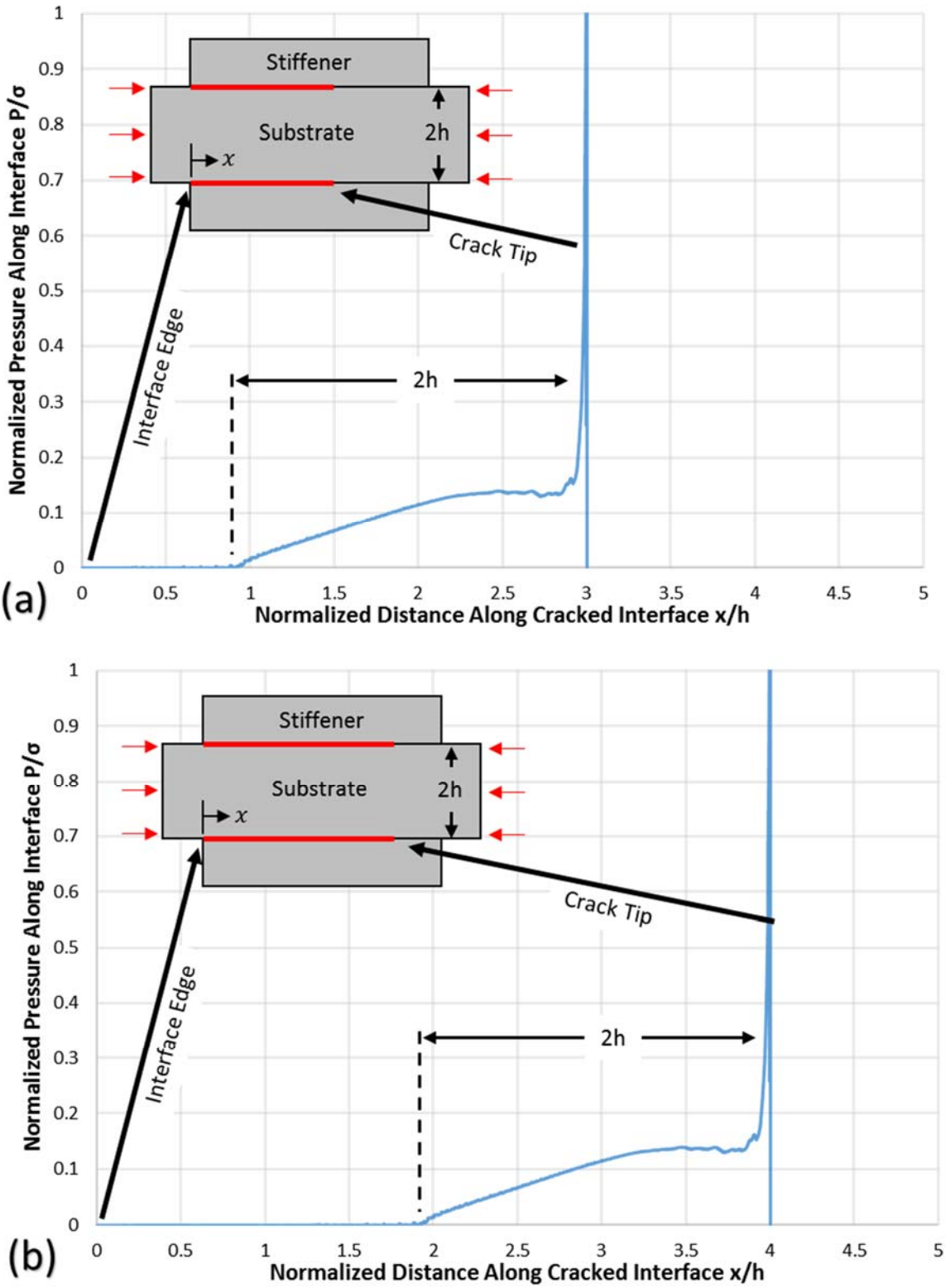

Figure 5-10: Plots of normalized pressure along cracked interface vs. normalized distance along crack interface for cracks of length (a) 3h and (b) 4h

5.3.1.1 Effect of Interfacial Friction

As there is a region of pressure acting on the cracked interfaces it is apparent that a friction force acting parallel to the crack growth direction will arise. This frictional force will impose a resistance to the crack growth and will lead to a decrease in the amount of energy available for crack growth. This in turn leads to an overestimation of the strain energy release rate during delamination because some of the energy that was thought to have driven the crack was actually being dissipated through frictional sliding. This is described generally in the following equation:

Equation 5-6

$$\Delta E_{total} = \Delta G + \Delta E_{\mu} + \Delta E_{other}$$

In this equation it is assumed the energy contribution from other sources is not dependent on the friction coefficient and that the total energy ΔE is constant. If the friction coefficient prescribed in the FE model is increased it should lead to a linear decrease in the measured steady state strain energy release rate and is shown in Figure 5-11. As the friction coefficient is increased from $\mu_f = 0$ to $\mu_f = 0.5$ there is an approximately 20% decrease in the measured strain energy release rate. That 20% change in the strain energy release rate is present because approximately 20% of the total available strain energy available for release was consumed by frictional sliding.

It is extremely important to take into account the effect of friction when calculating the strain energy release rate or inaccurate results will be obtained. It is also extremely important to make sure that the analysis explicitly account for all the material layers present in the system. When the difference in the material properties either side of a bimaterial interface change they directly affect the Dunders parameters from Equation 2-32 and

Equation 2-33. The Dunders parameters in turn have an effect on stress distribution in the bimaterial fracture zone and subsequently the strain energy release rate. Difference in the mechanical properties can have the same affect the magnitude of the interfacial crack pressure. To understand this behavior a number of different FE models, all with an epoxy bond line, were created; (a) one composed only of the substrate material, (b) one with the substrate, bond coat and top coat and (c) one with the substrate, bond coat, 1 μm thick thermally grown oxide and top coat. Model (a) is a homogeneous material system and $\beta = 0$. For model (b) and (c) the Dunders parameter β is $\beta = 0.272$ and $\beta = 0.318$ respectively. This increase in β has a direct impact on the steady-state strain energy release rate and can be seen in Figure 5-12.

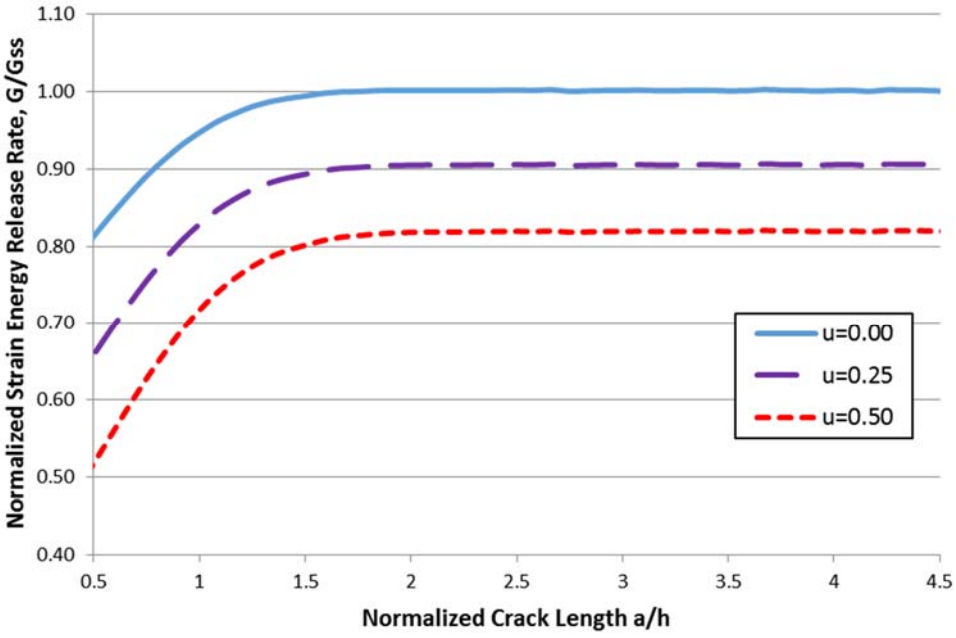

Figure 5-11: Normalized strain energy release rate vs. normalized crack length for FE model composed of only substrate material and with varying levels of interfacial friction

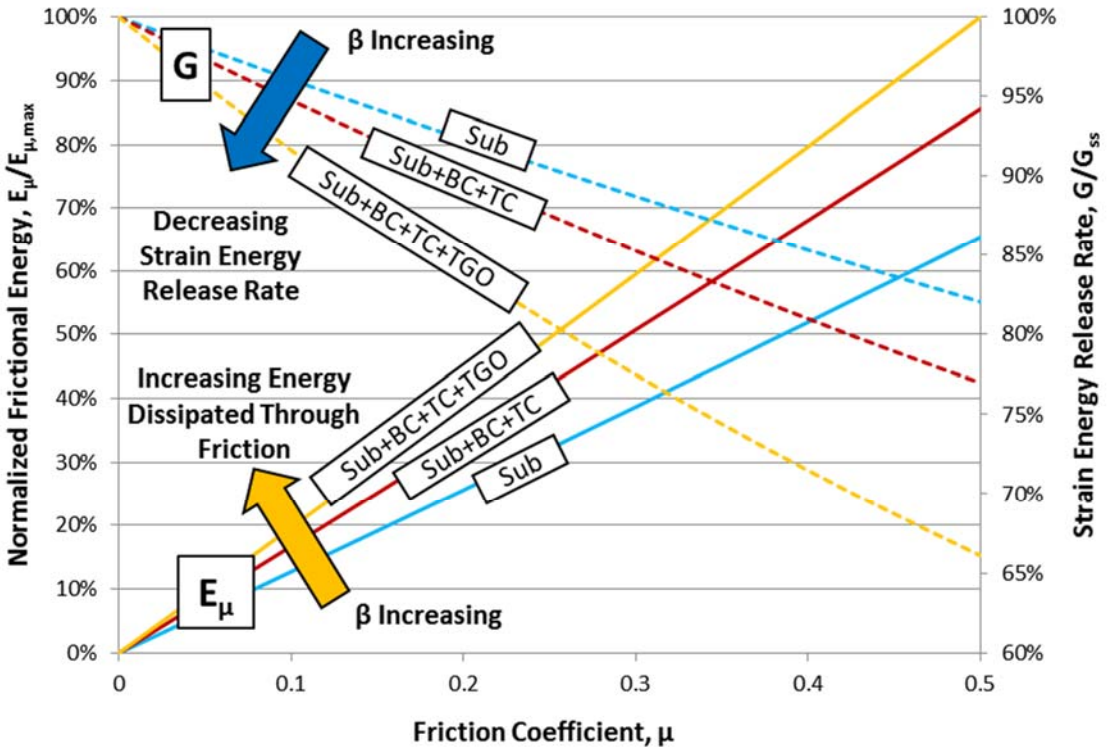

Figure 5-12: Combined plots of energy dissipated though frictional sliding and normalized strain energy release rate vs. friction coefficient for FE models composed of (a) the substrate only, (b) the substrate, bond coat and top coat and (c) the substrate, bond coat, thermally grown oxide, and top coat

5.3.1.2 Effects of TGO Thickness

From Figure 5-12 it is apparent that inclusion of the TGO is important to ensure accurate characterization of the strain energy release rate. One aspect of the material system that needs to be accounted for is that the TGO will grow from $\leq 250\ nm$ in the as-deposited state to $> 3\ \mu m$ close to the coating lifetime. As there is already approximately a 10% reduction in the measured strain energy release rate through inclusion of the TGO in the FE model, it is important to understand how the strain energy release rate changes with TGO thickness. A series of FE models were created with TGO thicknesses of 0 μm, 2 μm, 4 μm. Seam cracks were introduced into the models with an $^{a}/_{h}$ ratio of 3 so that steady-state conditions for the strain energy release rate were reached. The results of this can be

seen in Figure 5-13. The curve for the substrate only model shows that for a friction coefficient of 0.5, the actual strain energy release rate is approximately 77% of what would be expected from the analytical equation. For the remaining models with no TGO, a 2 μm thick TGO and a 4 μm thick TGO, the reductions are approximately 67%, 60% and 57% respectively. This is an important finding because it means that for a thermally cycled sample with a well-developed TGO layer, the analytical model could over-estimate the interfacial toughness by a factor of 2. It should also be apparent, from both the previous section and this section, that accurate measurement of the evolution of the TGO thickness during thermal cycling and of the interfacial friction coefficient is essential to accurately characterize the interfacial toughness throughout the coatings life.

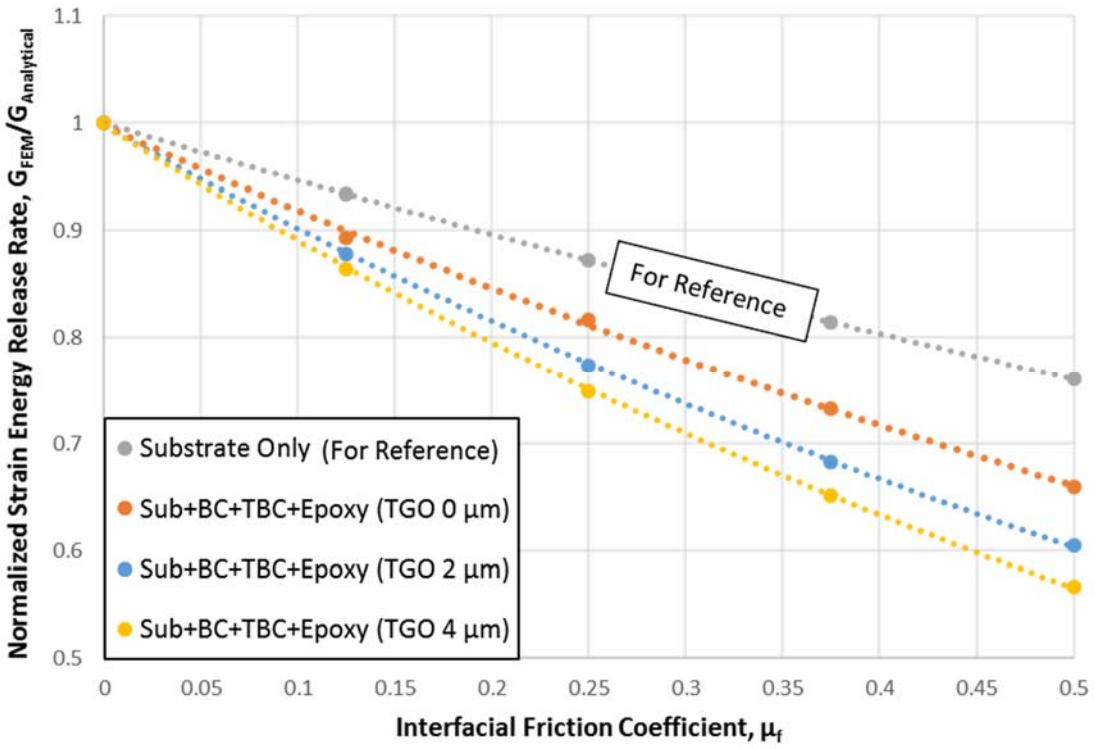

Figure 5-13: Normalized strain energy release rate vs interfacial friction coefficient for (a) substrate only and for substrate, bond coat, top coat and epoxy with (b) no TGO, (c) 2 micron thick TGO and (d) 4 micron thick TGO

5.3.1.3 Combined Friction and TGO Thickness Surface Fitting Method

In order to implement the findings of the previous section into a concise equation to analyze experimental results it is necessary to find a functional form for how the steady-state strain energy release rate varies with the TGO thickness and the interfacial friction coefficient. From examination of the curves in Figure 5-13, it is observed that they exhibit a decaying exponential behavior of the form:

Equation 5-7

$$\frac{G_{FEM}}{G_{Analytical}} = e^{-b*\mu_f}$$

It should be noted that this is an empirical fit unique to this system. By plotting the values of the fitting parameter "b" from Equation 5-7 against the TGO thickness it is found that the dependence on b with the TGO thickness is linear over the relevant range of t_{TGO}. This can be seen in Figure 5-14.

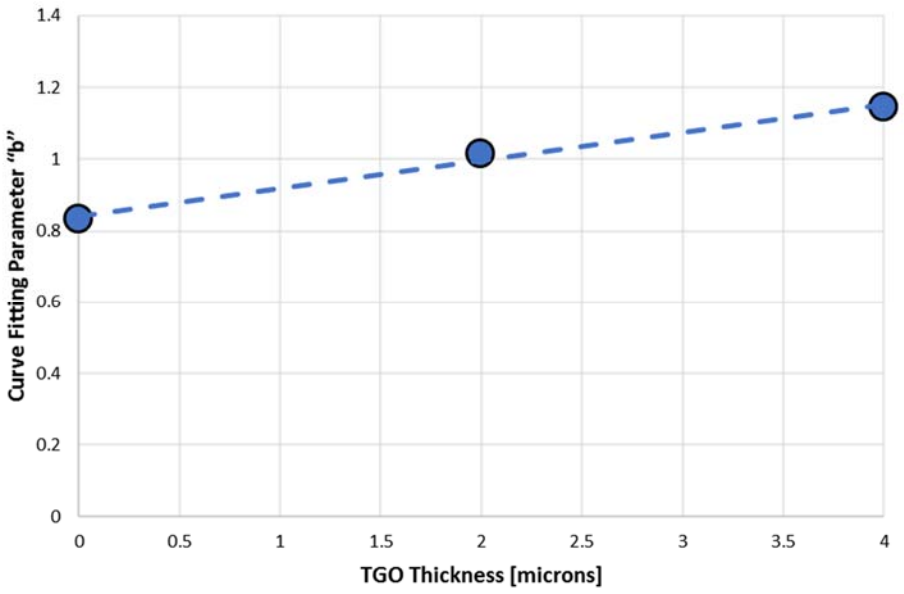

Figure 5-14: Curve fitting parameter "b" vs TGO thickness

The dependence of the fitting parameter on the TGO thickness is nearly linear and follows the following form (based on FE analysis):

Equation 5-8

$$b = 0.0781 * h_{TGO} + 0.8045$$

By combing Equation 5-7 and Equation 5-8 the following equation relating the TGO thickness and friction coefficient to the strain energy release rate can be defined:

Equation 5-9

$$G_{FEM} = G_{Analytical} * e^{-(0.0781*h_{TGO}+0.8045)\mu_f}$$

Combining this equation for the analytical strain energy release rate from Equation 3-9 yields:

Equation 5-10

$$G_{FEM} = G_c = \frac{\sigma^2 h}{E} e^{-(0.0781*h_{TGO}+0.8045)\mu_f}$$

where h is the height parameter of the CED sample and E is the elastic modulus of the substrate. This equation now allows for simple analysis of any experimental results and accounts for reductions in the interfacial toughness due to growth of the TGO and from interfacial friction. It should also be noted that this formulation holds for the specific geometry specified in this study. For subsequent studies on different TBC material systems or even other material systems, a simple calibration would have to be conducted by running a series of FE simulations like the ones outlined in Figure 5-13.

5.3.2 4-Point Bend Specimen

In order to assess whether analytical solutions of the 4-point bend specimen could be used directly or with modification, as with the CED specimen, FE modelling was utilized to

determine the relationship between the strain energy release rate and applied load under bending. Instead of using the J-integral method to calculate the strain energy release rate, another approach, known as the Virtual Crack Closure Technique (VCCT) was used. The VCCT is an energetic based approach that calculates the required crack extension necessary for crack growth with the total available energy for crack growth [14]. Original publication on the VCCT occurred in 1977 [14] and subsequent developments were made to further develop the analysis method [15-18]. Later work was conducted to apply the VCCT to FE software [19, 20] and it is now present in most major FE software packages. Further advancements in the method had been made to improve the efficiency of the technique and add additional features [21-25]. For a more complete review of the VCCT it is recommended to read the original publication on the VCCT [14] and an excellent review of the VCCT by Krueger titled *Virtual crack closure technique: History, approach, and applications* [26].

One of the main advantages of the VCCT over other fracture mechanics techniques is that it allows for determination of sample load-displacement during crack growth. This finding will be used to compare load-displacement data calculated with the VCCT to that of the analytical solution to determine whether the analytical solution can be used alone. The required input for the VCCT is the critical strain energy release rate for the pre-defined crack in the FE model. The method used in this study involves generating load-displacement curves for a number of different critical strain energy release rates and comparing them to the analytical solution. Utilizing the stress-plateau behavior during delamination for the 4-Point bend specimen, the critical cracking load from the FE

simulation can be compared the experimental results and to the critical cracking load expected from the analytical solution at the same strain energy release rate.

A series of FE simulations were conducted with varying critical strain energy release rates from $100\ {}^{J}/_{m^2}$ to $1000\ {}^{J}/_{m^2}$ in $100\ {}^{J}/_{m^2}$ increments. The samples were loaded to a maximum loading pin displacement of $200\ \mu m$ under quasi-static conditions. The resultant load-displacement curves can be seen in Figure 5-15. As the critical strain energy release rate supplied to the VCCT analysis increases, the cracking load also increases. It should also be noted that through the VCCT analysis, an initial crack pop-in load and subsequent load-drop to the plateau cracking load is captured. As the crack reaches directly over the inner loading pins, crack growth is arrested, and the load then begins to increase. The compliance of the sample also changes significantly from when the sample is initially loaded to after crack growth is arrested at the inner loading pins. This behavior is shown by observing the slop of the load-displacement curve in Figure 5-15 before and after the plateau cracking load, i.e. before crack growth and once the crack reaches the inner loading pins. Extraction of the critical loads was conducted using a custom MATLAB script shown in APPENDIX D: Plateau Load Calculation MATLAB File. The script allows for graphical selection of the region over which to average the cracking load. This file is used to extract both the FE results and to process experimental data.

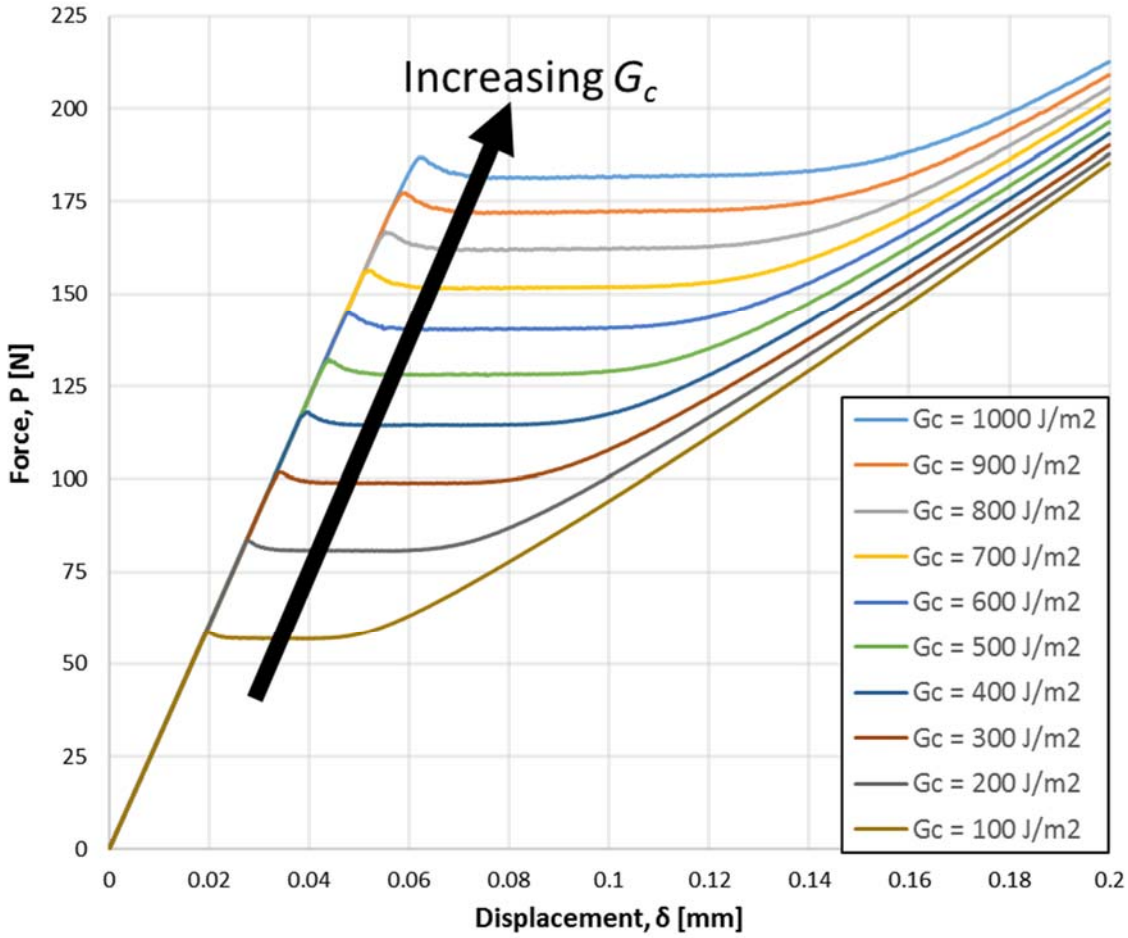

Figure 5-15: Force vs. displacement for FE simulations at varying supplied critical strain energy release rates

Critical cracking loads were extracted from the curves in Figure 5-15 and were used with calculate the strain energy release rate from the simplified analytical equation (Equation 4-4) and from the full analytical equation that explicitly accounts for all the material layers (Equation 4-5). These plots are shown in Figure 5-16. Both the simplified analytical model and full analytical model overestimate the strain energy release rate calculated from the FE simulation. All of the curves exhibit a power law behavior of the form $G_c = mP_c^2$. For the simplified analytical model $m = 0.1133$, the full analytical model $m = 0.0774$, and for the FE model $m = 0.0304$. Since the FE model is able to discretize the geometry and

loading conditions better than the analytical equation it is assumed that the FE behavior represents the actual loading conditions.

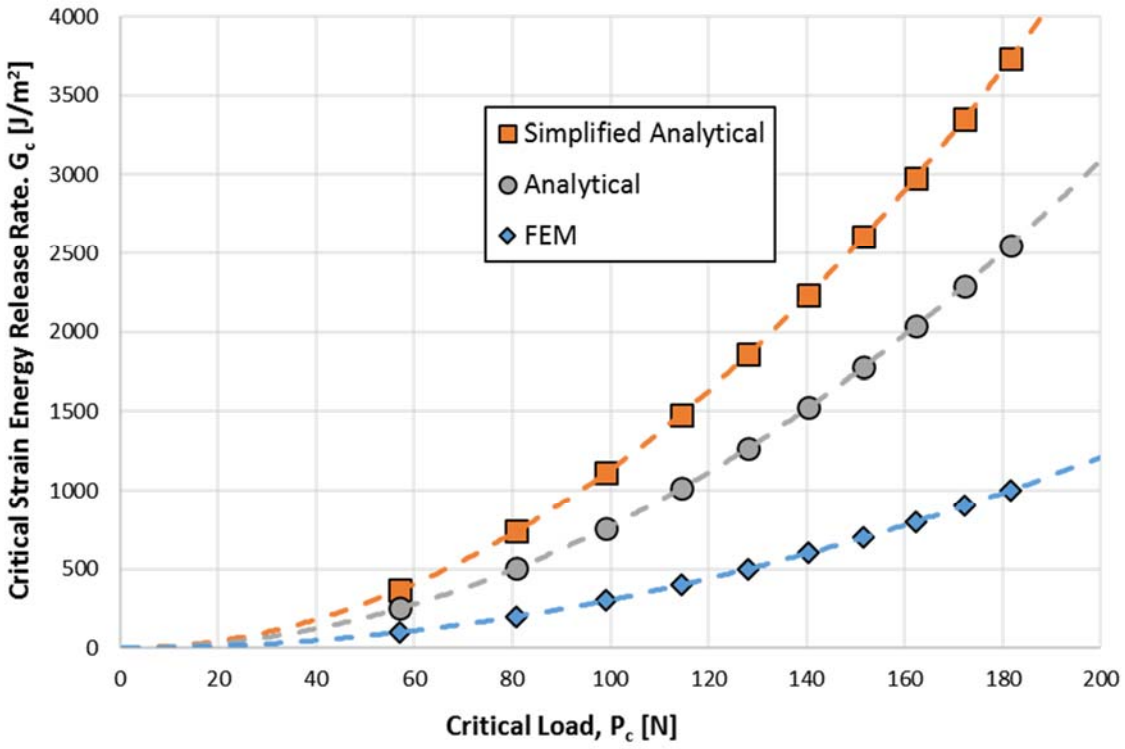

Figure 5-16: Critical strain energy release rate vs critical cracking load for (a) FE model with supplied G_c, (b) simplified analytical solution with P_c from FEM results and (c) analytical solution with P_c from FEM results

A simple modification to the analytical equations, in the form of a pre-factor, can be made to account for their overestimation. For analysis of experimental results with the simplified analytical equation, the following relation is found:

Equation 5-11

$$G_c = 0.2683 * G_{c,simplified}$$

and for the full analytical model:

Equation 5-12

$$G_c = 0.3928 * G_{c,full}$$

With the relations in Equation 5-11 and Equation 5-12 defined, either the simplified or full analytical models can be used to analyze experimental results making sure to include the appropriate pre-factors for the given material properties and geometries used in this study. It is also important to note that the simplified model overestimates the actual behavior by the most and the full analytical model lies in between the simplified model and the FEM results. This is largely attributed to the geometry of the sample, shown schematically in Figure 5-17. In most other studies the width to height ratio ranges from $^{w}/_{h} = 1 - 4$ [9, 27], which represent plane strain conditions.

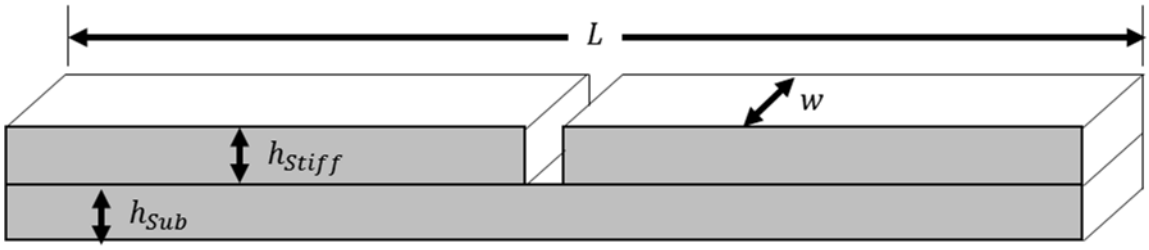

Figure 5-17: Generalized schematic of modified 4-point bend specimen

In the study the ratio was $^{w}/_{h} = \frac{1}{3}$, which lies in a transitional zone between plane strain and plane stress conditions. This exemplifies the importance to not only accurately account for every material layer present, but to account for the specific stress state in the sample that cannot always be captured by analytical models. In order to accomplish this goal, it is necessary to conduct the FE simulations presented in this study.

5.4 References for Chapter 5

1. Hutchinson, R.G. and J.W. Hutchinson, *Lifetime Assessment for Thermal Barrier Coatings: Tests for Measuring Mixed Mode Delamination Toughness.* Journal of the American Ceramic Society, 2011. **94**: p. s85-s95.
2. Institute, N.D., *High-temperature high-strength nickel base alloys*. 1995.
3. Eberl, C.G., D.S.; Wang, X.; He, M.Y.; Evans, A.G.; Hemker, K.J., *A method for in situ measurement of the elastic behavior of a columnar thermal barrier coating.* Acta Materialia, 2011. **59**: p. 3612-3620.
4. Evans, A.G., et al., *Mechanisms controlling the durability of thermal barrier coatings.* Progress in Materials Science, 2001. **46**(5): p. 505-553.
5. Zhang, B., *Experimental characterization of thermal barrier coatings using micro-scale bending techniques*, in *Department of Mechanical Engineering*. 2015, Johns Hopkins University: Baltimore, MD.
6. Materials, H.A. *Araldite 2011 Technical Data Sheet*. 2007.
7. Evans, A.G.R., M.; Dalgleish, B.J.; Charalambides, P.G., *The fracture energy of bimaterial interfaces.* Materials Science and Engineering, 1989. **126**.
8. Charalambides, P.G., et al., *A Test Specimen for Determining the Fracture Resistance of Bimaterial Interfaces.* Journal of Applied Mechanics, 1989. **56**(1): p. 77-82.
9. Théry, P.-Y., et al., *Spallation of two thermal barrier coating systems: experimental study of adhesion and energetic approach to lifetime during cyclic oxidation.* Journal of Materials Science, 2008. **44**(7): p. 1726-1733.
10. Hutchinson, J.W. and Z. Suo, *Mixed Mode Cracking in Layered Materials*, in *Advances in Applied Mechanics*, W.H. John and Y.W. Theodore, Editors. 1991, Elsevier. p. 63-191.
11. Hofinger, I., et al., *Modified four-point bending specimen for determining the interface fracture energy for thin, brittle layers.* International Journal of Fracture. **92**(3): p. 213-220.
12. Parks, D.M., *The Virtual Crack Extension Method for Nonlinear Material Behavior.* Computer Methods in Applied Mechanics and Engineering, 1977. **12**: p. 353-364.
13. Shih, C.F.M., B.; Nakamura, T., *Energy Release Rate along a Three-Dimensional Crack Front in a Thermall Stressed Body.* International Journal of Fracture, 1986. **30**: p. 79-102.
14. Rybicki, E.G.K., M.F., *A finite element calculation of stress intensity factors by a modified crack closure technique.* Engineering Fracture Mechanics, 1977. **9**: p. 931-938.

15. Rybicki, E.G.S., D.W.; Fox, J., *An energy release rate approach for stale crack growth in the free-edge delamination problem.* Journal of Composite Materials, 1977. **11**: p. 470-487.

16. Raju, I.S., *Calculation of strain-energy release rates with higher order and singular finite elements.* Engineering Fracture Mechanics, 1987. **28**: p. 251-274.

17. Buchholz, F.G.G., H.; Dreyer, K.H.; Krome, H. *2D-and 3D-applications of the improved and generalized modified crack closure integral method*. in *Computational Mechanics*. 1988. New York: Springer Verlag.

18. Miravete, A.J., M.A., *Application of the finite element method to prediction of onset of delamination growth.* Applied Mechanics Review, 2002. **55**(2): p. 89-105.

19. Ingraffea, A.W., P., *FRANC2D: A case study in transfer of software technology*, in *Research Transformed into Practice: Implementation of NSF Research*. 1995, ASCE Press: New York. p. 233-34.

20. Singh, R.C., B.J.; Wawrzynek, P.A.; Ingraffea, A.R., *Universal crack closure intefral for SIF estimation.* Engineering Fracture Mechanics, 1998. **60**(2): p. 133-146.

21. Freed, Y. and L. Banks-Sills, *A new cohesive zone model for mixed mode interface fracture in bimaterials.* Engineering Fracture Mechanics, 2008. **75**(15): p. 4583-4593.

22. Sun, Y. and M. Liu, *Analysis of the crack penetration/deflection at the interfaces in the intelligent coating system utilizing virtual crack closure technique.* Engineering Fracture Mechanics, 2015. **133**: p. 152-162.

23. Harvey, C.M., J.D. Wood, and S. Wang, *Brittle interfacial cracking between two dissimilar elastic layers: Part 1—Analytical development.* Composite Structures, 2015. **134**: p. 1076-1086.

24. Harvey, C.M., J.D. Wood, and S. Wang, *Brittle interfacial cracking between two dissimilar elastic layers: Part 2—Numerical verification.* Composite Structures, 2015. **134**: p. 1087-1094.

25. Krueger, R., *1 - The virtual crack closure technique for modeling interlaminar failure and delamination in advanced composite materials A2 - Camanho, Pedro P*, in *Numerical Modelling of Failure in Advanced Composite Materials*, S.R. Hallett, Editor. 2015, Woodhead Publishing. p. 3-53.

26. Krueger, R., *Virtual crack closure technique: History, approach, and applications.* Applied Mechanics Reviews, 2004. **57**(2): p. 109-143.

27. Thery, P.Y.P., M.; Dupeux, M.; Braccini, M., *Adhesion energy of a YPSZ EB-PVD layer in two thermal barrier coating systems.* Surface & Coating Technology, 2007. **202**: p. 648-652.

CHAPTER 6: EXPERIMENTAL RESULTS

This chapter presents experimental results for both Compression Edge-Delamination tests and Modified 4-Point Bend tests. For the compression Edge-Delamination test, the critical cracking stress will be measured using the DIC shear strain procedure outlined in Section 3.4.2.2. In addition, for this test, TGO thickness and interfacial friction was measured for specimens at various levels of furnace cycle lifetime. These results, along with the critical stresses for crack propagation, will be analyzed using Equation 5-10, such that accurate values of the strain energy release rate are calculated at various levels of thermal cycling lifetime. The suitability of this test method for the TBC material system, with extensions to other material systems is discussed. For the Modified 4-Point bend test, plateau cracking loads and subsequent strain energy release rates will be calculated using the methods outlined in Section 5.3.2 for as-deposited samples. As the two test methods conducted in this study occur at two different mode mixes, the variation of the critical strain energy release rate will be discussed. The calculated values will also be compared to previously reported results. Potential reasons for the increased values of the strain energy release rate over previously measured values and the asymmetry of the toughness curve will be discussed. Microscopy and fractography results related to the fracture surface of samples at various levels of thermal cycling will be presented. Efforts made to measure the pre-testing bond coat/top coat interface roughness using SEM techniques will be discussed. The use of a confocal laser scanning microscope (CLSM) to measure the 2-D post-test fracture surface roughness will be presented. Using the CLSM the relative area fraction of the bond coat, TGO and top coat was also measured and implications on the change of these area fractions as the level of furnace cycle lifetime increases will be discussed.

Preliminary results involving 3D reconstruction of the TGO as well as voids from images taken during serial sectioning is shown. Finally, chemical composition maps from electron microprobe analysis on both the fracture surface and of cross sections at various levels of furnace cycle lifetime will be presented.

6.1 Compression Edge-Delamination Test

A total of 14 tests were successfully conducted on CED samples. The samples were prepared by i) cutting of the substrate from single crystal René N5 provided by GE, ii) subsequent TBC bond coat and top coat application by GE, iii) thermal cycling to various levels of furnace cycle lifetime, iv) attaching of stiffener plates with epoxy, v) etching of the bond coat with an acid bath and vi) DIC speckle pattern application as detailed in Section 3.3. Compression of the samples was done in an MTS servo-hydraulic test machine with a cross-head displacement rate of $\dot{\delta} = 0.2\ \mu m/s$. This displacement rate corresponded to a macroscopic strain rate of $\dot{\varepsilon} = 10^{-5}$ and ensured that the tests were conducted under quasi-static conditions and that displacement control assumptions could be made for the fracture analysis. Images were captured at an image capture rate of 1 per second. This image capture rate yielded approximately between 1000-2000 images for each test and allowed for the total macroscopic strain between each image to correspond to $\varepsilon = 10^{-5}$. This was needed to assure high accuracy when determining the point at which cracking initiated. The critical load for crack propagation was identified using the DIC procedure presented in Section 3.4.2.2. The following figures show the critical cracking load calculation for each test.

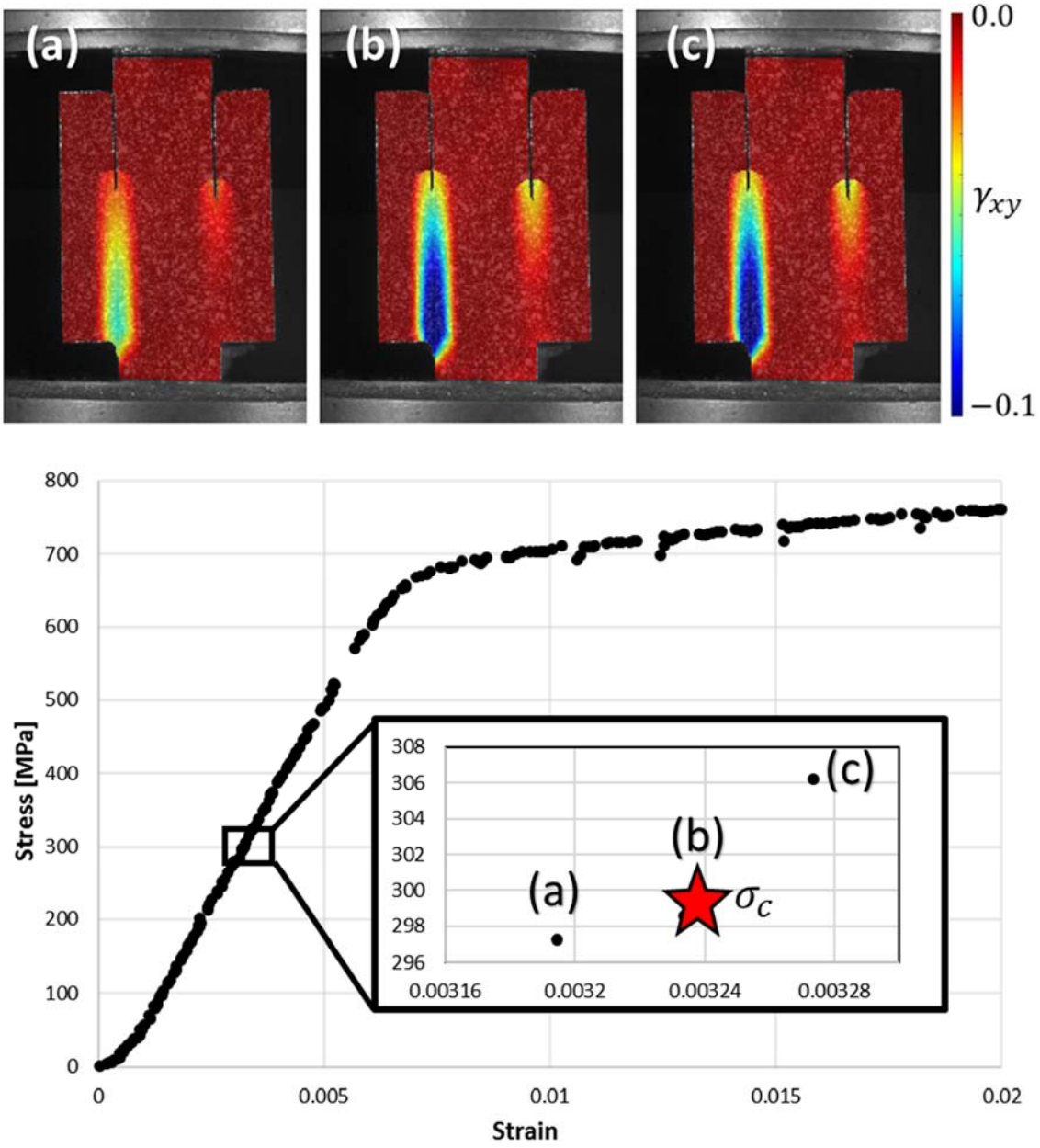

Figure 6-1: Calculation of the critical load for crack propagation in a CED specimen at 0% of furnace cycle lifetime (Sample 1) displaying DIC shear strain maps at (a) just prior to crack initiation, (b) the point at which crack initiation occurs and (c) just after crack initiation occurs. (Note: Crack propagation occurred in the linear elastic portion of the loading curve)

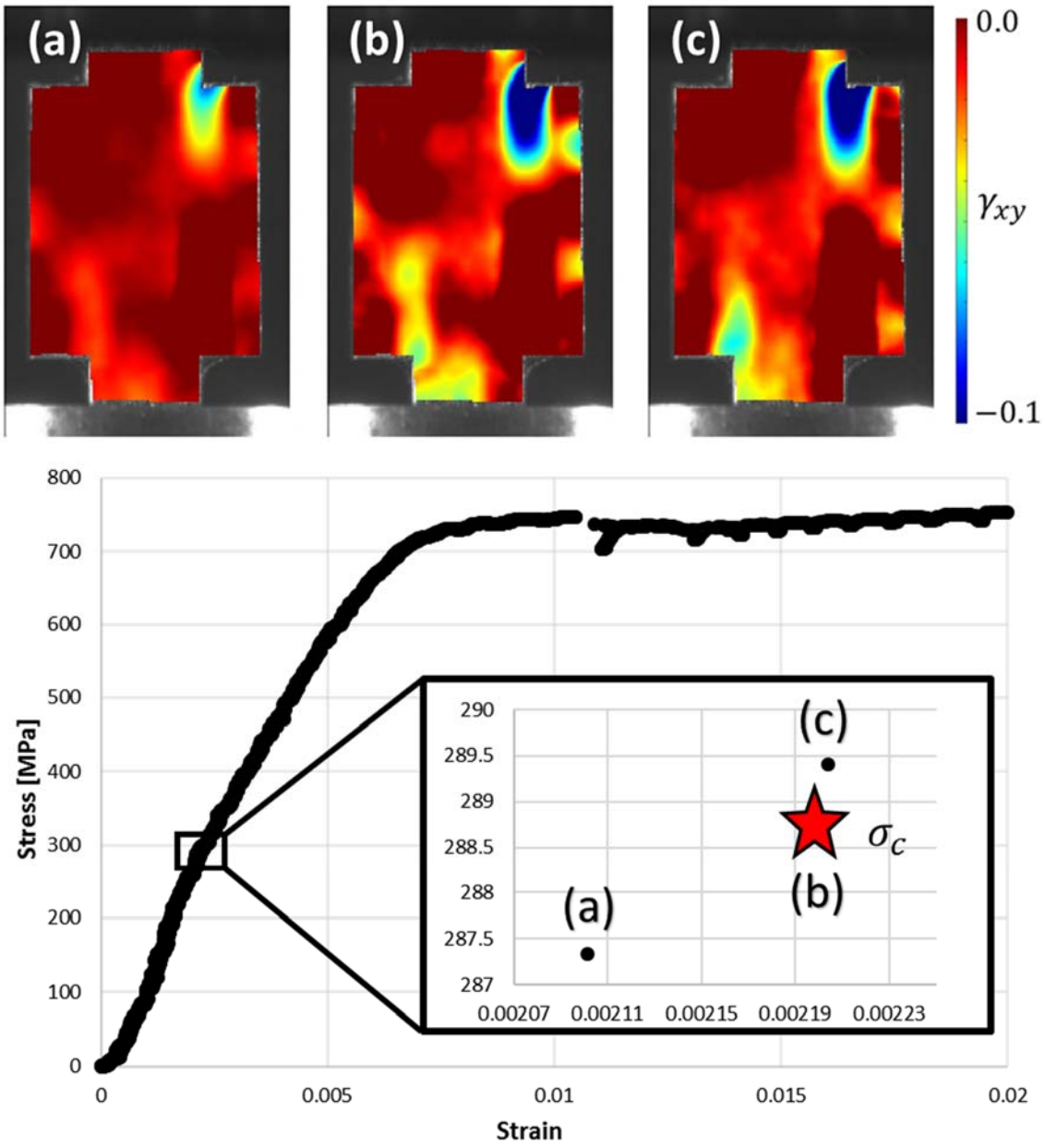

Figure 6-2: Calculation of the critical load for crack propagation in a CED specimen at 0% of furnace cycle lifetime (Sample 2) displaying DIC shear strain maps at (a) just prior to crack initiation, (b) the point at which crack initiation occurs and (c) just after crack initiation occurs. (Note: Crack propagation occurred in the linear elastic portion of the loading curve)

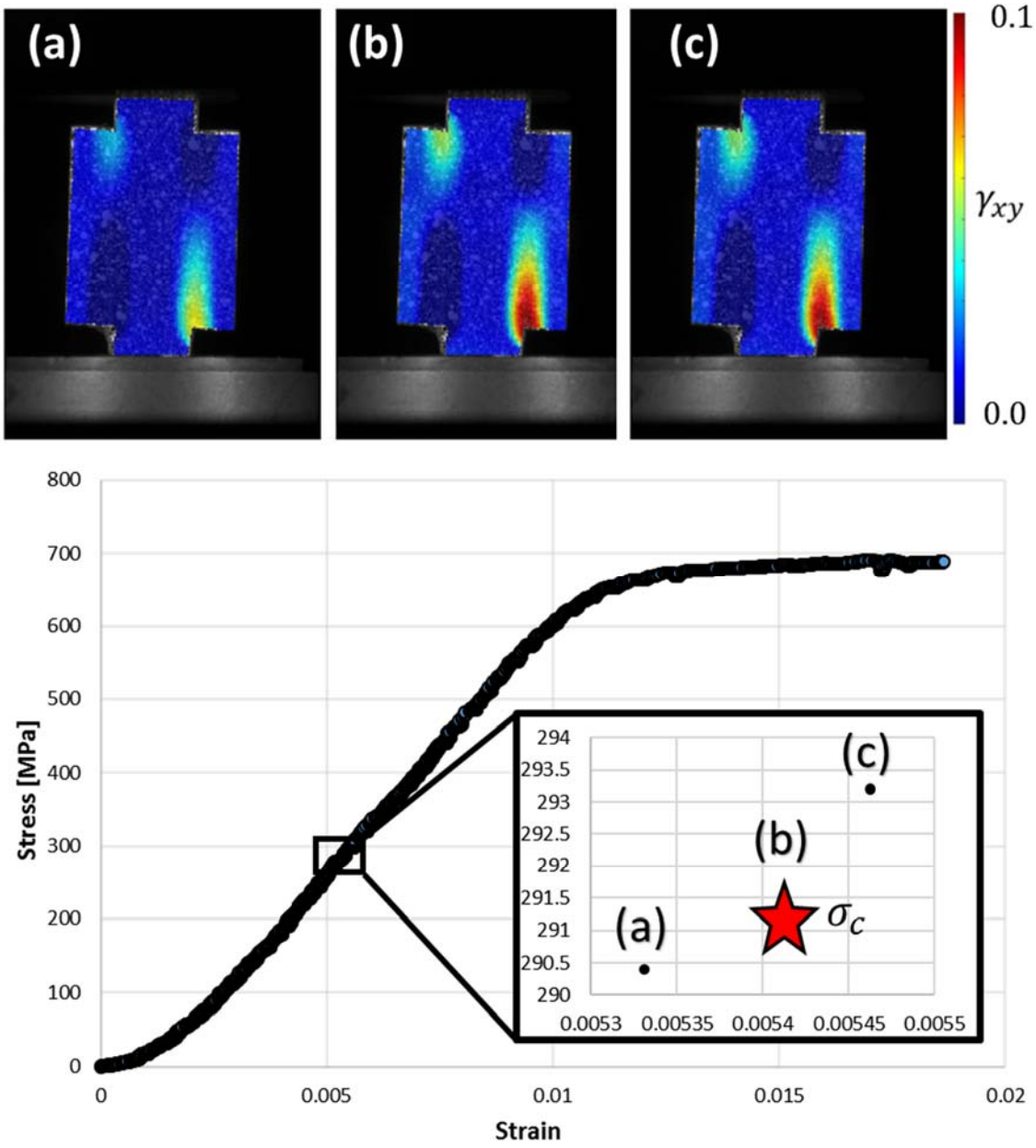

Figure 6-3: Calculation of the critical load for crack propagation in a CED specimen at 0% of furnace cycle lifetime (Sample 3) displaying DIC shear strain maps at (a) just prior to crack initiation, (b) the point at which crack initiation occurs and (c) just after crack initiation occurs. (Note: Crack propagation occurred in the linear elastic portion of the loading curve)

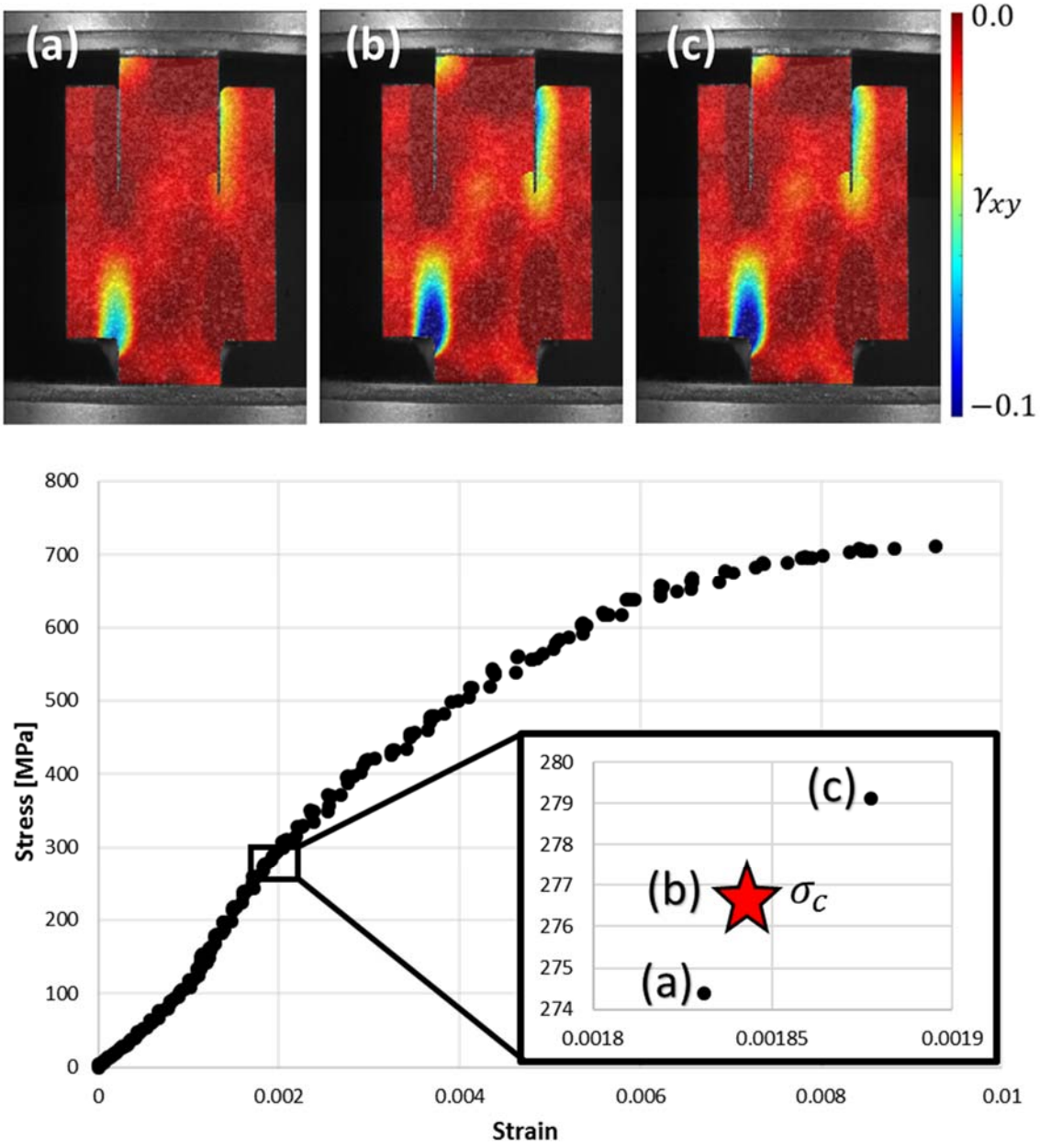

Figure 6-4: Calculation of the critical load for crack propagation in a CED specimen at 0% of furnace cycle lifetime (Sample 4) displaying DIC shear strain maps at (a) just prior to crack initiation, (b) the point at which crack initiation occurs and (c) just after crack initiation occurs. (Note: Crack propagation occurred in the linear elastic portion of the loading curve)

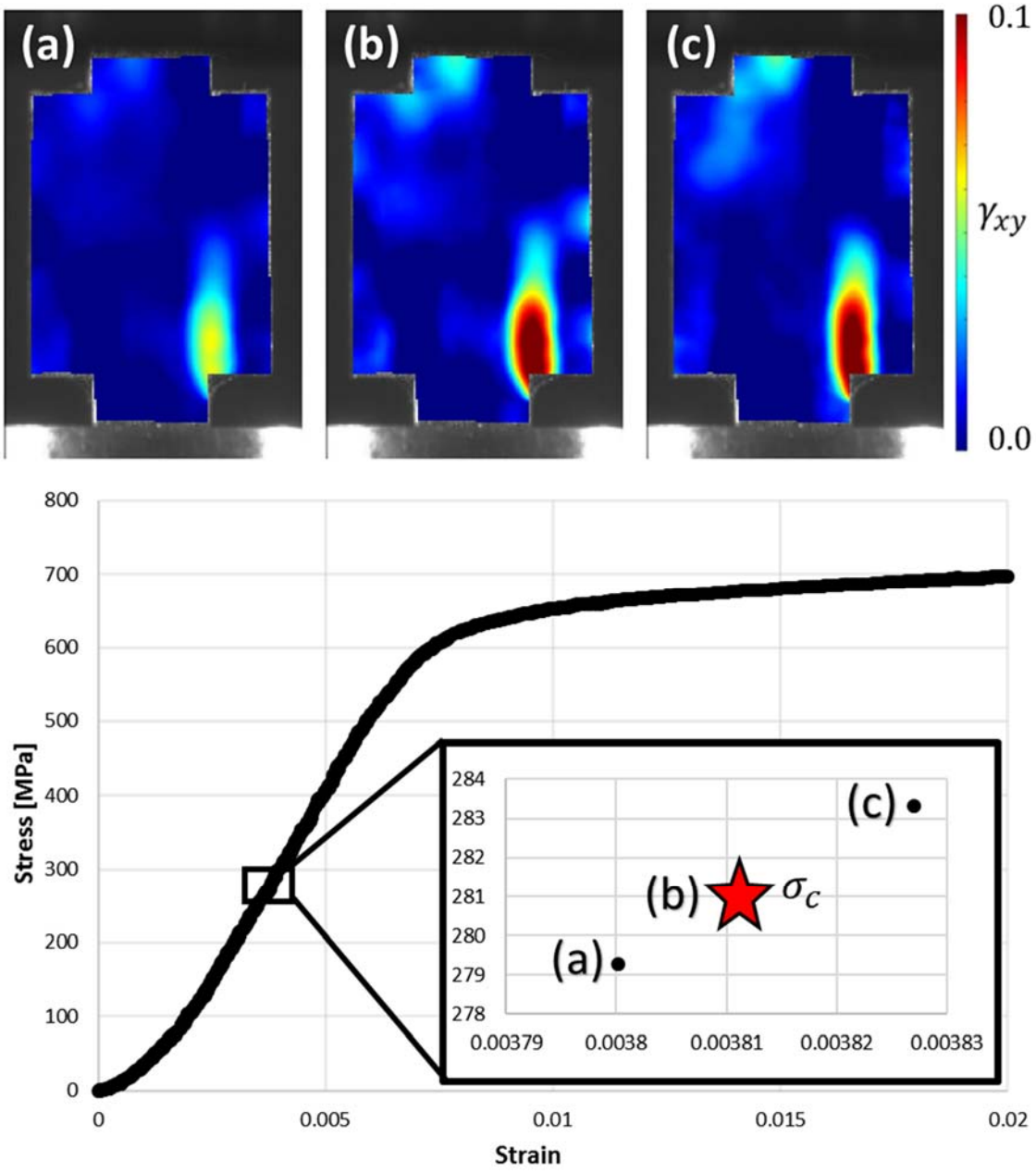

Figure 6-5: Calculation of the critical load for crack propagation in a CED specimen at 0% of furnace cycle lifetime (Sample 5) displaying DIC shear strain maps at (a) just prior to crack initiation, (b) the point at which crack initiation occurs and (c) just after crack initiation occurs. (Note: Crack propagation occurred in the linear elastic portion of the loading curve)

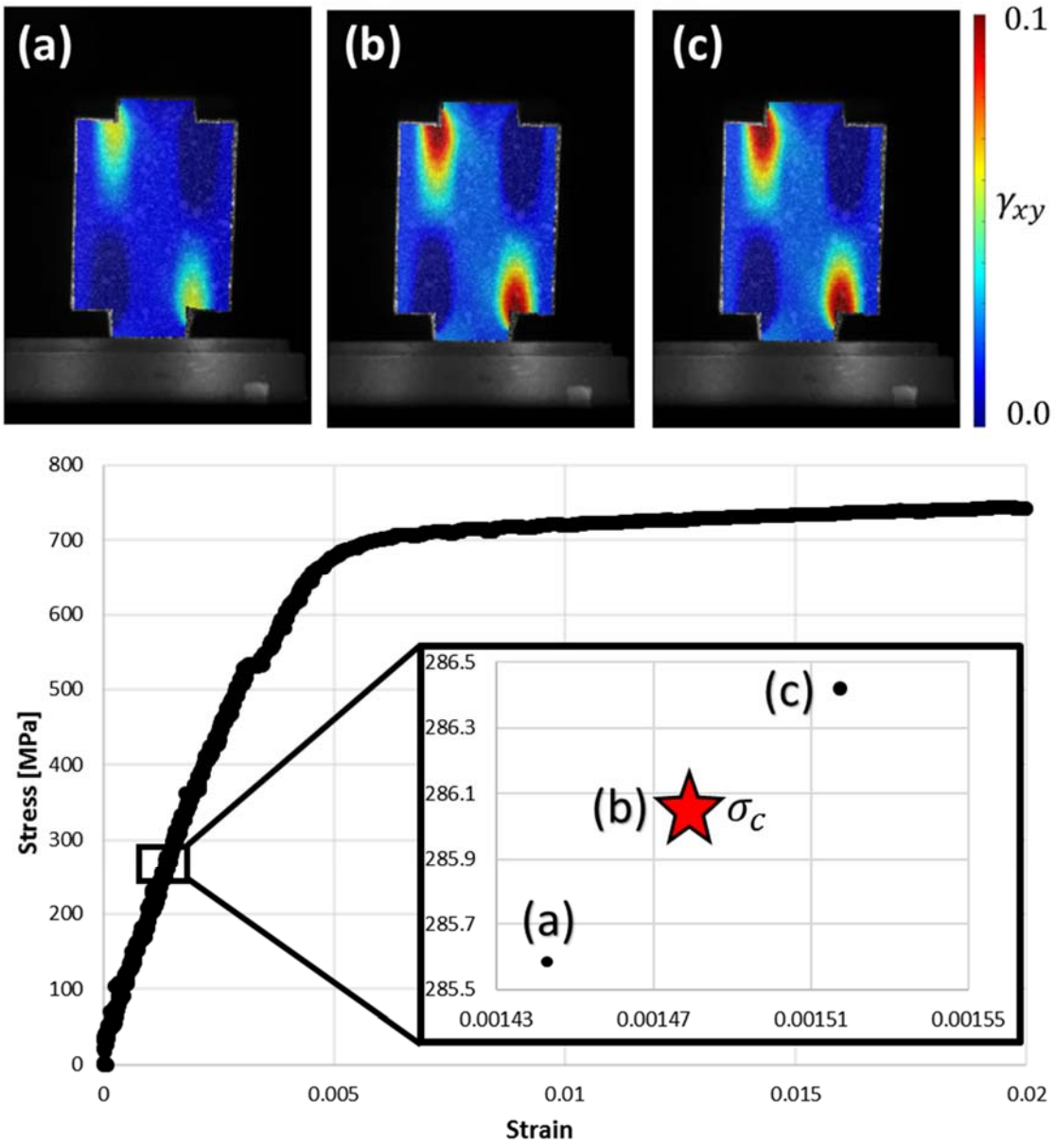

Figure 6-6: Calculation of the critical load for crack propagation in a CED specimen at 28% of furnace cycle lifetime (Sample 1) displaying DIC shear strain maps at (a) just prior to crack initiation, (b) the point at which crack initiation occurs and (c) just after crack initiation occurs. (Note: Crack propagation occurred in the linear elastic portion of the loading curve)

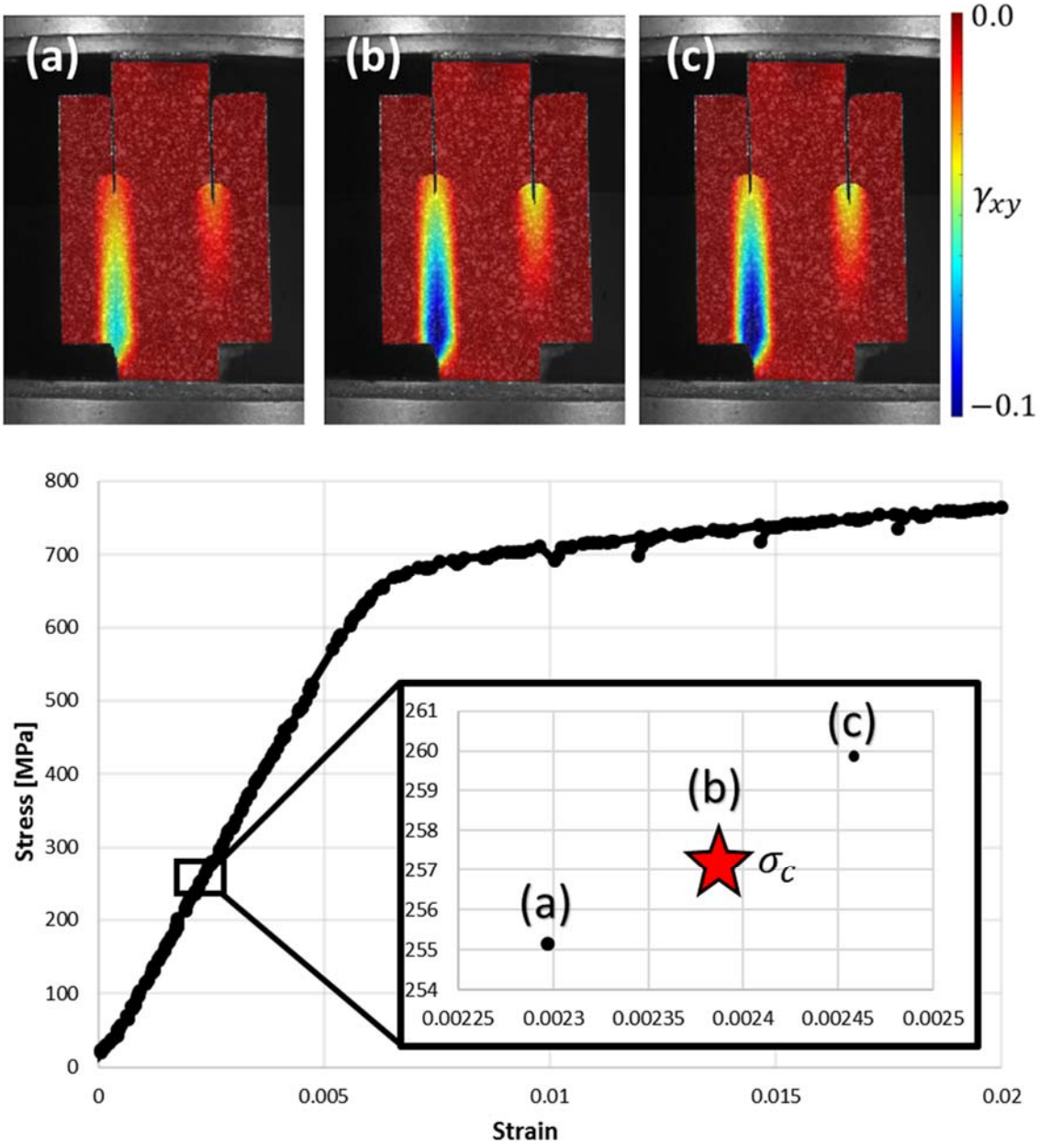

Figure 6-7: Calculation of the critical load for crack propagation in a CED specimen at 28% of furnace cycle lifetime (Sample 2) displaying DIC shear strain maps at (a) just prior to crack initiation, (b) the point at which crack initiation occurs and (c) just after crack initiation occurs. (Note: Crack propagation occurred in the linear elastic portion of the loading curve)

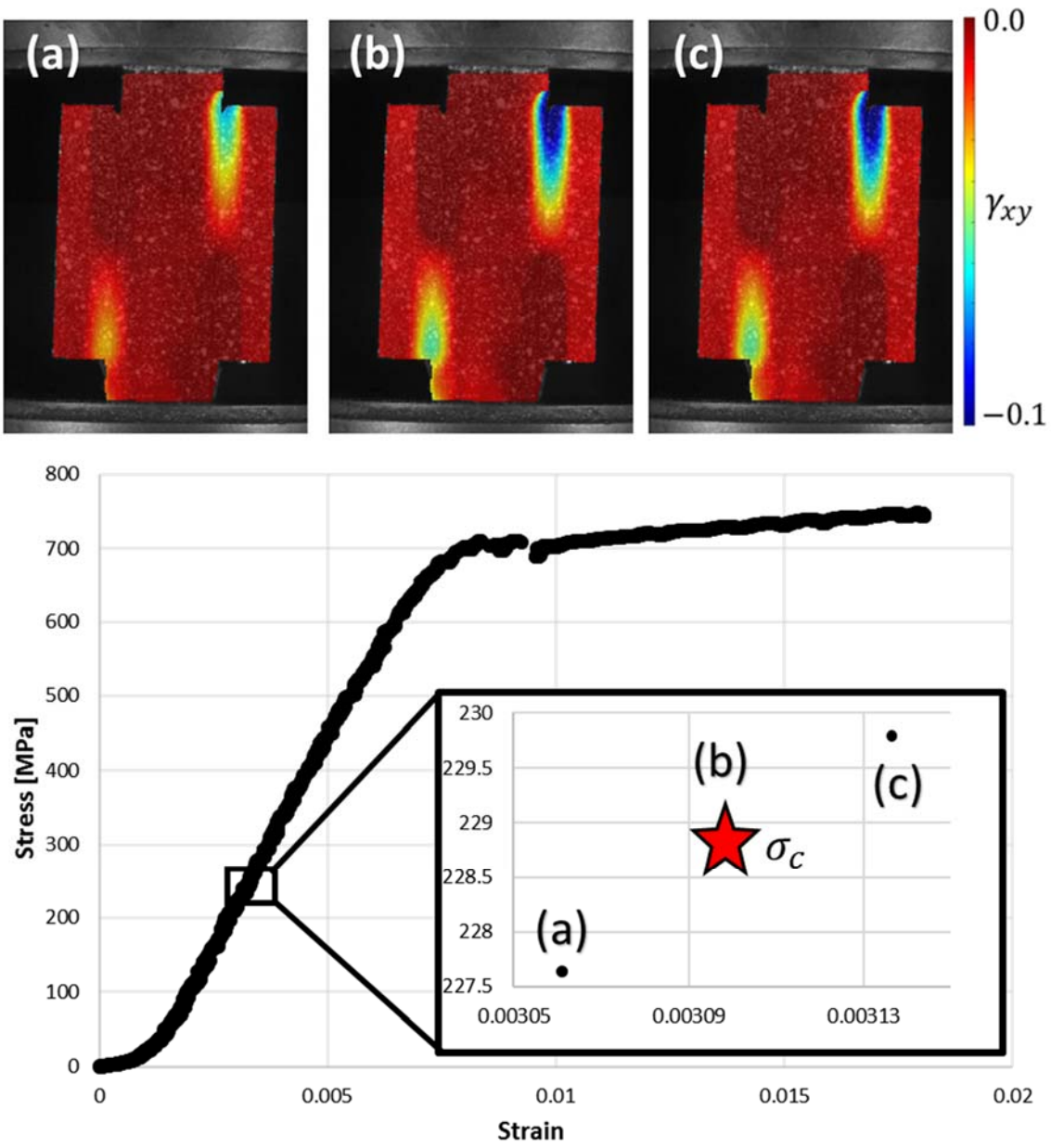

Figure 6-8: Calculation of the critical load for crack propagation in a CED specimen at 50% of furnace cycle lifetime (Sample 1) displaying DIC shear strain maps at (a) just prior to crack initiation, (b) the point at which crack initiation occurs and (c) just after crack initiation occurs. (Note: Crack propagation occurred in the linear elastic portion of the loading curve)

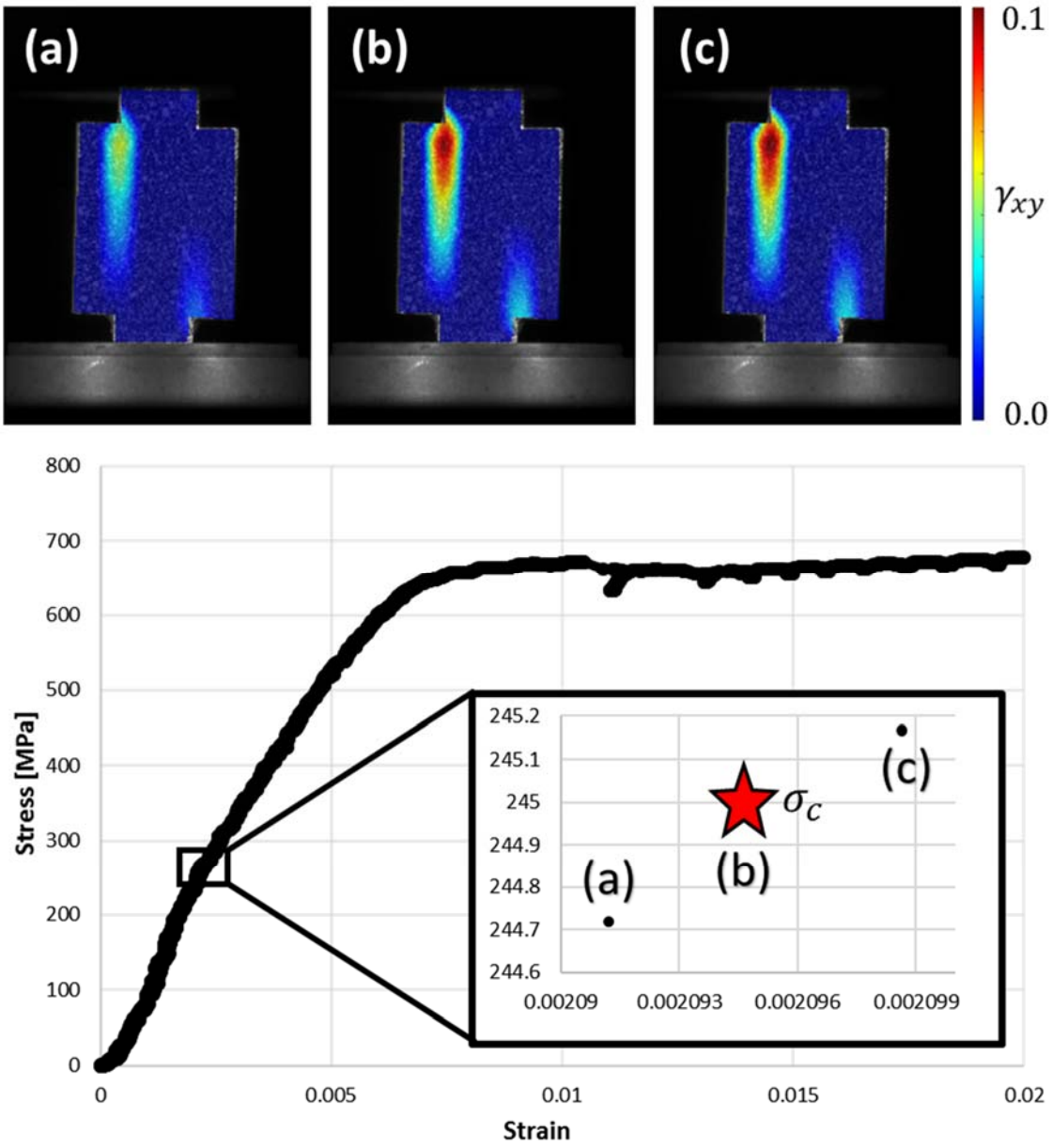

Figure 6-9: Calculation of the critical load for crack propagation in a CED specimen at 50% of furnace cycle lifetime (Sample 2) displaying DIC shear strain maps at (a) just prior to crack initiation, (b) the point at which crack initiation occurs and (c) just after crack initiation occurs. (Note: Crack propagation occurred in the linear elastic portion of the loading curve)

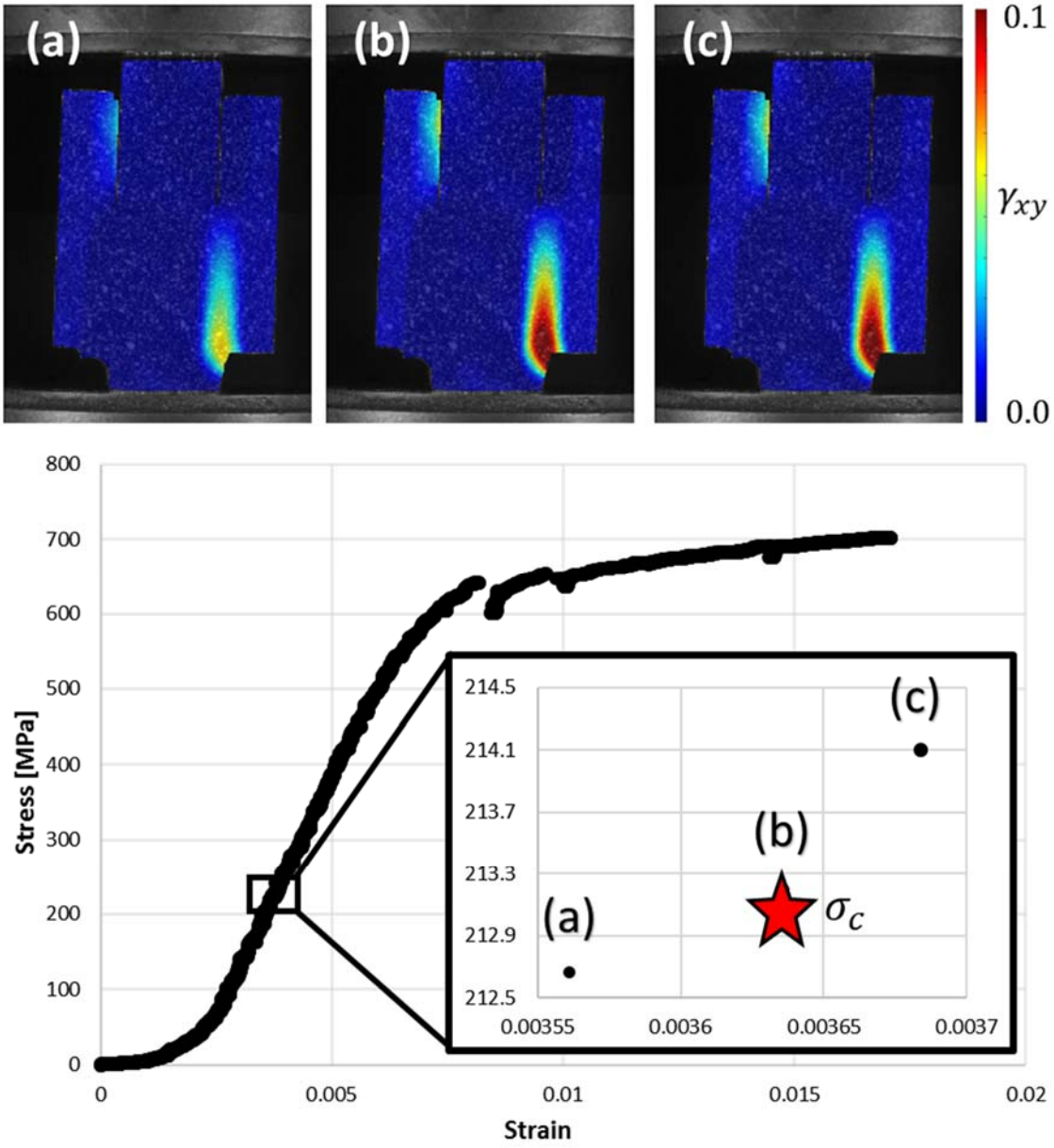

Figure 6-10: Calculation of the critical load for crack propagation in a CED specimen at 56% of furnace cycle lifetime (Sample 1) displaying DIC shear strain maps at (a) just prior to crack initiation, (b) the point at which crack initiation occurs and (c) just after crack initiation occurs. (Note: Crack propagation occurred in the linear elastic portion of the loading curve)

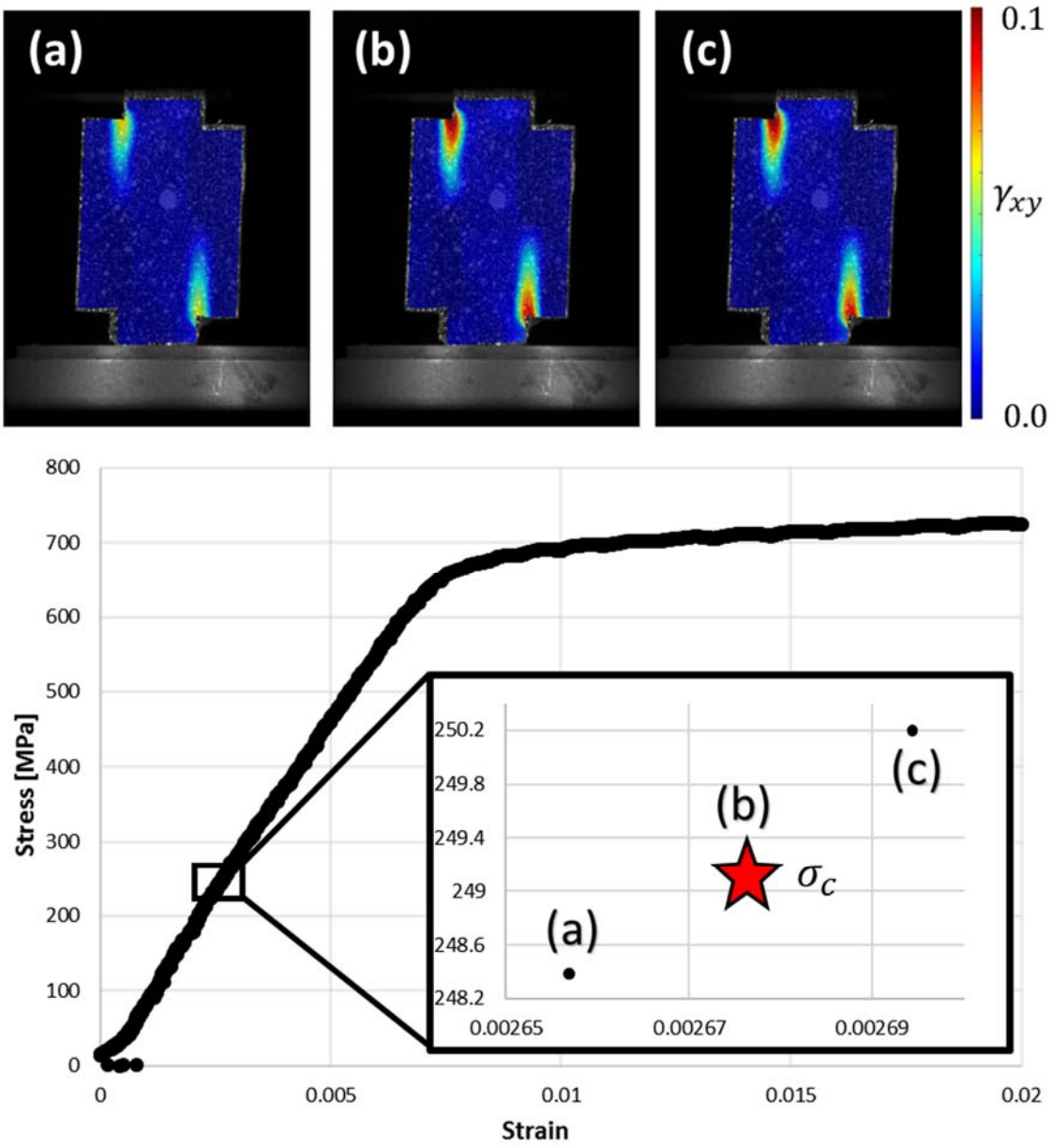

Figure 6-11: Calculation of the critical load for crack propagation in a CED specimen at 56% of furnace cycle lifetime (Sample 2) displaying DIC shear strain maps at (a) just prior to crack initiation, (b) the point at which crack initiation occurs and (c) just after crack initiation occurs. (Note: Crack propagation occurred in the linear elastic portion of the loading curve)

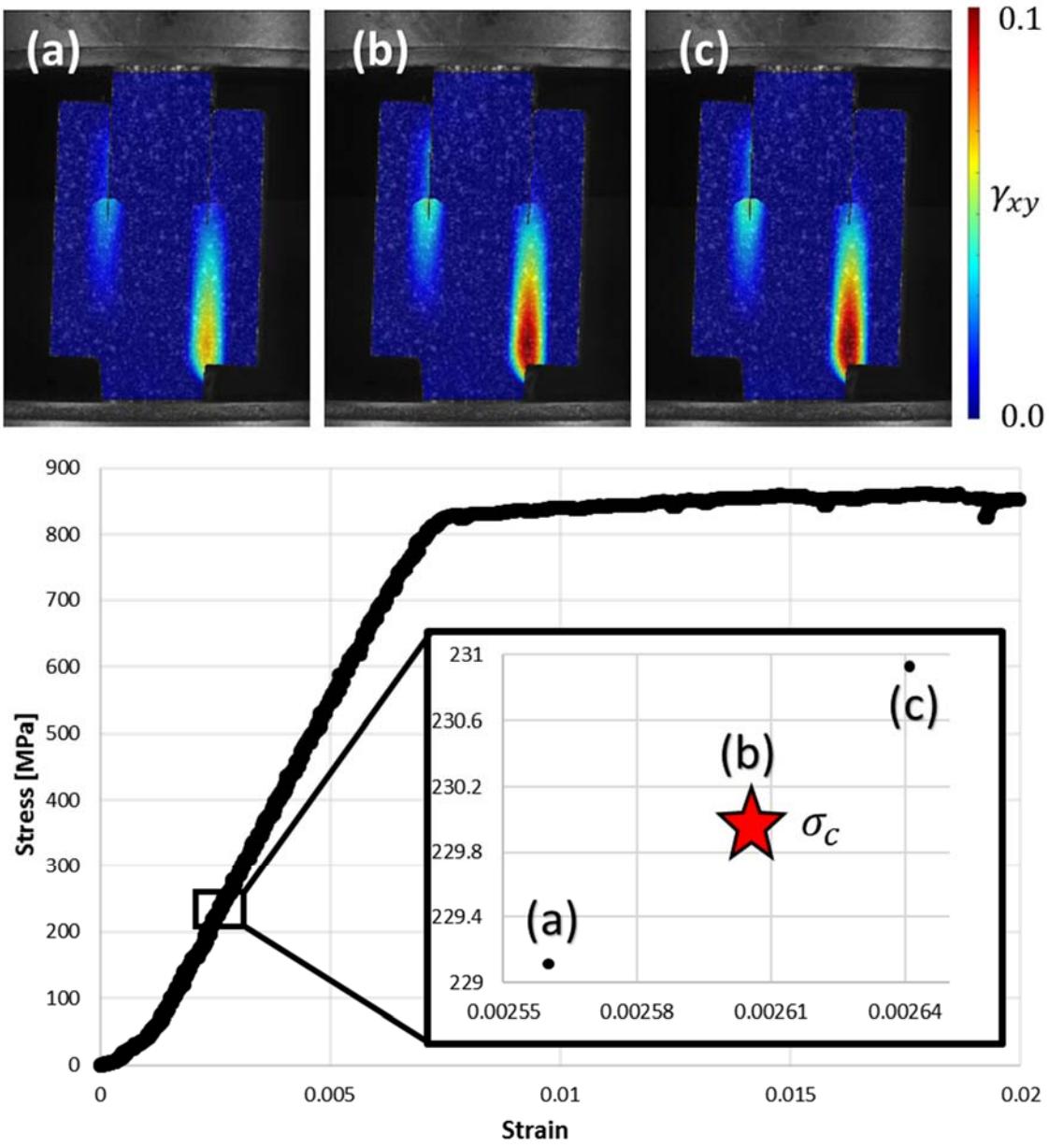

Figure 6-12: Calculation of the critical load for crack propagation in a CED specimen at 80% of furnace cycle lifetime (Sample 1) displaying DIC shear strain maps at (a) just prior to crack initiation, (b) the point at which crack initiation occurs and (c) just after crack initiation occurs. (Note: Crack propagation occurred in the linear elastic portion of the loading curve)

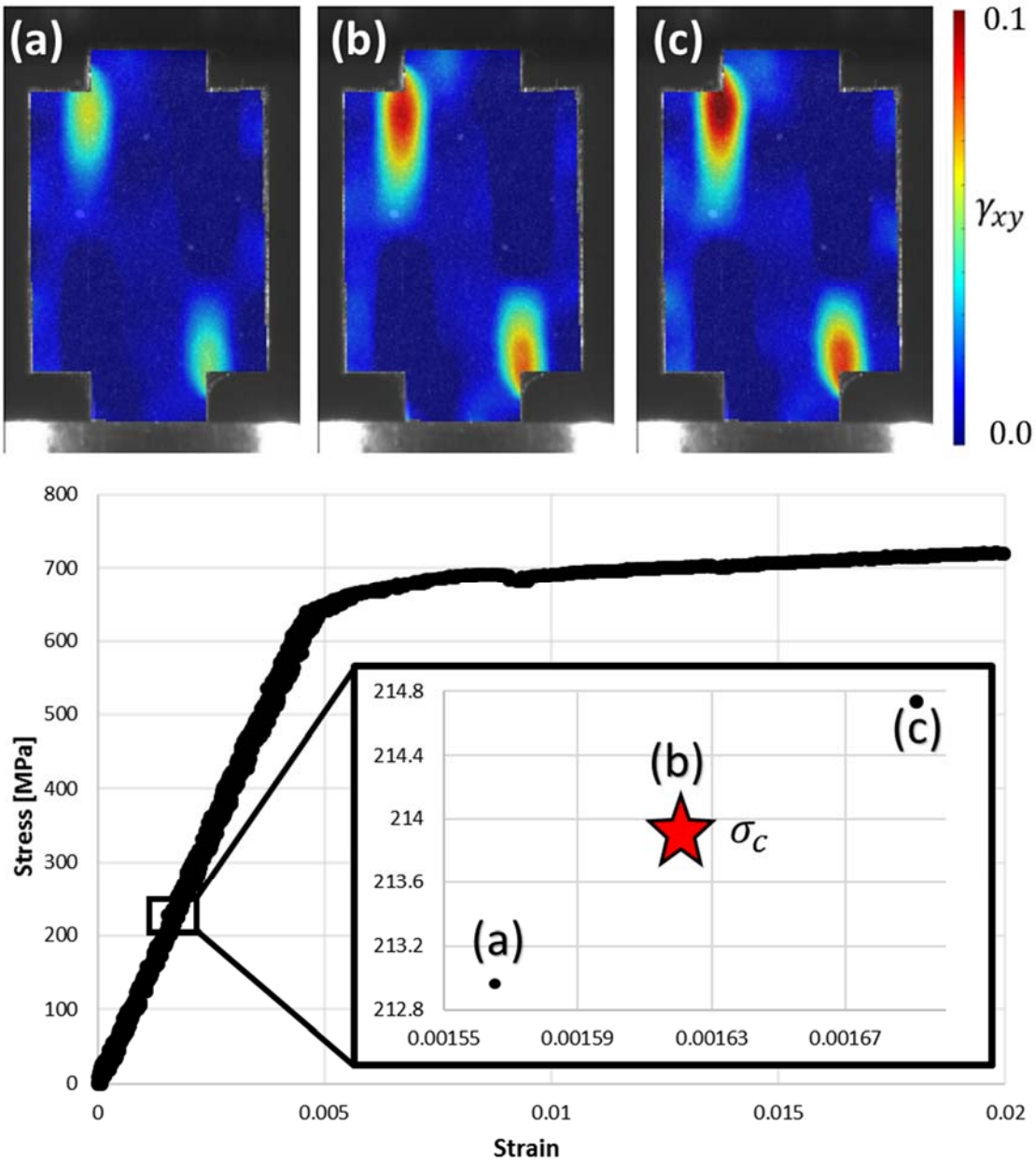

Figure 6-13: Calculation of the critical load for crack propagation in a CED specimen at 100% of furnace cycle lifetime (Sample 1) displaying DIC shear strain maps at (a) just prior to crack initiation, (b) the point at which crack initiation occurs and (c) just after crack initiation occurs. (Note: Crack propagation occurred in the linear elastic portion of the loading curve)

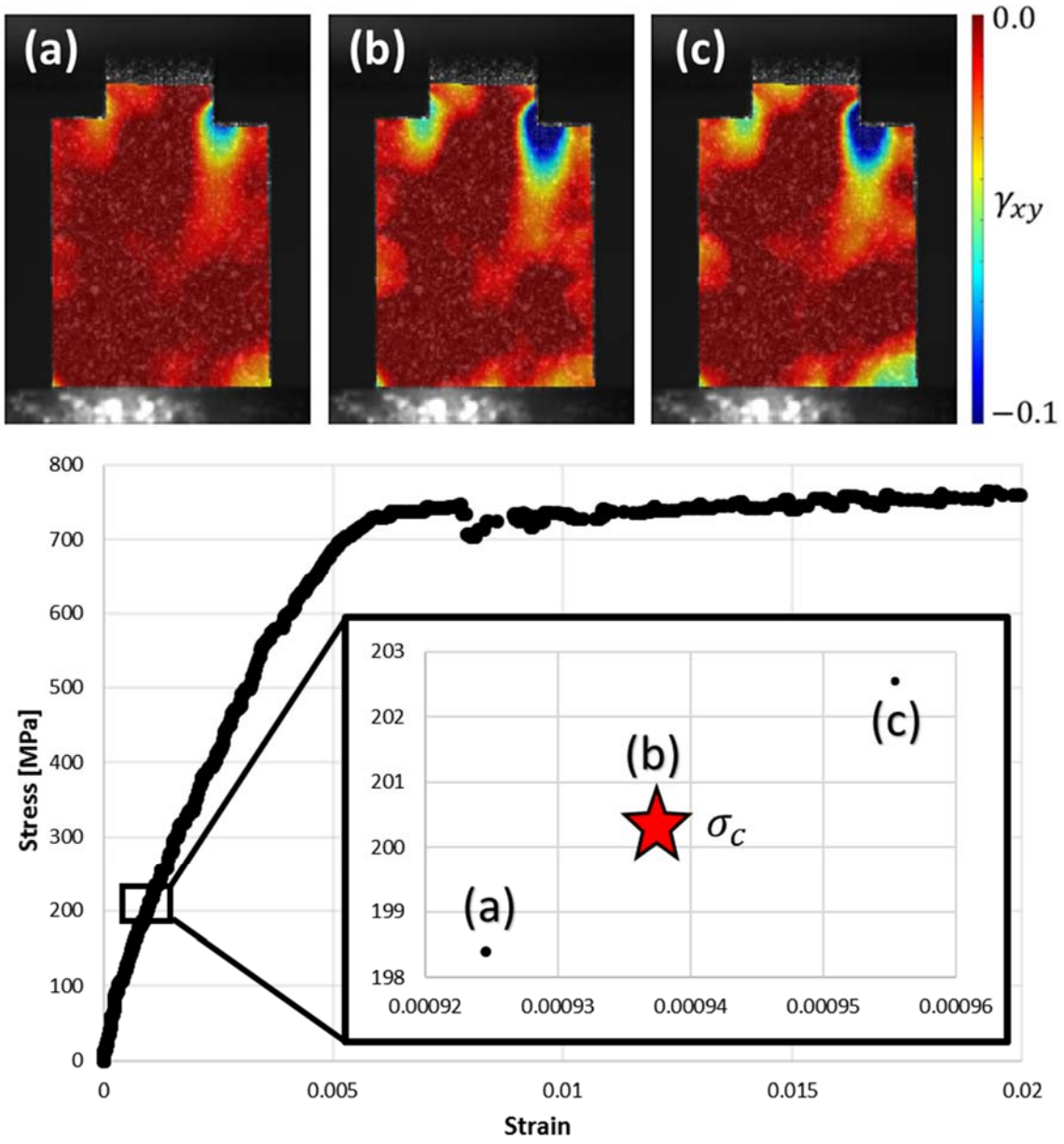

Figure 6-14: Calculation of the critical load for crack propagation in a CED specimen at 100% of furnace cycle lifetime (Sample 2) displaying DIC shear strain maps at (a) just prior to crack initiation, (b) the point at which crack initiation occurs and (c) just after crack initiation occurs. (Note: Crack propagation occurred in the linear elastic portion of the loading curve)

A summary of the critical cracking loads calculated above vs. the percentage of furnace cycle lifetime is shown in Figure 6-15.

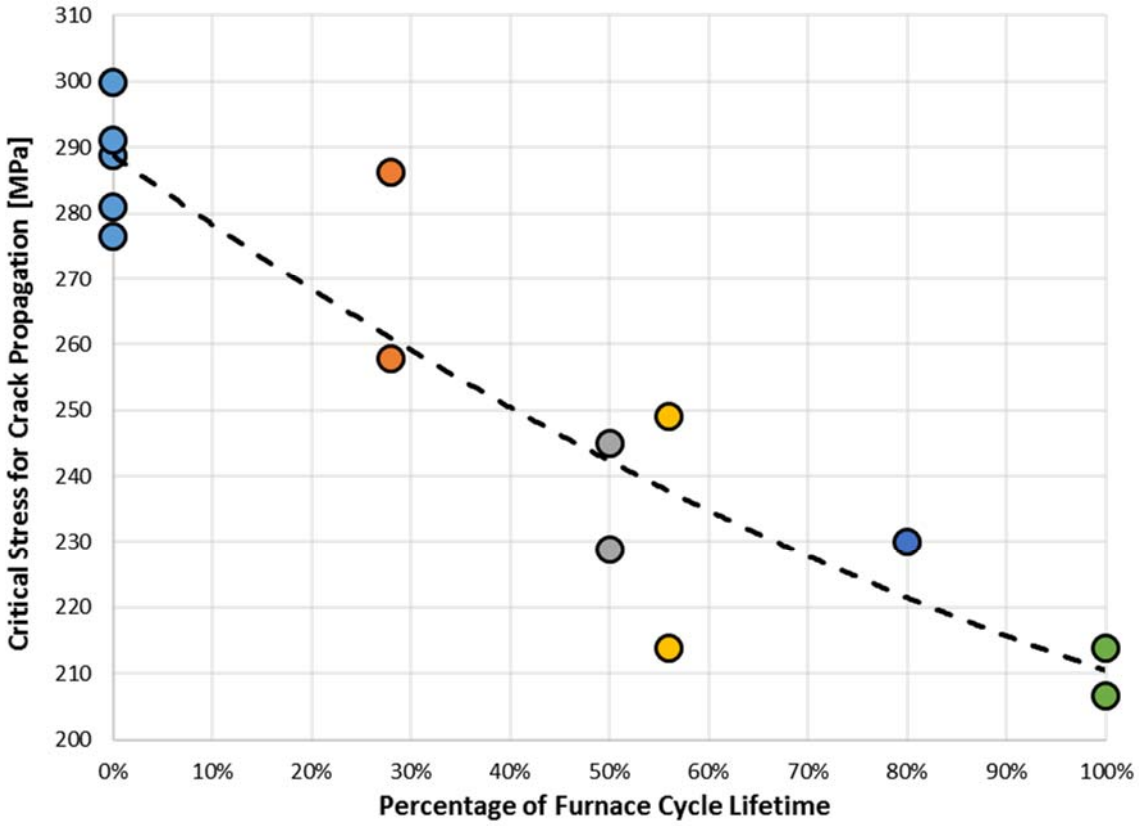

Figure 6-15: Critical stress for crack propagation vs. percentage of furnace cycle lifetime for Compression Edge-Delamination specimens

In all of the samples where stable crack growth was observed, one of the interfaces would always fail before the other one did. The first interface failure always occurred prior to plasticity in the substrate and the second interface failure always occurred after plasticity in the substrate occurred. In the samples when two interfaces began to crack prior to substrate plasticity, one of the interface cracks would arrest while the other one grew. In addition, the cracks did not always initiate at the acid-etched area, and sometime initiated at the opposite end of the interface.

In the as-deposited state, the samples required roughly 285 MPa of applied stress for crack initiation to begin and at 100% of furnace cycle lifetime they required roughly 210 MPa. As crack growth always occurred through one interface cracking before plastic deformation of the substrate, half of the total strain energy was released from the stiffeners and therefore the total energy release rate is half of what the modified-analytical equation (Equation 5-10) predicts. In order to calculate the interfacial toughness, it was necessity to characterize how the interfacial friction coefficient and the TGO thickness vary as a function of furnace cycle lifetime as they will directly affect the computer toughness.

6.1.1 Interfacial Friction Testing

Tests were conducted to characterize the interfacial friction coefficient between the post-test fracture surfaces of the CED samples. The substrate was attached to the load frame as shown in Figure 6-16. The delaminated stiffener plates composed of the stiffeners, epoxy bonding layer and the top coat side of the fracture surface were carefully cut into a total of 8 pieces using a diamond wire saw. Care was taken to not introduce damage to the fracture surface during this cutting procedure. The top coat side pieces were then placed on an area of the substrate where no friction test had been conducted previously, a hanging mass attached on top of the stiffener, and the push plate was moved so that it was almost touching the stiffener piece. The push plate was then moved towards the stiffener at a displacement rate of $\dot{\delta} = 1\ \mu m/s$. A schematic showing the orientation of delaminated stiffener on substrate, application of the load from hanging mass and direction of displacement from push plate is shown in Figure 6-17.

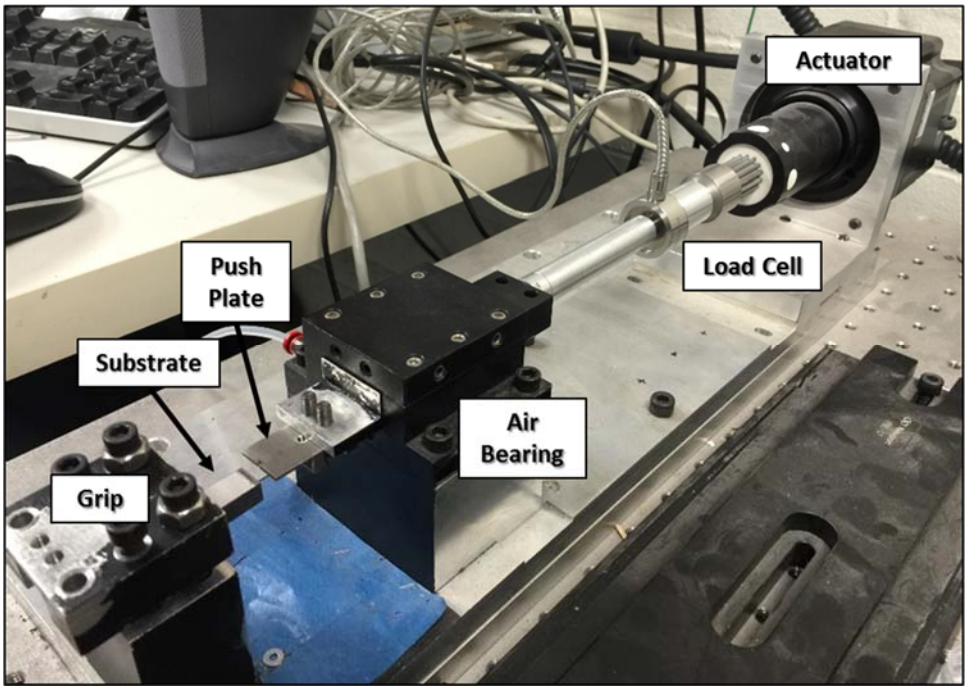

Figure 6-16: Schematic overview of interfacial friction testing setup

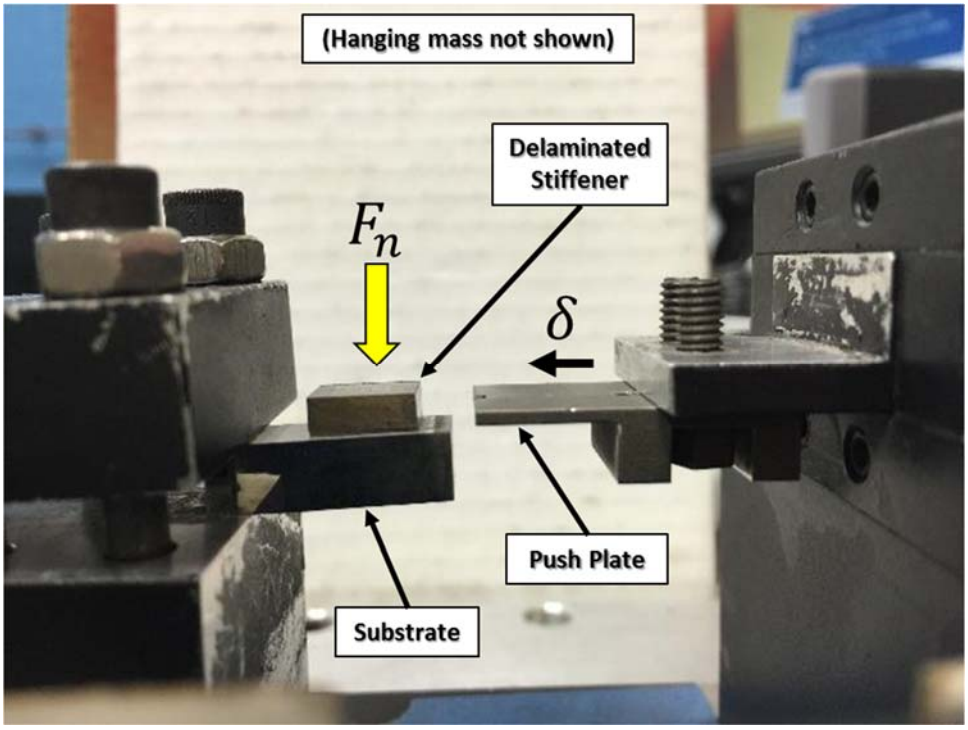

Figure 6-17: Schematic overview of orientation of delaminated stiffener on substrate, application of load from hanging mass and direction of displacement from push plate.

In Figure 6-17 the hanging mass is not shown as it would obstruct the view of the substrate and delaminated stiffener. A representative curve of the mass versus time results can be seen in Figure 6-18. Before the test was run the load cell was tared to zero-load. For the first 5 seconds the push plate was moving towards the stiffener. For the next 30 seconds the push plate began to make contact with the stiffener and settles into alignment. After this period the stiffener began to slide across the substrate with an initial peak in the applied load corresponding to the static friction and the subsequent sliding load corresponding to the dynamic friction. For the purpose of this study only the static friction coefficient is considered as the tests are conducted in a quasi-static.

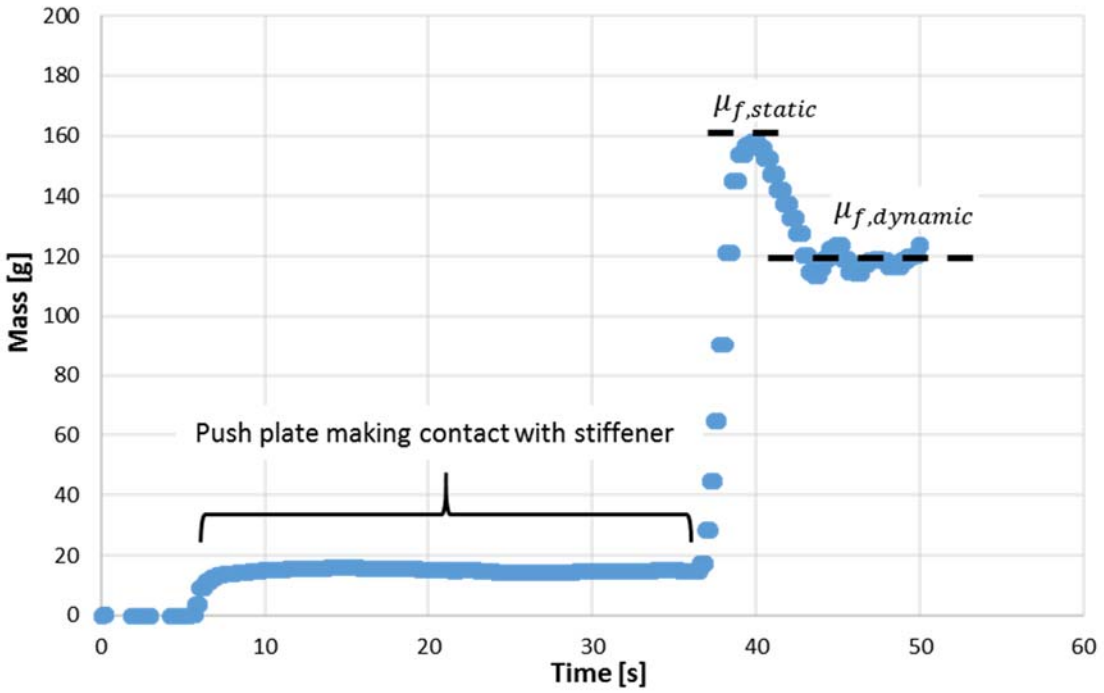

Figure 6-18: Representative plot of force [g] vs. time [s] for interfacial friction tests.

A total of 24 friction tests were conducted with 6 tests each at 0%, 28%, 56% and 100% of furnace cycle lifetime. Prior to testing the weight of each of the stiffener plates was measured along with the hanging mass so the applied normal force could be calculated.

During the test, the peak load was recorded as the load when the push plate is making contact with the stiffener to get the net applied load to the stiffener. The interfacial coefficient of static friction could then be calculated as:

Equation 6-1

$$\mu_{f,static} = \frac{m_{peak} - m_{contact}}{W_{stiffener} + W_{mass}}$$

In Equation 6-1, m_{peak} is the maximum lateral load experienced during the test, $m_{contact}$ is the load experienced when the push plate makes contact with the stiffener but prior to movement of the stiffener and $W_{stiffener}$ and W_{mass} are the weight of the stiffener and hanging mass respectively. A table of these values can be seen below:

Table 6-1: Raw data from interfacial friction testing of delaminated CED samples

		0% LT	28% LT	56% LT	100% LT
Mass [g]	Sample	1.0610	1.6972	1.7687	1.5477
	Hanging Mass	288.6000	288.6000	288.6000	288.6000
	Total	289.6610	290.2972	290.3687	290.1477
Peak-Settling Load [g]	Test 1	187.0029	107.7960	133.5461	198.1665
	Test 2	167.8027	144.0692	95.9093	190.2649
	Test 3	125.2563	129.8542	171.4748	129.6707
	Test 4	161.7246	139.5580	129.2867	135.3090
	Test 5	135.0194	132.7689	144.5236	125.3412
	Test 6	173.5350	175.7172	131.7251	182.6499
Friction Coefficient, μ_f	Test 1	0.6456	0.3713	0.4599	0.6830
	Test 2	0.5793	0.4963	0.3303	0.6558
	Test 3	0.4324	0.4473	0.5905	0.4469
	Test 4	0.5583	0.4807	0.4453	0.4663
	Test 5	0.4661	0.4574	0.4977	0.4320
	Test 6	0.5991	0.6053	0.4536	0.6295

When the friction coefficient for each test is plotted against the percentage of furnace cycle lifetime, shown in Figure 6-19, it is apparent that there is no general trend for the interfacial

friction coefficient. An average of the entire dataset was therefore taken to be $\mu_f = 0.51$ with a standard deviation of 0.1.

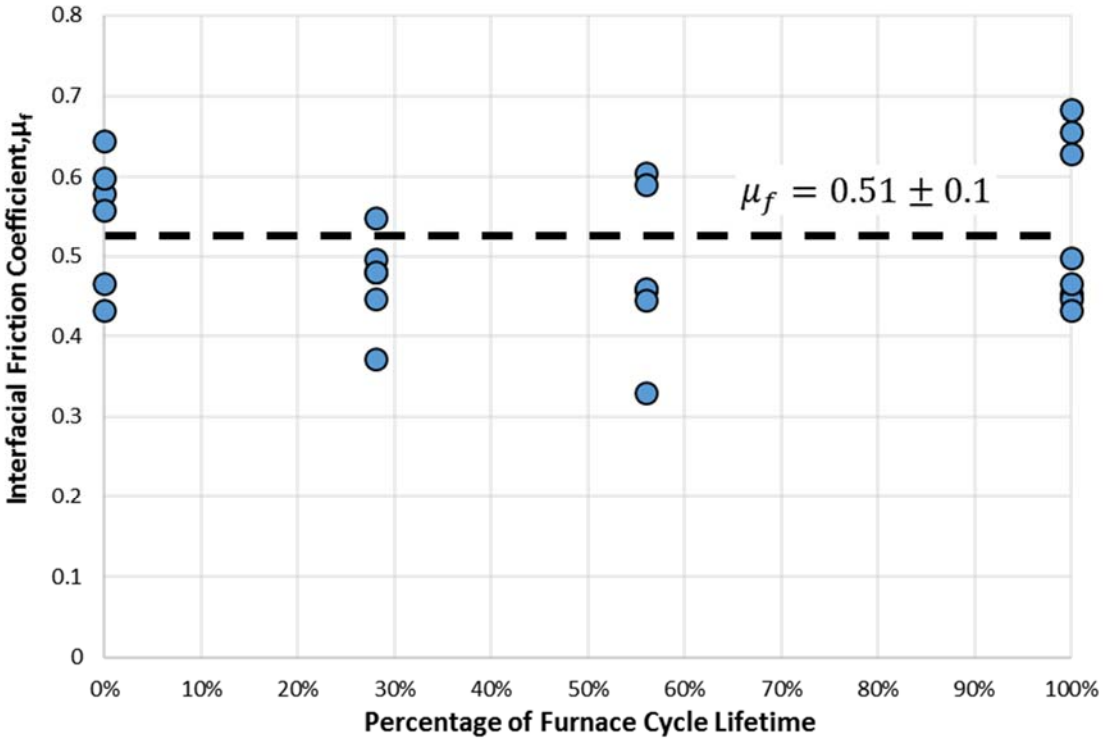

Figure 6-19: Interfacial friction coefficient vs. percentage of furnace cycle lifetime for post-morten CED specimens.

6.1.2 TGO Measurements

Measurements were taken to characterize the growth behavior of the TGO layer during thermal cycling. CED samples that were thermally cycled to 0, 120, 240 and 360 1-hour thermal cycles and were cross-sectioned using a diamond wire saw and polished with SiC sandpaper to 1200 (P-4000) grit with subsequent polishing with a colloidal alumina suspension with $0.05\ \mu m$ diameter particles. The polished samples were then cleaned in an isopropyl alcohol sonic bath and dried in a vacuum desiccating chamber. Prior to imaging, the samples were sputtered with carbon to minimize electrostatic charging of the ceramic surfaces. TGO thickness measurements were made at 20 different locations on each image

using ImageJ. The TGO exhibited parabolic growth as described in previous publications for the TBC material system [1, 2] with the modification to account for an initial oxide layer thickness:

Equation 6-2

$$h_{TGO} = \sqrt{2k_p N t_{HOT}} + h_{TGO,0}$$

In Equation 6-2, k_p is the parabolic rate constant, N are the number of thermal cycles, t_{HOT} is the total hot time during each thermal cycle and $h_{TGO,0}$ is the initial TGO thickness. The samples were subjected to 1-hour thermal cycles where the total hot time was 45 minutes and the cool down time was 15 minutes, which corresponds to a $t_{HOT} = 0.75\ hr$. The peak temperature that the samples experienced was 1150°C. The measured TGO thickness and parabolic fit can be seen in Figure 6-20. The initial TGO thickness was taken as the average TGO thickness in the as-deposited state and was $h_{TGO,0} = 0.21\ \mu m$. The curve fit was conducted in MATLAB using the *cftool* command and the parabolic rate constant was found to be $k_p = 0.0212\ \mu m^2/hr$. This value of the parabolic rate constant agrees well with published data for the same TBC material system [3, 4].

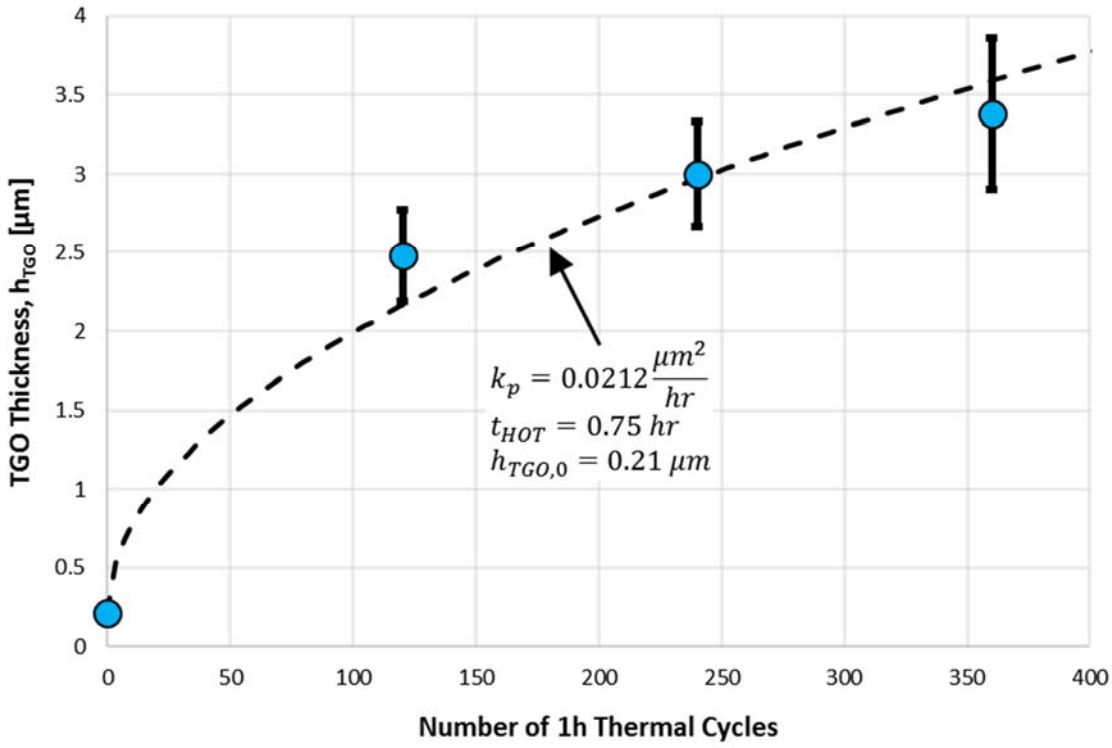

Figure 6-20: TGO thickness vs. number of 1-h thermal cycles at a peak temperature of 1150°C for TBC samples.

6.1.3 Strain Energy Release Rate

With determination of the critical stress for interface cracking, interfacial friction coefficient and the TGO thickness, the interfacial toughness can be calculated using Equation 5-10. The friction coefficient used was taken to be $\mu_f = 0.51$ and the TGO growth law was the same as defined in the previous section. The result of this analysis is shown in Figure 6-21. In the as-deposited state the average interfacial toughness is approximately $537\ J/m^2$ and drops to approximately $252\ J/m^2$, which corresponds to a drop in interfacial toughness of $285\ J/m^2$ over the lifetime of the TBC material system.

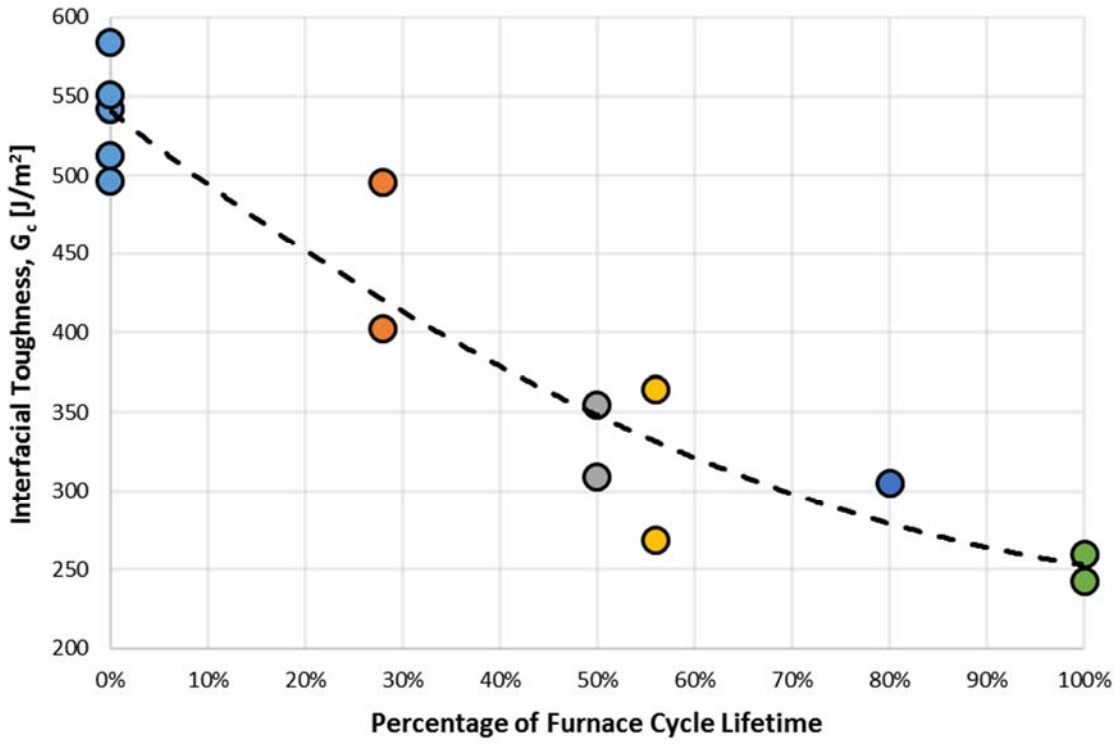

Figure 6-21: Interfacial toughness versus percentage of furnace cycle lifetime taking into account TGO variation with furnace cycle lifetime and interfacial friction coefficient.

The decay of the interfacial toughness follows an exponential law of the form:

Equation 6-3

$$G_c = 542.2e^{-0.0081N_{FC}}$$

where N_{FC} is the relative percentage of furnace cycle lifetime. The behavior of the interfacial toughness vs. the TGO thickness is fairly linear and is shown in Figure 6-22. The equation that best fits the data is shown by:

Equation 6-4

$$G_c = -83.4\, h_{TGO} + 562.1$$

As was shown in Figure 5-13, the importance of properly accounting for the TGO thickness and the interfacial friction can have a significant effect on the calculated interfacial toughness. It should be noted that while these fits are purely empirical, they will be of use

to future FE modelling as they can be discretized into the FE code and used to model lifetime behavior of the TBC system more effectively.

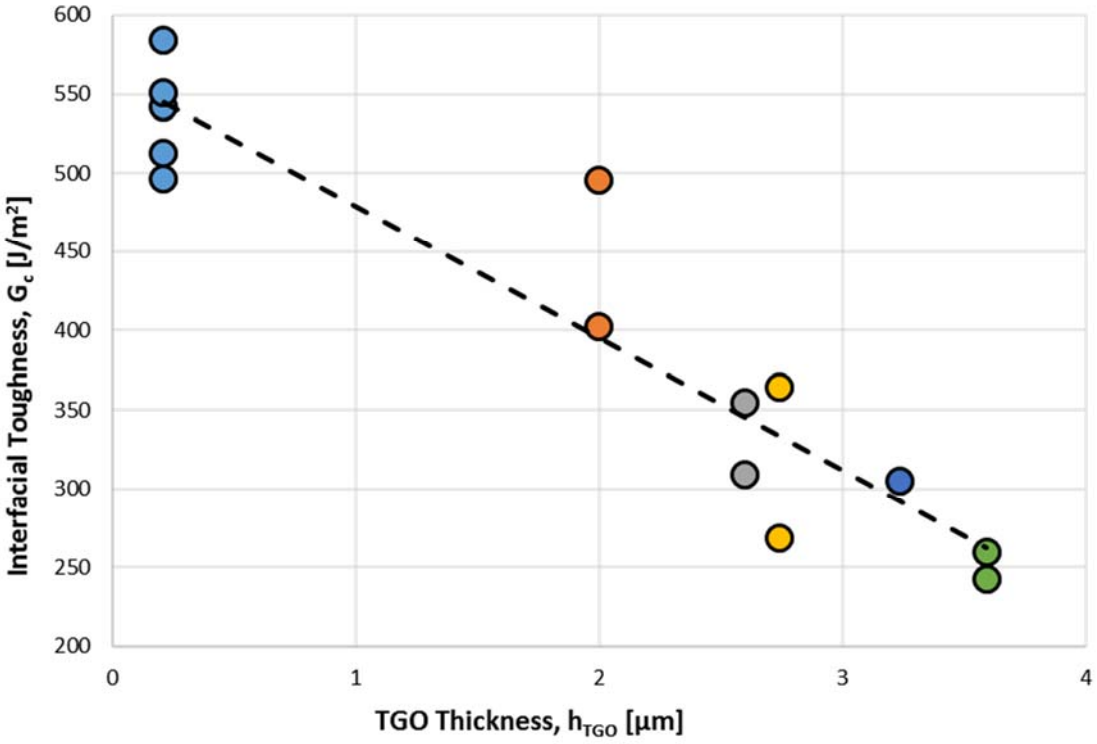

Figure 6-22: Interfacial toughness versus TGO thickness by taking into account effect of TGO variation and interfacial friction on the interfacial toughness

In Figure 6-23 the interfacial toughness vs. the percentage of furnace cycle life for different combinations of TGO thickness and interfacial friction coefficient is shown. Curve (a) is the interfacial toughness without taking into account the TGO in the FE model and not accounting for interfacial friction. Curve (b) and (c) are the toughness curves with 1 standard deviation below and above the measure values respectively for TGO thickness and interfacial friction. These curves take into account variability of the TGO thickness and interfacial friction and bounds the results of this study.

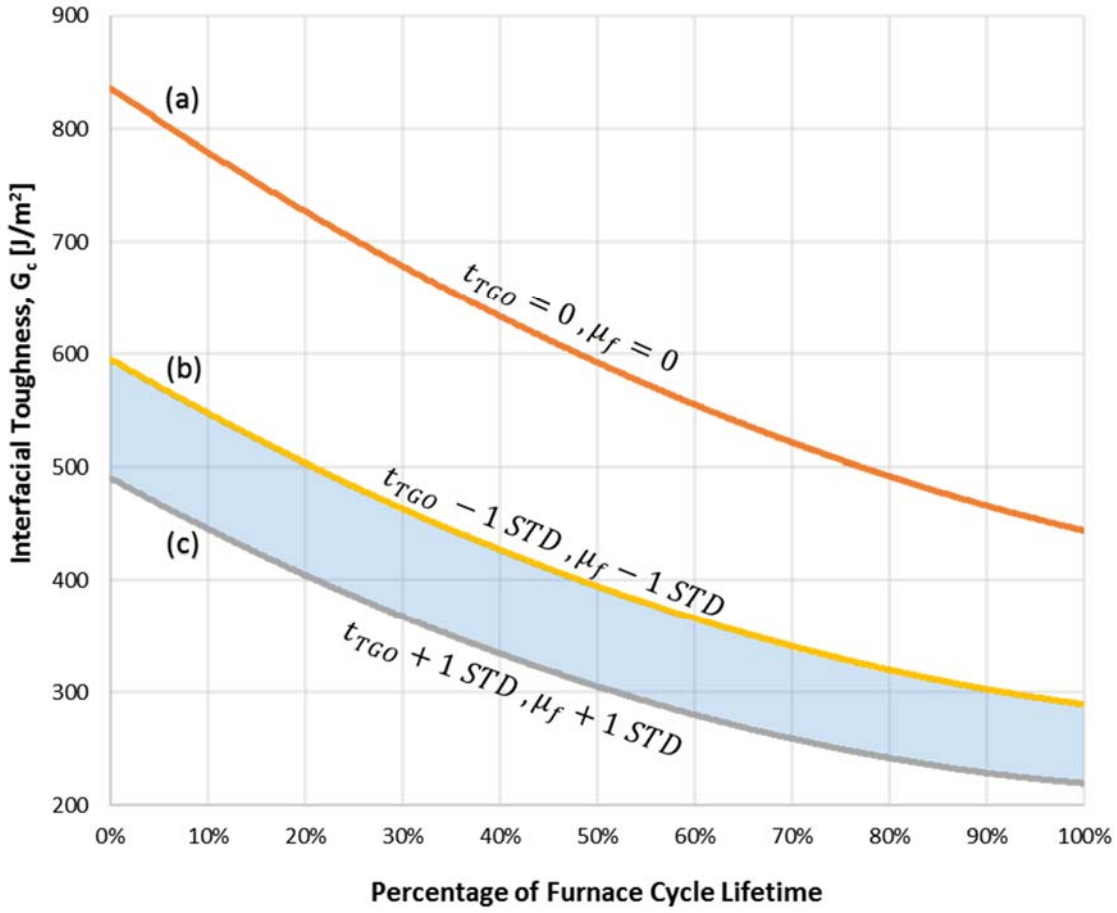

Figure 6-23: Interfacial toughness vs. percentage of furnace cycle lifetime for (a) no TGO and no interfacial friction, (b) TGO thickness and interfacial friction coefficient 1 standard deviation lower than measured and (c) TGO thickness and interfacial friction coefficient 1 standard deviation higher than measured.

6.2 Modified 4-Point Bend Test

A total of 17 tests were successfully conducted on the modified 4-point bend samples. The samples were prepared as outline in Section 4.3. Bending of the samples was conducted in a custom micro-bending test setup with a pin displacement rate of $\dot{\delta} = 0.5\ \mu m/s$. Additional details regarding this setup can be viewed in APPENDIX B: Micro-Bending System Overview. Images were capture at an image capture rate of 1 per second. This image capture rate yielded approximately 300-500 images for each test. Although the critical cracking loads were ultimately calculated from load versus time curves, the images

were processed using DIC techniques to generate in-plane shear maps. These maps were then used to ensure that symmetric crack growth occurs. Any test where symmetric crack growth did not occur was discarded. An example load vs. displacement curve can be seen in Figure 6-24.

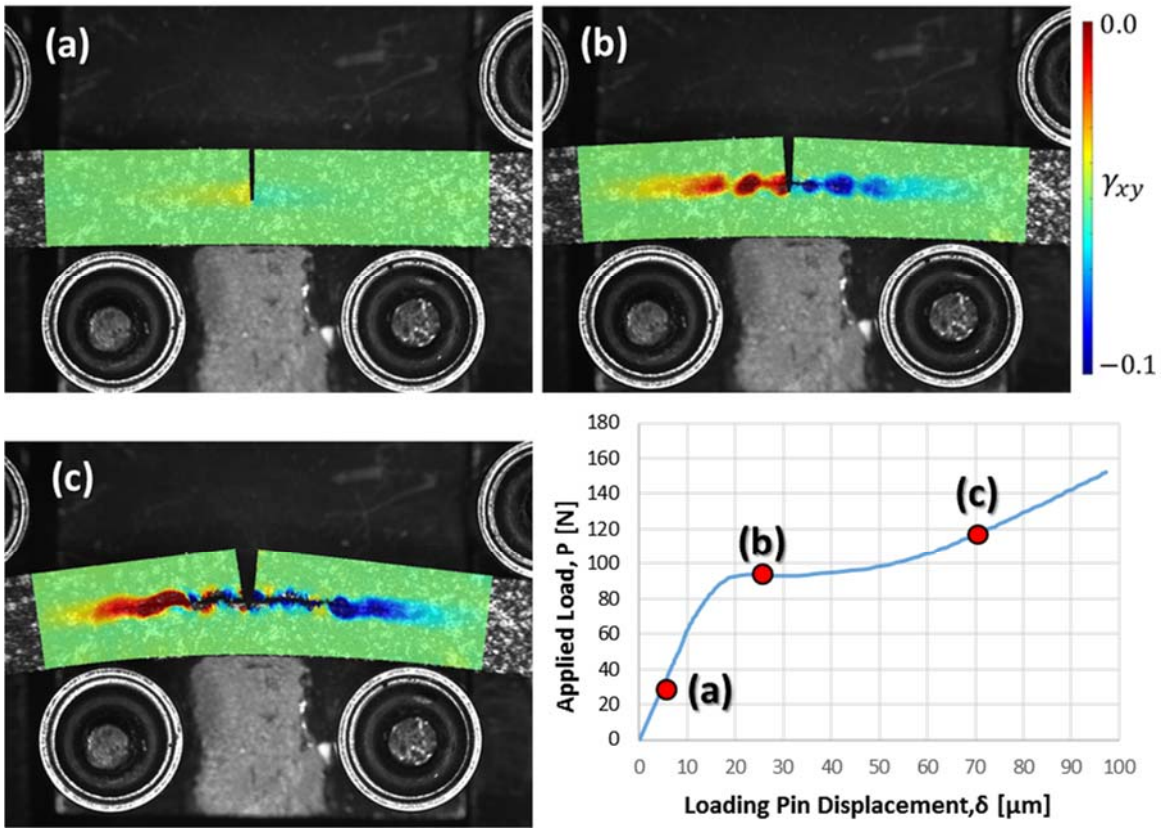

Figure 6-24: Representative load vs. displacement curve for modified 4-point bend test with in-plane shear maps for sample (a) prior to interface cracking, (b) beginning of cracking and (c) after crack arrest.

The images in the figure represent (a) during loading of the sample before crack growth, (b) right after the crack began to grow symmetrically and (c) after the crack growth had arrested and subsequent loading of the sample occurs outside of the plateau stress region. Image (b) shows the symmetric crack growth that occurred right as the crack "pop-in" event occurred and beginning of linear load-deflection during cracking. Image (c) shows the subsequent symmetric crack growth. For all tests the program outlined in APPENDIX

D: Plateau Load Calculation MATLAB File was utilized to calculate the critical cracking load. This program allows for selection of the portion of the load vs. time curve corresponding to the beginning and end of the plateau load region. The load values contained within these bounds are then averaged to calculate the average critical load.

6.2.1 Strain Energy Release Rate

With the critical cracking loads for each of the test samples, the interfacial toughness was calculated using Equation 5-11. A table of the critical load and interfacial toughness values can be seen in Table 6-4 and a corresponding plot is shown in Figure 6-25.

Table 6-2: Strain energy release rate, sample thickness, critical load for crack propagation and at each sample ID for tests conducted on modified 4-point bend tests in as-deposited state

Sample #	Sample Thickness [mm]	Pc [N]	Gc [J/m2]
4PB-B	2.53	97.40	118.82
4PB-C	1.86	84.52	122.10
4PB-D	2.23	94.12	126.08
4PB-E	2.18	96.20	134.67
4PB-F	1.89	79.65	106.33
4PB-G	2.19	93.29	125.91
4PB-I	2.10	94.35	134.55
4PB-J	2.08	87.49	116.97
4PB-K	2.08	86.03	112.77
4PB-L	2.02	95.48	143.12
4PB-M	2.09	94.52	135.75
4PB-N	2.11	97.08	141.89
4PB-P	1.95	88.14	126.13
4PB-R	2.09	94.01	134.09
4PB-S	1.86	81.09	112.04
4PB-T	2.13	84.33	105.88
4PB-U	1.57	76.40	117.86

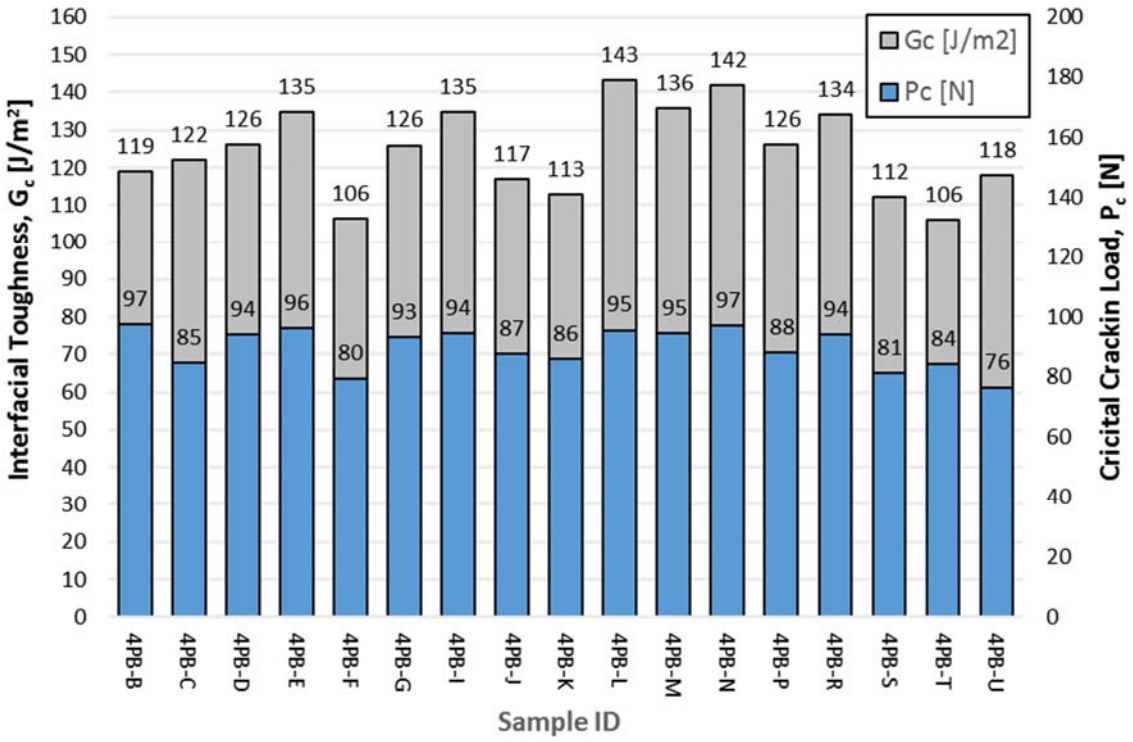

Figure 6-25: Strain energy release rate and critical cracking load vs. sample ID for tests conducted on modified 4-point bend tests in as-deposited state

The average value of interfacial toughness for the modified 4-point bend test was $G_c = 124.41\ J/m^2$ with a standard deviation of $11.34\ J/m^2$ and a total range of $37.23\ J/m^2$. The value reported in this study agrees well with the interfacial toughness of $G_c = 113\ J/m^2$ and standard deviation of $11.3\ J/m^2$ reported by Thery [5, 6].

6.3 Variation of G_c with Phase Angle

When the interfacial toughness data from this study is plotted alongside work done by other authors, a toughness vs. phase angle curve can be derived. A micromechanical model of interface toughness not been derived as of yet for TBC's and phenomenological models have shown to fit the toughness behavior exhibited by a large number of material systems very well. Once such toughness function was originally proposed in 1991 by Hutchinson et al. [7]:

Equation 6-5

$$G_c = G_{I,c}\{1 + tan^2[(1-\lambda)\phi]\}$$

In Equation 6-5, $G_{I,c}$ is the pure mode 1 critical interfacial toughness, λ is a fitting parameter that can vary between 0 and 1 and ϕ is the phase angle of fracture. One important aspect of this equation is that it is a symmetric function, i.e. $G_c|_{-90^\circ} = G_c|_{90^\circ}$. While this may work for certain material systems, it does not allow for any asymmetry that may be present in the toughness behavior. For the thermal barrier coating material system a potential asymmetry could arise from factors such as crack tip plasticity, micro cracking in the TGO and top coat and from the tension/compression asymmetry and columnar microstructure of the top coat. A modification of Equation 6-5 was determined in this study to allow for a phase angle shift to account for a potential asymmetry of the toughness function. This modification takes the following form:

Equation 6-6

$$G_c = G_{I,c}\{1 + tan^2[(1-\lambda)(\phi - \phi_0)]\}$$

where ϕ_0 is a phase angle shift that allows the function to be asymmetric.

A list of toughness values for TBC systems EBPVD 7%YSZ top coats in the as-deposited state for different tests methods can be seen in Table 6-3.

Table 6-3: Compiled results of interfacial toughness and phase angle values from tests conducted in this study and from other studies

Test Method	φ [°]	G_c [J/m^2]	Reference
Compression Edge-Delamination (JHU)	-89.5	537	Current Work
Micro-Bending (JHU)	17.9	27	Eberl et al., Acta Mat. (2011) [8]
	18	43	
	18.1	54	
	18.9	68	
	18.9	51	
	19.2	19	
	20.5	95	
Indentation	33.2	49	Beuth et al., Eng. Fracture Mech. (2001) [9]
4-Point Bend	40.5	113	Thery et al, Acta Mat. (2007) [5]
4-Point Bend (JHU)	40.5	124	Current Work
Buckling	60	75	Hutchinson et al., J Mech. And Phy. Of Solids (2000) [10]
Barb	65	36	Liu et al., Acta Mat. (2008) [11]
Pushout	65	84	Kim et al., Acta Mat. (2008) [12]

The compression edge-delamination test and the 4-point bend test were conducted for this thesis. The micro-bending test was conducted at Johns Hopkins in 2011 by Chris Eberl [8], indentation test by Beuth et al. [9], 4-point bend test by Thery at al. [5], buckling test by Hutchinson et al. [10], barb test by Lie et al. [11] and the pushout test by Kim et al. [12] were all taken from their respective publications. A plot of these results can be seen Figure 6-26. The dotted line in the figure shows a fit of Equation 6-6 to the data. The curve fit was conducted in MATLAB using the *cftool* command. The curve fit parameters are $G_{I,c} = 57.13\ J/m^2$, $\lambda = 0.33$ and $\phi_0 = 16.89°$. This value of λ lies perfectly within the range of 0.3-0.33 previously determined for TBC material systems [13, 14]. The most important aspect of the toughness curve presented is that the toughness at negative Mode II is almost

4 times higher than at positive mode II. There are a number of reasons that the negative mode II toughness is so much higher. One of the potentially most profound reasons is due to asperity strengthening of the interface [15, 16] coupled with the tension/compression asymmetry present in the top coat [17] as well as other possible mechanisms. A schematic of the mechanism by which asperity strengthening occurs is shown in Figure 6-27. If a normal stress, σ_{yy}, is applied to the crack there is a minimal effect of the surface roughness on the interfacial toughness. If a shear stress, σ_{xy}, is applied the contact points add an additional resistance to crack growth that must be accompanied by either an opening displacement applied to the crack faces or though subsequent fracture of the contact columns.

While the idea of asperity strengthening can be used to used to explain why the $\pm$ Mode II toughness is greater than the Mode I toughness, the idea of tension/compression asymmetry in the TBC top coat elastic modulus can help lead to an explanation for the cause of the asymmetry in the toughness curve. In the negative Mode II condition the top coat is in compression and the vertical gaps in the columnar microstructure of the top coat as pushed together and closed. In the positive Mode II conditions the top coat is in tension and the gaps in the top coat are allowed to open and can ultimately lead to vertical cracking between columns.

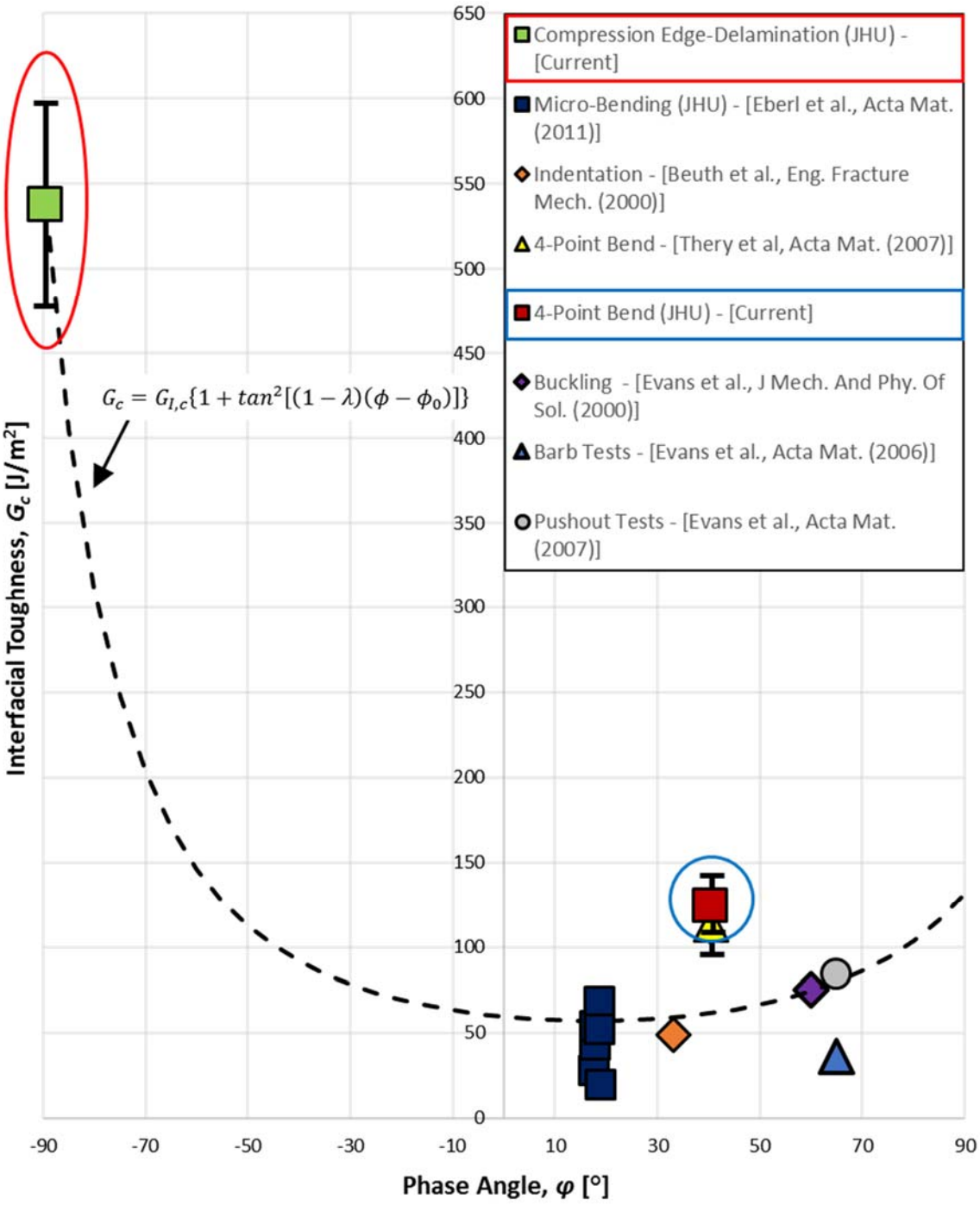

Figure 6-26: Interfacial toughness vs. phase angle for experimental measurements from this study and other selected studies with toughness curve shown in dashed line

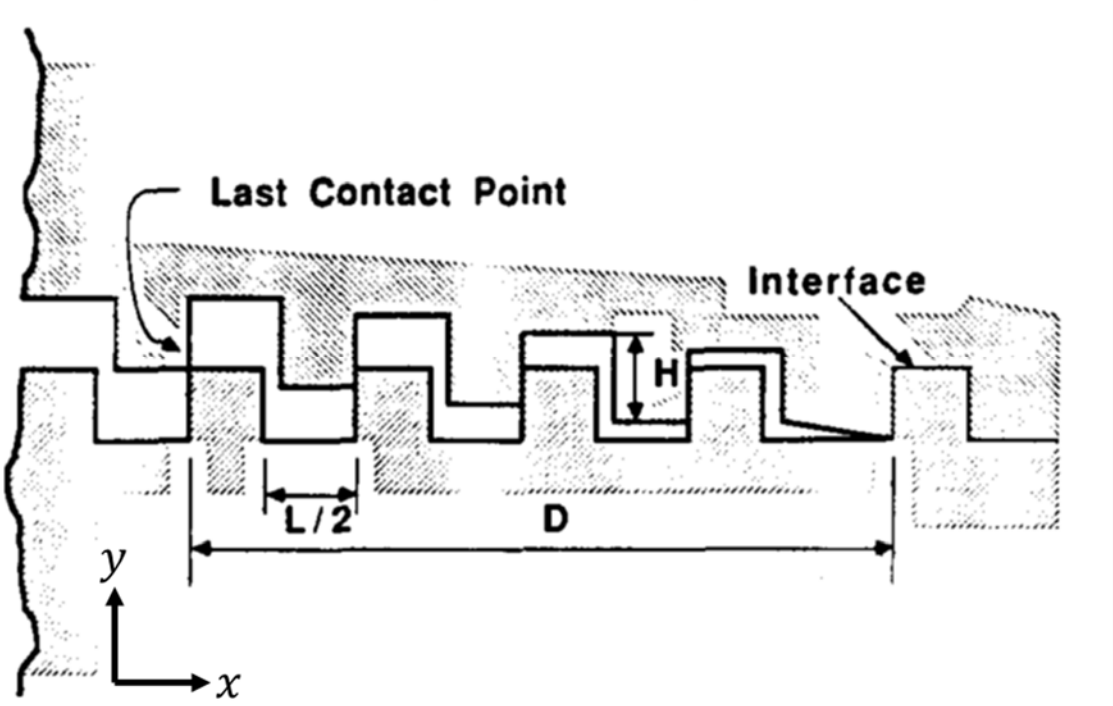

Figure 6-27: Schematic of contact zone illustrating crack face contact (Figure taken from [15])

This cracking of the top coat expends energy and ultimately reduces the total available strain energy available for delamination. These vertical cracks can also extend into the TGO and further reduce the stored elastic strain energy in the TGO. In addition, since preliminary results investigating the tension/compression asymmetry in the elastic modulus of the top coat have found it to be higher in compression than in tension [17], this leads to more elastic strain energy build up in the negative Mode II condition than in the positive Mode II condition. Further work needs to be conducted to better investigate the effect of top coat tension/compression asymmetry on the asymmetry of the toughness curve and could help to lead to a unified micromechanical model of TBC interfacial cracking.

6.4 Interface Roughness

To measure the interface roughness between the bond coat and top coat layers, CED samples at 0%, 20%, 50% and 100% of furnace cycle lifetime were first cross-sectioned

using a diamond wire saw. The cross-sections were then polished with SiC sandpaper up to 1200 (P-4000) grit with subsequent polishing with a colloidal alumina suspension with $0.05\ \mu m$ diameter particles. The polished samples were then cleaned in a sonicating bath and dried in a vacuum desiccator. Prior to imaging, the samples were sputtered with carbon to prevent electrostatic charging of the ceramic surfaces. At each level of thermal cycling, 8 images were captured with a total interface length of $225\ \mu m$ in each image. Each of the images were then thresholded using ImageJ and the coordinates of the interface saved in a comma separated values (.csv) file. A custom MATLAB script first applied a coordinate transformation to ensure the average line of the interface is perfectly horizontal. This step ensures proper calculation of the interface roughness. The roughness is then calculated by applying the following equation for the arithmetic mean roughness:

Equation 6-7

$$R_a = \frac{1}{n}\sum_{i=1}^{n}(y_i - \bar{y})$$

In this equation y_i is the height at point i and $\bar{y}$ is the average height of all the data points. Figure 6-28 shows, at each level of furnace cycle lifetime, all 8 images stitched together along with its thresholded interface profile. The measured roughness values are shown in Figure 6-29. The roughness values rise fairly slowly from $R_a = 1.8\ \mu m$ in the as-deposited state to $R_a = 2.5\ \mu m$ at 50% of lifetime and then rises more rapidly to $R_a = 3.5\ \mu m$ at the coating lifetime. This roughness evolution behavior is similar as to what has been reported previously [18].

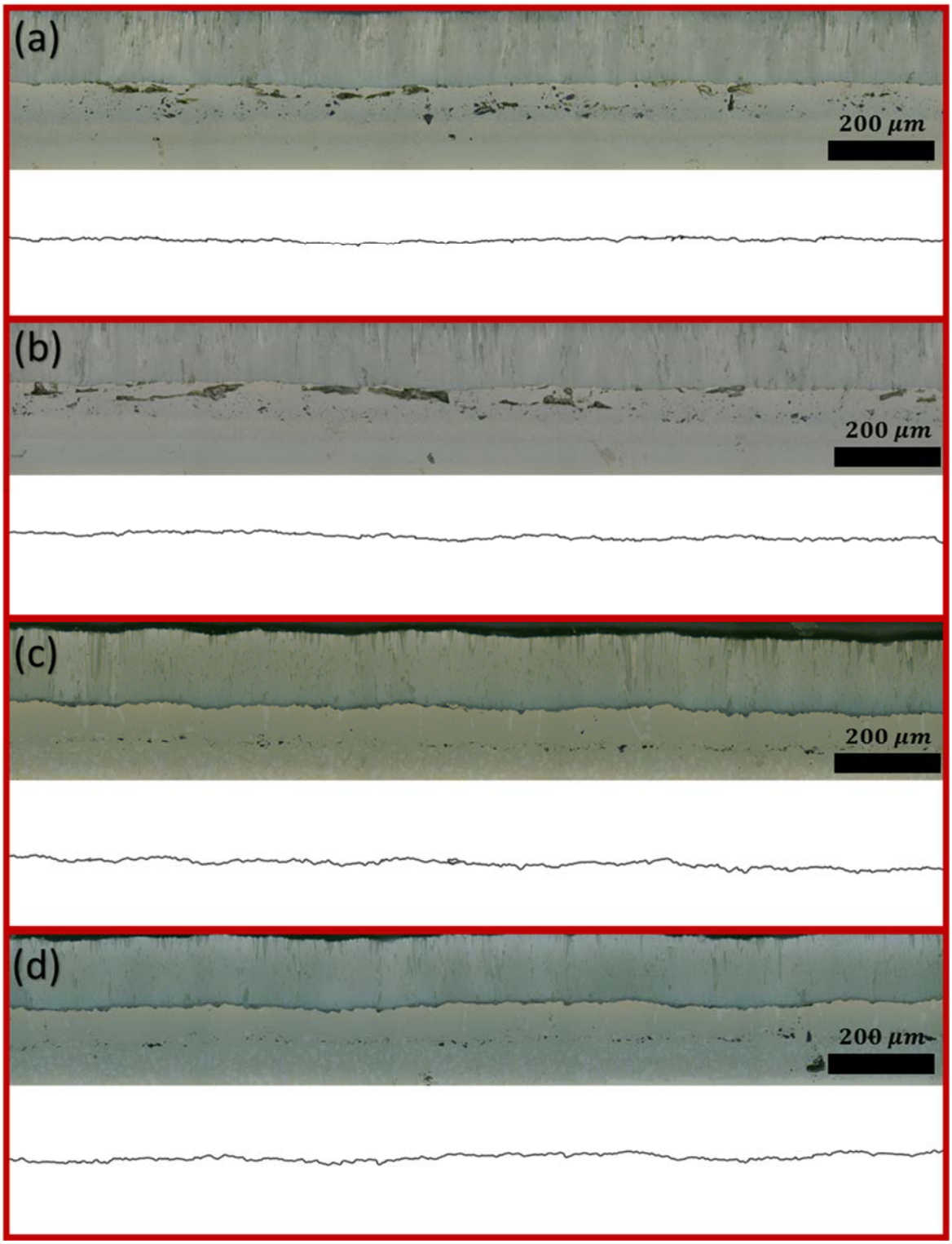

Figure 6-28: Stitched micrographs and accompanying thresholded interface profiles at (a) 0%, (b)20%, (c) 50% and (d) 100% of furnace cycle lifetimes

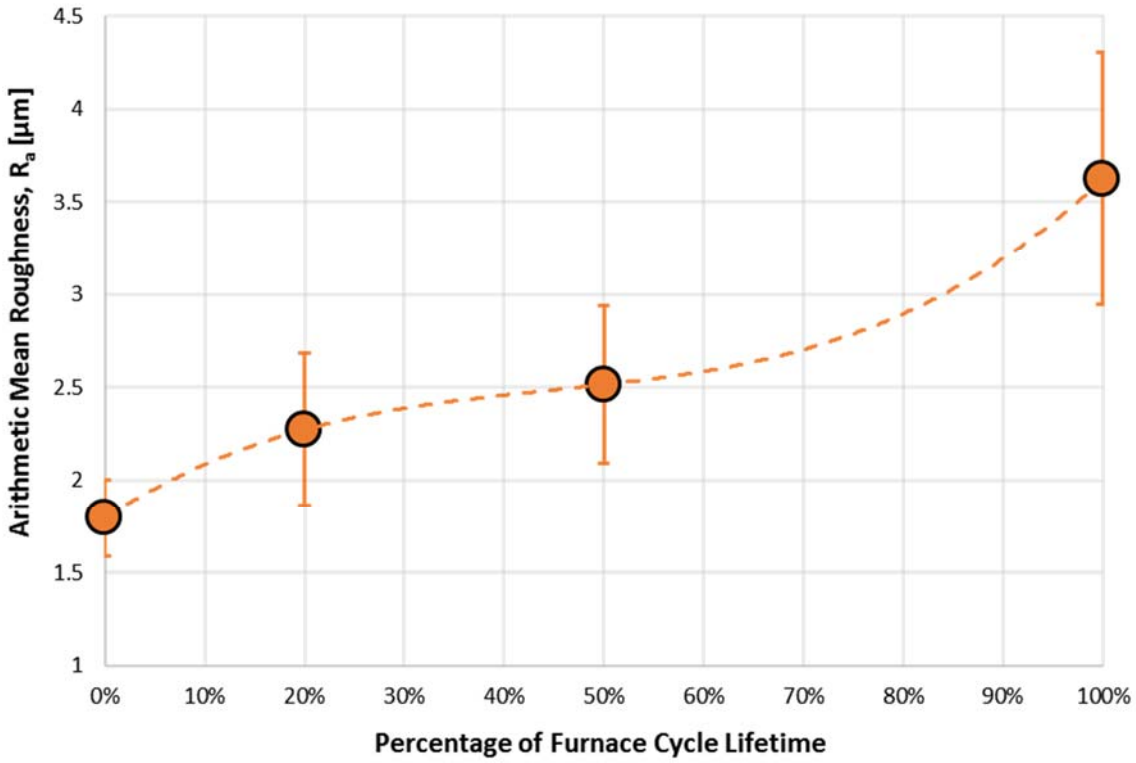

Figure 6-29: Plot of arithmetic mean roughness vs. percentage of furnace cycle lifetime for bond coat/top coat interface

6.5 Fracture Surface Roughness

The fracture surface roughness was calculated by imaging the fracture surface on the substrate side of the CED samples using a Keyence VK-X100 CLSM. The benefit of using a CLSM over a traditional light microscope is that by varying the height of the lens objective, a large depth of field is able to be captured even at high magnification. This allows for fully in-focus optical imaging of the surface at a magnification of 100x. The first publication of the CLSM technique was made by Paul Davidovitos and M. David Egger in two papers in 1969 and in 1971 [19, 20]. A good overview of the CLSM technique is presented in *Confocal Laser Scanning Microscopy*, by Stephen Paddock [21]. An example of the optical image captured is shown in Figure 6-30 with outlines of the bond coat, top coat and TGO shown and is composed of 9 images stitched together. The difference in the

optical properties of each material can ultimately be used to threshold the interface for relative area calculations.

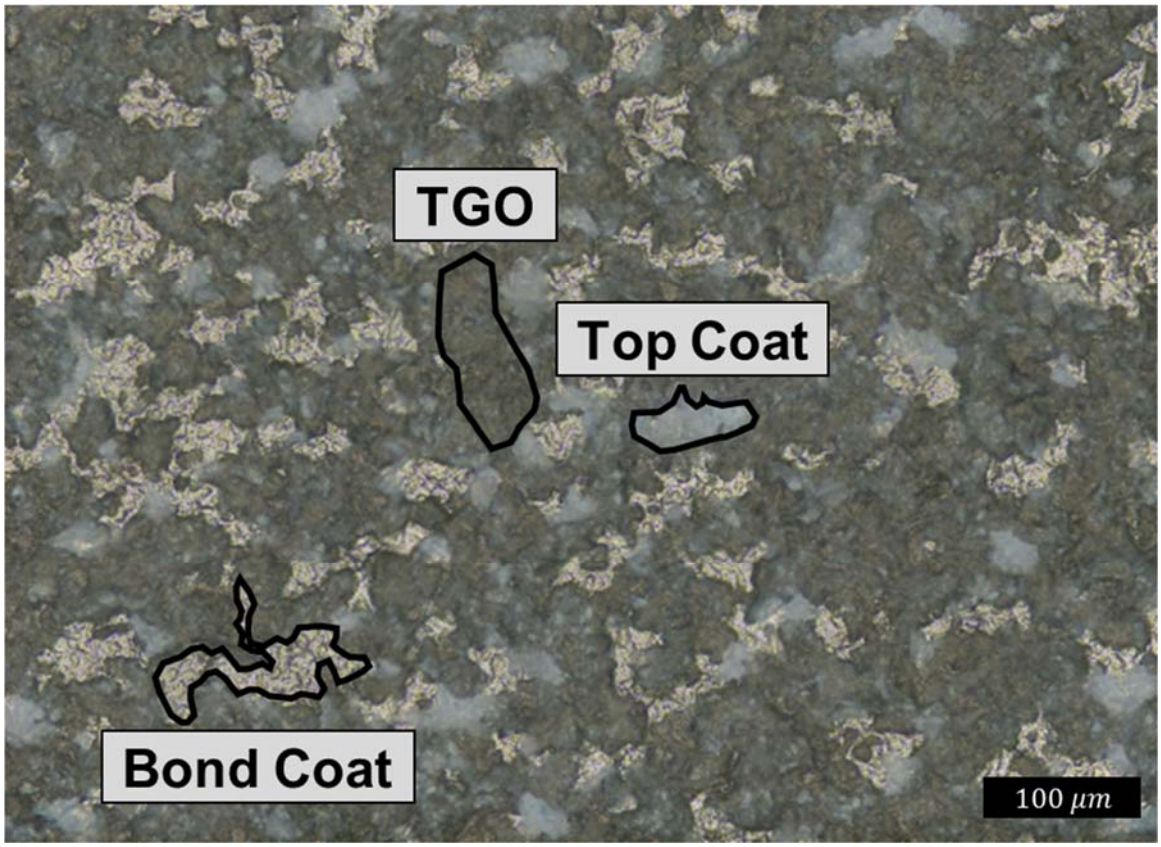

Figure 6-30: Optical image captured using Keyence VK-X100 Confocal Laser Scanning Microscope

The advantage of a CLSM over a traditional contact profilometer is that the profile measurement is made without touching the sample, and risking damaging the surface, and since the contact diameter is smaller than that of a contact profilometer, the sampling resolution is much higher. An example of the topographical information captured is shown in Figure 6-31.

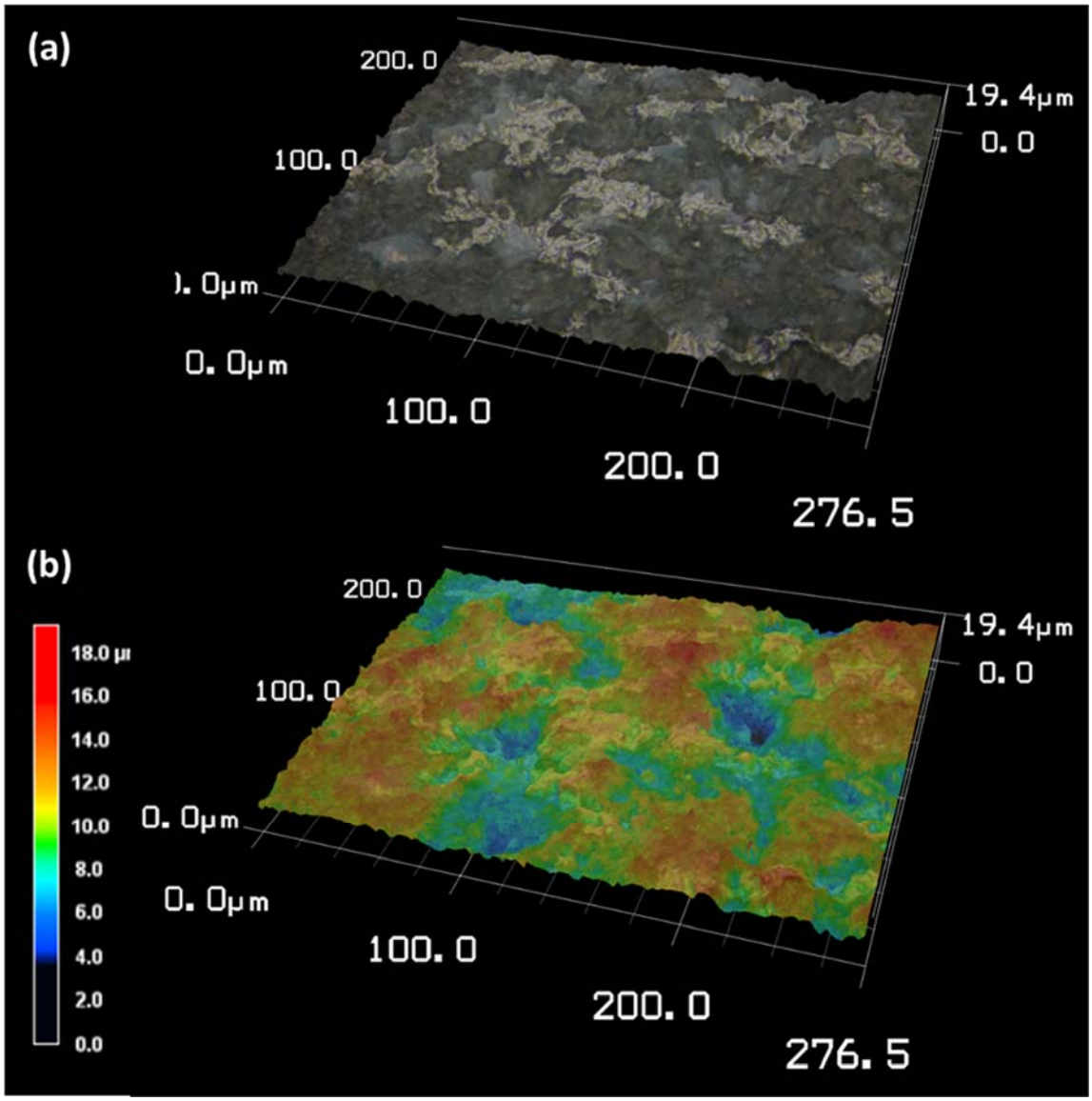

Figure 6-31: (a) Optical image overlaid on 3D topographical representation of fracture surface and (b) same overlay with additional shading corresponding to the measured height of the point on the interface for sample at 56% of furnace cycle lifetime.

In this figure, (a) shows the optical imaged overlaid on the 3D topographic representation of the fracture surface and (b) shows the same overlay but with additional shading corresponding to the height information gathered from the laser. It should be noted that this image is a smaller subset of the stitched image of the sample at 56% of furnace cycle lifetime.

The software provided with the Keyence VK-X100 also allows for direct calculation of the area surface roughness. The use of a CLSM to collect surface profile information and calculate surface roughness data has been used in numerous studies [22-25]. Nine optical images taken were of samples at 0%, 28%, 56% and 100% of furnace cycle lifetime and stitched together to create an image at each level of furnace cycling. The stitched images at each of the furnace cycle lifetimes, along with their measured average arithmetic mean roughness values, are shown in. Figure 6-32 and Figure 6-33.

The roughness values were calculated by using an area $150\ \mu m$ by $150\ \mu m$. This size was determined by observing the convergence behavior of the roughness with the area sampled. The result of this analysis can be seen in Figure 6-34. Successively larger square sampling areas, centered about the middle of the image, were used to calculate the arithmetic mean roughness. It was observed that the roughness converged at about a $150\ \mu m$ square edge size. With this sampling edge size defined, a total of 8 roughness measurements were made on each of the images. These calculated fracture surface roughness value are shown in Figure 6-35. There is little change in the fracture surface roughness between the as-deposited state and 28% of lifetime. Between 28% and 56% of lifetime the fracture surface roughness starts to rise and at 56% of lifetime rises rapidly to the roughness at lifetime of $R_a = 2.8\ \mu m$.

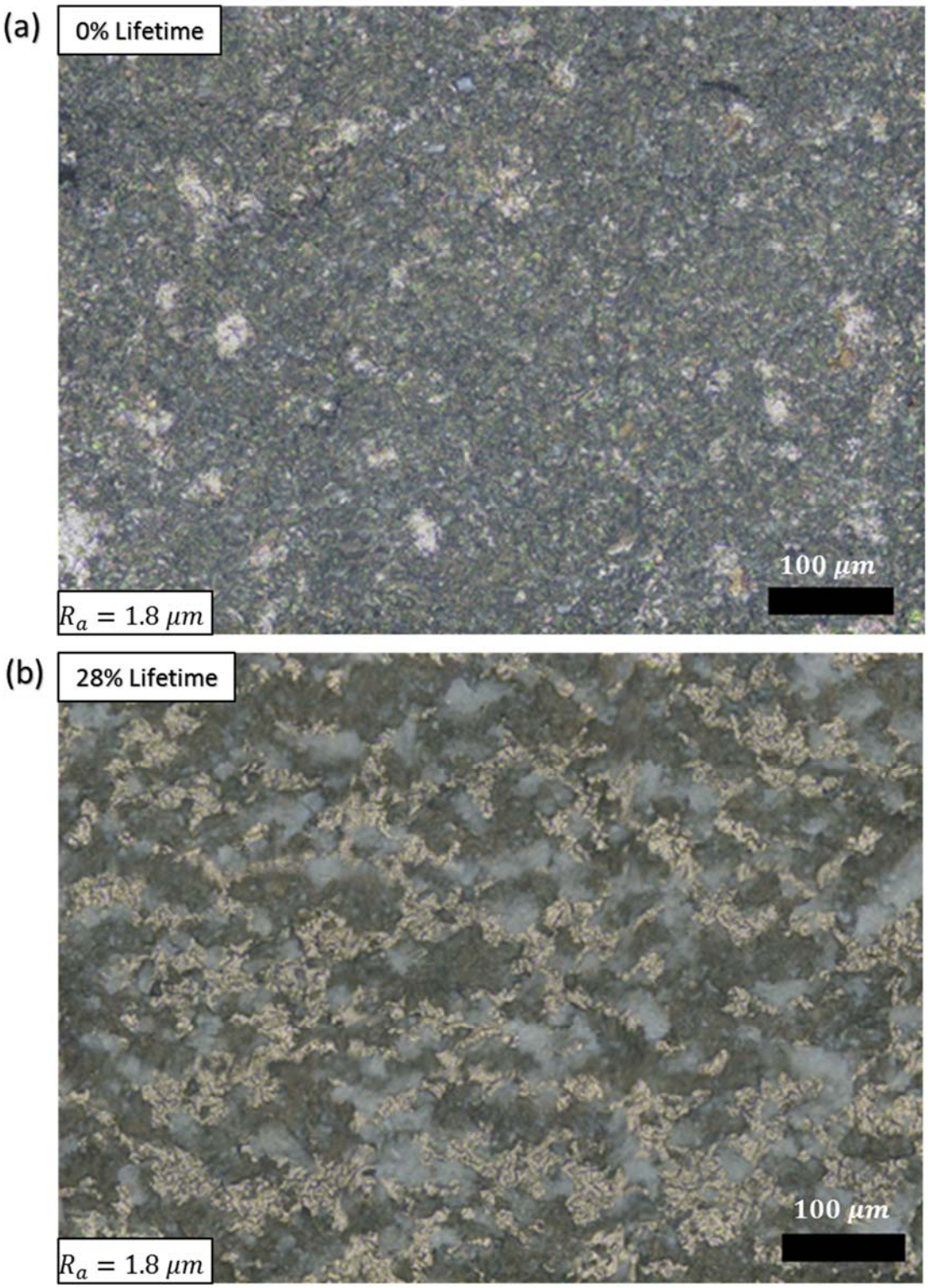

Figure 6-32: Optical images of the fracture surface of CED samples at (a) 0% Lifetime, (b) 28% Lifetime with calculated surface roughness values.

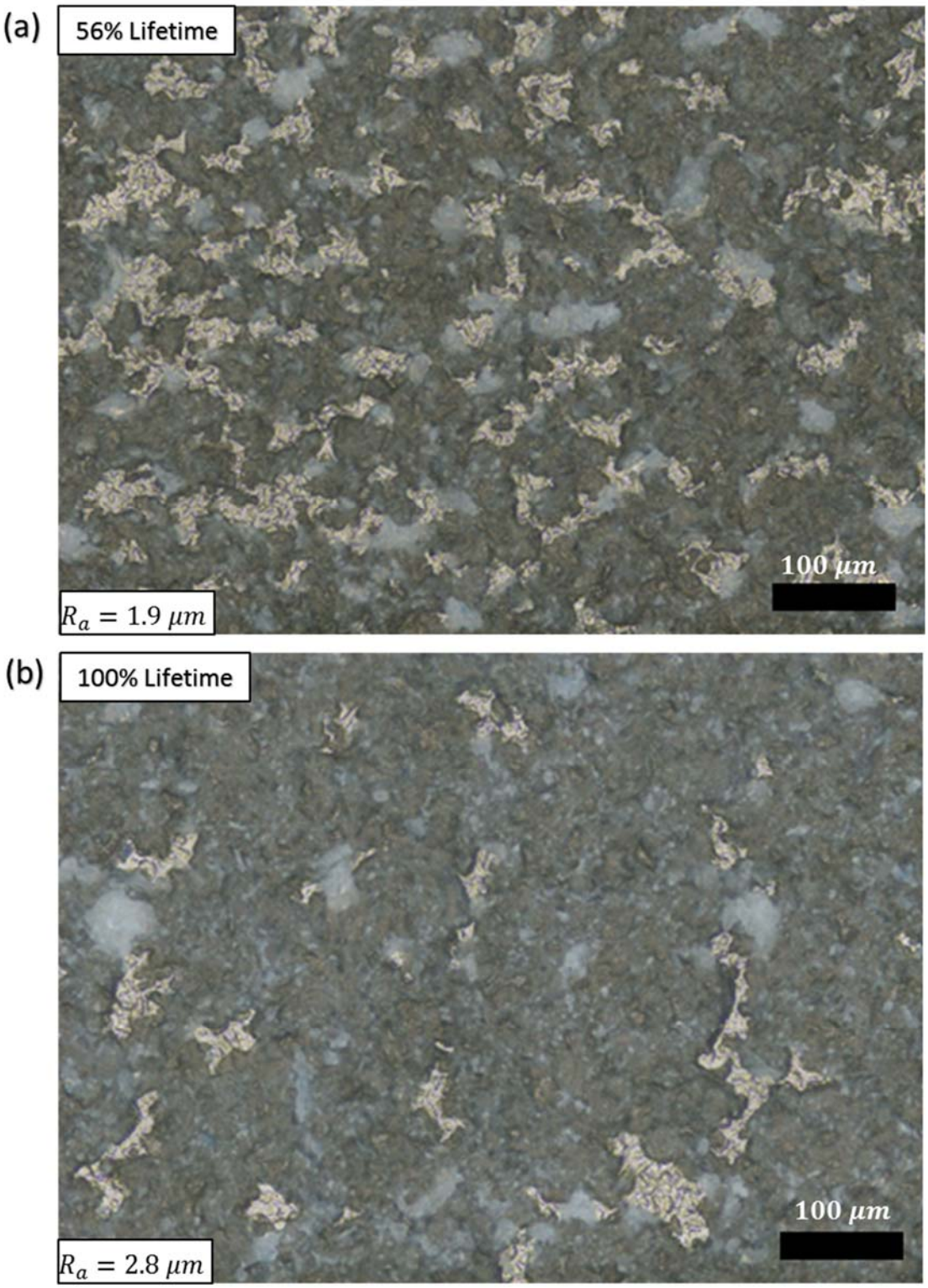

Figure 6-33: Optical images of the fracture surface of CED samples at (a) 56% Lifetime, (b) 100% Lifetime with calculated surface roughness values.

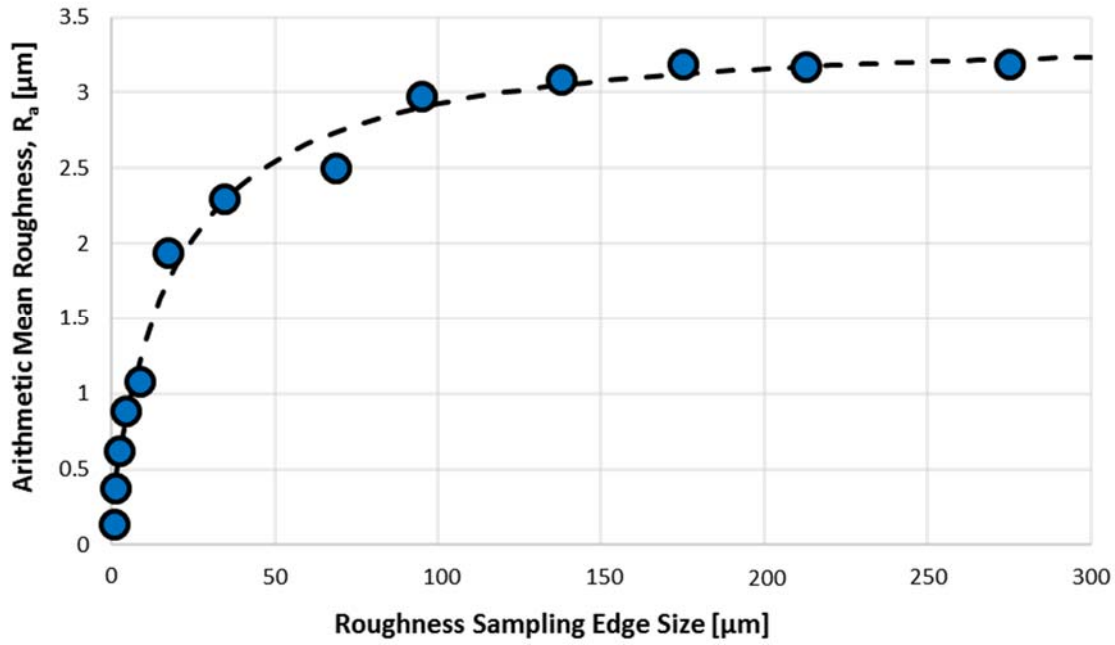

Figure 6-34: Arithmetic mean roughness vs. roughness sampling edge size of CED sample.

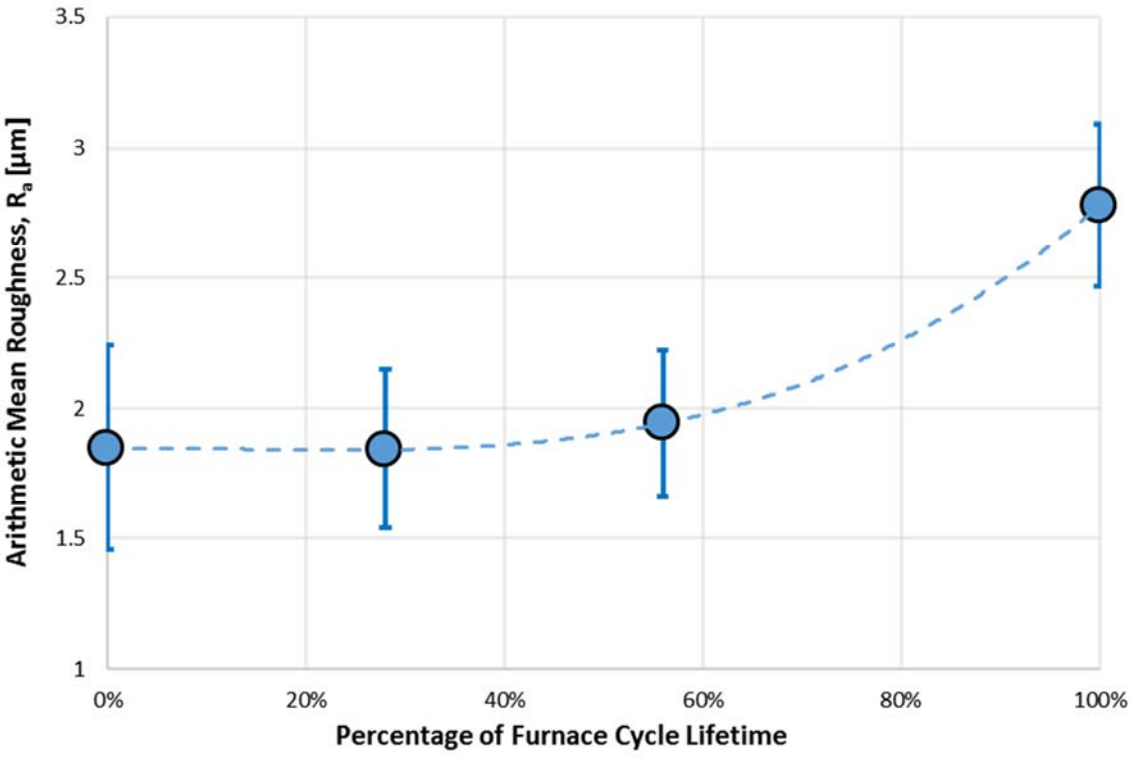

Figure 6-35: Arithmetic mean roughness vs percentage of furnace cycle lifetime for fracture surface of CED sample.

6.6 Area Fraction of BC/TGO/TBC on Fracture Surface

The relative area fraction of the bond coat, TGO and top coat were calculated by thresholding the stitched optical images of the substrate fracture surface, using ImageJ, that were captured with the CLSM. A plot of the evolution of each of these material constituents can be seen in Figure 6-36. An overlay of the thresholded areas used to generate Figure 6-36 is shown in Figure 6-37 and Figure 6-38. The blue areas correspond to where the TGO is present, the black to the bond coat and the red to the top coat. In the as-deposited state the TGO area fraction is ≈70% and rises to ≈80% at coating lifetime. For the bond coat, the relative area fraction in the as-deposited state is ≈20% and drops to ≈5% at coating lifetime. The area fraction of top coat starts off at ≈5% and at coating lifetime rises to ≈20%.

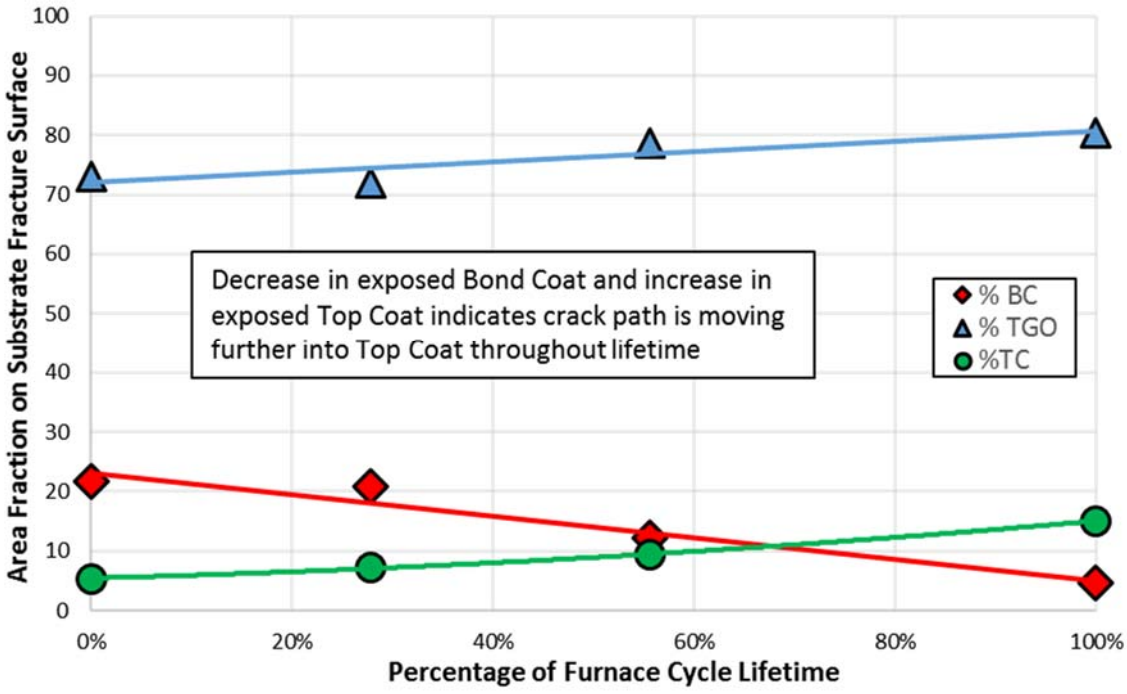

Figure 6-36: Percentage of fracture surface covered by (a) bond coat, (b) TGO and (c) TC vs. percentage of furnace cycle lifetime (calculated through thresholding in ImageJ)

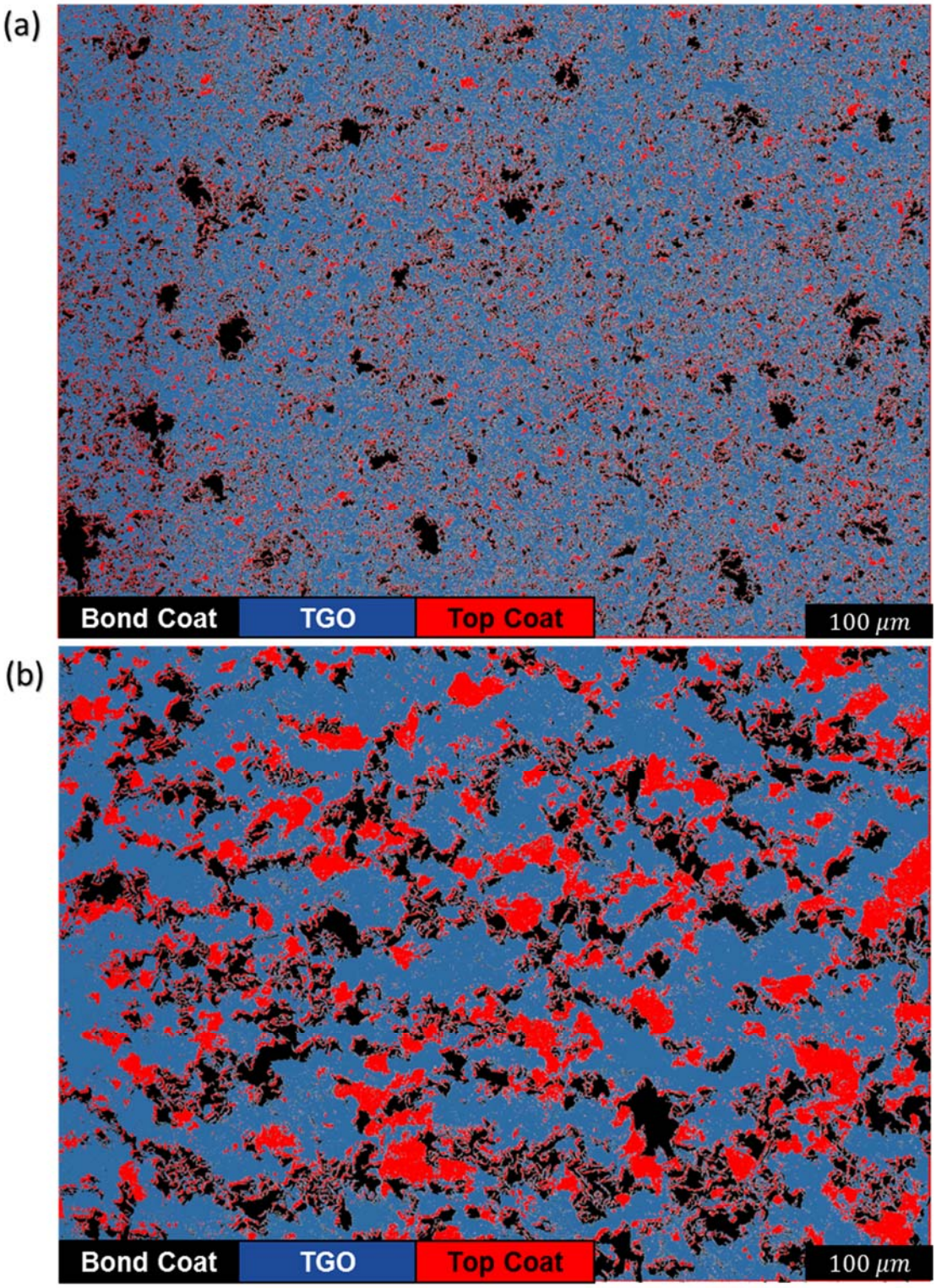

Figure 6-37: Thresholded image of fracture surface of CED sample at (a) 0% and (b) 28% of furnace cycle lifetime with constituent materials identified.

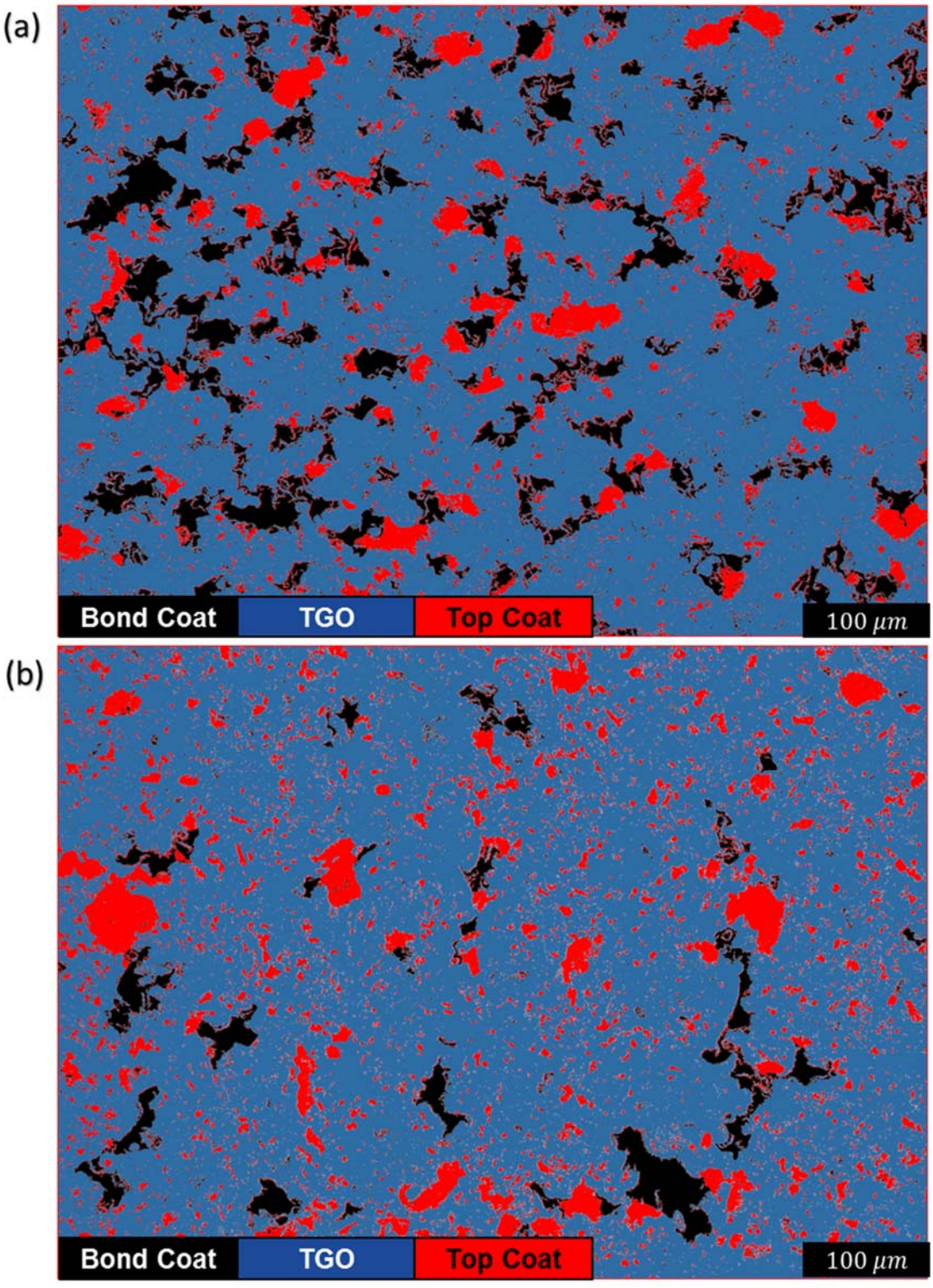

Figure 6-38: Thresholded image of fracture surface of CED sample at (a) 56% and (b) 100% of furnace cycle lifetime with constituent materials identified.

6.6.1.1 *Implications to Fracture Path*

There are a number of important implications to how the fracture path evolves through the coating lifetime. The first can be drawn by combining the information shown in Figure 6-29 and Figure 6-35, which can be seen in Figure 6-39. In the as-deposited state the roughness of the bond coat/top coat interface is the same as the roughness of the fracture path. This implies that the fracture path in the as-deposited state, follows the bond coat/top coat interface. As the level of furnace cycling increases, the fracture surface roughness quickly diverges away from the interface roughness. At 100% of coating lifetime, the fracture surface roughness is approximately 20% lower than the interface roughness. This strongly indicates that the delamination crack is no longer following the interface and is becoming more planar than the interface.

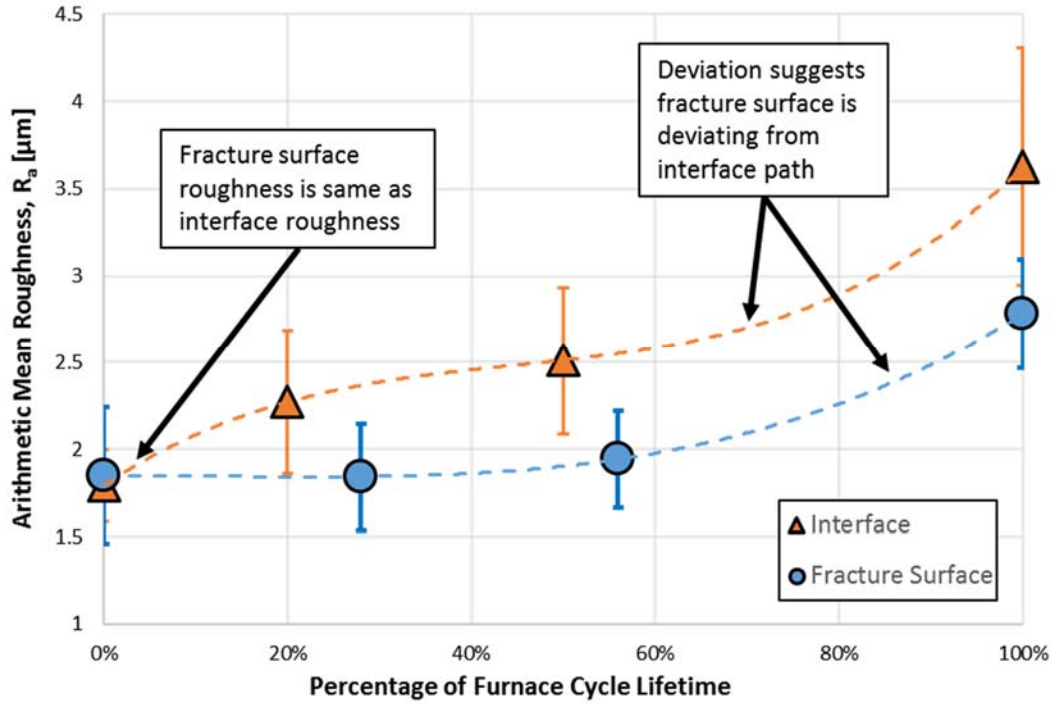

Figure 6-39: Comparison between arithmetic mean roughness vs. percentage of furnace cycle lifetime for the (a) bond coat/TGO/top coat interface and for the (b) fracture surface

It is possible for the crack path to follow any combination of 5 distinct paths; (a) intra-top coat fracture, (b) top coat/TGO delamination, (c) intra-TGO fracture, (d) TGO/bond coat delamination and (e) intra-bond coat fracture. This concept is represented schematically in Figure 6-40. For observation of the substrate side of the fracture surface, which would correspond to the lower part of the crack path in the figure, each of the crack paths would results in a different material layer being visible. The intra-top coat fracture would reveal the top coat, the top coat/TGO delamination and the intra-TGO fracture would reveal the TGO, and the TGO/bond coat delamination and intra-bond coat fracture would reveal the bond coat.

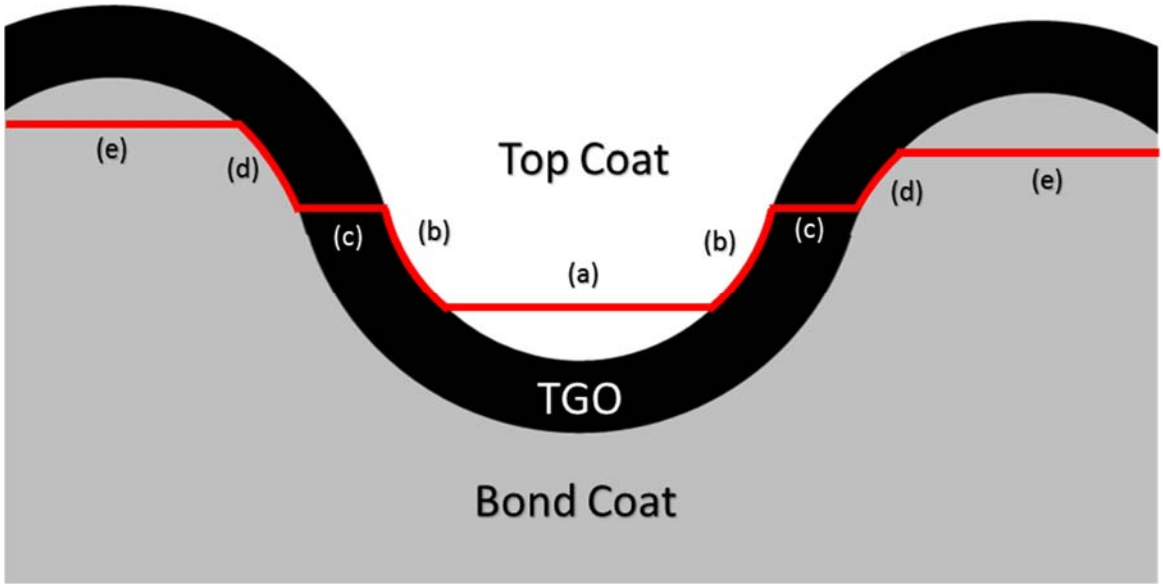

Figure 6-40: Schematic of the 5 different possible crack locations near the top coat/TGO/bond coat interface (substrate fracture surface considered results in any material below red crack line being visible on fracture surface)

Additional information can be inferred by observing the behavior present in Figure 6-36. While it is not explicitly apparent whether the increase in TGO is due to a relative change in the amount of top coat/TGO delamination or intra-TGO fracture, certain conditions must be satisfied to account for the changes in the relative bond coat and top coat. In the as-

deposited state (0% furnace cycle lifetime) there is TGO present and a higher amount of bond coat than top coat. At the coating lifetime (100% furnace cycle lifetime) there is still TGO present and there is a higher amount of top coat present than bond coat. A table describing the crack path requirements for these conditions at both 0% and 100% of furnace cycle lifetime can be seen in Table 6-4. For either of the furnace cycle levels there can either be top coat/TGO delamination or intra-TGO delamination to meet the requirement for TGO to be present. At 0% of lifetime a higher bond coat area would corresponds to predominantly TGO/bond coat delamination with some intra-bond coat cracking. Additionally, at 0% of lifetime a lower top coat area would correspond to these same conditions as well as top coat/TGO delamination and intra-TGO fracture. At 100% of lifetime a lower bond coat area would correspond to increased intra-top coat fracture, top coat/TGO delamination and intra-TGO fracture, while a higher top coat area would correspond to only intra-top coat fracture.

0% Lifetime					100% Lifetime			
	Condition					Condition		
Failure Mode	TGO Present	High BC	Low TC		**Failure Mode**	TGO Present	Low BC	High TC
intra-TC					intra-TC		X	X
TC/TGO	X		X	⇨	TC/TGO	X	X	
intra-TGO	X		X		intra-TGO	X	X	
TGO/BC		X	X		TGO/BC			
intra-BC		X	X		intra-BC			

Table 6-4: Comparison for conditions of relative material present for each type of crack path at (a) 0% furnace cycle lifetime and (b) 100% furnace cycle lifetime

With this information regarding the change in material layers present on the fracture interface and the deviation in the interface and fracture path roughness a conclusion can be drawn. All levels of furnace cycle lifetime must include some combination of top coat/TGO

delamination and intra-TGO delamination. As the level of furnace cycle lifetime increases, TGO/bond coat and intra-bond coat delamination decreases and intra-top coat fracture increases. This strongly implies that the crack path is moving further away from the bond/coat TGO interface and into the top coat as percentage of lifetime increases. While the data presented in this section implies strongly that the crack path is moving into the top coat, full 3D visualization of the cracked surface would accurately quantify the conclusions drawn.

6.7 Preliminary Serial Sectioning Results

In order to obtain 3D information about the crack path in delaminated samples, serial sectioning was employed. To obtain a serial set of images of a delaminated sample, the delaminated samples were embedded in epoxy and ground, polished and imaged at various depths. The micrographs facilitated visualization of the constituent materials. A serial section dataset was acquired at GE. The image area captured at each was $136\ \mu m$ by $103\ \mu m$ and a total of 40 images were captured. The amount of material removed between each step was $0.6\ \mu m$ for a total through sample depth of $23.4\ \mu m$.

The images were thresholded and then stitched together using the Dream.3D data analysis toolset commonly used to reconstruct microstructures from serial section data [26]. The data was saved as a .dream3d file and was then opened in Paraview for visualization of the stitched images [27]. An example of the raw images and their associated thresholded TGO maps can be seen in Figure 6-41. The tiles 1,2,3 and 40 are the raw images captured during the serial sectioning. The bond coat lies in the bottom portion of the image and the top coat is in the upper portion of the image with the TGO clearly visible in between the two. The tles i,ii,iii and xl are the thresholded TGO maps calculated in Dream.3D. When the images

are viewed using Paraview a 3D reconstruction of the TGO surface can be viewed. An overview of the results of the 3D reconstruction can be seen in Figure 6-42. The extreme images from the serial section dataset used to calculate the TGO surface are shown on this figure as well. In Figure 6-43 and Figure 6-44 views from the front, back, top coat side and bond coat side of the TGO are shown. The serial section acquisition and reconstruction is able to model the TGO surface with fine detail. One important aspect of the serial sectioning technique is assuring that proper and consistent contrast across all the images captured is maintained. This is needed to allow for proper differentiation between the TGO and porosity in and around the TGO. In the results presented here, interfacial pores are included in the TGO surface as they were not able to be sufficiently differentiated from the TGO surface. With proper image capture and reconstruction techniques, detailed statistics on the bond coat and top coat roughness as well as the pore content and location can be determined for cross-sections of interfaces. For samples that have been delaminated and mounted in epoxy, additional information regarding the relative volume of each material layer present on the fracture surface as well as comparison of the fracture surface path to the underlying natural interface roughness can be determined. These statistics, coupled with the information gathered in this study, have the potential to provide a more complete picture of the evolution of the crack path during thermal cycling. It will also give a better understanding of the exact mechanisms that control the durability of the interface and lead to toughness degradation.

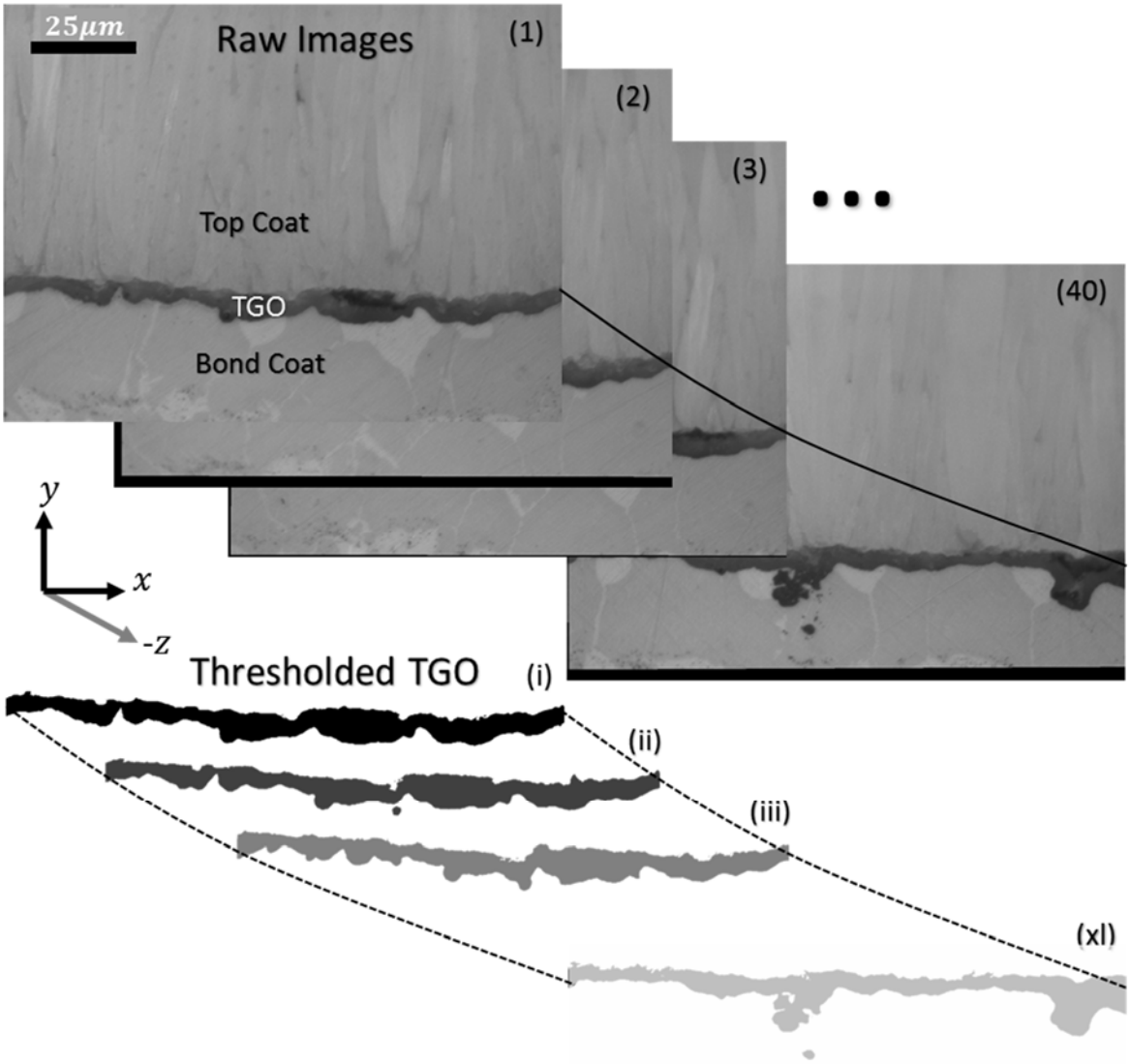

Figure 6-41: Representative raw images captured during serial sectioning and repsective thresholded TGO maps (distance between each images is 0.6 μm).

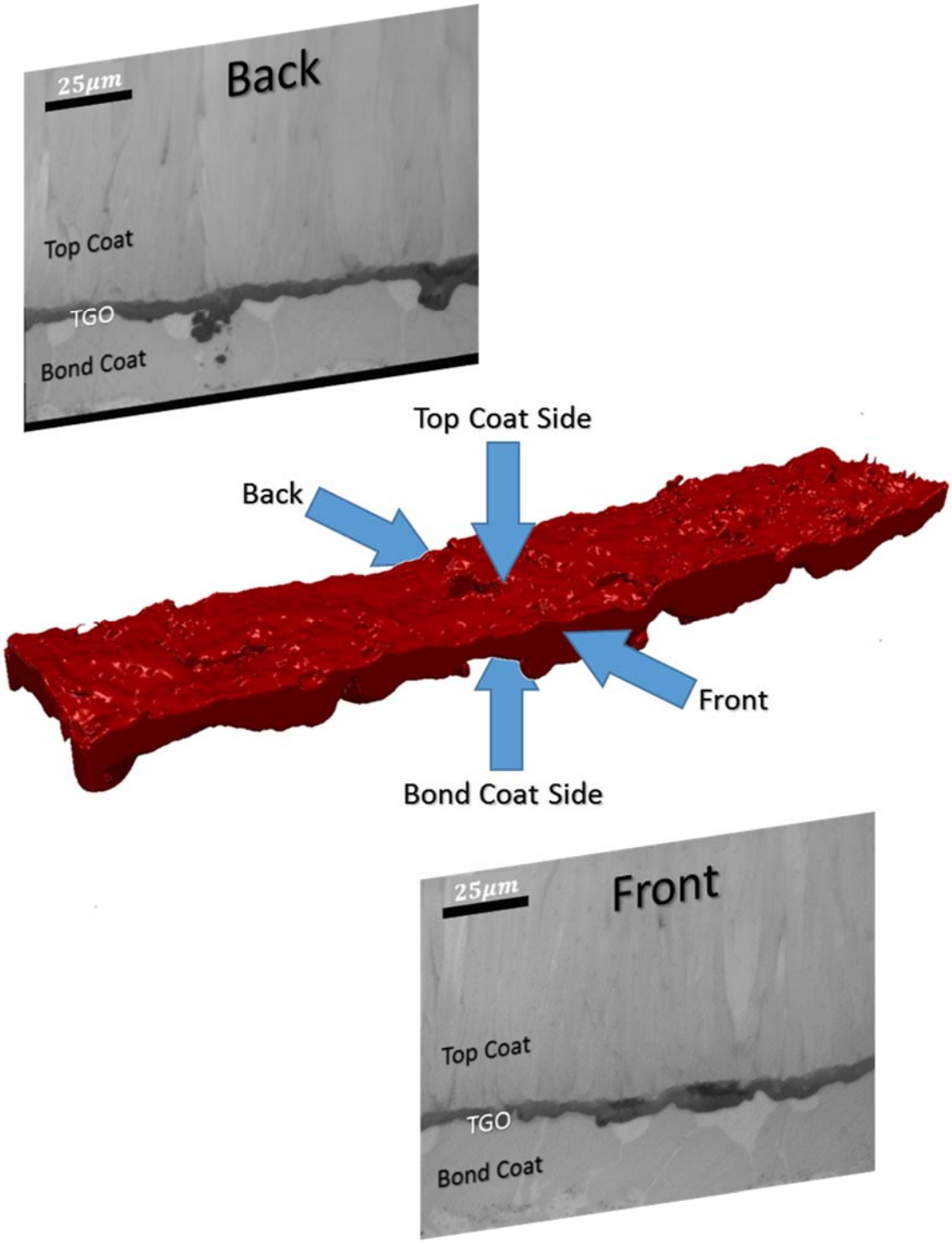

Figure 6-42: Overview of 3D reconstruction of TGO showing front and back images used in the calculation of the TGO.

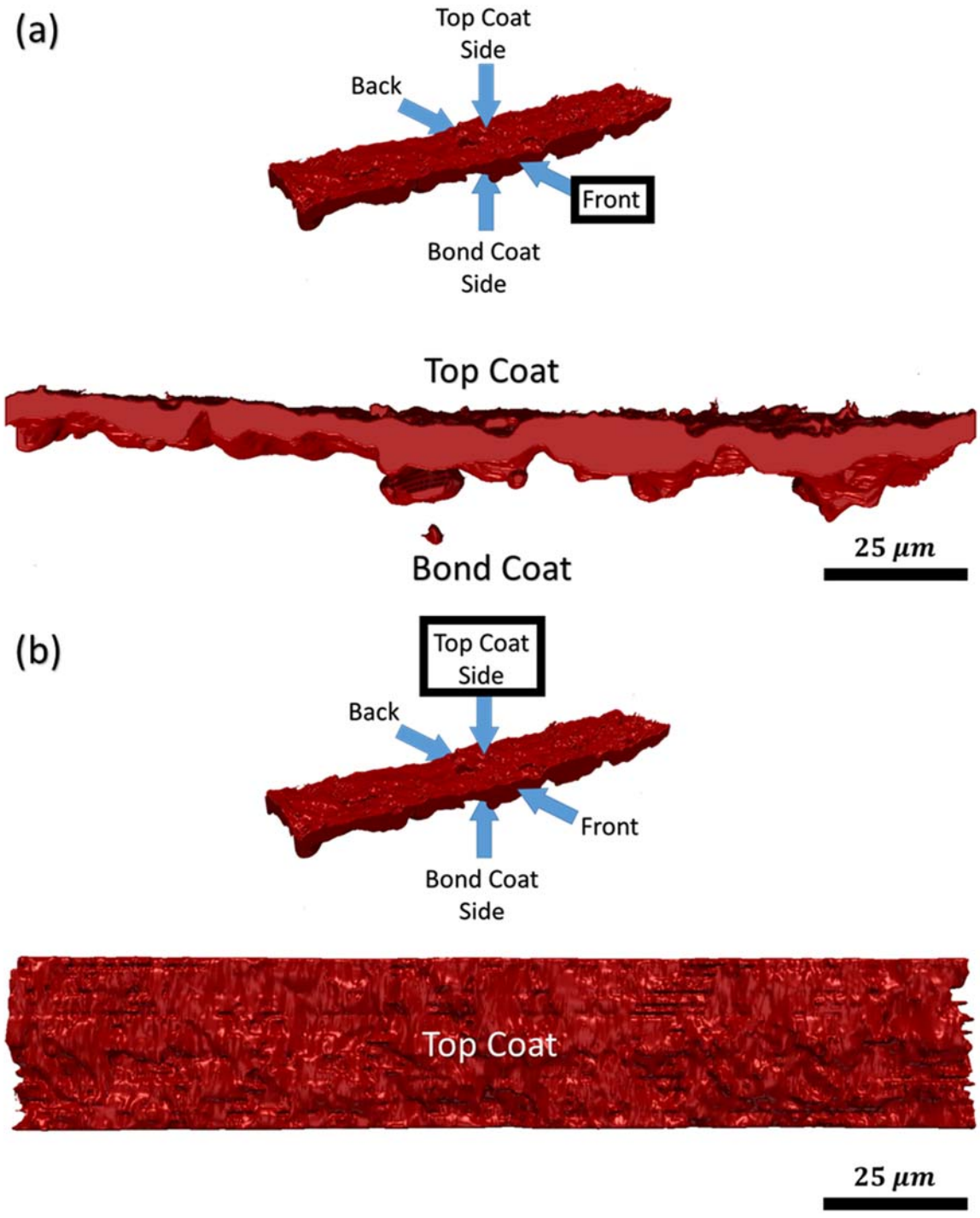

Figure 6-43: 3D reconstruction of TGO with views from the (a) front and (b) top coat side.

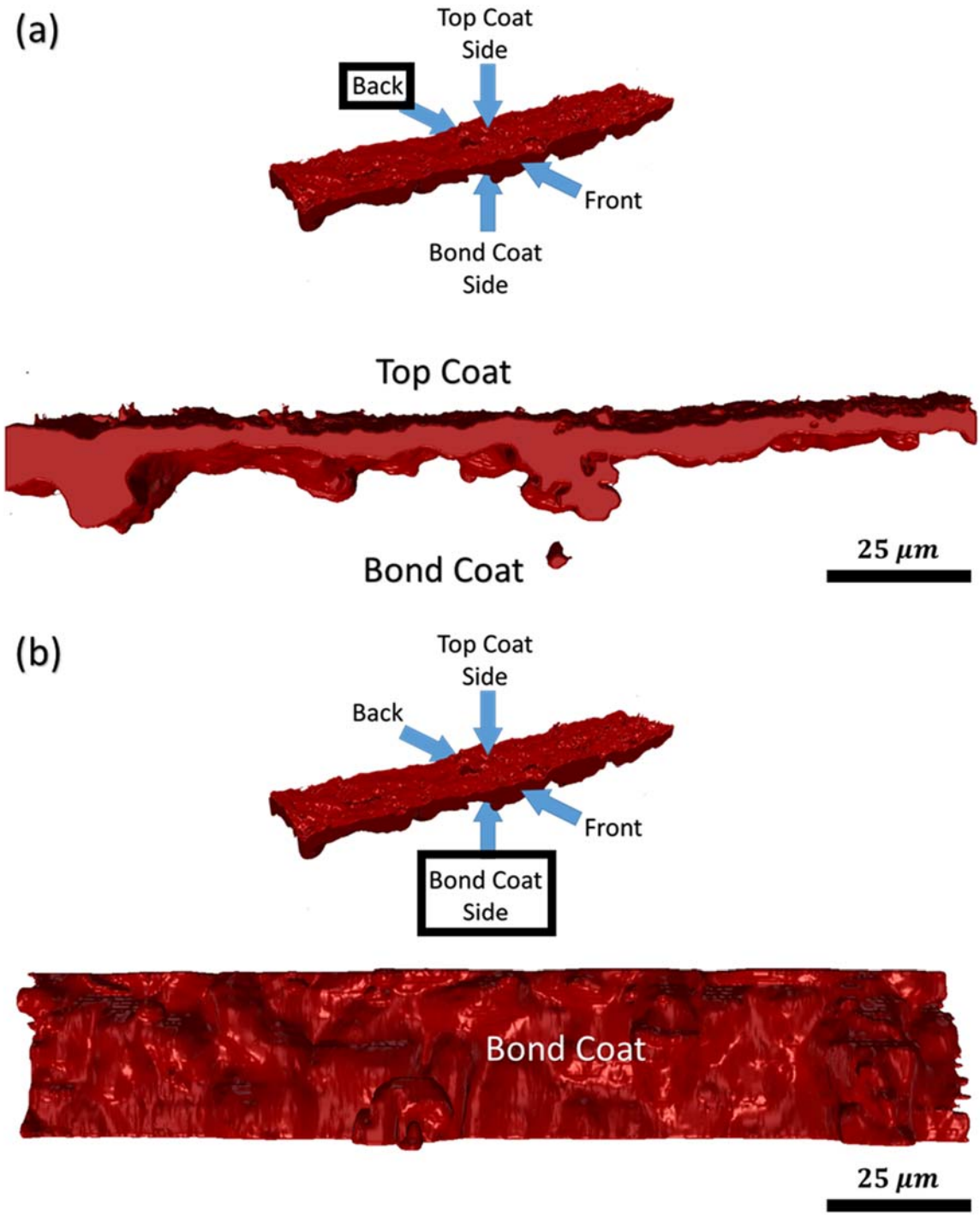

Figure 6-44: 3D reconstruction of TGO with views from the (a) back and (b) bond coat side.

6.8 Preliminary Chemical Analysis Results using Electron Microprobe

Electron microprobe analysis (EMPA) is an analytical technique that is used to establish chemical composition maps by measuring the resultant characteristic x-rays a sample when bombarded with an electron beam. The EMPA technique allows for high spatial resolution and sensitivity through the use of wavelength-dispersive x-ray spectroscopy (WDS). As opposed to energy-dispersive x-ray spectroscopy, where a broad spectrum of x-rays are samples, the WDS technique only counts x-rays of a single wavelength at one time. This allows for higher sensitivity than would able to detect with EDS, with newer EMPA machines utilizing WDS being able to detect as little as 10 ppm concentrations. For a more detailed overview on the EMPA technique the reader is encouraged to view *Electron Microprobe Analysis* by Reed [28] and *Scanning Electron Microscopy and X-Ray Microanalysis: A text for biologists, materials scientist and geologists* by Goldstein [29]. Numerous studies on TBC systems have utilized the EMPA technique to provide insight into the causes of failure mechanisms [30-32].

To investigate whether the drop in interfacial toughness was due to chemical changes within the TBC layers during thermal cycling, EMPA was conducted on CED samples at GE. Two scans were conducted on cross-sections of CED samples at 0% and 50% of furnace cycle lifetime. The generated chemical composition maps can be seen in Figure 6-45 and Figure 6-46. Each figure shown a backscattered electron (BSE) image and chemical composition maps for the following chemical spectra: O (K_α), Ni (K_α), Ta (L_α), Zr (L_α), N, (K_α), S (K_α) and Al (K_α).

No changes are observed within the top coat during thermal cycling. At 50% of furnace cycle lifetime the bond coat exhibits 4% increase in Ni content and a 5% reduction in Al

content. This behavior is expected as the upward flux of Al during thermal cycling reacts with O_2 to grow the α-Al_2O_3 TGO scale and is not indicative of deleterious Al depletion associated with premature spalling behavior [32, 33]. No appreciable change in the chemistry at the interface occurred during the transition from the as-deposited state to 50% of furnace cycle lifetime. Of importance is the relative absence of S from the interface as S has been shown to have deleterious effects on interfacial adhesion [34-37]. While the chemical analysis using EMPA did not show an observable change in the chemistry of the TBC system, it reinforces the idea that the cause of the interfacial degradation is due solely to morphological changes in the interface and not due to chemical changes.

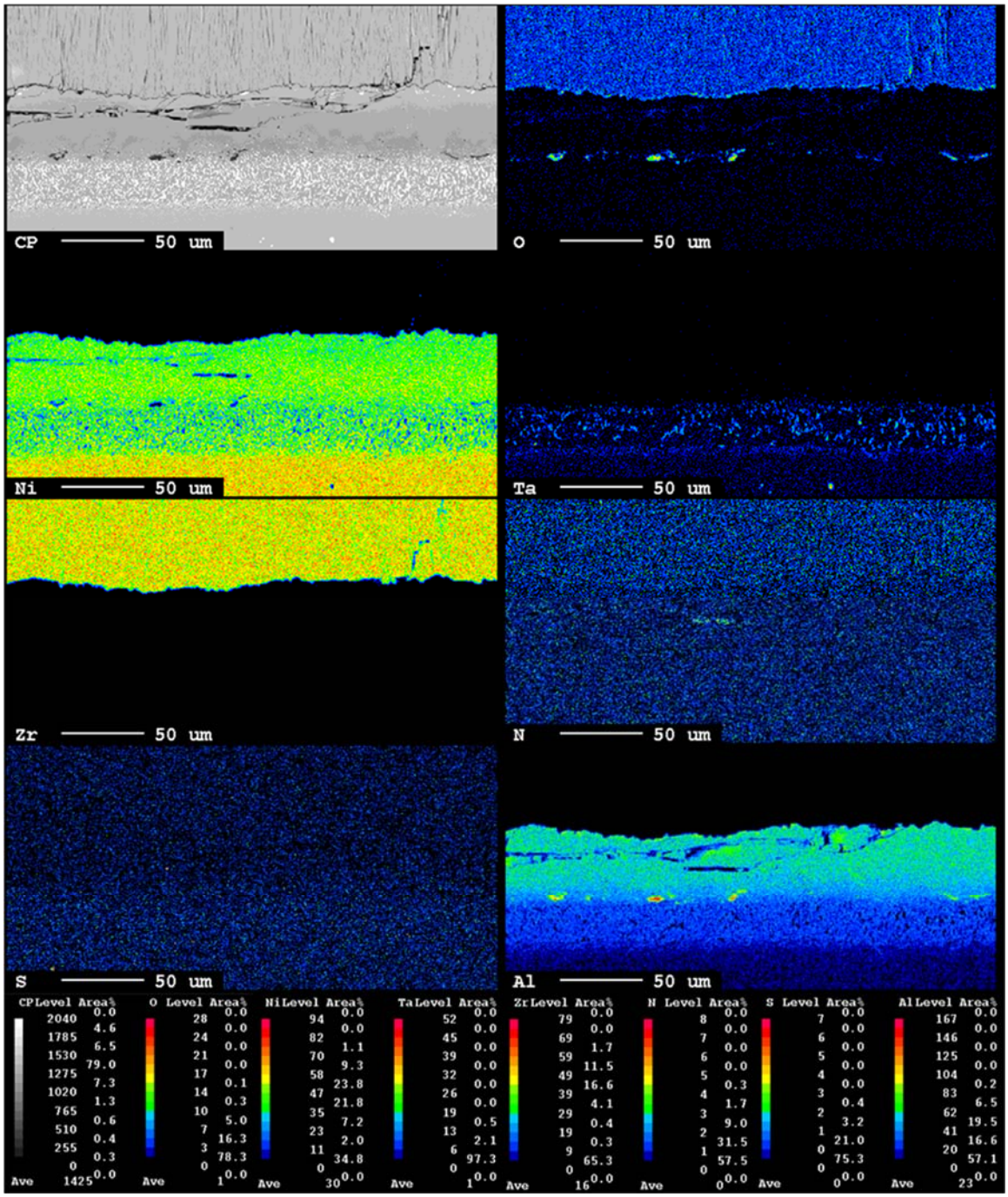

Figure 6-45: Chemical composition map of CED cross section at 0% of furnace cycle lifetime collected using electron microprobe as GE

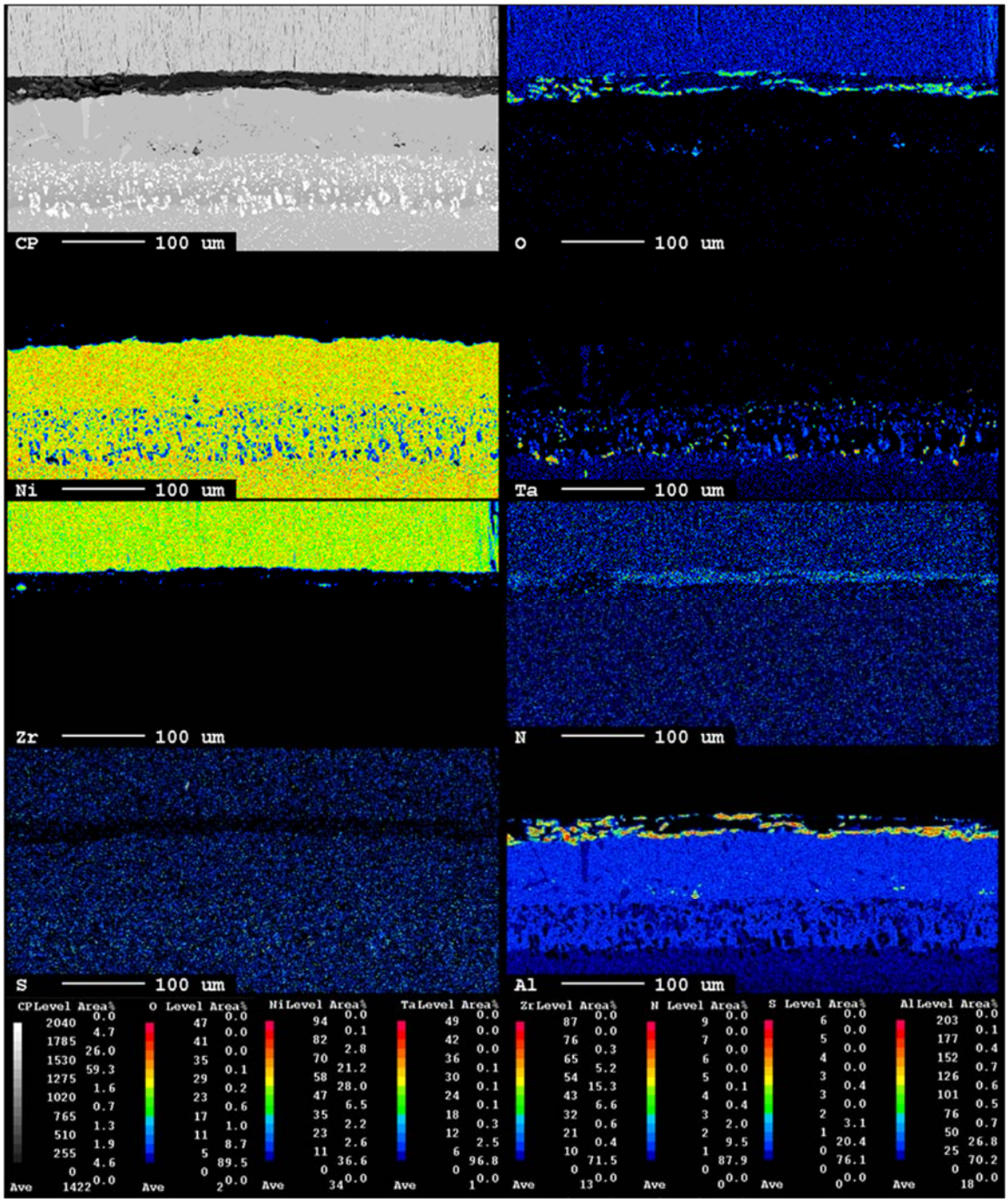

Figure 6-46: Chemical composition map of CED cross section at 50% of furnace cycle lifetime collected using electron microprobe as GE

6.9 References for Chapter 6

1. Evans, A.G.M., D.R.; Hutchinson, J.W.; Meier, G.H.; Pettit, F.S., *Mechanisms controlling the durability of thermal barrier coatings.* Progress in Materials Science, 2001. **46**: p. 505-553.
2. Karlsson, A.M.H., J.W.; Evans, A.G., *The displacement of the thermally grown oxide in thermal barrier systems upon temperature cycling.* Materials Science and Engineering, 2003. **A351**: p. 244-257.
3. Yu, Z.Z., Hengbei; Wadley, Haydn N.G., *The vapor deposition and oxidation of platinum- and yttrie-stabilized zirconia multilayers.* Journal of American Ceramics Society, 2011. **94**(8): p. 2671-2679.
4. Li, C.C.W., T.; Liu, X.J.; Zheng, Z.H.; Li, Q., *Evolution of mechanical properties of thermal barrier coatings subjected to thermal exposure by instrumented indentation testing.* Ceramics International, 2016. **42**: p. 10242-10250.
5. Thery, P.Y.P., M.; Dupeux, M.; Braccini, M., *Adhesion energy of a YPSZ EB-PVD layer in two thermal barrier coating systems.* Surface & Coating Technology, 2007. **202**: p. 648-652.
6. Théry, P.-Y., et al., *Spallation of two thermal barrier coating systems: experimental study of adhesion and energetic approach to lifetime during cyclic oxidation.* Journal of Materials Science, 2008. **44**(7): p. 1726-1733.
7. Hutchinson, J.W. and Z. Suo, *Mixed Mode Cracking in Layered Materials*, in *Advances in Applied Mechanics*, W.H. John and Y.W. Theodore, Editors. 1991, Elsevier. p. 63-191.
8. Eberl, C., et al., *In Situ Measurement of the Toughness of the Interface Between a Thermal Barrier Coating and a Ni Alloy.* Journal of the American Ceramic Society, 2011. **94**: p. s120-s127.
9. Vasinonta, A. and J.L. Beuth, *Measurement of interfacial toughness in thermal barrier coating systems by indentation.* Engineering Fracture Mechanics, 2001. **68**(7): p. 843-860.
10. Hutchinson, J.W., M.Y. He, and A.G. Evans, *The influence of imperfections on the nucleation and propagation of buckling driven delaminations.* Journal of the Mechanics and Physics of Solids, 2000. **48**(4): p. 709-734.
11. Liu, Y.-F., Y. Kagawa, and A.G. Evans, *Analysis of a "barb test" for measuring the mixed-mode delamination toughness of coatings.* Acta Materialia, 2008. **56**(1): p. 43-49.
12. Tanaka, M., et al., *Delamination toughness of electron beam physical vapor deposition (EB-PVD) Y2O3–ZrO2 thermal barrier coatings by the pushout method: Effect of thermal cycling temperature.* Journal of Materials Research, 2008. **23**(09): p. 2382-2392.

13. Wang, J.S. and A.G. Evans, *Measurement and analysis of buckling and buckle propagation in compressed oxide layers on superalloy substrates.* Acta Materialia, 1998. **46**(14): p. 4993-5005.

14. Wang, J.S. and A.G. Evans, *Effects of strain cycling on buckling, cracking and spalling of a thermally grown alumina on a nickel-based bond coat.* Acta Materialia, 1999. **47**(2): p. 699-710.

15. Cao, H.C.E., A.G., *An experimental study of the fracture resistance of bimaterial interfaces.* Mechanics of Materials, 1988. **7**(4): p. 295-304.

16. Evans, A.G.R., M.; Dalgleish, B.J.; Charalambides, P.G., *The fracture energy of bimaterial interfaces.* Materials Science and Engineering, 1989. **126**.

17. Zhang, B., *Experimental characterization of thermal barrier coatings using micro-scale bending techniques*, in *Department of Mechanical Engineering*. 2015, Johns Hopkins University: Baltimore, MD.

18. Zhou, L., et al., *Failure characteristics and mechanisms of EB-PVD TBCs with Pt-modified NiAl bond coats.* Materials Science and Engineering: A, 2015. **637**: p. 98-106.

19. Davidovits, P.E., M.D., *Scanning laser micrscope.* Nature, 1969. **223**: p. 831.

20. Davidovits, P.E., M.D., *Scanning laser microscope for biological investigations.* Applied Optics, 1971. **10**(7): p. 1615-1619.

21. Paddock, S.W., *Confocal Laser Scanning Microscopy.* BioTechniques, 1999. **27**: p. 992-104

22. Merson, E., et al., *Quantitative characterization of cleavage and hydrogen-assisted quasi-cleavage fracture surfaces with the use of confocal laser scanning microscopy.* Materials Science and Engineering: A, 2016. **665**: p. 35-46.

23. Ilčíková, M., et al., *Visualization of carbon nanotubes dispersion in composite by using confocal laser scanning microscopy.* European Polymer Journal, 2016. **79**: p. 187-197.

24. Sondej, F., A. Bück, and E. Tsotsas, *Comparative analysis of the coating thickness on single particles using X-ray micro-computed tomography and confocal laser-scanning microscopy.* Powder Technology, 2016. **287**: p. 330-340.

25. Zou, Y., M. Kaestner, and E. Reithmeier, *A method for multi-resolution characterization on porous surfaces by using a laser confocal scanning microscope.* Optics and Lasers in Engineering, 2015. **74**: p. 40-46.

26. Groeber, M.A. and M.A. Jackson, *DREAM.3D: A Digital Representation Environment for the Analysis of Microstructure in 3D.* Integrating Materials and Manufacturing Innovation, 2014. **3**(1): p. 1-17.

27. *Kitware* . http://www.paraview.org.

28. Reed, S.J.B., *Electron Microprobe Analysis (2nd Ed.)*. 1993: Cambridge University Press.

29. Goldstein, J.I.N., D.E.; Echlin, P.; Joy, D.C.; Lyman, C.E.; Lifshin, E.; Sawyer, L.C.; Michael, J.R., *Scanning Electron Microscopy and X-Ray Microanalysis: A text for biologists, materials scientists, and geologists (3rd Ed.)*. 2003: Penum Press.

30. Rabiei, A. and A.G. Evans, *Failure mechanisms associated with the thermally grown oxide in plasma-sprayed thermal barrier coatings.* Acta Materialia, 2000. **48**(15): p. 3963-3976.

31. Vidal-Sétif, M.H., et al., *Microstructural characterization of the interaction between 8YPSZ (EB-PVD) thermal barrier coatings and a synthetic CAS.* Surface and Coatings Technology, 2014. **239**: p. 41-48.

32. Renusch, D., M. Schorr, and M. Schütze, *The role that bond coat depletion of aluminum has on the lifetime of APS-TBC under oxidizing conditions.* Materials and Corrosion, 2008. **59**(7): p. 547-555.

33. Shillington, E.A.G. and D.R. Clarke, *Spalling failure of a thermal barrier coating associated with aluminum depletion in the bond-coat.* Acta Materialia, 1999. **47**(4): p. 1297-1305.

34. Smeggil, J.G., A.W. Funkenbusch, and N.S. Bornstein, *A relationship between indigenous impurity elements and protective oxide scale adherence characteristics.* Metallurgical Transactions A, 1986. **17**(6): p. 923-932.

35. Smialek, J.L., *Effect of sulfur removal on Al2O3 scale adhesion.* Metallurgical Transactions A, 1991. **22**(3): p. 739-752.

36. Rivoaland, L., et al., *The Effect of Sulfur Segregation on the Adherence of the Thermally-Grown Oxide on NiAl—I: Sulfur Segregation on the Metallic Surface of NiAl(001) Single-Crystals and at NiAl(001)/Al2O3 Interfaces.* Oxidation of Metals, 2003. **60**(1): p. 137-157.

37. Rivoaland, L., et al., *The Effect of Sulfur Segregation on the Adherence of the Thermally-Grown Oxide on NiAl—II: The Oxidation Behavior at 900°C of Standard, Desulfurized or Sulfur-Doped NiAl(001) Single-Crystals.* Oxidation of Metals, 2003. **60**(1): p. 159-178.

CHAPTER 7: CONCLUSIONS

This dissertation was conducted to characterize the interfacial toughness of the TBC top coat/bond coat interface under the failure conditions most representative of in-service TBC spallation (pure Mode II) using the newly develop CED test method. Additional work was done to understand how the toughness degrades with thermal exposure and how it varies with mode-mix utilizing the modified 4-point bend test.

7.1 Summary of Research

There are many complex mechanisms that lead to the degradation of the interfacial toughness in TBC systems that are used in aircraft and power generation jet turbine. Due to the complexity of these mechanisms no robust methods for lifetime assessment of these coatings that predict the degradation processes have been developed due to their intrinsic complexity. It is for this reason that direct measurements of TBC interfacial toughness are an essential of any lifetime assessment approach. Under the conditions most representative of TBC delamination during turbine service, characterization of the pure mode II interfacial toughness is of special importance.

- To determine the pure mode II toughness a theoretically proposed CED test method [1] was developed into a robust experimental framework. To explore the effect of mode-mix and to compare the results for this material system directly to previously published results another test method was desired in addition to the CED method. The modified 4-point bend test had been used successfully to calculate interfacial toughness values for EB-PVD coated specimens [2, 3] and was chosen due to its straightforward experimental and analysis procedure. With these two test methods:

i) the dependence of the interfacial toughness on mode-mix could be determined, ii) comparisons could be made against the results of this study to previous work, iii) the degradation of the interface through thermal cycling under pure mode II conditions could be measured and iv) important microstructural and chemical changes observed during thermal cycling could be linked to the observed degradation process.

- The mechanics behind both the CED and the modified 4-point bend tests were derived and the analytical results were used to design the geometry of the samples. To produce the CED samples a custom EB-PVD coating fixture was designed and created so that samples could be coated alongside production turbine blades. The creation of this fixture facilitated production of the CED samples as close to in-service hardware as possible. The modified 4-point bend sample were also coated in the same coating chamber as the in-service hardware, but the design of a custom coating fixture was not needed as it was determined samples could be tack welded to a Ni-based superalloy post for coating. Initial testing revealed the need for a pre-crack in both the CED and modified 4-point bend specimens. By researching methods for cleaning the bond coat and top coat layers off damaged in-service turbine blades, the recipe for a bond coat acid etchant was discovered. Unique methods for both the CED and modified 4-point bend specimens, using this acid etchant, were developed. This bond coat etching lead to the creation of pre-crack that enable successful testing of samples. In order to aid in the experimental analysis of the samples, measurements were made of the TGO thickness at various levels of furnace cycle lifetime. The resultant TGO growth behavior was

determined to be comparable to previously reported values. In order to characterize the interfacial friction coefficient, modifications were made to the micro-bending setup to conduct the tribological tests at various levels of furnace cycle lifetime. When the friction coefficient values were plotted against the percentage of furnace cycle lifetime, it was apparent that there was no general trend for the interfacial friction coefficient. An average of the entire dataset was taken and the interfacial friction coefficient was determined to be $\mu_f = 0.51$ with a standard deviation of 0.1.

- FE modelling was used to determine the phase angle of fracture for both the CED and modified 4-point bend specimens. For the CED and modified 4-point bend specimens, phase angles of $\phi = -89.7°$ and $\phi = 42.4°$ were determined, respectively. The use of detailed FE models elucidated the apparent decrease in interfacial toughness due to interfacial friction and variable TGO thickness on the CED samples. These results were then applied to an analytical framework where experimental results could be determined at any arbitrary TGO thickness and interfacial friction coefficient. As the growth behavior of the TGO was previously determined and the interfacial friction coefficient was calculated, a single equation was arrived at that could be used to analyze all CED results from this study. In the as-deposited state the average interfacial toughness was calculated to be $537\ J/m^2$ and at coating lifetime the interfacial toughens lowers to approximately $252\ J/m^2$, which corresponds to a drop in interfacial toughness of $285\ J/m^2$ over the lifetime of the material system.

- An inverse FE method utilizing the VCCT method was developed for analysis of the modified 4-point bend specimen. A series of simulations were conducted to find a numerical relation between the critical load during cracking and the interfacial toughness for the geometry and layer material properties used in this study. With this relation developed the interfacial toughness values were determined to be $G_c = 124.41\ J/m^2$ with a standard deviation of $11.34\ J/m^2$ and a total range of $37.23\ J/m^2$. The results for this test were within 10% of work previously conducted on EB-PVD coated specimens subjected to the same modified 4-point bend loading [2, 3].
- Before the undertaking of this study no general trend between the interfacial toughness and the mode-mix for TBC systems had been determined. Comparison of the interfacial toughness values from the CED and modified 4-point bend samples to those conducted in other studies resulted in the determination of an asymmetric toughness function describing the relation between the interfacial toughness and the phase angle of loading.
- To aid in the understanding of the experimental results a number of fractographic and microstructural observations were made. Measurement were made to determine the roughness of the bond coat/top coat interface on cross-sectioned samples at various levels of furnace cycle lifetime. Samples were imaged in the SEM, thresholded to reveal the interface profile using ImageJ and roughness values calculated using a custom MATLAB script. The roughness values were found to rise fairly slowly from $R_a = 1.8\ \mu m$ in the as-deposited state to $R_a = 2.5\ \mu m$ at 50% of lifetime and then rises more rapidly to $R_a = 3.5\ \mu m$ at the coating lifetime.

- To determine the roughness of the delaminated fracture surface, samples were imaged using confocal laser scanning microscope. From the results there was little change in the fracture surface roughness between the as-deposited state and 28% of lifetime. However, between 28% and 56% of lifetime the fracture surface roughness began to rise and at 56% of lifetime rese rapidly to the roughness of $R_a = 2.8\ \mu m$ at the coating lifetime. Comparison of the interface and fracture surface roughness reveled that in the as-deposited the roughness values were both the same value, but as the level of furnace cycle lifetime rose, the interfacial toughness became larger than the fracture surface roughness. This results indicated a divergence of the crack path away from the bond coat/top coat interface, in the as-deposisted state, as the level of furnace cycle lifetime rose. From the optical and laser image data captured using the CLSM, thresholded maps revealing the relative area percent of each material layer was determined. The results indicated that the crack path tended to move into the top coat as the number of furnace cycles increased.
- Preliminary work was also conducted to construct 3D images of the interface, including TGO and void morphology, using images captured though serial sectioning at GE. Preliminary chemical analysis was also conducted using EMPA that showed no appreciable change in the chemistry during thermal cycling. This result helped solidify the idea that the morphological changes, and not chemical changes, observed in the coating are the cause of interfacial toughness degradation.

7.2 Future Research Directions and Recommendations

- The salient findings in this study have helped to gain a better understanding of both the interfacial toughness evolution but also an insight into the underlying damage

mechanisms occurring. These finding also encourage further investigations into the role of substrate and bond coat composition on the interfacial toughness. In this study only one materials system was studied. A logical extension of this work would include testing of other combinations of substrate and bond coat compositions to see if they not only exhibit the same as-deposited behavior, but also their degradation through thermal cycling.

- This study used the CED test to determine the thermal cycling behavior under pure mode II conditions and used the modified 4-point bend test to determine the as-deposited interfacial toughness under mixed-mode conditions. Conducting interfacial toughness tests over a range of mode-mixes, but also at various levels of furnace cycle lifetime will provide a 3D landscape. This determination of the evolution of the interfacial toughness as a function of both mode-mix and thermal history will provide useful information that engine hardware designers will be able to take advantage of.
- In this study only the modified 4-point bend test was conducted to measure the interfacial toughness under mixed-mode conditions. One similar test method that can be utilized is the inverted modified 4-point bend test [1]. This test allows for measurement of the interfacial toughness at a mode-mix of $\phi = -60°$. The CED, modified 4-point bend and inverted modified 4-point bend tests would provide three measurements of the interfacial toughness at three different mode-mixes. These results would provide the necessary inputs to derive an asymmetric function solely from one controlled set of identically produced samples.

- Conducting tests not only at different mode-mixes but also at different levels of furnace cycle lifetime would provide a more detailed understanding of the lifetime behavior of the TBC system. An overview of the work conducted in this study, work conducted in other studies and the landscape for future work is shown in Figure 7-1. By filling in the shaded area of the plot, a more complete understanding of the dependence of the interfacial toughness on phase angle and percentage of furnace cycle lifetime can be determined. This would allow for industrial part manufacturers to better numerically model TBC lifetime on in-service components using FE analysis. This in turn would lead to better designed TBC systems capable of higher operating temperatures and longer lifetimes.

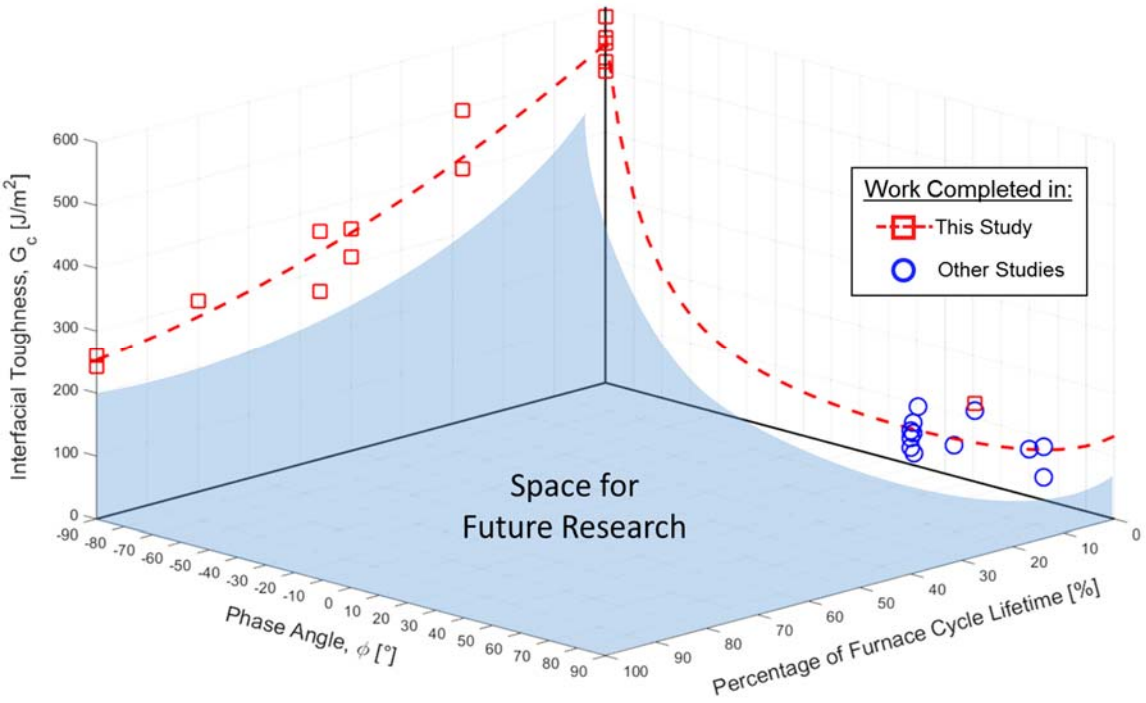

Figure 7-1: Plot of interfacial toughness results from this study, results from previously conducted work, and landscape for future investigations

- Expanding on the serial sectioning work will provide insight into the population of pre-cracks and initial delaminations and their locations within the coating system at various levels of furnace cycle lifetime. By gathering this knowledge estimates on the percentage of the interface already damaged can be collected. This information can be used to determine whether the measured drop in the interfacial toughness is due to a true degradation of the entire interface or if it is due to progressive cracking and delamination of the interface that lessens the whole bonded area. It will also allow for the collecting of invaluable statistics regarding the 3D growth behavior of the TGO. One important challenge to overcome in this work will be distinguishing between cracks inherent in the material system and cracks caused by sample preparation.
- Additional chemical characterization would be advantageous especially on smaller sampling areas around the interface. Although no chemical changes were observed in the preliminary set of samples tested, it is important to conduct more directed measurements to rule out the role of chemical changes that lead to interface degradation. This would solidify the hypothesis that morphological changes are the sole cause for interfacial toughness degradation. To ensure accurate measurement care will need to be taken to eliminate any potential contaminants on the samples that could provide spurious results.

In terms of the work presented in this study, a number of recommendations are given:

- The use of acid etching was utilized in this study to create initial regions of damage that acted like starter cracks. The use of sacrificial layers was not used due to potential contamination that could occur between sample for this study and in-

service hardware being coated in the same chamber. The use of thin layers of pure nickel, applied as either a thin foil or though sputtering, has been shown to be an effective material for creating an region of initial damage in modified 4-point bend tests [2, 3].

- In this study interfacial friction tests were conducted on substrate/stiffener pairs from the same fracture surface. One aspect of this testing that could not be accomplished was ensuring that the two sides of the fracture surface were perfectly mated with each other before the friction tests were conducted. This aspect of the tests may have neglected the contribution of asperity strengthening (presented in Section 6.3), which could potentially lead to a further decrease in the measured strain energy release rate as additional energy is being expended due to frictional effects. Conducting test on perfectly matched fracture surfaces would provide insight into whether asperity strengthening is playing a large role in the interfacial toughness calculation

7.3 References for Chapter 7

1. Hutchinson, R.G. and J.W. Hutchinson, *Lifetime Assessment for Thermal Barrier Coatings: Tests for Measuring Mixed Mode Delamination Toughness.* Journal of the American Ceramic Society, 2011. **94**: p. s85-s95.
2. Thery, P.Y.P., M.; Dupeux, M.; Braccini, M., *Adhesion energy of a YPSZ EB-PVD layer in two thermal barrier coating systems.* Surface & Coating Technology, 2007. **202**: p. 648-652.
3. Théry, P.-Y., et al., *Spallation of two thermal barrier coating systems: experimental study of adhesion and energetic approach to lifetime during cyclic oxidation.* Journal of Materials Science, 2008. **44**(7): p. 1726-1733.

APPENDIX A: MTS SERVO-HYDRAULIC SYSTEM OVERVIEW

Compression Loading Setup

The system used to conduct the compression edge-delamination test is an MTS servo-hydraulic test machine. The system includes a servo-hydraulic driven actuator with a linear variable displacement transducer (LVDT) used for displacement control and a 100 kN tension/compression load cell. The software used to control the test setup is MTS MultiPurpose TestWare (MPT) package. Image capture is accomplished through the use of a PixelLINK camera coupled with the PixeLINK Capture OEM image capturing software. Descriptions of the key components are given in the next sub-section, which is followed by an overview of the software and programs used to conduct the tests.

Overview of Key System Components

A close up image of the key testing equipment is shown in Figure 7-2. The sample is placed between 1” diameter tungsten carbide inserts in the loading platens to reduce the risk of platen damage and to ensure a non-compliant loading surface. A square enclosure made from Plexiglass Acrylic panels is used to protect the operator from any debris that might become ejected from either the sample or the tungsten carbine inserts during failure. A PixeLINK PL-B782 6.6MP CMOS Color camera is coupled with an Edmund Optics MMS Imaging Lens R-1 rear assembly and Obj-11 front objective. This combination allows for a field of view capable of capturing the entire sample with working distances between 100 mm to 200 mm. The entire imaging assembly is mounted on a tripod and positioned at an appropriate working distance.

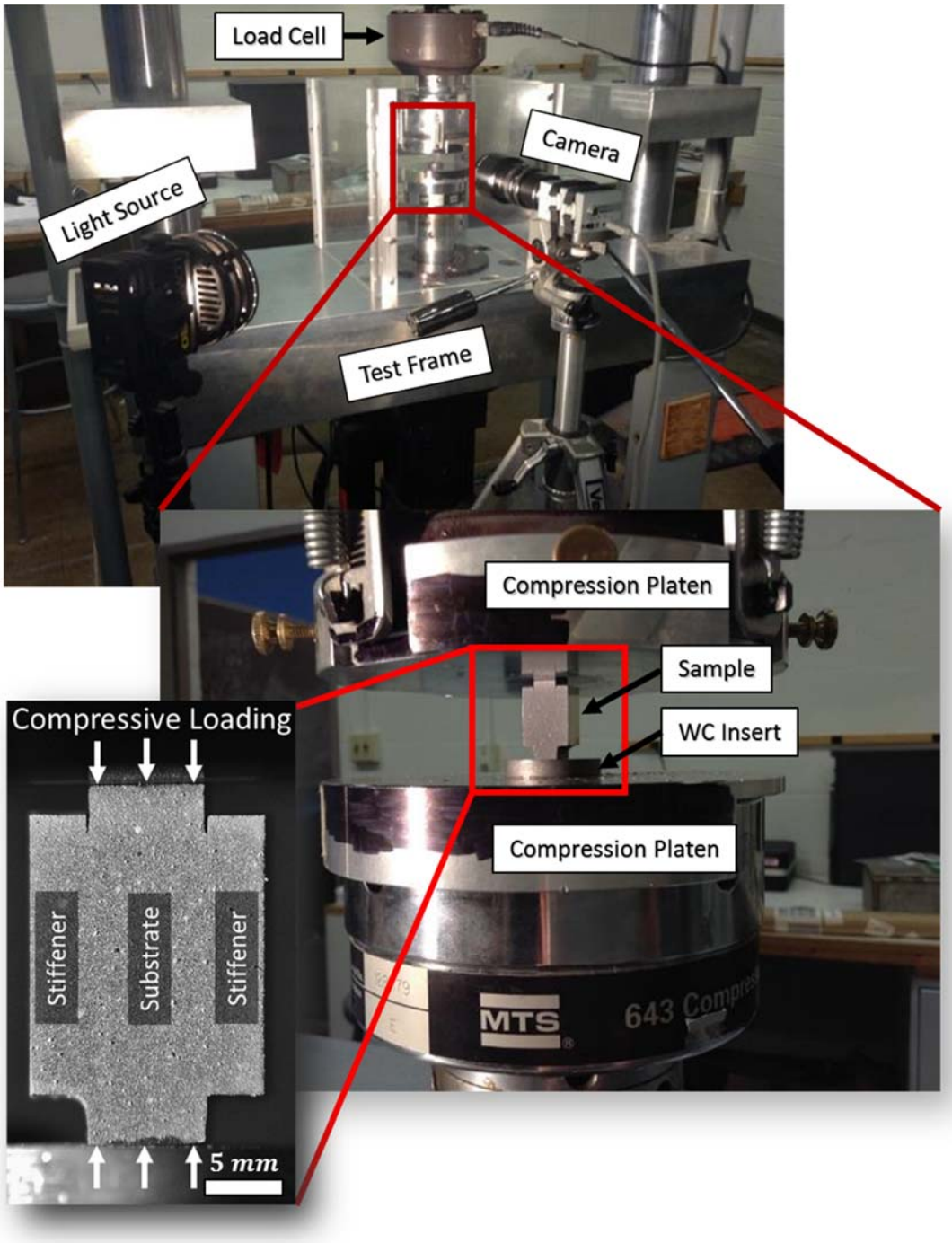

Figure 7-2: Photo of MTS servo-hydraulic test setup showing key components and orientation of sample between compression platens.

Lighting is accomplished through the use of a DiCon LED light source coupled with a dual branch adjustable light guide. The machine is controlled using a computer running the MTS

MultiPurpose TestWare software, which is capable of providing raw control of the system as well as run custom programs for the testing procedures.

Software Development and Functionality

The software used to control the compression program is the MTS MultiPorpose TestWare software that interfaces directly with the MTS servo-hydraulic control unit. The program steps are constructed from a series of distinct task types with editable parameters. These tasks can additionally have start and interrupt commands linked to them to allow for complex program structures. The program used for compression of the CED samples consists of the following steps:

1. Moving the actuator such that the sample is touching both of the compression platens with a 15 lb preload force.
2. A step where the system is commanded to maintain the constant preload of 15 lbs to ensure any settling of the sample on the platens occurs before additional loading.
3. A compression step where the sample is taken up to a specified maximum load while recording load data and capturing images.
4. Subsequent unloading of the sample until completely unloaded.

A more detailed flow chart of the sample is show in Figure 7-3.

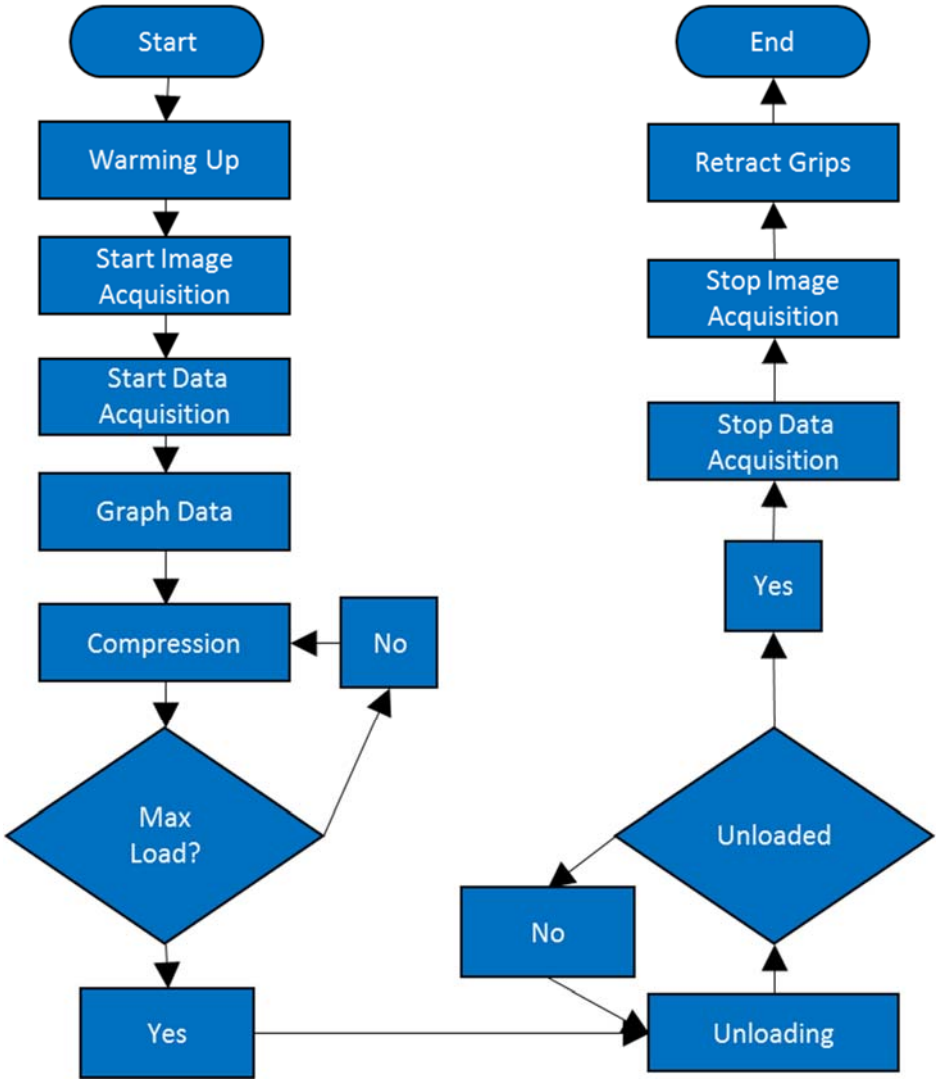

Figure 7-3: Flowchart of the basic program structure used to conduct the compression experiments of the CED sample.

For a more detailed descript of each of the steps the reader is encouraged to view the program screenshots at the end of this Appendix section.

Performance: Validation and Diagnostics

To ensure proper load measurements the test setup and the load cell were serviced by MTS prior to the beginning of this study. The entire compression machine was tested and tuned for optimal performance and the load cell was calibrated against a series of standard test specimens. Internal testing was also conducted to ensure that the accuracy of the load cell

would be sufficient to capture the small changes in load that occur during fracture events. In order to accomplish this, uniaxial compression of ASTM A36 mild steel and 6061-T6 aluminum were conducted. DIC was used to calculate sample displacements and a MATLAB script was used to stitch the load measurements with the calculated DIC strain measurements. The elastic modulus and yield strength was then determined for each material and a comparison was made to literature values. A compilation of the stress-strain curves for (a) the steel alloy and the (b) aluminum alloy can be seen in Figure 7-4. The modulus values were calculated during the unload/load portions of the stress-strain curve and the yield strength was calculated using the 0.2% strain offset method. For the ASTM A36 mild steel the average calculated modulus was $198.4\ GPa$, which corresponds to a 0.8% error from the reported value of $200\ GPa$ [1]. In addition, the average calculated yield strength was $246\ MPa$, which corresponds to a 1.6% error from the reported yield strength of $250\ MPa$ [1]. For the 6061-T6 aluminum alloy the average calculated modulus was $71.3\ GPa$, which corresponds to a 3.5% error from the reported value of $68.9\ GPa$ [2]. In addition, the average calculated yield strength was $298.2\ MPa$, which corresponds to a 8.0% error from the reported value of $276\ MPa$ [2]. The calculated error is well within acceptable experimental error and the setup was determined to be acceptable for use in this study.

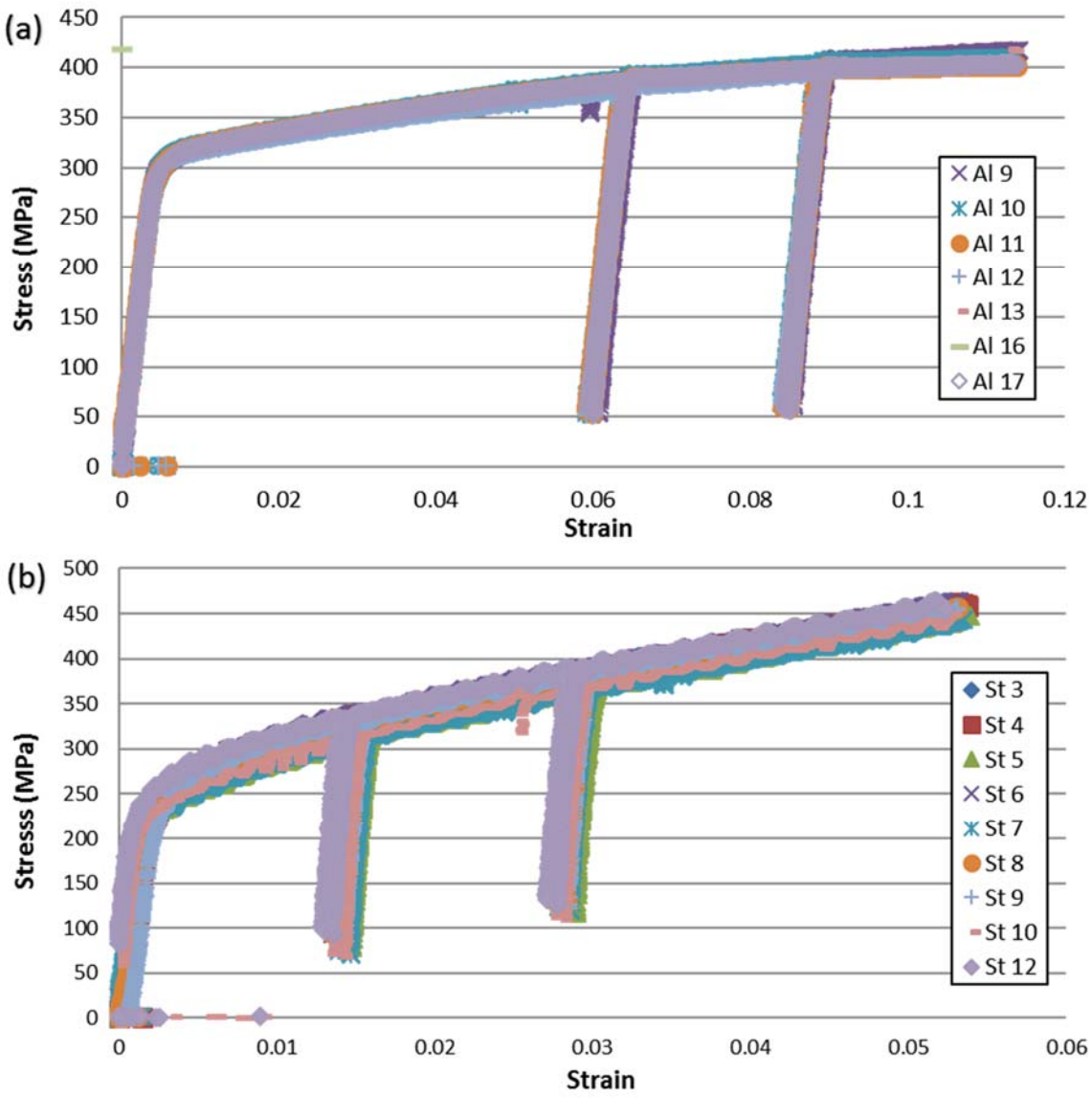

Figure 7-4: Compilation of stress-strain curves for (a) ASTM A36 mild steel and (b) 6061-T6 aluminum alloy.

MPT Procedure Editor: Main Panel

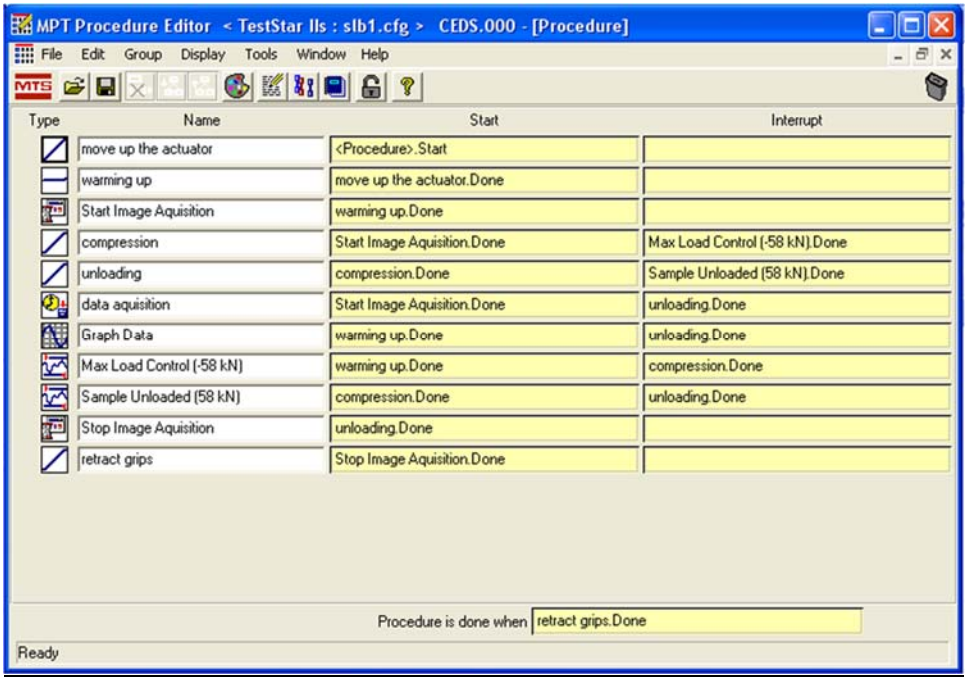

MPT Procedure Editor: Move Up Actuator

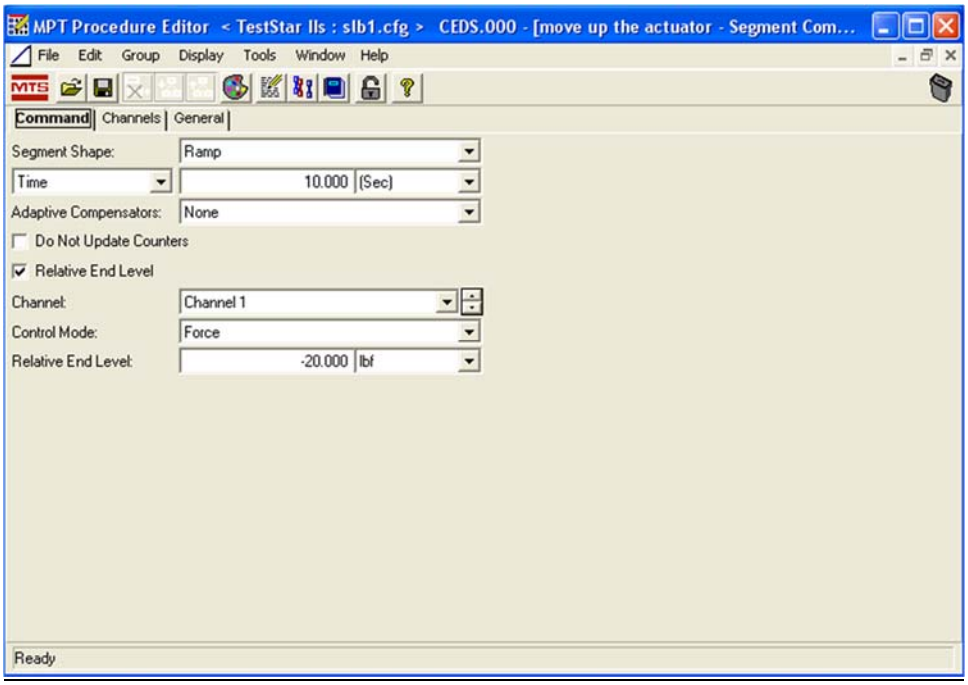

MPT Procedure Editor: Warming Up

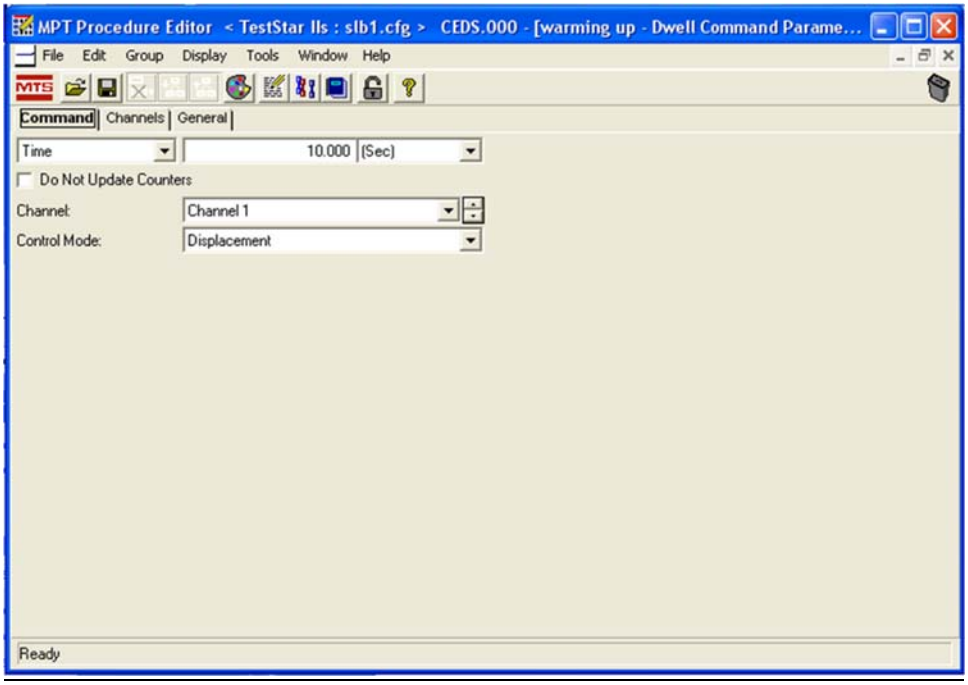

MPT Procedure Editor: Start Image Acquisition

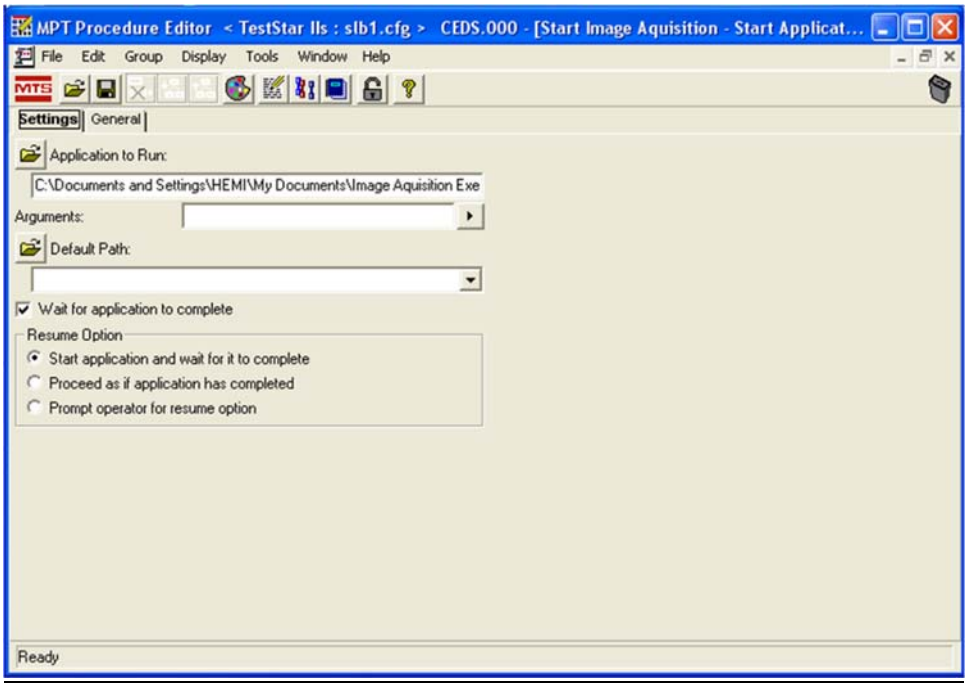

MPT Procedure Editor: Compression

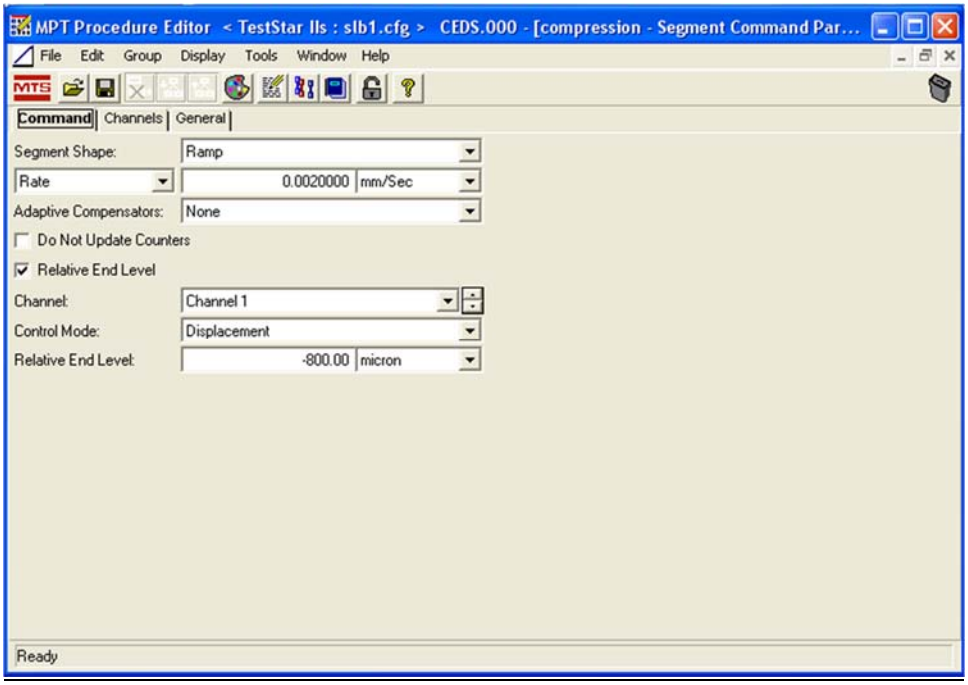

MPT Procedure Editor: Unloading

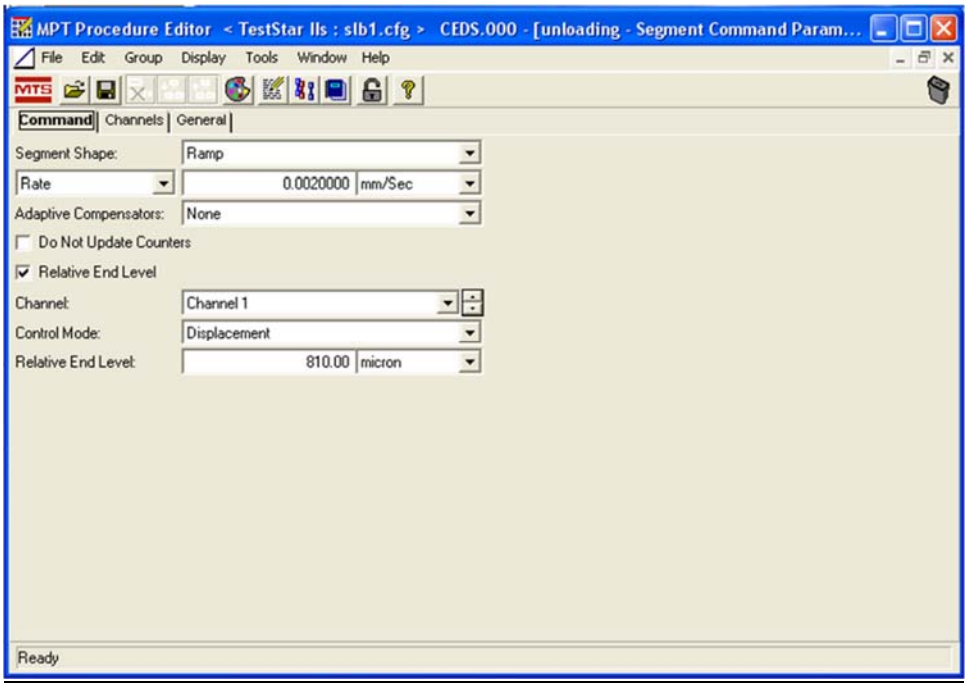

MPT Procedure Editor: Data Acquisition

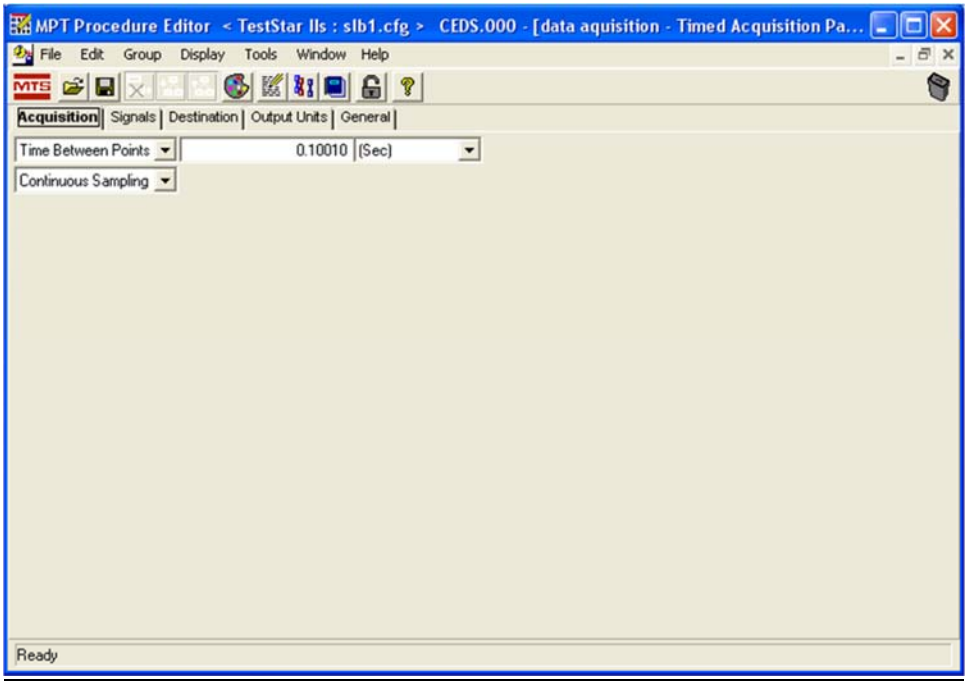

MPT Procedure Editor: Graph Data

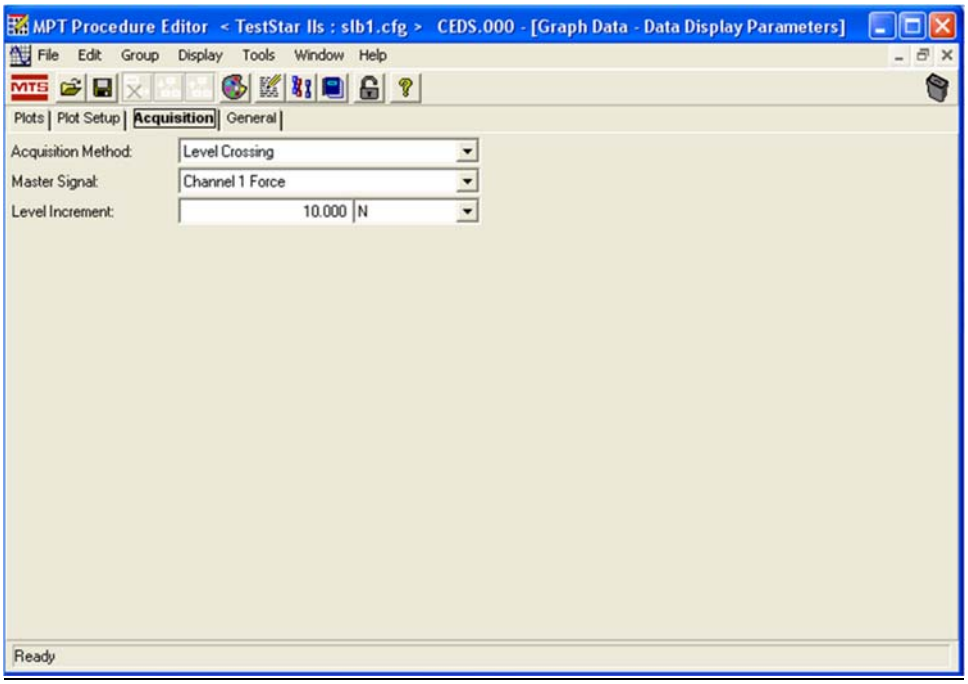

MPT Procedure Editor: Max Load Control

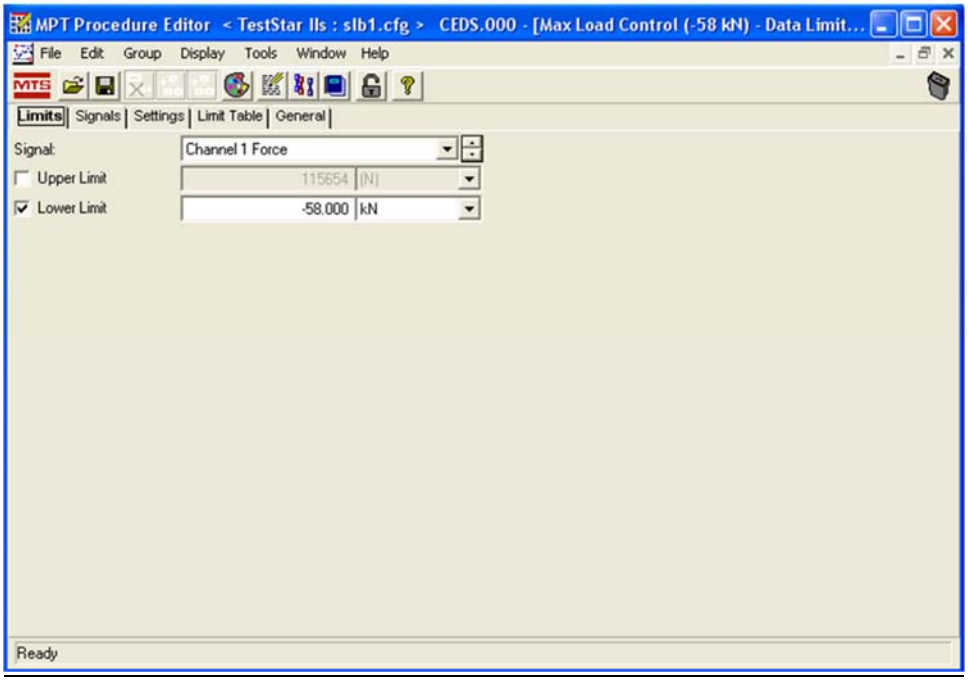

MPT Procedure Editor: Sample Unloaded

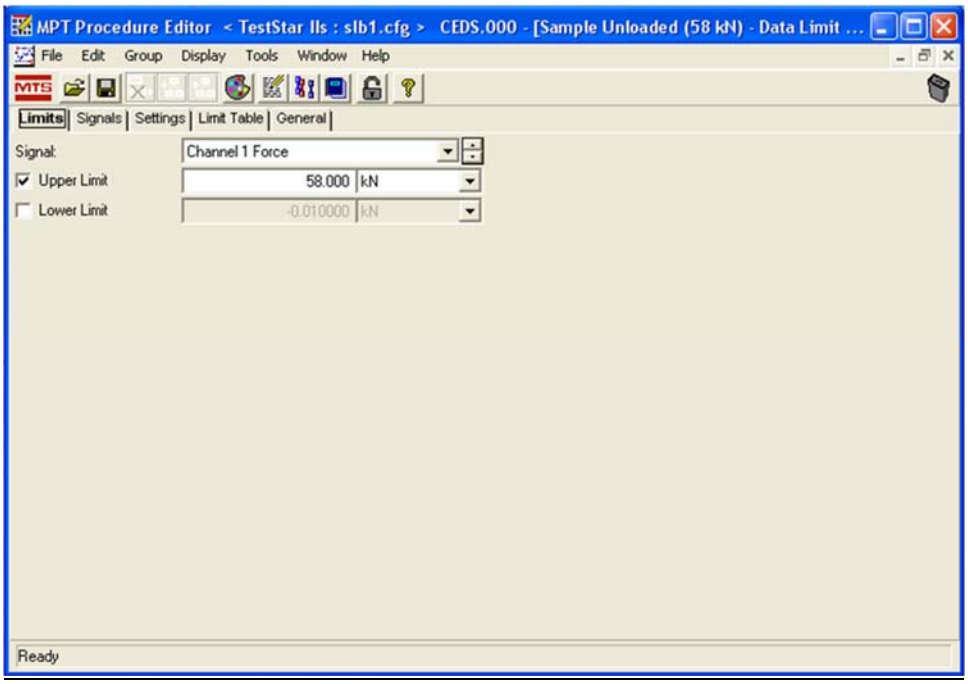

MPT Procedure Editor: Stop Image Acquisition

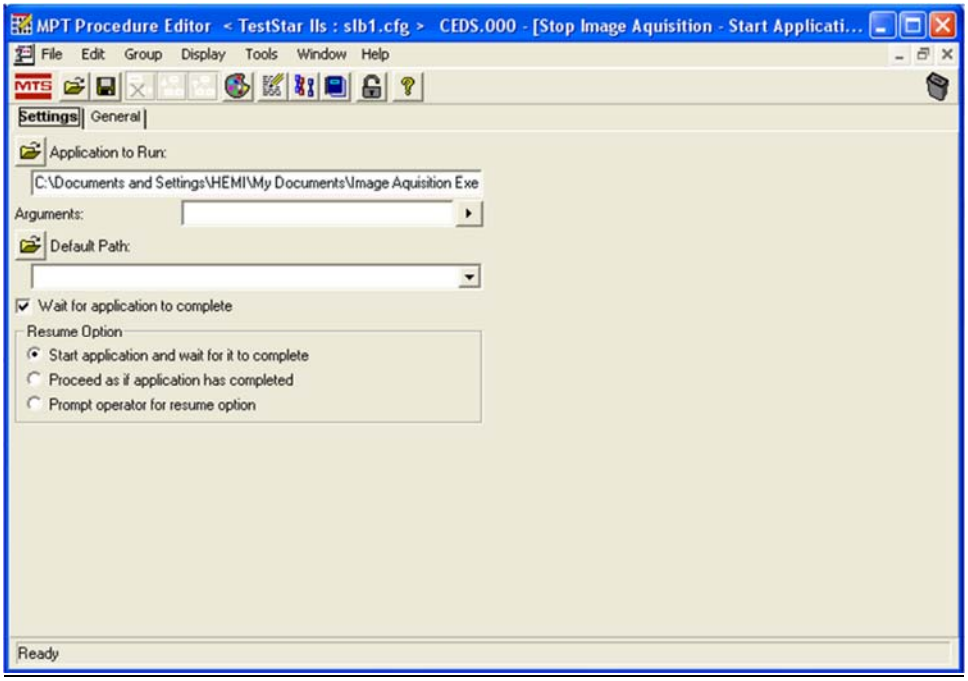

MPT Procedure Editor: Retract Grips

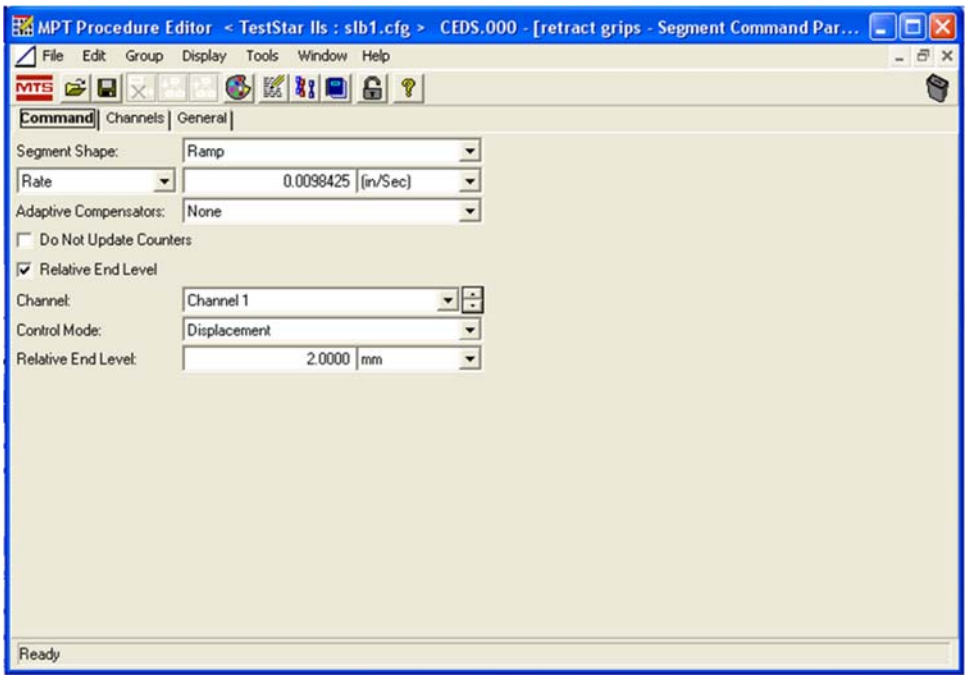

References for Appendix A

1. AZoM. *ASTM A36 Mild/Low Carbon Steel*. [Website] 2012 05/23/2014 [cited 2016.

2. International, A., *Metals Handbook, Vol.2 - Properties and Selection: Nonferrous Alloys and Special-Purpose Materials*. 1990.

APPENDIX B: MICRO-BENDING SYSTEM OVERVIEW

The system used to conduct the 4-point bend test and the interfacial friction testing is a custom made tension/compression setup made at Johns Hopkins and used in previous studies [1]. The system includes a Zaber NA34C60 stepper motor actuator with a minimum speed of $0.9302\ \mu m/s$, a maximum speed of $30\ mm/s$ and a maximum continuous thrust of $325.2\ lb$. Load measurement is accomplished through a Futek LCM300 500 lb tension/compression load cell. As the load cell rating is higher than the maximum capacity of the actuator, care is given to ensure no damage is done to the actuator. The software used to control the test setup is a custom written LabVIEW script originally written for use in another study at Johns Hopkins [1]. The script was updated to work with newer version of LabVIEW and for use with the Futek load cell and the Zaber actuator that were not present when the program was originally written. An overview of this script is outlined in at the end of this section. The Futek load cell was supplied with a certificate of calibration and therefore no additional verification was necessary. For a more detailed outline of the bending setup, the reader is encouraged to view the dissertation *Characterization of Interfacial Adhesion Between Carbon-Carbon Composite and Plasma-Sprayed Aluminum Oxide* by Justin S. Jones [1].

LabVIEW Program Front Panel

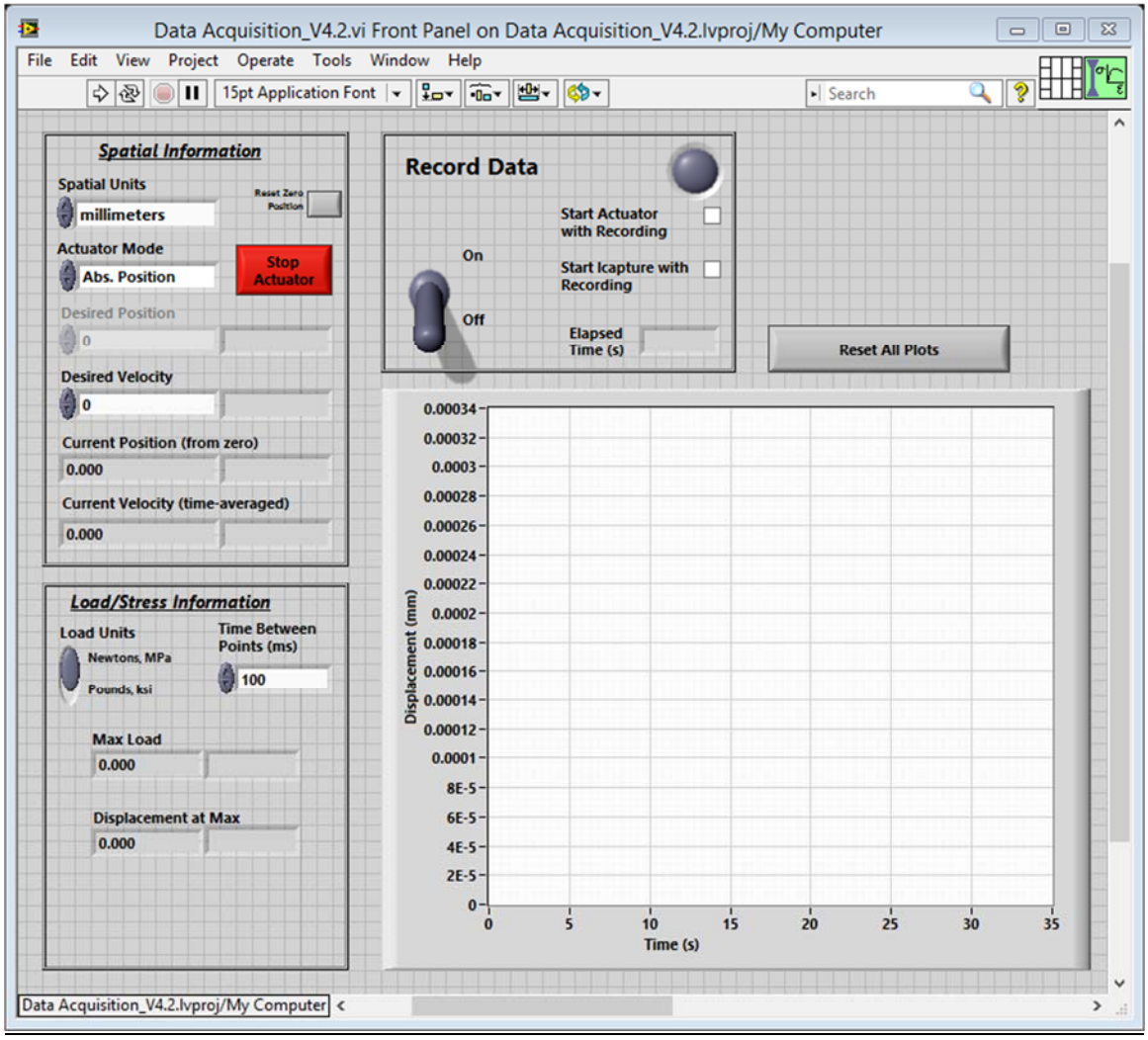

LabVIEW Wire Diagram Panel A

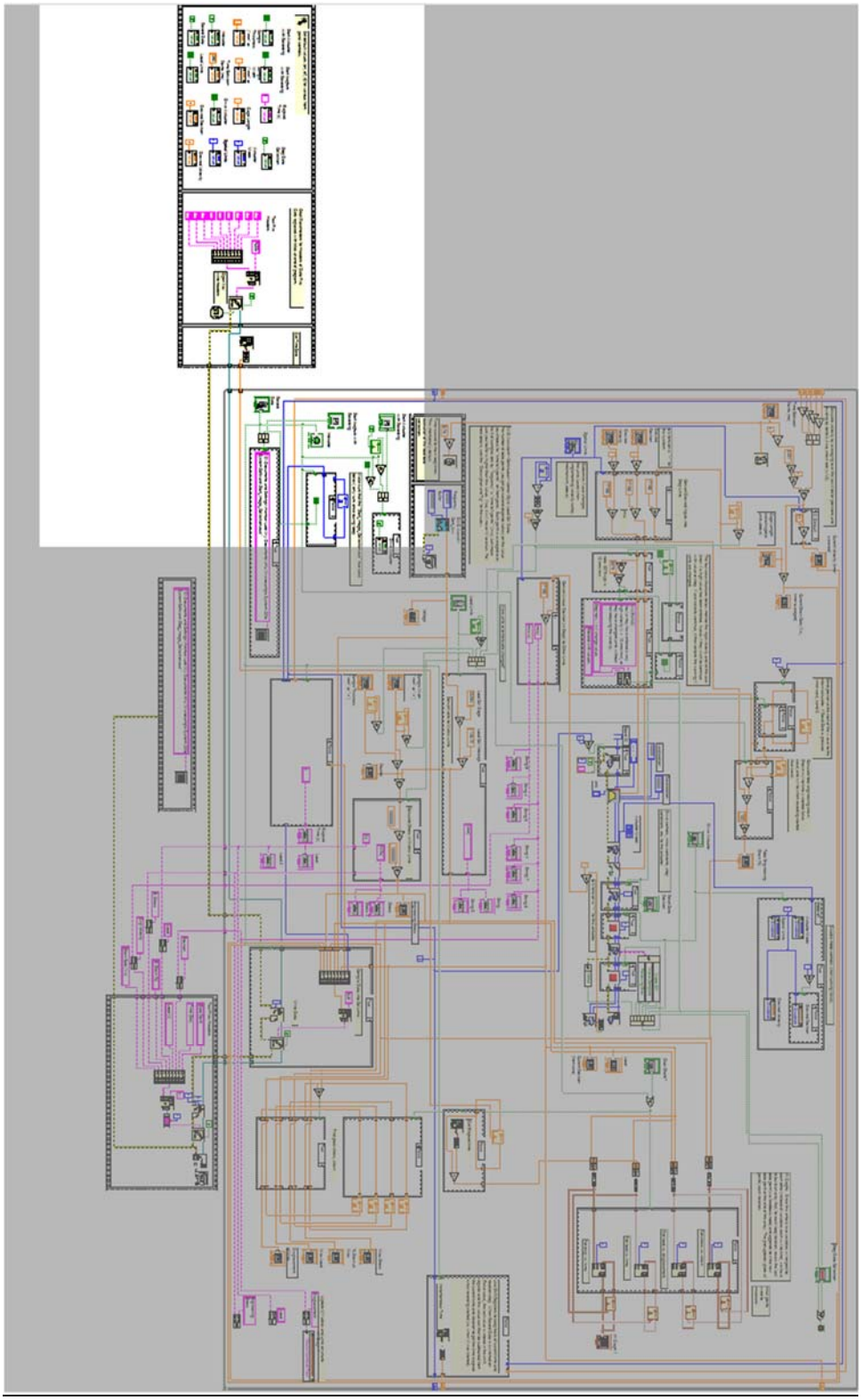

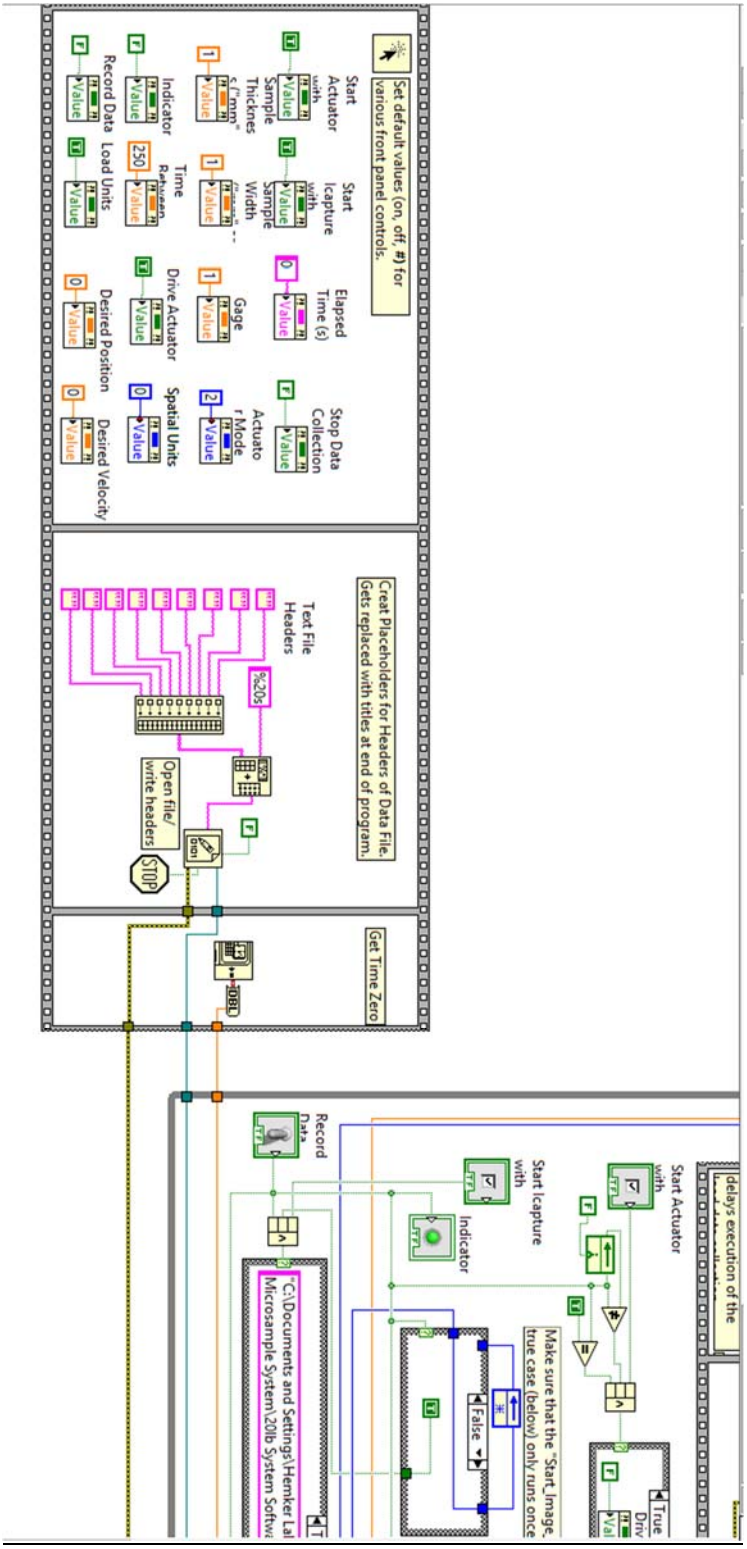
Set default values (on, off, #) for various front panel controls.
Start Actuator with
Start Icapture with
Sample Thickness (mm)
Sample Width (mm)
Elapsed Time (s)
Stop Data Collection
Indicator
Time Between
Gage
Actuator Mode
Record Data
Load Units
Drive Actuator
Spatial Units
Desired Position
Desired Velocity
Value
250
Creat Placeholders for Headers of Data File. Gets replaced with titles at end of program.
Text File Headers
%20s
Open file/ write headers
STOP
Get Time Zero
delays execution of the
Start Actuator with
Start Icapture with
Indicator
Record Data
Make sure that the "Start_Image true case (below) only runs once
False
True
Val
C:\Documents and Settings\Hemker Lal Microsample System\20lb System Softwa

LabVIEW Wire Diagram Panel B

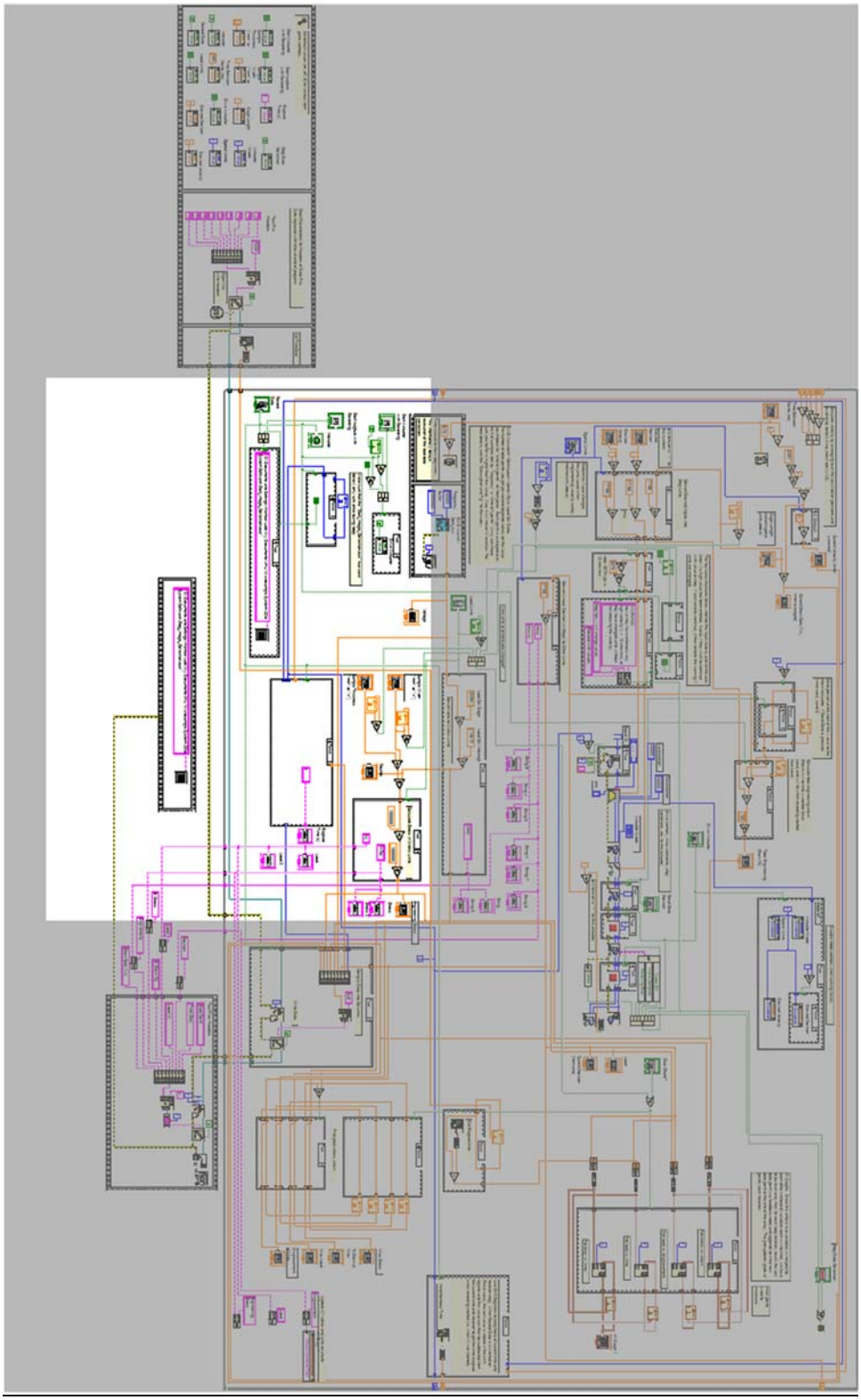

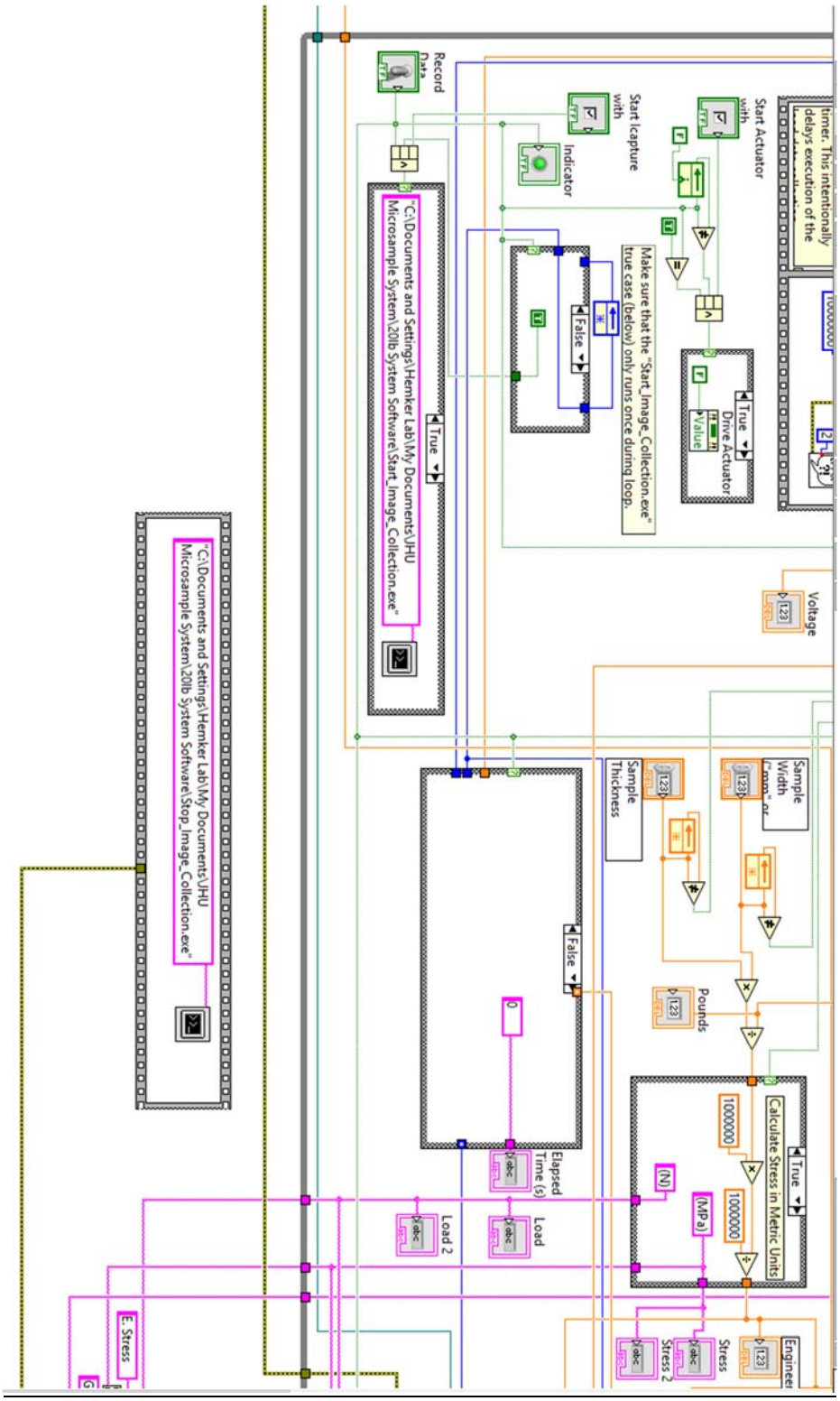
timer. This intentionally delays execution of the
Start Actuator with
Start Icapture with
Indicator
Record Data
Make sure that the "Start_Image_Collection.exe" true case (below) only runs once during loop.
Drive Actuator
Value
True
False
"C:\Documents and Settings\Hemker Lab\My Documents\JHU Microsample System\20lb System Software\Start_Image_Collection.exe"
"C:\Documents and Settings\Hemker Lab\My Documents\JHU Microsample System\20lb System Software\Stop_Image_Collection.exe"
Voltage
Sample Thickness
Pounds
Calculate Stress in Metric Units
1000000
(N)
(MPa)
Elapsed Time (s)
Load
Load 2
Stress
Stress 2
E. Stress

LabVIEW Wire Diagram Panel C

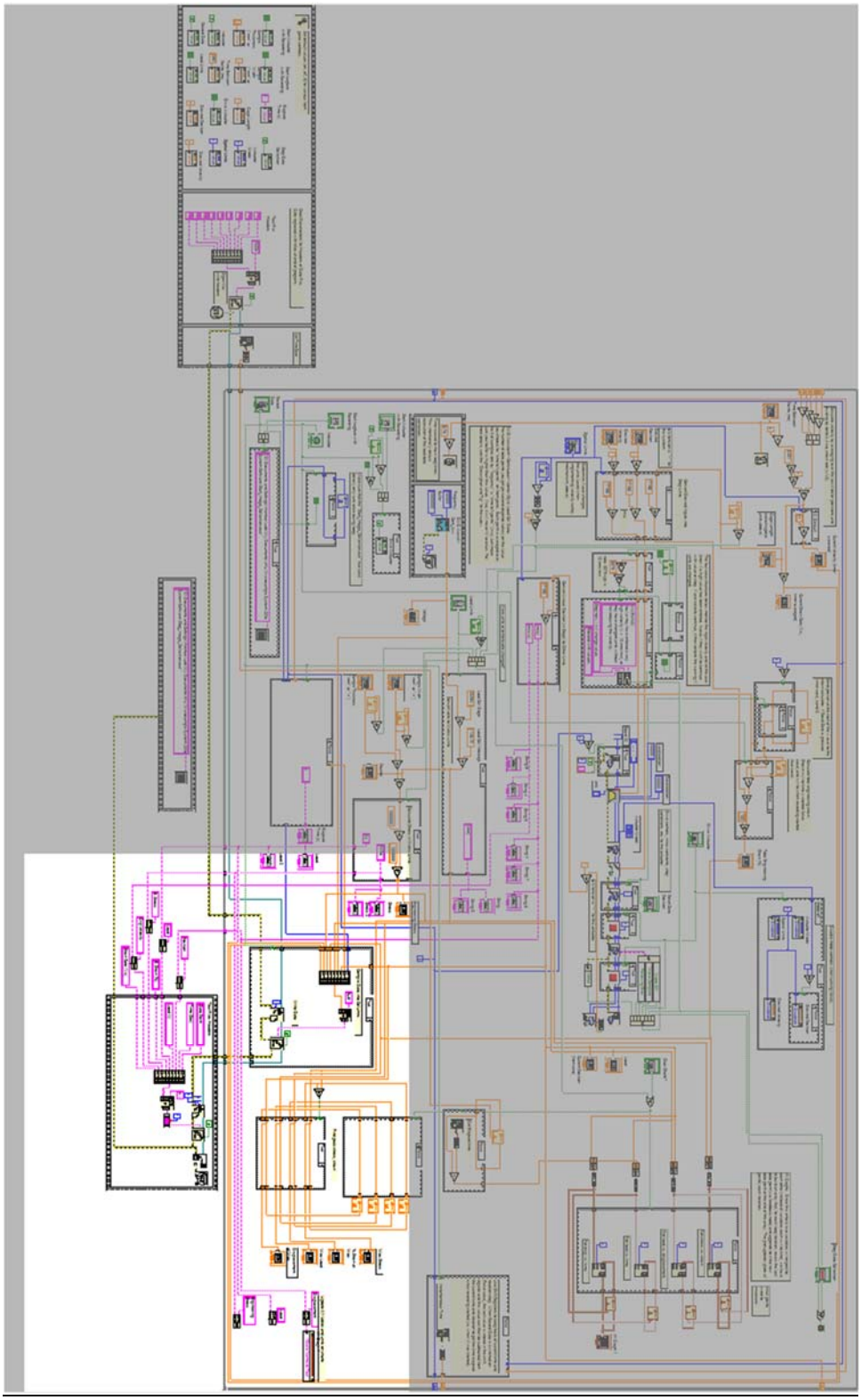

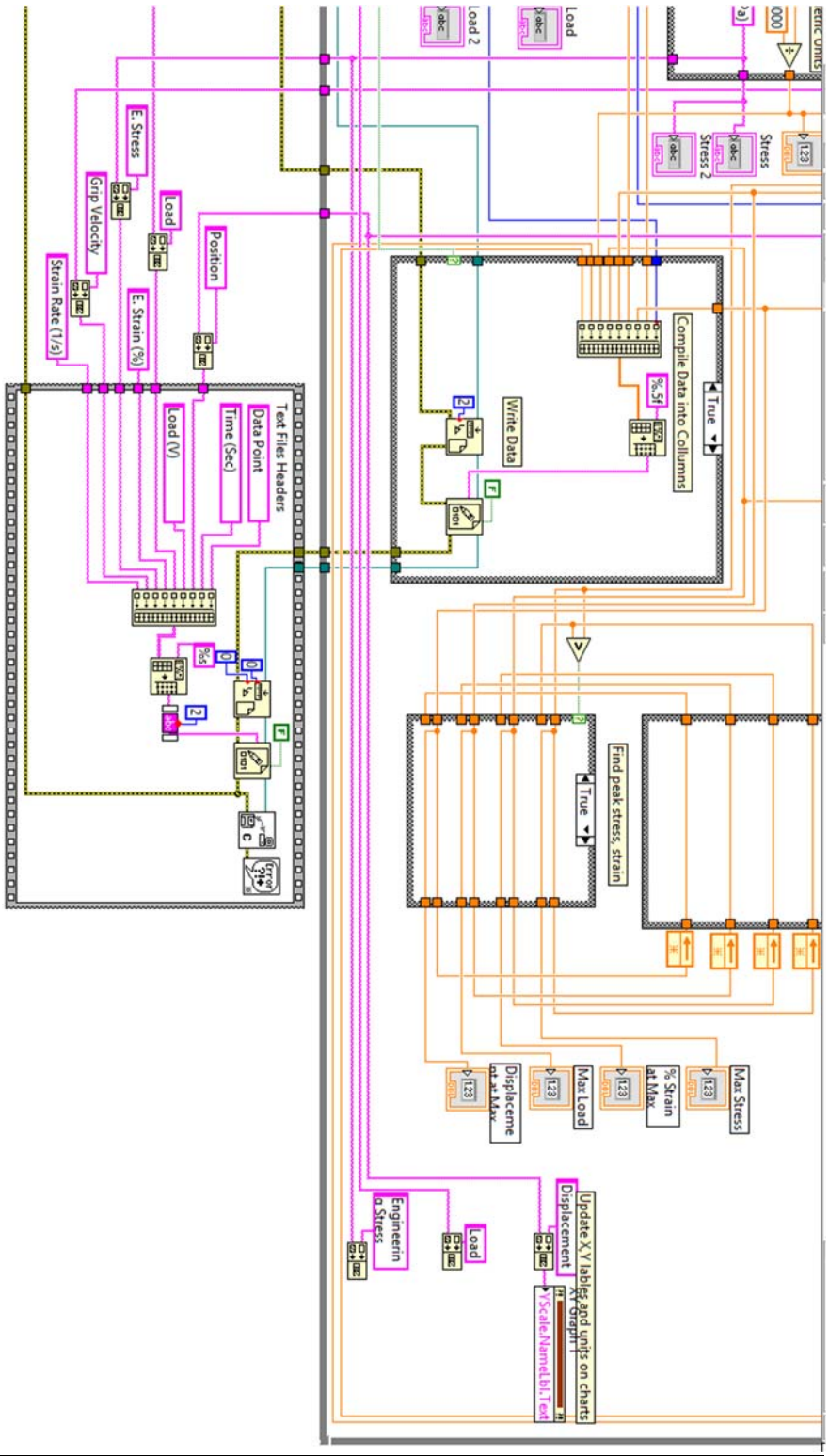
Load 2
Load
Stress
Stress 2
E. Stress
Grip Velocity
Load
Position
Strain Rate (1/s)
E. Strain (%)
Compile Data into Columns
True
Write Data
Text Files Headers
Load (V)
Time (Sec)
Data Point
Find peak stress, strain
True
Displaceme
Max Load
% Strain
Max Stress
Engineerin
Stress
Load
Displacement
Update X,Y lables and units on charts
XY Graph
YScale.NameLbl.Text

LabVIEW Wire Diagram Panel D

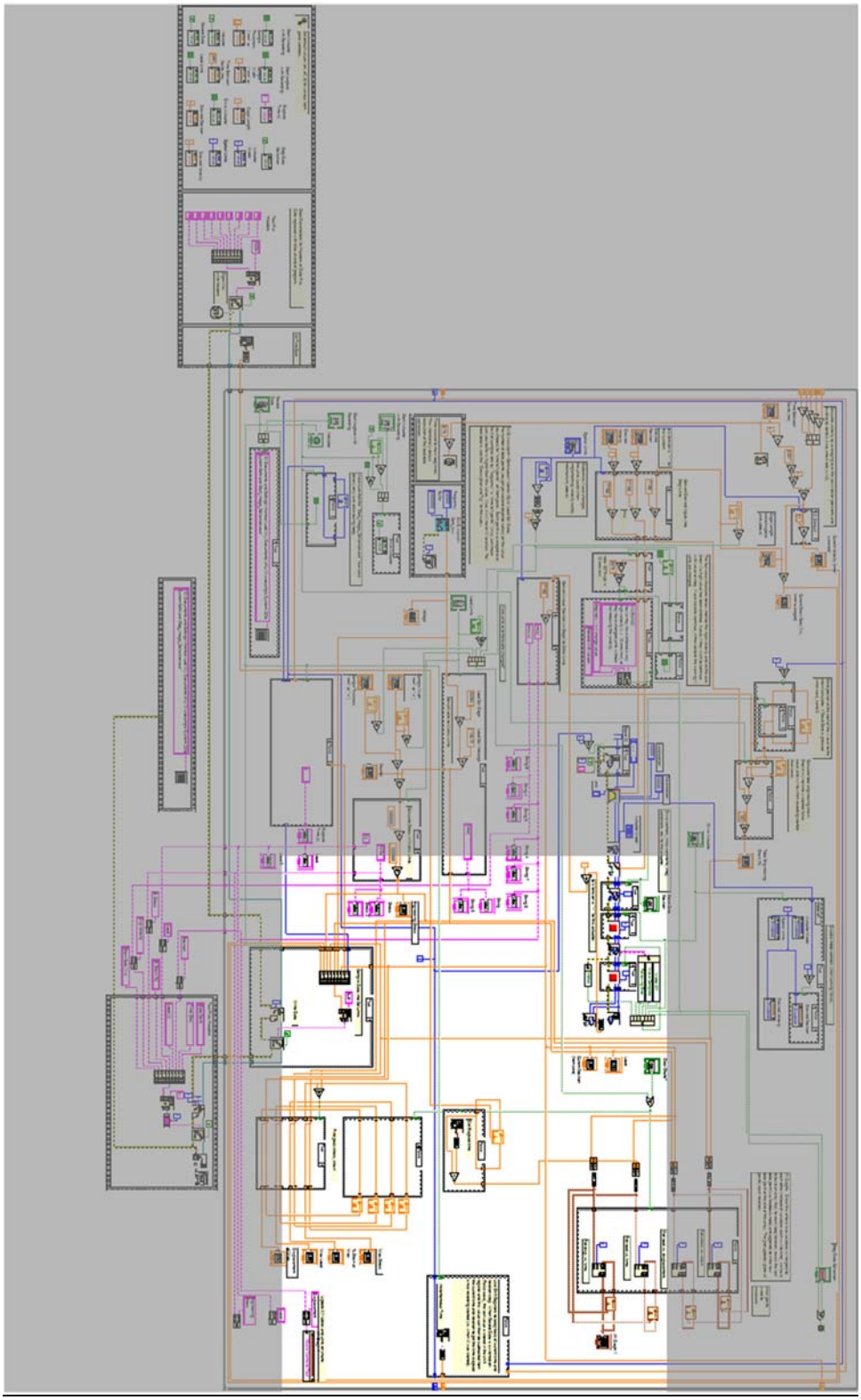

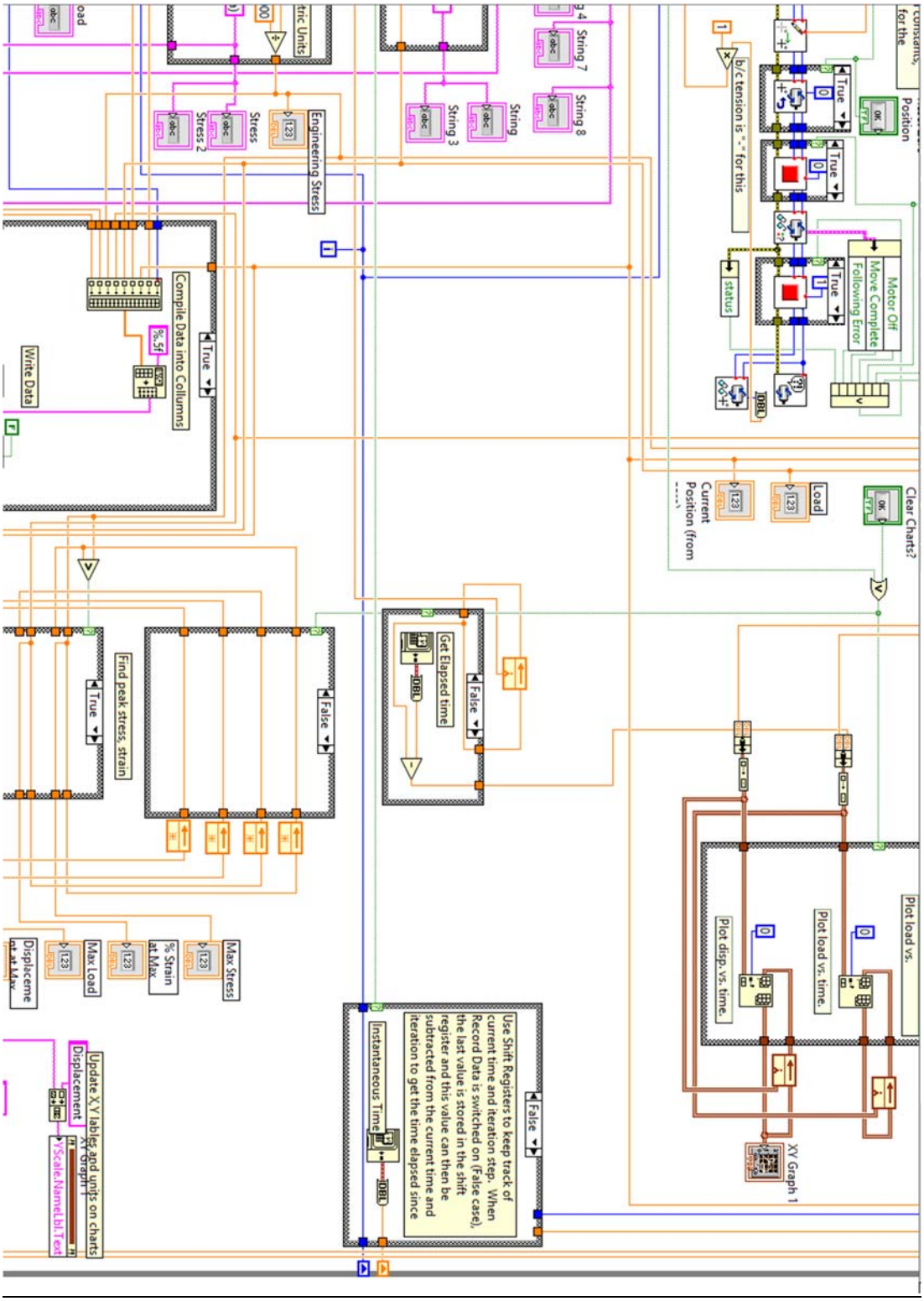
Position
b/c tension is "-" for this
True
Motor Off
Move Complete
Following Error
status
Clear Charts?
Load
Current Position (from
String 7
String 8
String 3
String
Stress 2
Stress
Engineering Stress
Compile Data into Columns
%.5f
Write Data
Get Elapsed time
False
Find peak stress, strain
Plot load vs.
Plot disp. vs. time.
Plot load vs. time.
XY Graph 1
Use Shift Registers to keep track of current time and iteration step. When Record Data is switched on (False case), the last value is stored in the shift register and this value can then be subtracted from the current time and iteration to get the time elapsed since
Instantaneous Time
Max Load
% Strain at Max
Max Stress
Displaceme
Update XY labels and units on charts
Displacement
XY Graph
YScale.NameLbl.Text

LabVIEW Wire Diagram Panel E

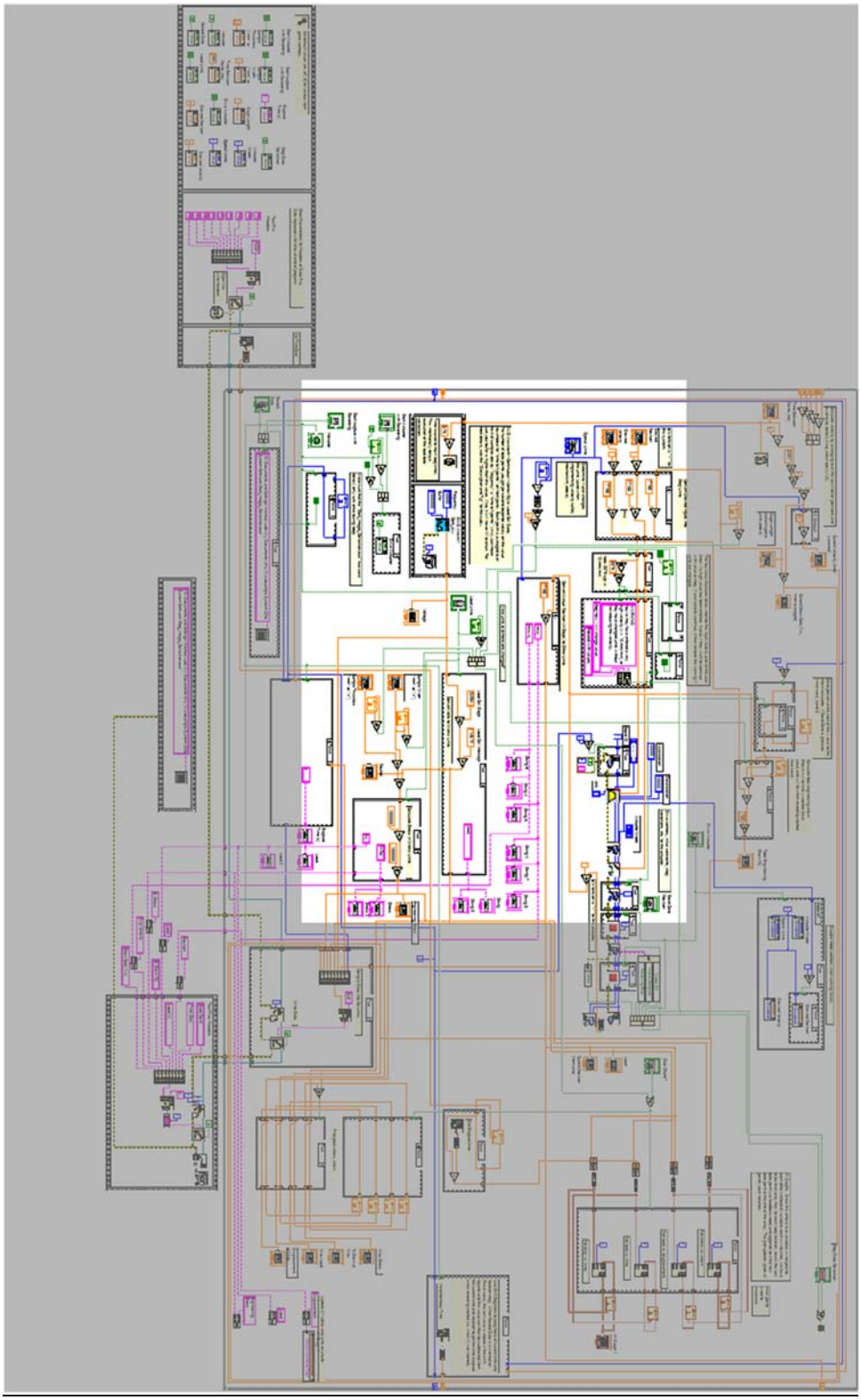

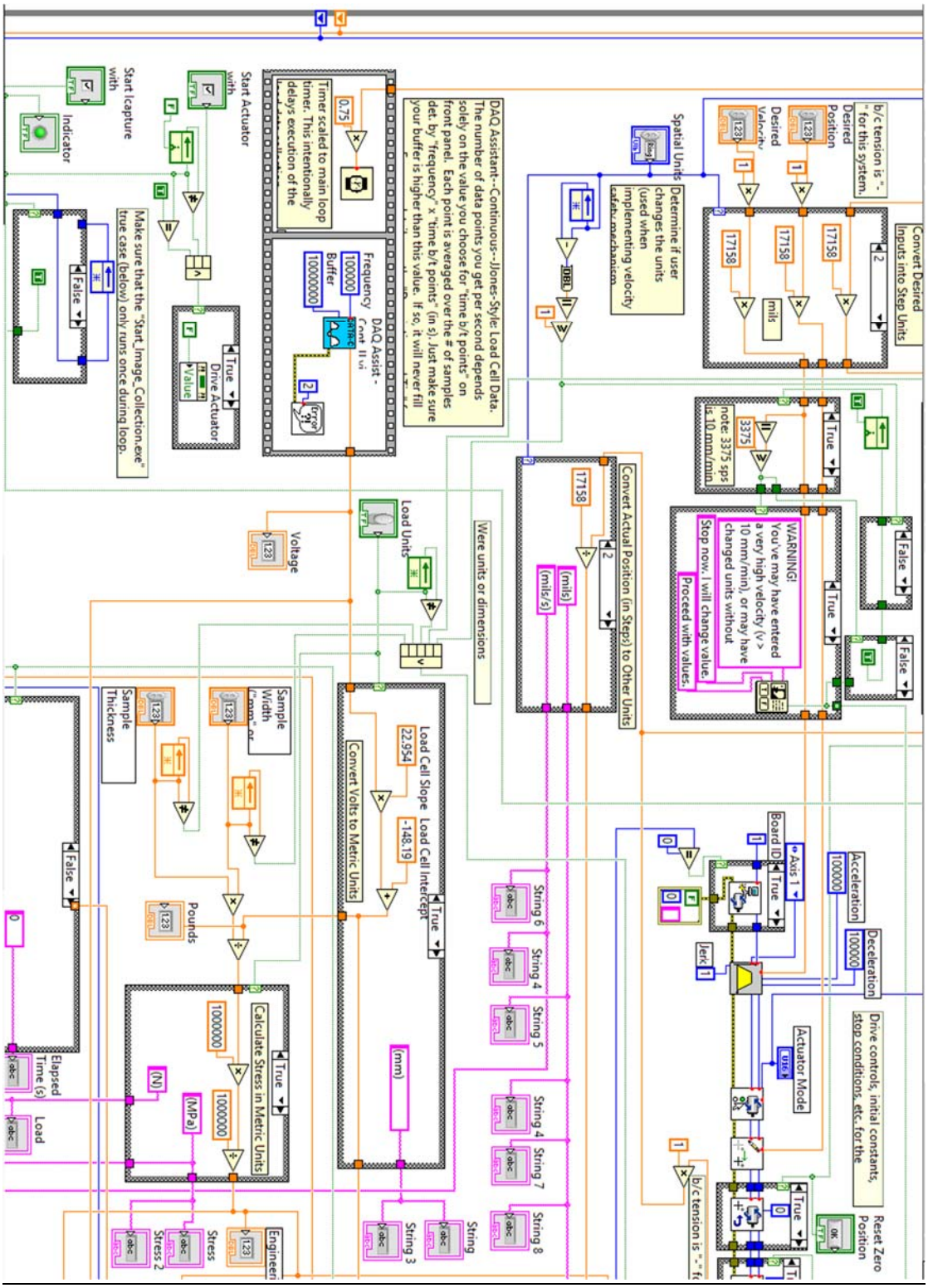
Convert Desired Inputs into Step Units
b/c tension is "-" for this system.
Desired Position
Desired Velocity
17158
mils
Spatial Units
Determine if user changes the units (used when implementing velocity
DBL
3375
note: 3375 sps is 10 mm/min
WARNING! You've may have entered a very high velocity (v > 10 mm/min), or may have changed units without
Stop now. I will change value.
Proceed with values.
Convert Actual Position (in Steps) to Other Units
(mils)
(mils/s)
DAQ Assistant--Continuous--Jlones-Style: Load Cell Data.
The number of data points you get per second depends solely on the value you choose for "time b/t points" on front panel. Each point is averaged over the # of samples det. by "frequency" x "time b/t points" (in s). Just make sure your buffer is higher than this value. If so, it will never fill
Timer scaled to main loop timer. This intentionally delays execution of the
0.75
Frequency
100000
Buffer
10000000
DAQ Assist -
Start Actuator with
Start Capture with
Indicator
Make sure that the "Start_Image_Collection.exe" true case (below) only runs once during loop.
Drive Actuator
Value
Were units or dimensions
Load Units
Voltage
Load Cell Slope
22.954
Load Cell Intercept
-148.19
Convert Volts to Metric Units
Sample Thickness
Sample Width
Pounds
Calculate Stress in Metric Units
1000000
(N)
(MPa)
(mm)
Elapsed Time (s)
Load
Stress
Stress 2
Engineeri
String
String 3
String 4
String 5
String 6
String 7
String 8
Board ID
Axis 1
Acceleration
100000
Deceleration
100000
Jerk
1
Actuator Mode
Drive controls, initial constants, stop conditions, etc. for the
Reset Zero Position
OK

LabVIEW Wire Diagram Panel F

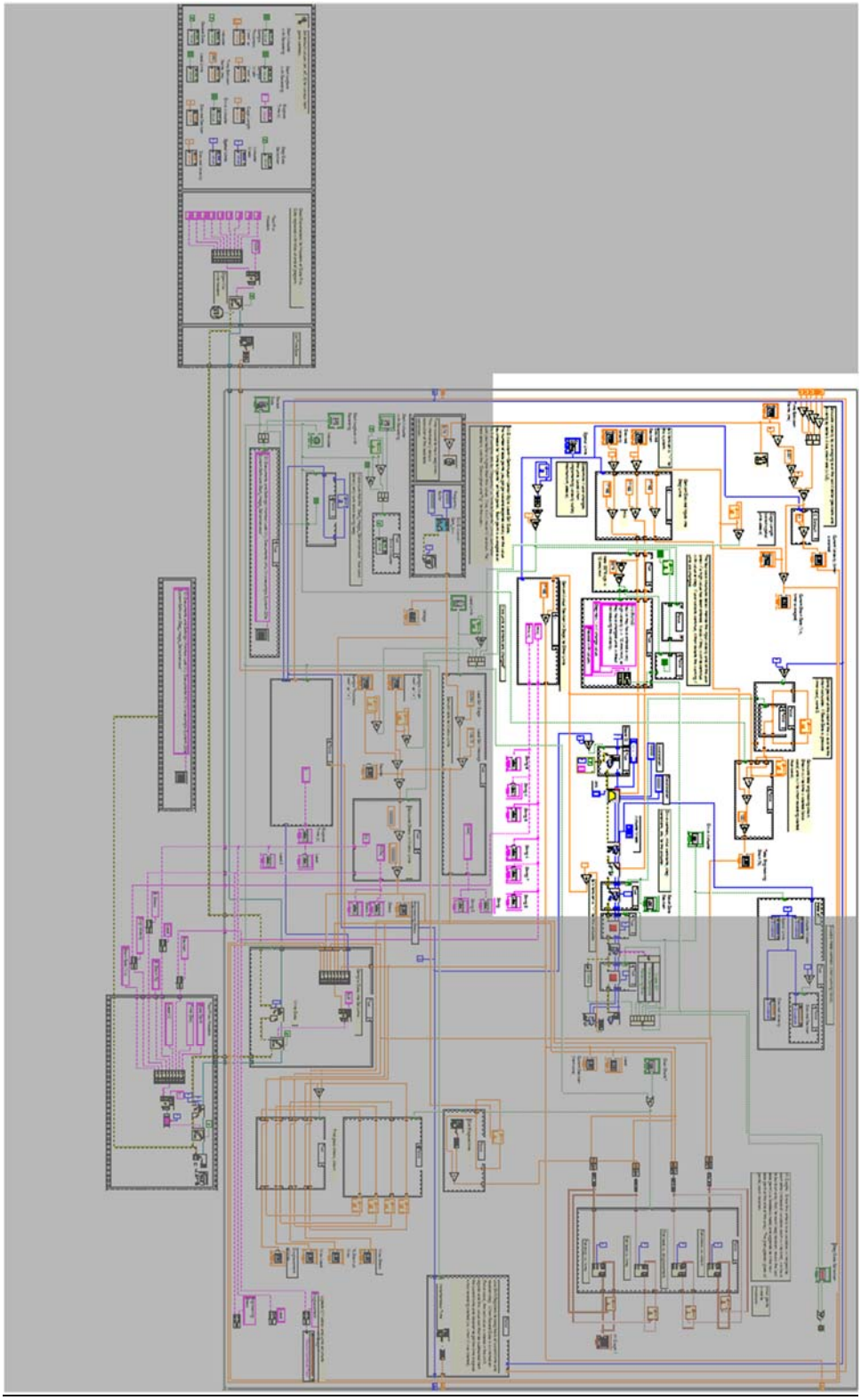

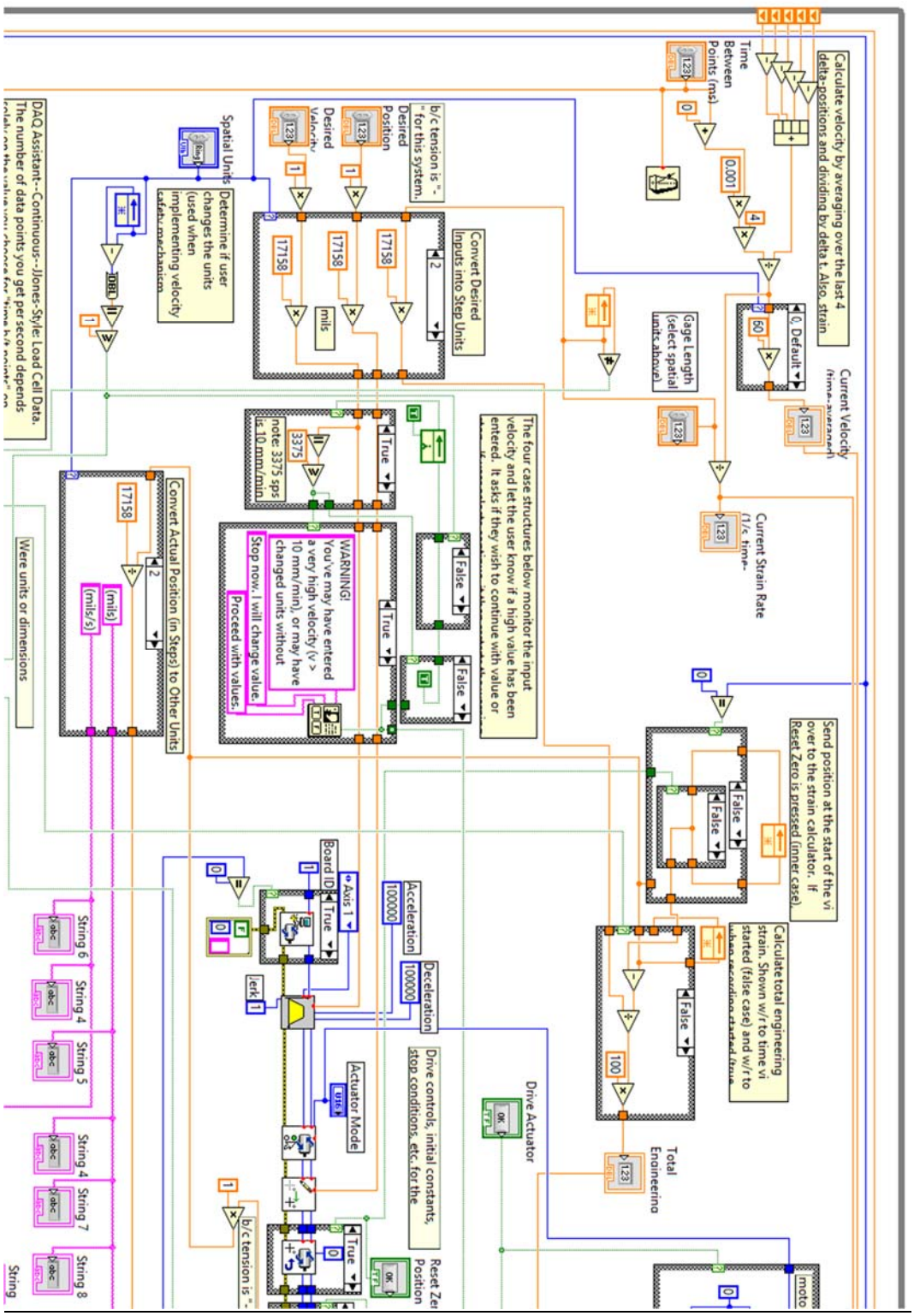
Calculate velocity by averaging over the last 4 delta-positions and dividing by delta t. Also, strain
Time Between Points (ms)
Current Velocity
Current Strain Rate
Gage Length (select spatial units above)
Total Engineering
Convert Desired Inputs into Step Units
Desired Position
Desired Velocity
b/c tension is "-" for this system.
Spatial Units
Determine if user changes the units (used when implementing velocity safety mechanism
DAQ Assistant--Continuous--JJones-Style Load Cell Data. The number of data points you get per second depends
The four case structures below monitor the input velocity and let the user know if a high value has been entered. It asks if they wish to continue with value or
note: 3375 sps is 10 mm/min
WARNING! You've may have entered a very high velocity (v > 10 mm/min), or may have changed units without
Stop now. I will change value.
Proceed with values.
Convert Actual Position (in Steps) to Other Units
Were units or dimensions
Send position at the start of the vi over to the strain calculator. If Reset Zero is pressed (inner case).
Calculate total engineering strain. Shown w/r to time vi started (false case) and w/r to
Drive Actuator
Drive controls, initial constants, stop conditions, etc. for the
Reset Zero Position
Actuator Mode
Acceleration
Deceleration
Board ID
Axis 1
Jerk
String 6
String 4
String 5
String 4
String 7
String 8
String

LabVIEW Wire Diagram Panel G

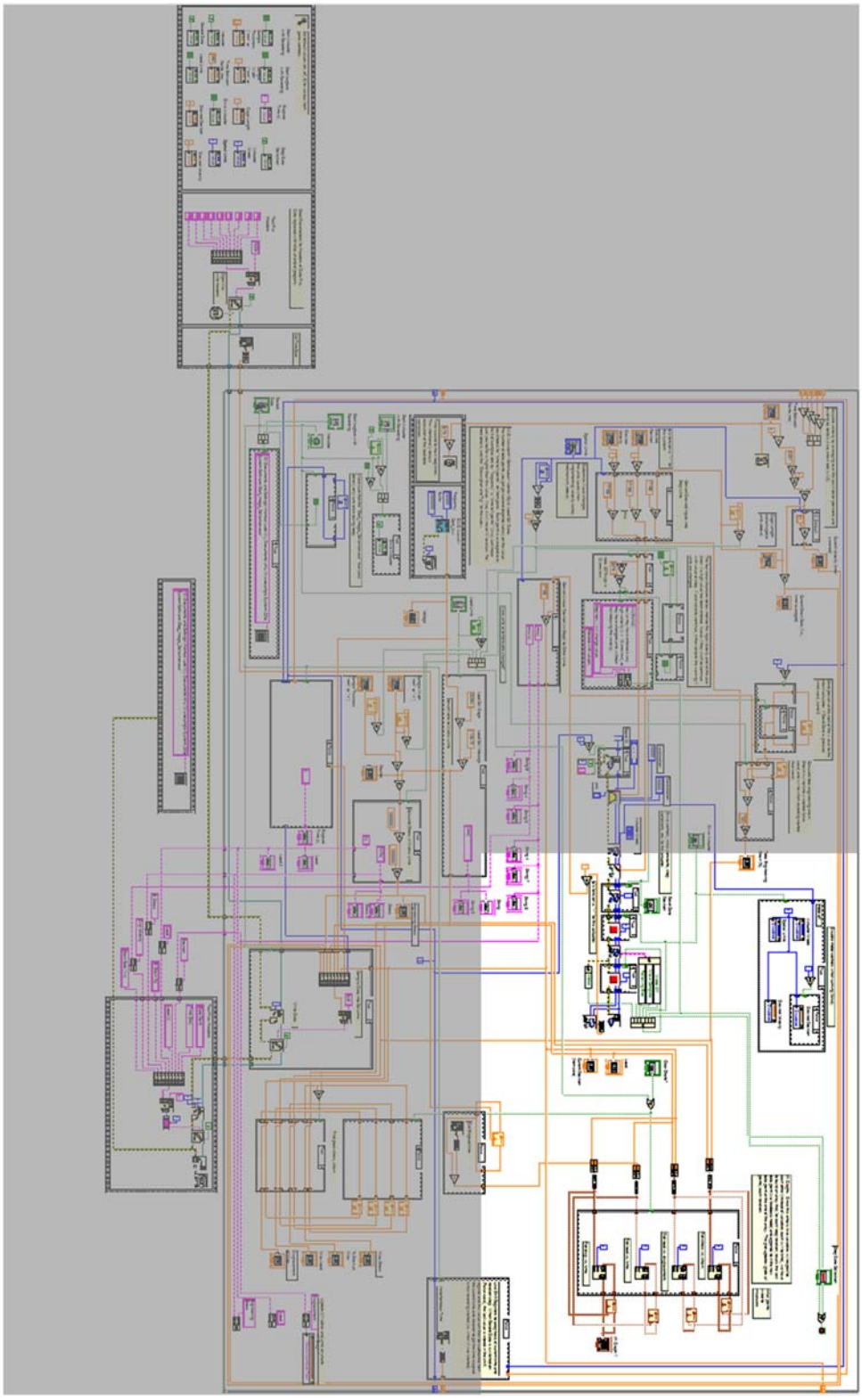

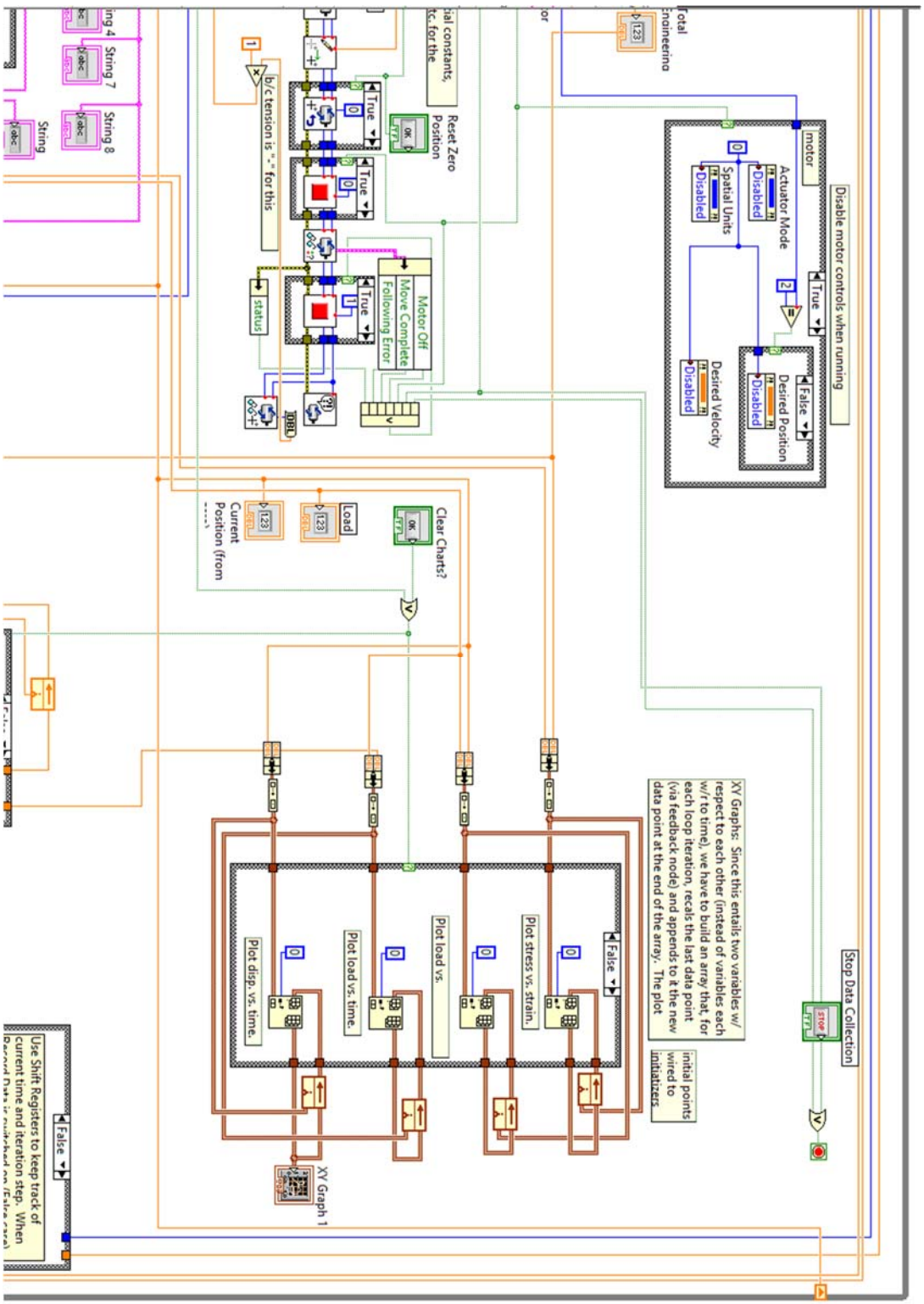
Disable motor controls when running
motor
Actuator Mode
Disabled
Spatial Units
Disabled
Desired Position
Disabled
Desired Velocity
Disabled
True
False
Stop Data Collection
stop
Reset Zero Position
Motor Off
Move Complete
Following Error
status
b/c tension is "-" for this
Clear Charts?
Load
Current Position (from
Plot disp. vs. time.
Plot load vs. time.
Plot load vs.
Plot stress vs. strain.
XY Graph 1
XY Graphs: Since this entails two variables w/ respect to each other (instead of variables each w/r to time), we have to build an array that, for each loop iteration, recalls the last data point (via feedback node) and appends to it the new data point at the end of the array. The plot initial points wired to initializers
Use Shift Registers to keep track of current time and iteration step. When
String
String 7
String 8

References for Appendix B

1. Jones, J.S., *Characterization of interfacial adhesion between carbon-carbon composite and plasme-sprayed aluminum oxide*, in *Department of Mechanical Engineering*. 2009, Johns Hopkins University: Baltimore, MD. p. 278.

APPENDIX C: 4-POINT BEND NEUTRAL AXIS MATLAB FILE

```
% File Name: Geometry_Calculation.m
%
% Description: Determines the thickness of the stiffener required to
keep
% the neutral axis along the tgo/top coat interface
%
% Syntax: n/a
%
% Inputs:
%    none
%
% Outputs:
%    h6 - height of stiffener
%
% Other m-files required: none
% Subfunctions: coating_energy_released_function
%               neutral_axis_function
% MAT-files required: none

% Author: Simon Lockyer-Bratton
% email: slockye3@jhu.edu
% Date Created: 03-January-2013
% Last revision: 06-June-2016

%------------- BEGIN CODE --------------

function [h1,h6] = Geometry_Calculation()

% Fraction of Strain Energy Released from Coating Layers to Drive
% Delamination
fraction_released = 0.1;

% Determines the thickness of the Stiffener from the Coating Energy
% Released Graph Shown in the Paper
h1 = coating_energy_released_function(fraction_released); % [m]

% Bond Coat Thickness
h2 = 100E-6; % [m]

% Top Coat Thickness
h3 = 150E-6; % [m]

% TGO Thickness
h4 = 0.21E-6; % [m]

% Epoxy Thickness
h5 = 100E-6;

% Substrate/Stiffener Linear Isotropic Elastic Properties
E = 128E9; % [Pa]
v = 0.33;
```

```
% Load Cell Capacity
Pmax_lb = 500; % [lb]
Pmax = Pmax_lb*4.44822162; % [N]

% Actual Load at Some Fraction of Load Cell Capacity
P_scale = 0.9;
P = Pmax/P_scale; % N

% Stiffener Thickness Needed to Ensure Neutral Axis is on TGO/TC
Interface
h6 = neutral_axis_function(h1); % [m]

% Plotting Variables
offset = 50;
del = 30;
xpos = 2600;

% Sample Width Variation from 500 microns to 4 mm
b = 500E-6:1E-6:4E-3; % [m]

% Averages Stiffener and Substrate Thicknesses for Use in Calculations
h = (h1+h6)/2; % [m]

lo = 20E-3; % [m]
li = 10E-3; % [m]

% Calculates Maximum Strain Energy Release Rate as a Function of the
% Substrate Width at a Given Fraction of Load Cell Capacity
G = ((3*(P^2)*((lo-li)^2)*(1-v^2))./(16*E.*b*h^3));

plot(b*(1E6),G,'--r','LineWidth',3)
hold on

line([min(b)*(1E6) max(b)*(1E6)],[450 450],'Color','m','LineWidth',3)
hold on
line([min(b)*(1E6) max(b)*(1E6)],[100 100],'Color','k','LineWidth',3)
hold on
line([min(b)*(1E6) max(b)*(1E6)],[50 50],'Color','b','LineWidth',3)
axis([min(b)*(1E6) max(b)*(1E6) 0 max(G)])

hleg1 = legend(['G_{c,max}'],['G = 450 J/m^{2}'],['G = 100
J/m^{2}'],['G = 50 J/m^{2}']);
set(gca,'FontSize',16)
set(hleg1,'FontSize',20)
xlabel('b [\mum]','FontSize',20)
ylabel('Strain Energy Release Rate [J/m^{2}]','FontSize',20)
if P_scale == 1
    title(sprintf('G_{c,max} as a Function of Width Parameter b for P =
P_{max}'),'FontSize',22)
else
    title(sprintf('G_{c,max} as a Function of Width Parameter b for a
%g lb Load Cell at %.4g%% Capacity',Pmax_lb,100*P_scale),'FontSize',22)
end

end

%%
```

```
function [output] = coating_energy_released_function(fraction_released)

% Creates symbolic variables for ease of calculation
syms h t h1 h2 h3 h4

y = 1.586133*((h+t)/t)^(-1.115993);

y = subs(y,[h,t],[h4,h2+h3]);

% Solves symbolic equation
h_temp = solve(y == fraction_released,h4);

% Output is required substrate thickness to meet energy released
criterion
output = eval(subs(h_temp,[h2,h3],[100E-6,150E-6]));

end

%%
function [output] = neutral_axis_function(h_eval)

% Calculates the required stiffener height for the neutral axis to lie
on
% the tgo/top coat interface by taking the position of the neutral axis
% from the bottom of the substrate layer

% Creates symbolic variables for ease of calculation
syms b h_Sub h_BC h_TGO h_TC h_Epoxy h_Stiff E_Sub E_BC E_TGO E_TC
E_Epoxy E_Stiff

% Transformed area definitions
n_BC = E_BC/E_Sub;
n_TGO = E_TGO/E_Sub;
n_TC = E_TC/E_Sub;
n_Epoxy = E_Epoxy/E_Sub;

% Calculates transformed areas
A_Sub = h_Sub*b;
A_BC = n_BC*h_BC*b;
A_TGO = n_TGO*h_TGO*b;
A_TC = n_TC*h_TC*b;
A_Epoxy = n_Epoxy*h_Epoxy*b;
A_Stiff = h_Stiff*b;

% Neutral axis of each layer is defined
y_Sub = h_Sub/2;
y_BC = h_Sub+(h_BC/2);
y_TGO = h_Sub+h_BC+(h_TGO/2);
y_TC = h_Sub+h_BC+h_TGO+(h_TC/2);
y_Epoxy = h_Sub+h_BC+h_TGO+h_TC+(h_Epoxy/2);
y_Stiff = h_Sub+h_BC+h_TGO+h_TC+h_Epoxy+(h_Stiff/2);

% Calculates sums of Areas*y_bar and Areas
sumAy =
A_Sub*y_Sub+A_BC*y_BC+A_TGO*y_TGO+A_TC*y_TC+A_Epoxy*y_Epoxy+A_Stiff*y_S
tiff;
sumA = A_Sub+A_BC+A_TGO+A_TC+A_Epoxy+A_Stiff;
```

```
% Location of the neutral axis (right above TGO)
d = h_Sub+h_BC+h_TGO;

% Equation for the neutral axis positions (y_bar=0 at tgo/top coat
% interface)
y_bar = simplify(sumAy/sumA-d);

% Solves symbolic function for the stiffener height
h_Stiff_solved = solve(y_bar==0,'h_Stiff');

% Creates an inline function from the solved symbolic function
h_Stiff_solved_in = inline(h_Stiff_solved);

% Propert and height definitions
E_Sub = 128; % [GPa]
E_BC = 153; % [GPa]
E_TGO = 300; % [GPa]
E_TC = 50; % [GPa]
E_Epoxy = 1.3; % [GPa]
h_BC = 100E-6; % [m]
h_TGO = 0.21E-6; % [m]
h_TC = 150E-6; % [m]
h_Epoxy = 100E-6; % [m]

% Evaluates the stiffener height with given inputs
h_Stiff_eval =
h_Stiff_solved_in(E_BC,E_Epoxy,E_Sub,E_TC,E_TGO,h_BC,h_Epoxy,h_eval,h_T
C,h_TGO);

% Ignores negative root as it has no physical meaning
for i = 1:2
    if h_Stiff_eval(i,:)>0
        output = h_Stiff_eval(i,:);
        break
    end
end

end

%------------- END OF CODE -----------
```

APPENDIX D: PLATEAU LOAD CALCULATION MATLAB FILE

```
% File Name: Data_Average.m
%
% Description: Calculates the average plateau load during delamination
in
% a 4-point bend test by graphically selecting the plateau load region
% from an experimental load-deflection curve
%
% Syntax: n/a
%
% Inputs:
%    data - Excel file containing stress-strain data (.xlsx)
%
% Outputs:
%    Pc - Average plateau stress value
%
% Other m-files required: none
% Subfunctions: none
% MAT-files required: none

% Author: Simon Lockyer-Bratton
% email: slockye3@jhu.edu
% Date Created: 05-June-2015
% Last revision: 30-May-2016

%------------- BEGIN CODE --------------

clear,clc

% Select text file to extract data from
[Filename, Pathname] = uigetfile('*.xlsx','Please Select Load
Displacement XLSX File');

% Load data from selected text file
data = xlsread([Pathname '\' Filename]);

% Allocate displacement and load to corresponding columns
displacement = data(:,1);
force = data(:,2);

% Plot stress vs. strain for point selection
plot(displacement,force,'k')
axis([min(displacement) max(displacement) min(force) max(force)*1.2])
hold on
xlabel('Displacement [mm]')
ylabel('Force [N]')
title('Force vs. Displacement')

% Select points
title('Please Select Lower Bound')
[displacement_min,~] = ginput(1);
minimum = find(displacement>=min(displacement_min),1);
```

```
hold on
line([displacement(minimum) displacement(minimum)],[0 max(force)*1.2])

title('Please Select Lower Bound')
[displacement_max,~] = ginput(1);
maximum = find(displacement>max(displacement_max),1);
hold on
line([displacement(maximum) displacement(maximum)],[0 max(force)*1.2])
pause(0.1)

close all

Pc = mean(force(minimum:maximum));

msgbox(['P_c = ' num2str(Pc) ' N'])

%------------- END OF CODE -----------
```

VITA

Simon Lockyer-Bratton was born in Fairfax, Virgina on July 17th 1988. Simon later moved to Scottsdale, Arizona and graduated from Chaparral High School in 2006. He then went on to study Mechanical Engineering at Northern Arizona University (NAU) in Flagstaff, Arizona and performed research under the advisement of Professor Brent Nelson. In May 2011, Simon completed his undergraduate studies and earned a Bachelor of Science in Engineering degree in Mechanical Engineering. In the fall of 2012, Simon joined the Department of Mechanical Engineering at Johns Hopkins University (JHU) to pursue his graduate studies under the guidance of Kevin J. Hemker. In December of 2012 he earned a Master of Science in Engineering degree in Mechanical Engineering and continued on fulfilling the requirements for a Doctor of Philosophy in Mechanical Engineering in July 2016. Upon graduation, Simon will join Exponent Failure Analysis Associates as an Associate Consultant in the Materials and Corrosion Engineering group in Menlo Park, California.